Can GNSS contribute to improving the ITRF definition ?

Paul Rebischung

To cite this version:

Paul Rebischung. Can GNSS contribute to improving the ITRF definition ?. Astrophysics [astro-ph]. Observatoire de Paris, 2014. English. NNT : . tel-02095157

HAL Id: tel-02095157
https://hal.science/tel-02095157

Submitted on 10 Apr 2019

OBSERVATOIRE DE PARIS

ÉCOLE DOCTORALE
ASTRONOMIE ET ASTROPHYSIQUE D'ÎLE-DE-FRANCE

DOCTORAT ASTRONOMIE ET ASTROPHYSIQUE

Paul REBISCHUNG

CAN GNSS CONTRIBUTE TO IMPROVING THE ITRF DEFINITION?

Thèse dirigée par M. Zuheir ALTAMIMI et M. Tim SPRINGER

Soutenue le 13 juin 2014

Jury :

Mme Nicole CAPITAINE	Présidente du Jury
M. Athanasios DERMANIS	Rapporteur
M. Urs HUGENTOBLER	Rapporteur
M. Gérard PETIT	Examinateur
M. Félix PEROSANZ	Examinateur
M. Zuheir ALTAMIMI	Directeur de thèse
M. Tim SPRINGER	Co-directeur de thèse

Institut National de l'Information Géographique et Forestière (IGN)
Laboratoire de Recherche en Géodésie (LAREG)
5 rue Thomas Mann, 75205 Paris Cedex 13, France

The stars are indifferent to astronomy.
– Peter J. Caws

Résumé

Les systèmes globaux de navigation par satellite (GNSS) jouent un rôle fondamental dans l'élaboration du repère international de référence terrestre (ITRF). Cependant, les GNSS ne se sont jusqu'à présent pas révélés aptes à déterminer de manière fiable l'échelle terrestre ni la position du centre de masse de la Terre (géocentre) et n'ont donc pas contribué à définir l'échelle de l'ITRF ni son origine. L'incapacité des GNSS à déterminer l'échelle terrestre indépendamment de biais conventionnels de centres de phase satellites est un problème bien connu. En revanche, leur incapacité à correctement observer le mouvement du géocentre restait jusqu'alors inexpliquée.

Nous avons étudié cette question sous l'angle de la colinéarité entre paramètres d'un ajustement par moindres carrés. Pour prendre en compte plusieurs particularités du problème de la détermination du géocentre par GNSS, un diagnostic de colinéarité généralisé a été développé. Il a ainsi été mis en évidence que la détermination du géocentre par GNSS est sujette à de sérieux problèmes de colinéarité à cause de l'estimation simultanée de décalages d'horloges et de paramètres troposphériques dans les analyses de données GNSS.

Différentes pistes ont finalement été étudiées en vue d'une possible future contribution des GNSS à la définition de l'échelle et de l'origine de l'ITRF : l'étalonnage de l'antenne d'au moins un satellite GNSS, l'invariabilité temporelle des biais de centres de phase satellites, l'analyse simultanée de données GNSS acquises par des stations terrestres et des satellites bas, la modélisation d'horloges satellites ultra-stables et la réduction des erreurs de modélisation orbitale.

Mots-clés : ITRF, GNSS, origine, échelle, géocentre, colinéarité, multicolinéarité, facteur d'inflation de la variance, corrélation

Abstract

Global Navigation Satellite Systems (GNSS) play a fundamental role in the elaboration of the International Terrestrial Reference Frame (ITRF). However, GNSS have so far not proven able to reliably determine the terrestrial scale nor the location of the Earth's center of mass (geocenter) and have thus not contributed to defining the ITRF scale nor its origin. The weak ability of GNSS to determine the terrestrial scale apart from conventional satellite phase center offsets is well understood. On the other hand, their inability to reliably monitor geocenter motion was so far not clearly explained.

We investigated this question from the perspective of collinearity among the parameters of a least-squares regression. A generalized collinearity diagnosis was therefore developed and allows handling several peculiarities of the GNSS geocenter determination problem. It revealed that the determination of all three components of geocenter motion with GNSS suffers from serious collinearity issues due to the simultaneous estimation of epoch-wise station and satellite clock offsets and of tropospheric parameters in global GNSS data analyses.

Several prospects were finally investigated in view of a possible future contribution of GNSS to the definition of the ITRF scale and origin: the antenna calibration of at least one GNSS satellite, the time invariability of the satellite phase center offsets, the simultaneous analysis of GNSS data collected by ground stations and low Earth orbiting satellites, the modelling of ultra-stable satellite clocks and the mitigation of orbit modelling errors.

Keywords: ITRF, GNSS, origin, scale, geocenter, collinearity, multicollinearity, variance inflation factor, correlation

Résumé substantiel

La disponibilité d'un système de référence terrestre et de sa réalisation physique, un repère de référence terrestre, est nécessaire à de vastes domaines d'applications qui nécessitent de localiser ou de suivre les mouvements d'objets autour de la Terre. Dans le domaine particulièrement exigeant des sciences de la Terre, le système international de référence terrestre (ITRS) est aujourd'hui largement adopté. Il s'agit d'un repère idéal attaché à la croûte terrestre et défini par son origine (le centre des masses de la Terre ou géocentre), son échelle (cohérente avec la définition SI du mètre) et son orientation. Sa réalisation physique, le repère international de référence terrestre (ITRF) consiste en un jeu de coordonnées pour un ensemble de points géodésiques et de points de référence d'instruments géodésiques.

La détermination des coordonnées ITRF repose actuellement sur les observations de quatre techniques de géodésie spatiale: l'interférométrie à très longue base (VLBI), la télémétrie laser sur satellite (SLR), les systèmes globaux de navigation par satellite (GNSS) et le système de détermination d'orbite et de radiopositionnement intégré par satellite (DORIS). Un point particulièrement crucial de l'élaboration de l'ITRF réside en la définition de son échelle et de son origine. Tandis que l'échelle terrestre peut être en principe déterminée par les quatre techniques contribuant à l'ITRF, seuls le VLBI et le SLR ont jusqu'à présent contribué à la définition de l'échelle de l'ITRF. De la même façon, les trois techniques satellitaires (SLR, GNSS et DORIS) peuvent en principe déterminer la position du centre des masses de la Terre. Mais seul le SLR a jusqu'à présent contribué à définir l'origine de l'ITRF.

La contribution des GNSS à l'ITRF est fondamentale par plusieurs aspects. C'est par les GNSS que sont assurés la dissémination de l'ITRF et le lien entre les trois autres techniques. Les GNSS ont de plus la contribution la plus robuste et précise à la détermination des coordonnées ITRF et de certains paramètres d'orientation de la Terre. La contribution des GNSS à l'ITRF est néanmoins affectée par diverses erreurs systématiques et reste donc perfectible. En particulier, l'information d'origine et d'échelle issue de l'analyse de données GNSS n'a jusqu'à présent pas été jugée assez fiable pour pouvoir contribuer à définir l'origine et l'échelle de l'ITRF. Cette situation a été la motivation principale de cette thèse. Nous avons ainsi chercher à comprendre l'incapacité des GNSS déterminer l'échelle terrestre et la position du géocentre de manière fiable et à proposer des pistes pour améliorer cette détermination.

Le problème fondamental concernant la détermination de l'échelle terrestre par GNSS avait en fait déjà été identifié par Springer (2000) et Zhu et al. (2003). Dans une analyse globale de données GNSS, il existe en effet une corrélation quasiment parfaite entre l'échelle terrestre, les biais de centres de phase satellites, les délais troposphériques zénithaux humides et les décalages d'horloges des stations et des satellites. Comme un étalonnage d'antenne n'est disponible pour aucun des satellites actuellement en orbite, cette corrélation quasi-parfaite empêche une détermination fiable de l'échelle terrestre par GNSS indépendamment de biais conventionnels de centres de phase satellites.

En revanche, l'incapacité des GNSS à correctement observer le mouvement du géocentre restait inexpliquée au début de cette thèse. Afin de clarifier cette situation, nous avons choisi d'étudier la question sous l'angle de la colinéarité entre paramètres d'un ajustement par moindres carrés. Pour prendre en compte plusieurs particularités du problème de la détermination du géocentre par GNSS, un diagnostic de colinéarité généralisé, basé sur la notion de facteur d'inflation de la variance (VIF), a ainsi été développé. Il permet d'évaluer et d'expliquer la colinéarité de tout paramètre explicite ou implicite d'une régression par moindres carrés généralisés en présence de contraintes.

Ce diagnostic de colinéarité généralisé a ensuite été appliqué au problème de la détermination du géocentre par SLR. Il a ainsi été mis en évidence que la détermination des coordonnées X et Y du géocentre par SLR n'est sujette à aucun problème de colinéarité. Dans des analyses simulées de données SLR, un VIF de l'ordre de 9 a cependant été obtenu pour la coordonnée Z du géocentre. Cette situation de colinéarité modérée s'explique par une corrélation entre la coordonnée Z du géocentre et les éléments osculateurs des satellites. Elle peut contribuer à expliquer, conjointement avec la répartition inégale des stations SLR, la moindre qualité de la composante Z du mouvement du géocentre observé par SLR comparée à ses composantes X et Y.

Dans des analyses simulées de données GNSS, une situation totalement différente a été mise en évidence par notre diagnostic de colinéarité généralisé. Il a en effet été démontré que les trois coordonnées du géocentre sont extrêmement colinéaires aux autres paramètres estimés dans des analyses globales de données GNSS. Cette situation d'extrême colinéarité explique pourquoi les trois composantes de l'origine de repères terrestres estimés par GNSS correspondent à des quasi-singularités et pourquoi le mouvement du géocentre ne peut être restitué de manière fiable par des analyses GNSS standards.

Parmi les paramètres estimés dans des analyses globales de données GNSS, deux catégories particulières expliquent quasi-entièrement l'extrême colinéarité des coordonnées du géocentre : les décalages d'horloges des stations et des satellites et les paramètres troposphériques. Il est ainsi possible de conclure que l'incapacité des GNSS, par opposition au SLR, à observer le mouvement du géocentre de manière fiable est due à l'estimation simultanée de décalages d'horloges par époque et de paramètres troposphériques.

Après avoir identifié les causes de l'incapacité des GNSS à déterminer de manière fiable l'échelle terrestre et le mouvement du géocentre, nous avons étudié différentes pistes qui pourraient éventuellement mener à une future contribution des GNSS à la définition de l'échelle et de l'origine de l'ITRF. Premièrement, le problème de l'échelle serait entièrement résolu si l'antenne d'au moins un satellite pouvait être étalonnée indépendamment de toute échelle terrestre conventionnelle. Cela pourrait devenir le cas si les étalonnages d'antenne effectuées pour les satellites Galileo avant leur lancement étaient rendus publics. Une autre possibilité consisterait à étalonner les antennes des satellites GNSS par rapport aux antennes étalonnées de satellites bas (Haines et al., 2004). Cependant, cette méthode est actuellement sujette à d'importantes erreurs systématiques qui restent à comprender et à atténuer.

Mais avant que des étalonnages absolus d'antennes satellites ne deviennent disponibles, la stabilité à long terme des biais de centres de phase satellites permet déjà d'envisager une contribution des GNSS à la définition de la dérive d'échelle de l'ITRF. En supposant l'invariabilité temporelles de ces biais, Collilieux and Schmid (2012) ont en effet montré que les contributions des différents centres d'analyse de l'IGS à l'ITRF2008 pouvaient fournir des estimations intrinsèques de la dérive d'échelle du repère terrestre avec une précision d'environ 0.25 mm/an. La voie d'une contribution des GNSS à la définition de la dérive d'échelle du prochain ITRF2013 est donc ouverte.

En vue d'améliorer la détermination du mouvement du géocentre par GNSS et d'une possible future contribution des GNSS à la définition de l'origine de l'ITRF, deux pistes complémentaires peuvent enfin être envisagées. La première serait d'améliorer la sensibilité des analyses GNSS aux coordonnées du géocentre en réduisant leur colinéarité. A cet égard, une première piste prometteuse est l'analyse simultanée de données GNSS acquises par des stations terrestres et des satellites bas. L'inclusion d'observations acquises par des satellites bas dans une analyse GNSS permet en effet de décorreler les coordonnées du géocentre des décalages d'horloges satellites. A l'heure actuelle, cette méthode ne permet cependant pas encore d'obtenir une estimation réaliste du mouvement du géocentre.

Une seconde piste prometteuse pour réduire la colinéarité des coordonnées du géocentre dans les analyses GNSS est la modélisation des décalages d'horloges satellites sous une autre forme que par des paramètres estimés indépendamment à chaque époque d'observation. De telles modélisations sont déjà possibles pour des satellites particuliers équipés d'horloges de dernière génération (G062, GIOVE-B) et seront également applicables à l'ensemble de la future constellation Galileo. Des variations périodiques non modélisées de ces horloges, dues par exemple à des variations de température, pourraient cependant compremettre toute réduction significative de la colinéarité de la composante Z du géocentre par ce biais.

Outre de la diminution des problèmes de colinéarité, une amélioration de la détermination du géocentre par GNSS peut également être attendue du perfectionnement de la modélisation des orbites des satellites GNSS, et plus particulièrement des forces non-gravitationnelles agissant sur ces satellites. A cet égard, des paramétrisations alternatives ou bien des modèles analytiques précis de ces forces non-gravitationnelles pourraient finir par permettre d'estimer le mouvement du géocentre de façon fiable par GNSS. Mais le meilleur moyen de surmonter les problèmes de modélisation des forces non-gravitationnelles serait probablement d'équiper les futurs satellites GNSS d'accéléromètres 3D.

Il existe ainsi plusieurs pistes pouvant éventuellement déboucher sur une observation fiable du mouvement du géocentre par GNSS. Pour le moment, il est cependant difficile de prévoir si l'une de ces pistes finira par donner des résultats satisfaisants, de quelle(s) piste(s) il s'agira et dans combien de temps. Il apparaît néanmoins raisonnable d'envisager que les GNSS ne deviendront pas capables de rivaliser avec le SLR pour la définition de l'origine de l'ITRF à court terme.

Contents

Introduction

The availability of a Terrestrial Reference System (TRS) and of its physical realization, a Terrestrial Reference Frame (TRF), is fundamental for a wide range of applications which involve locating or tracking objects around the Earth. In the particularly demanding domain of Earth and space sciences, the International Terrestrial Reference System (ITRS) is nowadays widely adopted. It is an ideal reference system attached to Earth's crust and defined by its origin (the center of mass of the Earth), its scale (given by the SI meter) and its orientation. Its physical realization is the International Terrestrial Reference Frame (ITRF), which consists of coordinates for a set of geodetic markers and reference points of geodetic instruments.

The determination of the ITRF coordinates currently relies on the observations of four space geodetic techniques: Very Long Baseline Interferometry (VLBI), Satellite Laser Ranging (SLR), Global Navigation Satellite Systems (GNSS) and Doppler Orbitography and Radiopositioning Integrated by Satellite (DORIS). A particularly crucial point in the elaboration of the ITRF is the definition of its origin and of its scale. While all four contributing techniques are in principle sensitive to the terrestrial scale, only VLBI and SLR have so far contributed to the definition of the ITRF scale. Similarly, while all three satellite techniques (SLR, GNSS and DORIS) are in principle sensitive to the location of the Earth's center of mass, only SLR has so far contributed to defining the ITRF origin.

The contribution of GNSS to the ITRF is fundamental in several respects. However, the terrestrial scale and origin information stemming from GNSS data analyses has so far not been considered reliable enough to contribute to the definition of the ITRF scale and origin. For now, GNSS alone could thus not suffice to completely define an accurate TRF. This situation was the main motivation of this thesis. In view of improving it, we therefore sought to investigate and resolve the weak ability of GNSS to determine the terrestrial scale and the location of the Earth's center of mass.

In Chapter 1, the general context of this work is set and several fundamental notions are introduced. Chapter 2 provides a detailed description of the GNSS contribution to the ITRF and identifies the current related challenges. Chapter 3 presents the mathematical concepts that were used and developed during this thesis so as to investigate the weak ability of GNSS to determine the terrestrial scale and the location of the Earth's center of mass. Chapter 4 then provides a detailed understanding of this weak ability. In Chapter 5, several prospects are finally investigated that could eventually lead to a future contribution of GNSS to defining the ITRF origin and scale.

Chapter 1

ITRF, geocenter motion and related challenges

This first chapter is intended to set the overall scene in which the present thesis took place. It inevitably starts by introducing several fundamental notions (Sect. 1.1), in particular the International Terrestrial Reference Frame (ITRF) whose improvement was the underlying objective of the thesis, and geocenter motion which received a particular focus in our work. To provide insight into the concrete nature of the ITRF, the whole procedure used to build the ITRF from the observations of several geodetic techniques is then detailed in Sect. 1.2. Similarly, the various approaches allowing to estimate geocenter motion from geodetic observations are presented in Sect. 1.3. In Sect. 1.4, the current scientific challenges related to the ITRF are finally summarized.

1.1 Fundamental notions

The ability to locate or track objects around the Earth is today fundamental for a wide range of applications. This first concerns the scientific observation of various geophysical processes such as tectonic plate motions, earthquakes, crustal deformations of various origins, post-glacial rebound, present-day ice melting or sea-level rise. But this ability is also relevant to other scientific domains such as time transfer and even fundamental physics (Antonello et al., 2012). Wide ranges of non-scientific activities are finally concerned including navigation, civil engineering and agriculture.

Another requirement of today's Earth and space science is to accurately monitor the Earth's variable rotation in space. It is in particular essential to the precise tracking of satellites for, e.g., gravitational studies, to the precise manoeuvring of interplanetary flights, to the reduction of any astronomical observation and also provides insight into the Earth's internal structure.

Both these requirements could not be met without the availability of a Terrestrial Reference System (TRS) and of its physical realization, a Terrestrial Reference Frame (TRF). Such a frame indeed materialises a system of coordinates in which objects all around the Earth can be quantitatively positioned and also serves as a representation of the Earth for describing its motion in space.

This section starts by defining the notions of TRS (Sect. 1.1.1) and TRF (Sect. 1.1.2) introduced by Kovalevsky and Mueller (1981) and by briefly presenting the International Terrestrial Reference System (ITRS; Sect. 1.1.3) and its realization, the International Terrestrial Reference Frame (ITRF; Sect. 1.1.4). The Earth Orientation Parameters (EOPs) used to describe the Earth's variable rotation in space are then defined in Sect. 1.1.5. The concept of geocenter motion is finally introduced in Sect. 1.1.6.

1.1.1 Terrestrial reference system

Since Galileo understood the relative nature of motion, it has been accepted that "motion and position are not absolute concepts and can be described only with respect to some reference" (Kovalevsky and Mueller, 1989). In the Newtonian framework, positions, motions and the laws of physics are thus always attached to a reference system, i.e. a coordinate system of the 3-dimensional space. To locate or track objects located on the Earth's surface, it is convenient to adopt a particular sort of reference system, called *Terrestrial Reference System* (TRS) and defined as follows.

According to conventions of the International Earth Rotation and Reference Systems Service (IERS; Petit and Luzum, 2010), a TRS is an Euclidean affine frame (O, E) attached to the solid surface of the Earth and such that:

- its origin O is close to the Earth's center of mass;
- $E = (e_X, e_Y, e_Z)$ is a right-handed, orthogonal basis;
- the basis vectors all have the same norm $\lambda = \|e_X\| = \|e_Y\| = \|e_Z\|$ which is close to the SI meter;
- the Z axis is the Earth's rotation axis, while the X and Y axes lie in the equatorial plane.

A TRS is thus entirely characterized by its *origin*, its *scale* λ and the *orientation* of its basis vectors.

The transformation from one TRS to another is therefore a 3-dimensional similarity which can be written:

$$\boldsymbol{X}_2 = \boldsymbol{X}_1 + \boldsymbol{T} + k\boldsymbol{\mathcal{R}}\boldsymbol{X}_1 \tag{1.1}$$

where:

- $\boldsymbol{X}_1$ and $\boldsymbol{X}_2$ are the coordinates of a point M in two different TRS;
- $\boldsymbol{T} = [t_X, t_Y, t_Z]^T$ is the translation vector between both TRS origins;
- k is the ratio between both TRS scales;
- $\boldsymbol{\mathcal{R}}$ is the rotation matrix between both TRS orientations.

Geodetic TRS are usually close enough to each other so that a linearized similarity transformation can be used:

$$\boldsymbol{X}_2 = \boldsymbol{X}_1 + \boldsymbol{T} + d\boldsymbol{X}_1 + \boldsymbol{R}\boldsymbol{X}_1 \tag{1.2}$$

where:

- $d = k - 1$;
- $\boldsymbol{R} = \begin{bmatrix} 0 & -r_Z & r_Y \\ r_Z & 0 & -r_X \\ -r_Y & r_X & 0 \end{bmatrix}$;
- r_X, r_Y and r_Z are the rotation angles around the X, Y and Z axes respectively.

Note that the transformation between two TRS is generally function of time, so as to reflect the temporal variations between their origins, scales and orientations.

1.1.2 Terrestrial reference frame

Thus defined, a TRS is an ideal mathematical concept and cannot serve to quantify the position or motion of an object nor the orientation of the Earth without a physical realization. Such a realization is generally achieved by a given set of physical points precisely located in the TRS coordinate system. The realization of a TRS through such a set of reference coordinates is called a *Terrestrial Reference Frame* (TRF). Locating an object in a TRS is actually achieved by positioning this object relatively to the TRF points. These points are usually geodetic markers attached to the Earth's crust or the reference points of geodetic instruments. Their coordinates are determined from the statistical adjustment of geodetic observations and are thus associated with statistical information, i.e. a covariance matrix which reflects the precision of the adjusted coordinates.

Table 1.1 Main geophysical deformations affecting the Earth's crust

Type	Time scale	Magnitude
Co-seismic displacements	Nearly instantaneous	Up to several m
Solid Earth tides	Mainly daily and sub-daily, but also small long-period tides	Several tens of cm
Tidal ocean loading deformations	Mainly daily and sub-daily, but also small long-period tides	Several cm
Non-tidal loading deformations	Sub-monthly to inter-annual, but mainly annual	Up to several cm
Post-seismic relaxation	Up to several years	Up to several m
Tectonic plate motions	Secular	Several cm/year
Post-glacial rebound	Secular	Up to 2 cm/year

The Earth's crust continuously undergoes various geophysical deformations (Table 1.1). So that a TRF remains usable with a certain accuracy over a certain time span, it is necessary that the reference coordinates of the TRF points reflect these geophysical deformations, at least down to a certain magnitude. Real or apparent displacements of the reference points due to non-geophysical causes (i.e. discontinuities due to monumentation or instrumentation changes) need to be taken into account as well. The reference coordinates of a TRF point are thus function of time, with the following generic form:

$$\boldsymbol{X}(t) = \boldsymbol{X}^R(t) + \sum_i \delta\boldsymbol{X}_i(t) \tag{1.3}$$

where:

- the $\delta\boldsymbol{X}_i(t)$ are conventionally computed displacements that account for certain well modeled geophysical deformations;
- $\boldsymbol{X}^R(t)$ are so-called regularized coordinates, i.e. the part of the reference coordinates which is actually determined from geodetic observations.

The conventional corrections $\delta\boldsymbol{X}_i(t)$ recommended by the IERS currently include solid Earth tides, tidal ocean loading deformations, S_1 and S_2 atmospheric pressure loading deformations, rotational deformations due to polar motion and ocean pole tide loading deformations.

Until now, the regularized coordinates of TRF points have traditionally been represented as piecewise linear functions. This parameterization accounts for long-term linear displacements and for instantaneous position/velocity changes of the reference points. On the other hand, it does not handle non-conventional, non-linear displacements such as non-linear non-tidal loading deformations and can only crudely approximate post-seismic relaxation.

The more and more demanding requirements for TRF accuracy make it nowadays important to consider alternative parameterizations capable of representing such non-linear displacements. One possibility in that sense is to adopt more complex parametric models for regularized coordinates. Collilieux (2008) and Altamimi et al. (2013) thus propose to augment the traditional piecewise linear parameterization with sines and cosines at various periods to account for periodic non-tidal loading deformations, while Lercier et al. (2013) introduce exponential and/or logarithmic functions to account for post-seismic relaxation.

Another, more radical possibility is to model regularized coordinates by a series of coordinates $\boldsymbol{X}^R(t_i)$ valid over short successive time intervals and obtained from independent epoch-wise adjustments (Blossfeld et al., 2013) or from a sequential adjustment (Wu et al., 2012a) of geodetic observations.

1.1.3 The International Terrestrial Reference System

The International Terrestrial Reference System (ITRS) is a particular TRS formally adopted by the International Association of Geodesy (IAG) since 1991 and by the International Union of Geodesy and Geophysics (IUGG) since 2007. It is defined by the following conventions:

- the ITRS origin is the center of mass for the whole Earth, including oceans and atmosphere;
- the ITRS length unit (scale) is the SI meter;
- the ITRS orientation at epoch 1984.0 is that of the Bureau International de l'Heure (BIH) reference system;
- the time evolution of the ITRS orientation is defined by a no-net-rotation condition over the whole Earth's crust.

1.1.4 The International Terrestrial Reference Frame

Since 1988, the IERS has produced twelve realizations of the ITRS called International Terrestrial Reference Frames (ITRF). The ITRS realization currently in use is the ITRF2008 (Altamimi et al., 2011). A new realization called ITRF2013 is now under preparation.

Since the sixth ITRS realization (ITRF94; Boucher et al., 1996), the ITRF regularized coordinates have been represented by piecewise linear functions. An ITRF thus consists of positions and velocities for a set of geodetic markers and reference points of geodetic instruments, as well as of the associated covariance matrix. But note that daily series of Earth Orientation Parameters (Sect. 1.1.5) are also part of the ITRS realizations since the penultimate ITRF2005 (Altamimi et al., 2007).

Since the ITRF94, the ITRF coordinates are determined from the observations of four space geodetic techniques[1]:

- Very Long Baseline Interferometry (VLBI);
- Satellite Laser Ranging (SLR);
- Global Navigation Satellite Systems (GNSS);
- Doppler Orbitography and Radiopositioning Integrated by Satellite (DORIS).

A brief description of these techniques is given in Sect. 1.2.1.

The strategy for determining the ITRF coordinates from these geodetic observations has considerably evolved over time. The computation strategy used for the latest ITRF release is described in Sect. 1.2.

1.1.5 Earth orientation parameters

The celestial counterpart of the ITRS is the *International Celestial Reference System* (ICRS). It is an ideal coordinate system with its origin at the barycenter of the solar system and whose axes have a fixed orientation with respect to distant celestial objects. The ICRS is realized by the *International Celestial Reference Frame* (ICRF), i.e. a set of extragalactic objects with reference coordinates. The ICRS/ICRF serve as reference to locate or track celestial objects. However, for the purpose of determining the orbits of Earth satellites, it is more convenient to use a translated version of the ICRS, the *Geocentric Celestial Reference System* (GCRS), which has the same origin as the ITRS, i.e. close to the Earth's center of mass.

Monitoring the Earth's rotation concretely comes to knowing the relative orientation between the axes of the ITRS and those of the GCRS. According to the IERS Conventions (Petit and Luzum, 2010), the rotation from the ITRS to the GCRS at time t is conventionally decomposed into a sequence of three rotation matrices:

$$\boldsymbol{X}_{GCRS}(t) = \boldsymbol{Q}(t)\boldsymbol{R}(t)\boldsymbol{W}(t)\boldsymbol{X}_{ITRS}(t) \tag{1.4}$$

where:

- $\boldsymbol{Q}(t)$ accounts for precession and nutation, i.e. motion of the Earth's rotation axis in the GCRS (in space). $\boldsymbol{Q}(t)$ depends on the pole coordinates in the GCRS

---

[1] Lunar Laser Ranging (LLR) observations were additionally used to determine the ITRF2000 (Altamimi et al., 2002).

(celestial pole coordinates) $X(t)$ and $Y(t)$. These coordinates are the sum of conventional pole coordinates derived from the IAU 2006 precession-nutation model (Wallace and Capitaine, 2006) and of small corrections $\delta X(t)$ and $\delta Y(t)$ known as celestial pole offsets.

- $\boldsymbol{R}(t)$ represents a clockwise rotation around the Earth's rotation axis by the Earth rotation angle $ERA(t)$. $ERA(t)$ can be decomposed into an angle varying uniformly with the International Atomic Time (TAI) and a correction representing variations of the Earth's angular velocity. This correction is directly related to the difference $DUT1^{tot}(t)$ between the Universal Time $UT1$ and the Coordinated Universal Time UTC. $DUT1^{tot}(t)$ is the sum of conventionally modelled variations due to solid Earth tides, ocean tides and libration and of non-conventionally modelled variations $DUT1(t)$.
- $\boldsymbol{W}(t)$ accounts for polar motion, i.e. motion of the Earth's rotation axis in the ITRS (with respect to the Earth's crust). $\boldsymbol{W}(t)$ depends on the pole coordinates in the ITRS $x_p^{tot}(t)$ and $y_p^{tot}(t)$. These coordinates are the sum of conventionally modelled variations due to ocean tides and libration and of non-conventionally modelled variations $x_p(t)$ and $y_p(t)$.

The Earth's orientation in space is thus defined by a set of five parameters ($\delta X(t)$, $\delta Y(t)$, $DUT1(t)$, $x_p(t)$ and $y_p(t)$) called Earth Orientation Parameters (EOPs). These parameters are usually represented by continuous piecewise linear functions (daily offsets at midnight) or by discontinuous piecewise linear functions (daily offsets at noon and daily rates). Daily EOP estimates derived from geodetic observations are regularly published by the IERS.

The latest ITRF realizations have included a subset of three EOPs, namely $DUT1(t)$, $x_p(t)$ and $y_p(t)$, represented by daily offsets at noon and daily rates. In the following, we will only consider the same three EOPs with the same parameterization as in the ITRF. The term EOPs will thus refer to daily pole coordinates x_p and y_p at noon, daily pole rates $\dot{x}_p$ and $\dot{y}_p$, daily $DUT1$ offsets and daily values of the length of day LOD, i.e. the opposite of $DUT1$'s rate integrated over one day.

1.1.6 Geocenter motion

Let CM denote the center of mass of the whole Earth system (i.e. of the solid Earth and its fluid envelopes) and CF denote the center of figure of the solid Earth's surface. *Geocenter motion* is usually defined, with varying sign conventions, as the relative motion between CM and CF. Following Wu et al. (2012b), we define it here as the motion of CM with respect to CF and denote it $\Delta\boldsymbol{r}_{CM/CF}$. Informally speaking, geocenter motion can be seen as the net displacement of the Earth system's mass with respect to the Earth's crust. The geophysical cause of geocenter motion is the permanent redistribution of masses within the Earth system, from daily and sub-daily periods (e.g. ocean tides) to secular time scales (e.g. post-glacial rebound, present-day ice melting) via seasonal and inter-annual periods (e.g. water mass exchanges).

As discussed by Dong et al. (2003), geocenter motion has direct consequences on the nature of the ITRF origin. While the IERS Conventions stipulate that the ITRF origin should coincide with CM, this is currently not the case at all time scales. Firstly, geocenter motion induced by ocean tides is in principle correctly represented as part of the conventionally modelled station displacements recommended by the IERS. Secondly, long-term geocenter motion can be accounted for by the ITRF station velocities, so that there should in principle be no offset nor drift between the ITRF origin and CM. But finally, non-conventionally modeled, non-linear geocenter motion can currently not be accounted for by the ITRF coordinates due to their linear parameterization. Against the conventional definition of the ITRF origin, there consequently exist non-linear variations between the ITRF origin and CM, that mostly consist of an annual signal with an amplitude of a few mm.

However, as detailed by Wu et al. (2012b), some stringent geodetic applications, like the monitoring of surface mass transport by GRACE or the precise orbit determination of, e.g., altimetry satellites, cannot simply ignore this part of geocenter motion not captured in the ITRF coordinates. The IERS is therefore currently considering the adoption of a conventional model for the annual part of geocenter motion. But another solution to handle non-conventionally modeled, non-linear geocenter motion is to refine the parameterization of the ITRF station coordinates. If the current piecewise linear parameterization is augmented with annual periodic terms (as planned for the next ITRF2013), then the annual part of geocenter motion could for instance be directly accounted for by the ITRF coordinates. In a TRF where regularized station coordinates would be represented by discrete time series (as investigated by Wu et al. (2012a) or Blossfeld et al. (2013)), geocenter motion could even be handled at all time scales, so that the TRF origin could coincide with CM at all times.

1.2 Practical computation of the ITRF

This section aims at describing the complete procedure that was used to build the latest ITRF release (ITRF2008) starting from the observations of the four contributing techniques. This procedure involved four main steps:

- *analysis* of the observations of each technique by several Analysis Centers (ACs) on a weekly or daily basis;

- *combination* of the AC solutions of each technique on a weekly or daily basis;
- *stacking* of the combined solutions of each technique into long-term linear frames (i.e. determination of regularized station coordinates as piece-wise linear functions in technique-specific terrestrial reference frames);
- *combination* of the technique long-term frames together with local ties.

After brief presentations of the four contributing techniques (Sect. 1.2.1), this section describes the four steps of the ITRF computation procedure (Sect. 1.2.2 to 1.2.5). A special emphasis is finally put on the origin and the scale of the ITRF, their definition and their importance (Sect. 1.2.6).

1.2.1 Contributing techniques

The Very Long Baseline Interferometry (VLBI) technique relies on the simultaneous collection, by several radio-telescopes, of the signal emitted by an astronomical radio-source such as a quasar (quasi-stellar radio-source). Correlating the collected signals allows to determine the time differences between their arrivals at the different telescopes and hence the geometry of the telescope network. Moreover, the observation of several radio-sources allows to determine the orientation of the telescope network relatively to the sources, i.e. to determine the Earth Orientation Parameters.

Unlike VLBI, the three other techniques contributing to the ITRF rely on satellite tracking data. In the case of Satellite Laser Ranging (SLR), a global network of ground stations send ultra-short laser pulses to satellites equipped with retro-reflectors and then collect the reflected signals. Measures of the signal travel times thus provide a set of precise station-satellite ranges from which the satellite orbits can be determined together with the ground station coordinates and a subset of Earth Orientation Parameters.

Similarly to SLR, the contribution of Global Navigation Satellite Systems (GNSS) to the ITRF relies on the measurement of station-satellite ranges. But a major difference with SLR is that GNSS are based on *one-way* propagated signals. Concretely, satellite constellations broadcast microwave signals collected by a global network of ground stations. The signal emission and reception dates are respectively given by the satellite and station clocks. The signal travel times are therefore not directly accessible, but require the synchronization of the satellite and station clocks to a common time reference. As with SLR, the GNSS satellite orbits, the ground station coordinates and a subset of Earth Orientation Parameters can be estimated from a global set of GNSS data. But the satellite and station clock offsets as well as other nuisance parameters also need to be considered. More detail on the analysis of global GNSS datasets is given in Sect. 2.1.2.

The last geodetic technique contributing to the ITRF, DORIS, also relies on one-way propagated signals between ground stations and satellites. But DORIS being an uplink system, the signals are broadcast by a global network of ground beacons and received by some number of satellites. The DORIS satellite receivers have historically collected frequency shift (Doppler) measurements, but the new generation of DORIS receivers now provides similar travel time measurements as GNSS. As with SLR and GNSS, the DORIS satellite orbits, the ground station coordinates and a subset of Earth Orientation Parameters can be estimated from a global dataset of DORIS measurements.

1.2.2 Analysis

International services of the IAG (the IVS, ILRS, IGS and IDS respectively for VLBI, SLR, GNSS and DORIS) are in charge of collecting and providing data from the four techniques contributing to the ITRF. Each of the services comprises several Analysis Centers (ACs) whose role is to derive geodetic products from the data. On the basis of a given time period (e.g. one week, one day or one VLBI session), an AC concretely gathers a set of observations $\boldsymbol{l}$ and estimates a set of parameters $\boldsymbol{x}$ that best fits these observations. The adjusted parameters include:

- the coordinates of the observing stations;
- parameters describing the satellite orbits for SLR, GNSS and DORIS;
- the coordinates of the observed quasars for VLBI;
- all or a subset of the Earth Orientation Parameters;
- parameters describing the tropospheric delays of the propagated signals;
- other technique-specific biases such as SLR station range biases, GNSS station and satellite clock offsets, GNSS phase cycle ambiguities, DORIS beacon frequency offsets...

ACs may use various parameter adjustment methods, such as the widely employed generalized least-squares regression (Sect. B.1), that all lead to a so-called normal equation:

$$\boldsymbol{N}(\boldsymbol{x} - \boldsymbol{x}_0) = \boldsymbol{b} \tag{1.5}$$

where $\boldsymbol{x}_0$ is a set of a priori parameters. It is possible to *reduce* specific parameters from such a normal equation so as to retain a subset of parameters of interest only (Sect. B.3.1). In their contributions to the ITRF, the ACs thus reduce all parameters but the station coordinates and the EOPs, so that we will now consider that $\boldsymbol{x}$ contains only those parameters.

None of the geodetic techniques provides enough information to unambiguously estimate station coordinates and EOPs. This translates to the fact that the normal matrix $\boldsymbol{N}$ is singular so that the normal equation has an infinite number of solutions. The singularities inherent to the four contributing techniques are the following:

- None of the four techniques is able to determine the orientation of the station network with respect to the crust simultaneously with the EOPs. The pole coordinates and *DUT1* are indeed not intrinsic quantities, but completely depend on the orientation of the terrestrial frame realized by the station coordinates. In other words, any rotation of the station network can be compensated by variations of the EOPs without any impact on the geodetic observations. The normal matrices of all techniques therefore have three orientation singularities.
- As an interferometric technique, VLBI is additionally insensitive to the origin of the terrestrial frame. Translating the whole station network would indeed not change the reception time differences of the quasar signals at the different telescopes. A VLBI normal matrix thus has three origin singularities.
- The three satellite techniques (SLR, GNSS and DORIS), even if the orientation of the station network is fixed, are insensitive to *DUT1*. A variation of *DUT1* can indeed be compensated by a rotation of the whole satellite constellation (through variations of the reduced orbital parameters) without affecting satellite tracking observations. SLR, GNSS and DORIS normal matrices consequently have one *DUT1* singularity.

To obtain a unique solution from the normal equation, ACs consequently need to impose some additional constraints to the estimated parameters. ACs may use different kind of constraints, for instance minimal constraints (Sect. B.2.3). But, provided that the constraints are applied as pseudo-observations (Sect. B.2.1) with respect to the a priori parameters and that they compensate all singularities of the normal matrix, any kind of constraints results into a constrained normal equation:

$$(\boldsymbol{N} + \boldsymbol{N}_c)(\boldsymbol{x} - \boldsymbol{x}_0) = \boldsymbol{b} \tag{1.6}$$

where $\boldsymbol{N}_c$ is the normal matrix of constraints and $\boldsymbol{N} + \boldsymbol{N}_c$ is invertible. Such a constrained normal equation leads to a unique solution:

$$\hat{\boldsymbol{x}} = \boldsymbol{x}_0 + (\boldsymbol{N} + \boldsymbol{N}_c)^{-1}\boldsymbol{b} \tag{1.7}$$

The covariance matrix associated with the estimated parameters $\hat{\boldsymbol{x}}$ is:

$$\boldsymbol{Q} = (\boldsymbol{N} + \boldsymbol{N}_c)^{-1} \tag{1.8}$$

The AC contributions to the ITRF concretely consist in weekly, daily or VLBI-session-wise time series of either non-constrained normal equations (i.e. $\boldsymbol{x}_0$, $\boldsymbol{N}$ and

$\boldsymbol{b}$) or constrained solutions (i.e. $\boldsymbol{x}_0$, $\hat{\boldsymbol{x}}$, $\boldsymbol{N}_c$ and $\boldsymbol{Q}$) provided in the SINEX format[2]. It is possible, from a constrained solution, to recover the non-constrained normal equation by:

$$\begin{cases} \boldsymbol{N} = \boldsymbol{Q}^{-1} - \boldsymbol{N}_c \\ \boldsymbol{b} = \boldsymbol{Q}^{-1}(\boldsymbol{x} - \boldsymbol{x}_0) \end{cases} \tag{1.9}$$

A third possible type of AC contributions consist in minimally constrained solutions, in which case ACs may only provide $\boldsymbol{x}_0$, $\hat{\boldsymbol{x}}$ and $\boldsymbol{Q}$, but not necessarily the constraints $\boldsymbol{N}_c$ they applied.

1.2.3 Intra-technique combination

Each of the geodetic technique services also comprises a combination center whose role is to merge the solutions provided by the various ACs into unique combined solutions. These intra-technique combinations are performed on the same time basis as the analysis (i.e. one week, one day or one VLBI session) and essentially consist in a weighted averaging of the AC solutions. The intra-technique combinations can either be described as combinations of *normal equations* or as combinations of *solutions*. Both approaches are often opposed (e.g. Seitz et al., 2012), but are in fact strictly equivalent under a few mild conditions. We describe here the intra-technique combination methodology as a combination of solutions.

Suppose that data from one geodetic technique have been analysed by several ACs over the same time span so that we dispose of a set of s SINEX files containing either non-constrained normal equations, constrained solutions with information about the applied constraints or minimally constrained solutions. By removing the possibly applied constraints using Eq. 1.9 and inverting the non-constrained normal equations using minimal constraints, it is possible to bring all AC contributions to minimally constrained solutions. So we will now assume to dispose of a set of s minimally constrained solutions $(\boldsymbol{x}^i, \boldsymbol{Q}^i)_{1\leq i\leq s}$ [3].

Each set of parameters $\boldsymbol{x}^i$ is composed of station positions and of Earth Orientation Parameters. In the formalism of the combination of solutions, the $\boldsymbol{x}^i$ are used as pseudo-observations to estimate combined station positions and combined EOPs via the following observation equations (Altamimi et al., 2004):

---

[2] Solution Independent Exchange Format (`http://www.iers.org/IERS/EN/Organization/AnalysisCoordinator/SinexFormat/sinex__cont.html`)

[3] Combining minimally constrained solutions is in fact the first condition for the equivalence with the combination of normal equations.

$$\left\{\begin{array}{rcl}
X^i & = & X^c + t_X^i + d^i X^c - r_Z^i Y^c + r_Y^i Z^c \\
Y^i & = & Y^c + t_Y^i + d^i Y^c + r_Z^i X^c - r_X^i Z^c \\
Z^i & = & Z^c + t_Z^i + d^i Z^c - r_Y^i X^c + r_X^i Y^c \\
x_p^i & = & x_p^c + r_Y^i \\
y_p^i & = & y_p^c + r_X^i \\
\mathit{DUT1}^i & = & \mathit{DUT1}^c - r_Z^i / f \\
\dot{x}_p^i & = & \dot{x}_p^c \\
\dot{y}_p^i & = & \dot{y}_p^c \\
\mathit{LOD}^i & = & \mathit{LOD}^c
\end{array}\right. \tag{1.10}$$

where:

- X^i, Y^i, Z^i denote the coordinates of a particular station in the input solution i (in m);
- X^c, Y^c, Z^c denote the coordinates of the same station in the combined solution;
- x_p^i, y_p^i, $\mathit{DUT1}^i$, $\dot{x}_p^i$, $\dot{y}_p^i$, LOD^i denote EOP estimates in the input solution i (in rad and rad/d);
- x_p^c, y_p^c, $\mathit{DUT1}^c$, $\dot{x}_p^c$, $\dot{y}_p^c$, LOD^c denote the corresponding combined EOPs;
- t_X^i, t_Y^i, t_Z^i, d^i, r_X^i, r_Y^i, r_Z^i denote seven optional transformation parameters[4] (three translations, one scale factor and three rotations in m, unitless and in rad respectively) between the terrestrial frame realized by the input solution i and the combined terrestrial frame;
- $f = 1.002737811911354448$ is the conventional rate of advance of the Earth Rotation Angle ERA with respect to $\mathit{UT1}$.

These observation equations can be put in the following matrix form:

$$\begin{bmatrix} \boldsymbol{x}^1 \\ \vdots \\ \boldsymbol{x}^s \end{bmatrix} = \begin{bmatrix} \boldsymbol{J}^1 & \boldsymbol{A}^1 & & \\ \vdots & & \ddots & \\ \boldsymbol{J}^s & & & \boldsymbol{A}^s \end{bmatrix} \begin{bmatrix} \boldsymbol{x}^c \\ \boldsymbol{\theta}^1 \\ \vdots \\ \boldsymbol{\theta}^s \end{bmatrix} \tag{1.11}$$

where:

- $\boldsymbol{J}^i = \partial \boldsymbol{x}^i / \partial \boldsymbol{x}^c$ is a matrix of ones and zeros which associates each parameter in $\boldsymbol{x}^i$ to the corresponding combined parameter in $\boldsymbol{x}^c$;

---

[4] The second and last condition for the equivalence with the combination of normal equations is that only the transformation parameters corresponding to singularities of the technique are estimated (e.g. rotations only for the satellite techniques; rotations and translations for VLBI). It is nevertheless possible to set up additional transformation parameters both in the combination of normal equations and in the combination of solutions, with still equivalent results.

- $\boldsymbol{\theta}^i$ is a vector containing the transformation parameters between the input solution i and the combined solution;
- $\boldsymbol{A}^i = \partial \boldsymbol{x}^i / \partial \boldsymbol{\theta}^i$. For instance, if $\boldsymbol{x}^i$ is made of $3k$ station coordinates followed by 6 EOPs ($\boldsymbol{x}^i = [X_1, Y_1, Z_1, \ldots, X_k, Y_k, Z_k, x_p, y_p, DUT1, \dot{x}_p, \dot{y}_p, LOD]^T$) and if all seven transformation parameters are set up for the input solution i ($\boldsymbol{\theta}^i = [t_X^i, t_Y^i, t_Z^i, d^i, r_X^i, r_Y^i, r_Z^i]^T$), then $\boldsymbol{A}^i$ has the following form:

$$\boldsymbol{A}^i = \begin{bmatrix} 1 & 0 & 0 & X_1 & 0 & Z_1 & -Y_1 \\ 0 & 1 & 0 & Y_1 & -Z_1 & 0 & X_1 \\ 0 & 0 & 1 & Z_1 & Y_1 & -X_1 & 0 \\ \vdots & \vdots & \vdots & \vdots & \vdots & \vdots & \vdots \\ 1 & 0 & 0 & X_k & 0 & Z_k & -Y_k \\ 0 & 1 & 0 & Y_k & -Z_k & 0 & X_k \\ 0 & 0 & 1 & Z_k & Y_k & -X_k & 0 \\ 0 & 0 & 0 & 0 & 0 & 1 & 0 \\ 0 & 0 & 0 & 0 & 1 & 0 & 0 \\ 0 & 0 & 0 & 0 & 0 & 0 & -1/f \\ 0 & 0 & 0 & 0 & 0 & 0 & 0 \\ 0 & 0 & 0 & 0 & 0 & 0 & 0 \\ 0 & 0 & 0 & 0 & 0 & 0 & 0 \end{bmatrix} \tag{1.12}$$

Although this is clearly not the case since common data are processed by the various ACs, the pseudo-observation sets $(\boldsymbol{x}^i)_{1 \leq i \leq s}$ are generally assumed to be statistically independent. The covariance matrix associated with the whole set of pseudo-observations is therefore taken as a block-diagonal matrix with blocks $(\lambda^i \boldsymbol{Q}^i)_{1 \leq i \leq s}$. The λ^i's are AC-dependent scaling factors required because (a) the AC covariance matrices are not consistently scaled with each other (due to the different software and strategies used) and (b) the AC solutions may be of different qualities. The λ^i's need to be initialized with some a priori knowledge. They are then iteratively updated using some variance component estimation technique, usually the so-called *degree of freedom estimator* technique (Sillard, 1999; Bähr et al., 2007).

The observation equations 1.11 and the block-diagonal covariance matrix described above form a generalized least-squares system. Because possible outliers in the input AC solutions need to be detected and removed and because the AC scaling factors need to be iteratively estimated, this system has to be iteratively solved until no outliers remain and the AC scaling factors have converged.

Provided that minimally constrained solutions are combined and that only the transformation parameters corresponding to singularities of the technique are estimated, the obtained combined normal equation has the same characteristics and singularities as the AC normal equations: the combination is in this case a simple weighted averaging of the AC normal equations. Like the AC normal equations, the combined normal equation thus cannot be solved without additional (e.g. minimal) constraints. And like the AC contributions, the technique combined contributions to the ITRF consist in weekly, daily or VLBI-session-wise time series of either non-constrained normal equations or constrained solutions provided in the SINEX format.

1.2.4 Long-term stacking

The next step in the elaboration of the ITRF consists, for each of the four techniques, in stacking the time series of weekly, daily or VLBI-session-wise combined frames into a long-term frame. This step is performed by the IERS ITRS Centre. Like the intra-technique combination, this long-term stacking can either be described as a stacking of *normal equations* or as a stacking of *solutions*. But both approaches are again strictly equivalent under the same conditions as described in Sect. 1.2.3. We describe here the long-term stacking methodology as a stacking of solutions.

Say that we dispose, for a given technique, of a time series of s minimally constrained solutions $(\boldsymbol{x}^i, \boldsymbol{Q}^i)_{1 \leq i \leq s}$, each referred to a specific epoch t^i (e.g. the middle of the analysis week). Although EOPs are included in the technique long-term frames since the ITRF2005 (Altamimi et al., 2007), we suppose here, for the sake of simplicity, that the parameter sets $(\boldsymbol{x}^i)_{1 \leq i \leq s}$ are restricted to station positions only. Stacking these solutions into a long-term frame consists in taking the $\boldsymbol{x}^i$'s as pseudo-observations to estimate the station positions at some reference epoch t^{ref} together with the station velocities. The corresponding observation equations are as follows:

$$\left\{ \begin{array}{lcl} X^i & = & X^c + (t^i - t^{ref})\dot{X}^c + t^i_X + d^i X^c - r^i_Z Y^c + r^i_Y Z^c \\ Y^i & = & Y^c + (t^i - t^{ref})\dot{Y}^c + t^i_Y + d^i Y^c + r^i_Z X^c - r^i_X Z^c \\ Z^i & = & Z^c + (t^i - t^{ref})\dot{Z}^c + t^i_Z + d^i Z^c - r^i_Y X^c + r^i_X Y^c \end{array} \right. \tag{1.13}$$

where:

- X^i, Y^i, Z^i denote the coordinates of a particular station in the input solution i;
- X^c, Y^c, Z^c denote the coordinates of the same station in the stacked solution at the epoch t^{ref};
- $\dot{X}^c$, $\dot{Y}^c$, $\dot{Z}^c$ denote the velocity of the same station in the stacked solution;
- t^i_X, t^i_Y, t^i_Z, d^i, r^i_X, r^i_Y, r^i_Z denote seven optional transformation parameters (three translations, one scale factor and three rotations) between the terrestrial frame realized by the input solution i and the stacked terrestrial frame.

These observation equations can be put in the following matrix form:

$$\begin{bmatrix} \boldsymbol{x}^1 \\ \vdots \\ \boldsymbol{x}^s \end{bmatrix} = \begin{bmatrix} \boldsymbol{J}^1 & (t^1 - t^{ref})\boldsymbol{J}^1 & \boldsymbol{A}^1 & & \\ \vdots & \vdots & & \ddots & \\ \boldsymbol{J}^s & (t^s - t^{ref})\boldsymbol{J}^s & & & \boldsymbol{A}^s \end{bmatrix} \begin{bmatrix} \boldsymbol{x}^c \\ \dot{\boldsymbol{x}}^c \\ \boldsymbol{\theta}^1 \\ \vdots \\ \boldsymbol{\theta}^s \end{bmatrix} \tag{1.14}$$

where:

- $\boldsymbol{x}^c$ and $\dot{\boldsymbol{x}}^c$ respectively contain the station positions at t^{ref} and the station velocities in the stacked frame;
- $\boldsymbol{J}^i = \partial \boldsymbol{x}^i / \partial \boldsymbol{x}^c$ is a matrix of ones and zeros which associates each parameter in $\boldsymbol{x}^i$ to the corresponding parameter in $\boldsymbol{x}^c$;
- $\boldsymbol{\theta}^i$ is a vector containing the transformation parameters between the input solution i and the combined solution;
- $\boldsymbol{A}^i = \partial \boldsymbol{x}^i / \partial \boldsymbol{\theta}^i$ has the same form as in Eq. 1.12 - except for the EOP part - if all seven transformation parameters are set up for the input solution i.

Like in the intra-technique combination, the pseudo-observation sets $(\boldsymbol{x}^i)_{1 \leq i \leq s}$ are assumed to be independent, so that the covariance matrix associated with the whole set of pseudo-observations is taken as a block-diagonal matrix with blocks $(\boldsymbol{Q}^i)_{1 \leq i \leq s}$. (No scaling factors are needed here provided that the input solutions were obtained with a homogeneous combination strategy.) The observation equations 1.14 and this block-diagonal covariance matrix form a generalized least-squares system which is iteratively solved until no outlier remain in the input solutions.

Depending on which transformation parameters are set up, the stacked normal equation may have some number of singularities. For example, if X translations are set up for all input solutions, the resulting stacked normal equation will have one "translation singularity" (adding some constant to the X coordinates of all stations can be compensated by subtracting this constant to all X translation parameters) as well as one "translation rate singularity" (adding some constant to the X velocities of all stations can be compensated by subtracting a trend from the time series of X translation parameters). The stacked normal equation may thus have up to fourteen singularities in case where all seven transformation parameters are set up for all input solutions.

Each of these fourteen singularities can be cancelled by means of two different kinds of constraints. For instance, in the case where three translation parameters are set up for all input solutions, the six subsequent singularities can first be compensated by imposing no-net-translation and no-net-translation-rate constraints (Sect. B.2.5) between the stacked frame and some external reference frame. The other alternative is to use so-called *internal constraints* (Altamimi et al., 2006), i.e. to impose that the time series of transformation parameters between the input solutions and the combined solution have zero means and zero drifts. For instance, to compensate the two singularities due to the estimation of X translations for all input solutions, the internal constraint equations would read:

$$\left\{ \begin{array}{c} \sum_{i=1}^{s} t_X^i = 0 \\ \sum_{i=1}^{s} (t^i - t^{ref}) t_X^i = 0 \end{array} \right. \tag{1.15}$$

1.2.5 Inter-technique combination

The final step in the elaboration of the ITRF is to merge the four technique-specific long-term frames into a unique multi-technique frame, the ITRF itself. This step is also performed by the IERS ITRS Centre and can again be equivalently described - under certain conditions - as a combination of solutions or as a combination of normal equations. In the formalism of the combination of solutions, the station positions and velocities from the four technique-specific long-term frames are taken as pseudo-observations to estimate the station positions and velocities in the ITRF. Up to fourteen transformation parameters (three translations, one scale factor, three rotations and all their rates) may also be estimated between each of the technique-specific solutions and the combined solution. If any of these fourteen parameters is estimated for all of the technique-specific solutions, then one singularity arises in the combined normal equation and needs to be compensated by some constraint.

As the technique-specific frames do not share common points, additional information has to be brought in order to tie them into a unique frame. That is where sites hosting instruments from several of the four techniques come into play. Local tie surveys are occasionally performed at such co-location sites, providing information about the relative positions of the reference points of the various instruments within the site. These local ties are thus included as pseudo-observations in the ITRF inter-technique combination. Moreover, all instruments within one co-location site can reasonably be assumed to have the same velocity, so that velocity equality constraints can be additionally included in the ITRF inter-technique combination.

Local ties and velocity equality constraints at co-location sites are currently the only information allowing to tie the technique-specific frames into a unique common frame and have therefore a primordial importance in the ITRF elaboration. Although this importance has been constantly stressed over the past years, the distribution and quality of local ties, but also the quality of the geodetic stations at co-location sites still remain a major limiting factor of the ITRF accuracy (Altamimi et al., 2011).

1.2.6 ITRF datum definition

An especially important aspect of the ITRF elaboration is the definition of its origin, its scale and its orientation (i.e. its *datum*), so that they best meet the ITRS specifications (Sect. 1.1.3). This section describes the strategy that was used to define the ITRF2008 datum, i.e. which transformation parameters were estimated and which constraints were applied

ITRF orientation definition The ITRF orientation is the least crucial part of its datum definition as it is only a matter of convention: as stated in Sect. 1.2.2, none of the four techniques is indeed able to provide any absolute orientation information. During the ITRF2008 inter-technique combination, rotation and rotation rate parameters were thus estimated for all the four techniques, while no-net-rotation and no-net-rotation-rate constraints were simply applied with respect to the previous ITRF2005 via a subset of high quality geodetic stations.

ITRF origin definition The definition of the ITRF origin is much more crucial. As stated in Sect. 1.1.6, with the current parameterization of the ITRF station coordinates, the ITRF origin cannot coincide with the center of mass of the Earth (CM) at all time scales, but can only linearly follow CM. This linear following of CM is nevertheless critical for the observation of long-term geophysical processes such as sea-level rise (Beckley et al., 2007; Collilieux et al., 2011), post-glacial rebound or present-day ice melting.

In principle, all three satellite techniques contributing to the ITRF could serve to define its origin. In the analysis of SLR, GNSS and DORIS data, the orbits of the tracked satellites are indeed represented by differential motion equations that only hold in a CM-centred frame (i.e. no degree-1 Stokes coefficients are included). The daily or weekly frames resulting from the analysis of SLR, GNSS and DORIS data should thus have CM as their natural origin. However, the analysis of the technique solutions provided for the ITRF2008 revealed that the origin information from the GNSS and DORIS solutions was of much lower quality than the origin information coming from SLR (Altamimi and Collilieux, 2010; Altamimi et al., 2011; Collilieux et al., 2011; Valette et al., 2010). Only the origin information from the input SLR solutions was therefore used to define the origin of the ITRF2008.

Concretely, during the ITRF2008 inter-technique combination, translation and translation-rate parameters were estimated for the VLBI, GNSS and DORIS solutions, but not for the SLR solution. The ITRF2008 thus inherited the origin and the origin rate of the stacked SLR frame. Previously, during the long-term stacking of the weekly combined SLR solutions into the stacked SLR frame, translation parameters had been estimated for each of the weekly solutions and internal constraints had been used to define the origin and the origin rate of the stacked SLR frame. There is consequently no offset nor drift in the time series of translations between the weekly combined SLR solutions and the ITRF2008, which is a way to ensure that the ITRF2008 origin linearly follows the CM sensed by SLR.

ITRF scale definition Like the definition of its origin, the definition of the ITRF scale is critical for the observation of long-term geophysical processes, especially sea-level rise using GPS-corrected tide-gauge records. All the four contributing techniques are in principle sensitive to the terrestrial scale. But only the scale information coming from the SLR and VLBI solutions was retained for the ITRF2008. During the stacking of the combined SLR and VLBI solutions, scale factors were estimated and internal constraints were used to define the scales and scale rates of the stacked SLR and VLBI frames. Then, during the inter-technique combination, scale and scale rate parameters were estimated for all of the four technique-specific solutions. The mean of the SLR and VLBI scale parameters was constrained to zero, so that the ITRF2008 scale is finally a mean of the terrestrial scales sensed by SLR and VLBI. The scale rate of ITRF2008 was defined in the same way, as a mean of the scale rates sensed by SLR and VLBI.

1.3 Geocenter motion estimation

This section first aims at describing the different methods with which geocenter motion can be estimated from geodetic observations, namely the *network shift approach* (Sect. 1.3.1), the *degree-1 deformation approach* (Sect. 1.3.2) and Lavallée et al. (2006)'s *unified approach* (Sect. 1.3.3). The current status of the geodetic estimation of geocenter motion is then summarized in Sect. 1.3.4.

1.3.1 Network shift approach

As explained in Sect. 1.2.6, the analysis of satellite tracking data for some given period gives in theory access to the tracking station coordinates in CM-centred frames. Daily or weekly SLR, GNSS and DORIS solutions should thus have the quasi-instantaneous CM as their origins. On the other hand, as explained in Sect. 1.1.6, the origin of a long-term linear frame such as the ITRF only linearly follows CM. The net translations between quasi-instantaneous SLR, GNSS or DORIS frames and the ITRF should therefore reflect the non-linear part of geocenter motion (Dong et al., 2003; Collilieux et al., 2009). This way of estimating non-linear geocenter motion as net translations between quasi-instantaneous frames and a long-term linear frame is often called *network shift approach*.

Because the whole Earth's crust is not uniformly covered with geodetic stations, the center of figure CF of the solid Earth's surface is in fact not accessible with the network shift approach. Rather than providing estimates of the CM/CF offset, this approach in fact leads to estimates of the offset between CM and the so-called *center of network* CN, i.e. the barycenter of the station network. Because of their non-uniform distribution and of the local motions affecting the tracking stations, relative motion occurs between CN and CF. This spurious contribution to geocenter motion estimated with the network shift approach is known as *network effect* (Collilieux et al., 2009).

The observation equations of the network shift approach are the following:

$$\begin{bmatrix} X - X_R \\ Y - Y_R \\ Z - Z_R \end{bmatrix} = \begin{bmatrix} t_X \\ t_Y \\ t_Z \end{bmatrix} + d \begin{bmatrix} X_R \\ Y_R \\ Z_R \end{bmatrix} + \begin{bmatrix} 0 & -r_Z & r_Y \\ r_Z & 0 & -r_X \\ -r_Y & r_X & 0 \end{bmatrix} \begin{bmatrix} X_R \\ Y_R \\ Z_R \end{bmatrix} \tag{1.16}$$

where:

- X, Y, Z denote the coordinates of a given station in the quasi-instantaneous frame;
- X_R, Y_R, Z_R denote the ITRF coordinates of the same station (propagated at the epoch of the quasi-instantaneous frame);
- t_X, t_Y, t_Z are three translation parameters between the quasi-instantaneous frame and the ITRF representing the CN-CM offset;
- r_X, r_Y, r_Z are three rotation parameters between the quasi-instantaneous frame and the ITRF representing the difference between the conventional orientations of both frames;
- d is an optional scale factor between the quasi-instantaneous frame and the ITRF, which, according to Lavallée et al. (2006) or Collilieux et al. (2012), should preferably not be estimated so as to mitigate the network effect.

1.3.2 Degree-1 deformation approach

The part of geocenter motion which is neither conventionally modelled nor accounted for by the ITRF station velocities (i.e. between daily and secular time scales) is expected to be mostly due to the redistribution of mass within the Earth's fluid envelopes. Such surface mass redistributions not only induce geocenter motion, but also cause variations in the pressure exerted on the Earth's crust, hence elastic deformations of the Earth known as loading deformations.

According to the theory of the surface loading deformations of a spherical, non-rotating, elastic, isotropic Earth developed by Farrell (1972), the response of the Earth to some surface load is proportionally dependent on the applied load in the spherical harmonic domain. The proportionality coefficients relating the radial and tangential deformations of the solid Earth's surface to the load are the so-called *load Love numbers* which depend on assumed rheological properties of the Earth. More precisely, let us consider a latitude- and longitude-dependent surface load $\sigma(\phi, \lambda)$ expressed in kg/m^2. This surface load can be decomposed as follows on a basis of spherical harmonic functions:

$$\sigma(\phi, \lambda) = \sum_{l=0}^{+\infty} \sum_{m=0}^{l} \left(\sigma_{l,m}^{C} Y_{l,m}^{C}(\phi, \lambda) + \sigma_{l,m}^{S} Y_{l,m}^{S}(\phi, \lambda) \right) \tag{1.17}$$

where:

- $Y_{l,m}^{C}$ and $Y_{l,m}^{S}$ are spherical harmonic functions here defined by:

$$\begin{bmatrix} Y_{l,m}^{C}(\phi, \lambda) \\ Y_{l,m}^{S}(\phi, \lambda) \end{bmatrix} = \sqrt{\frac{2l+1}{4\pi} \frac{(l-m)!}{(l+m)!}} P_l^m(\sin\phi) \begin{bmatrix} \cos(m\lambda) \\ \sin(m\lambda) \end{bmatrix} \tag{1.18}$$

- P_l^m are the associated Legendre functions defined by:

$$P_l^m(x) = \frac{(-1)^m}{2^l l!} \sqrt{(1-x^2)^m} \frac{d^{l+m}}{dx^{l+m}} (x^2-1)^l \tag{1.19}$$

- l and m are respectively called spherical harmonic *degree* and *order*;
- the $\sigma_{l,m}^{C}$'s and $\sigma_{l,m}^{S}$'s are the spherical harmonic coefficients of the load.

According to Farrell (1972)'s theory, the deformation of the solid Earth's surface induced by such a load $\sigma(\phi, \lambda)$ can be written:

$$dE(\phi, \lambda) = \frac{1}{\rho_E} \sum_{l=0}^{+\infty} \sum_{m=0}^{l} \frac{3l'_l}{2l+1} \frac{1}{\cos\phi} \left(\sigma_{l,m}^{C} \frac{\partial Y_{l,m}^{C}(\phi, \lambda)}{\partial \lambda} + \sigma_{l,m}^{S} \frac{\partial Y_{l,m}^{S}(\phi, \lambda)}{\partial \lambda} \right) \tag{1.20}$$

$$dN(\phi, \lambda) = \frac{1}{\rho_E} \sum_{l=0}^{+\infty} \sum_{m=0}^{l} \frac{3l'_l}{2l+1} \left(\sigma_{l,m}^{C} \frac{\partial Y_{l,m}^{C}(\phi, \lambda)}{\partial \phi} + \sigma_{l,m}^{S} \frac{\partial Y_{l,m}^{S}(\phi, \lambda)}{\partial \phi} \right) \tag{1.21}$$

$$dU(\phi, \lambda) = \frac{1}{\rho_E} \sum_{l=0}^{+\infty} \sum_{m=0}^{l} \frac{3h'_l}{2l+1} \left(\sigma_{l,m}^{C} Y_{l,m}^{C}(\phi, \lambda) + \sigma_{l,m}^{S} Y_{l,m}^{S}(\phi, \lambda) \right) \tag{1.22}$$

where:

- $dE(\phi,\lambda), dN(\phi,\lambda), dU(\phi,\lambda)$ respectively denote the East, North and vertical displacements (in m) of the Earth's surface point located at latitude ϕ and longitude λ;
- h'_l and l'_l are respectively the radial and tangential load Love numbers of degree l, which, for degree 1, depend on the frame in which the Earth's surface deformations should be expressed (Blewitt, 2003);
- ρ_E denotes the mean Earth density expressed in kg/m^3.

On the other hand, it can be shown by surface integration (Trupin et al., 1992; Lavallée et al., 2006) that the geocenter motion induced by the load $\sigma(\phi,\lambda)$ can be expressed as a function of the degree-1 load coefficients:

$$\Delta \boldsymbol{r}_{CM/CF}(\sigma) = \frac{1}{\rho_E}\left(\frac{(h'_1)_{CE} + 2(l'_1)_{CE}}{3} - 1\right)\begin{bmatrix}\sigma^C_{11}\\ \sigma^S_{11}\\ \sigma^C_{10}\end{bmatrix} \tag{1.23}$$

where $(h'_1)_{CE}$ and $(l'_1)_{CE}$ are the degree-1 Load love numbers consistent with a CE-centred frame (CE denotes the center of mass of the solid Earth).

Consequently, if deformations of the Earth's crust can be monitored by a network of geodetic stations, the corresponding load coefficients can be inferred using Eq. 1.20-1.22 and the corresponding loading-induced geocenter motion can finally be obtained with Eq. 1.23. This way of estimating geocenter motion, known as *degree-1 deformation approach*, was first introduced by Blewitt et al. (2001). The corresponding observation equations can be written as follows:

$$\begin{aligned}\begin{bmatrix}X - X_R\\ Y - Y_R\\ Z - Z_R\end{bmatrix} &= \begin{bmatrix}t_X\\ t_Y\\ t_Z\end{bmatrix} + \begin{bmatrix}0 & -r_Z & r_Y\\ r_Z & 0 & -r_X\\ -r_Y & r_X & 0\end{bmatrix}\begin{bmatrix}X_R\\ Y_R\\ Z_R\end{bmatrix}\\ &+ \frac{\boldsymbol{R}^T}{\rho_E}\begin{bmatrix}\frac{(l'_1)_{CF}}{\cos\phi}\frac{\partial Y^C_{10}(\phi,\lambda)}{\partial\lambda} & \dots & \frac{3l'_{l_{max}}}{2l_{max}+1}\frac{1}{\cos\phi}\frac{\partial Y^S_{l_{max}l_{max}}(\phi,\lambda)}{\partial\lambda}\\ (l'_1)_{CF}\frac{\partial Y^C_{10}(\phi,\lambda)}{\partial\phi} & \dots & \frac{3l'_{l_{max}}}{2l_{max}+1}\frac{\partial Y^S_{l_{max}l_{max}}(\phi,\lambda)}{\partial\phi}\\ (h'_1)_{CF}Y^C_{10}(\phi,\lambda) & \dots & \frac{3h'_{l_{max}}}{2l_{max}+1}Y^S_{l_{max}l_{max}}(\phi,\lambda)\end{bmatrix}\begin{bmatrix}\sigma^C_{10}\\ \vdots\\ \sigma^S_{l_{max}l_{max}}\end{bmatrix}\end{aligned} \tag{1.24}$$

where:

- X, Y, Z denote the coordinates of a given station in some quasi-instantaneous frame;
- X_R, Y_R, Z_R denote the coordinates of the same station in some long-term linear frame, propagated at the epoch of the quasi-instantaneous frame;
- the coordinate differences $X - X_R$, $Y - Y_R$, $Z - Z_R$ constitute the inverted

deformation field, in which long-term deformations due to e.g. plate tectonic motion and post-glacial rebound are supposedly removed, so that only non-linear deformations assumed to be loading-induced remain;

- t_X, t_Y, t_Z are three translation parameters between the quasi-instantaneous frame and the long-term frame. Their estimation ensures that the remaining deformations are expressed in a CF-centred frame, which is why CF-consistent degree-1 load Love numbers are used in the observation equations;
- r_X, r_Y, r_Z are three rotation parameters between the quasi-instantaneous frame and the long-term frame representing the difference between the conventional orientations of both frames;
- ϕ and λ denote the latitude and longitude of the station;
- $\boldsymbol{R} = \begin{bmatrix} -\sin\lambda & \cos\lambda & 0 \\ -\sin\phi\cos\lambda & -\sin\phi\sin\lambda & \cos\phi \\ \cos\phi\cos\lambda & \cos\phi\sin\lambda & \sin\phi \end{bmatrix}$ is the rotation matrix from the geocentric frame to the station topocentric (East, North, Up) frame;
- l_{max} is the truncation degree up to which the surface load coefficients are estimated;
- the estimated degree-1 load coefficients $\sigma_{10}^C, \sigma_{11}^C, \sigma_{11}^S$ can be converted into geocenter motion using Eq. 1.23.

1.3.3 Unified approach

Both previously presented geocenter estimation approaches make use of distinct information. The information used in the network shift approach is the realization of CM stemming from the satellite motion equations. On the other hand, this information is cancelled in the degree-1 deformation approach because of the estimation of "nuisance" translation parameters. The degree-1 deformation approach thus entirely relies on independent information, i.e. non-translational deformations.

Lavallée et al. (2006) proposed a unified geocenter motion estimation approach which makes use of both information. Their approach is based on the modelling of surface loading deformations in a CM-centred frame. Unlike in a CF-centred frame, surface loading deformations expressed in a CM-centred frame indeed contain a translational part. Lavallée et al. (2006)'s idea was thus to use both the realization of CM by orbit dynamics and the non-translational deformations contained in global GPS solutions in order to estimate surface load coefficients, hence geocenter motion.

The observation equations of this unified approach can be written, with the same notations as in Sect. 1.3.2, as:

$$\begin{bmatrix} X - X_R \\ Y - Y_R \\ Z - Z_R \end{bmatrix} = \begin{bmatrix} 0 & -r_Z & r_Y \\ r_Z & 0 & -r_X \\ -r_Y & r_X & 0 \end{bmatrix} \begin{bmatrix} X \\ Y \\ Z \end{bmatrix} + \frac{\boldsymbol{R}^T}{\rho_E} \begin{bmatrix} \frac{(l'_1)_{CM}}{\cos\phi} \frac{\partial Y^C_{10}(\phi,\lambda)}{\partial\lambda} & \cdots & \frac{3l'_{l_{max}}}{2l_{max}+1} \frac{1}{\cos\phi} \frac{\partial Y^S_{l_{max}l_{max}}(\phi,\lambda)}{\partial\lambda} \\ (l'_1)_{CM} \frac{\partial Y^C_{10}(\phi,\lambda)}{\partial\phi} & \cdots & \frac{3l'_{l_{max}}}{2l_{max}+1} \frac{\partial Y^S_{l_{max}l_{max}}(\phi,\lambda)}{\partial\phi} \\ (h'_1)_{CM} Y^C_{10}(\phi,\lambda) & \cdots & \frac{3h'_{l_{max}}}{2l_{max}+1} Y^S_{l_{max}l_{max}}(\phi,\lambda) \end{bmatrix} \begin{bmatrix} \sigma^C_{10} \\ \vdots \\ \sigma^S_{l_{max}l_{max}} \end{bmatrix} \tag{1.25}$$

The main difference with the degree-1 deformation observation equations is that no translation parameters are estimated, so that the realization of CM by orbit dynamics is conserved and that loading deformations are modelled in a supposedly CM-centred frame, which is why CM-consistent degree-1 load Love numbers are used.

1.3.4 Current status

The geodetic estimation of geocenter motion, especially of its annual part, has considerably improved in the past few years. The basic degree-1 deformation approach described in Sect. 1.3.2 has in particular evolved towards global inversion approaches that incorporate GRACE and ocean bottom pressure data in addition to GPS-sensed crust deformations (Davis et al., 2004; Wu et al., 2006; Jansen et al., 2009; Rietbroek et al., 2011) and the annual geocenter motions obtained from such recent global inversions are now in excellent agreement (Ries, 2013).

The annual geocenter motion estimated from SLR solutions using the network shift approach is also in good agreement with global inversion results, although the latest SLR-only-derived amplitudes of the X and Z annual geocenter signals are consistently larger than global-inversion-derived amplitudes (Ries, 2013). But, according to Wu et al. (2013), this last point of disagreement is understood - it would be due to the uneven distribution of SLR stations and the subsequent network effect in the SLR network shift results - and can be resolved by the sequential adjustment of SLR frames with VLBI, GNSS and DORIS frames, as presented by Wu et al. (2012a).

The fact that two independent methods agree tends to prove that the annual geocenter motion is now correctly observed, so that a conventional annual geocenter motion model could soon be adopted by the IERS. This also opens bright perspectives for the observation of possible sub-annual and/or inter-annual geocenter motions.

On the other hand, the situation is not as bright as regards the network shift estimation of geocenter motion from DORIS and GNSS solutions. Although DORIS-derived geocenter time series recently benefited from tremendous improvements (Gobinddass et al., 2009a,b), they remain much noisier than SLR-derived time series and affected by systematic errors, especially in the Z component (Altamimi and Collilieux, 2010; Altamimi et al., 2011; Valette et al., 2010). GNSS as well have so far not proven able to reliably observe geocenter motion with the network shift approach (see Sect. 2.4 and Collilieux et al., 2011) although they benefit from many more satellites and a much denser tracking network than SLR. In other words, the realization of CM by orbit dynamics is not as reliable in GNSS and DORIS solutions as in SLR solutions and that is why neither DORIS nor GNSS did contribute to defining the origin of ITRF2008.

1.4 Today's challenges for the ITRF

As mentioned in Sect. 1.1, the availability of a Terrestrial Reference Frame is fundamental for a wide range of scientific and civilian applications. One of these applications with particular high stakes is the observation of sea level change caused by climate change, which is also today's most demanding application in terms of TRF accuracy. Blewitt et al. (2010) assessed the TRF requirement for the observation of sea level change to an accuracy level of 1 mm and a stability level of 0.1 mm/yr. These levels are now one of the fundamental objectives of the GGOS initiative (Gross et al., 2009). However, the accuracy and stability of the ITRF2008 are likely still about one order of magnitude larger than these requirements. In particular, external evaluations of the origin of ITRF2008 assessed its stability to a level of 0.5 mm/yr (Wu et al., 2011; Collilieux et al., 2014) or even 0.9 mm/yr along the Z axis (Argus, 2012). Given the discrepancy between the terrestrial scales given by VLBI and SLR, the accuracy of the ITRF2008 scale is believed not to be better than 1.2 ppb (8 mm; Altamimi et al., 2011), while its stability is believed to be at the order of 0.2 to 0.3 mm/yr (Wu et al., 2011; Collilieux and Schmid, 2012; Collilieux et al., 2014). In order to meet the GGOS requirements, efforts therefore need to be undertaken at different levels.

It is first widely accepted that the ground geodetic infrastructure needs to be improved. The distribution of SLR and VLBI stations over the Earth is currently poor and, as mentioned in Sect. 1.2.5, the distribution and quality of local ties between the four techniques contributing to the ITRF is also one major limiting factor of the ITRF accuracy. But, although several initiatives aiming at improving the ground geodetic infrastructure are currently emerging (VLBI 2010, NASA's and Australia's space geodesy projects), the few next ITRS realizations will likely still have to accommodate to imperfect ground networks.

An alternative strategy is to reduce the dependency of the ITRF on local ties by making use of so-called *space ties*, i.e. satellites tracked with at least two different techniques like Jason-1, Jason-2, HY-2A or Envisat. By simultaneously analysing SLR, GNSS and DORIS data collected by ground stations and such multi-technique satellites, consistent multi-technique terrestrial frames could be obtained without the need of ground local ties. However, this approach raises numerous methodological issues (in particular the consistent tying of the different instruments on board of multi-technique satellites) and is still an open area of research.

Besides such "technique tying improvements", it is also clear that the current ITRF formulation needs to be revised. As pointed out in Sect. 1.1.2 and Sect. 1.1.6, the GGOS requirements cannot be attained with the current piecewise linear parameterization of station motions. Different alternatives to this traditional parameterization are currently under study (see Sect. 1.1.2).

Finally, efforts also need to be undertaken in order to mitigate the systematic errors that affect station positions estimated with the different geodetic techniques. Imperfect modelling of the geodetic observations during their analysis indeed induces biases and time-dependent errors in the station positions input to the ITRF (see Sect. 2.2). This has of course direct consequences on the accuracy of the ITRF station coordinates. But such technique-dependent biases also compromise the correct use of local ties in the ITRF inter-technique combination. Moreover, global systematic errors are also the reason why DORIS and GNSS can currently not contribute to the definition of the ITRF origin. The generic question underlying this thesis (Can GNSS contribute to improving the ITRF definition?) relates to this last category of desired improvements.

Chapter 2

GNSS contribution to the ITRF: issues and challenges

To apprehend how GNSS could contribute to meeting the ITRF-related challenges identified in Sect. 1.4, a deeper insight into the GNSS contribution to the ITRF is necessary. The first section of this chapter (Sect. 2.1) thus gives a thorough description of this contribution. The next sections introduce specific issues and challenges related to the GNSS contribution to the ITRF and their current understanding, namely:

- the systematic errors affecting GNSS station position estimates (Sect. 2.2),
- the determination of the terrestrial scale with GNSS (Sect. 2.3),
- the determination of geocenter motion with GNSS (Sect. 2.4).

2.1 GNSS contribution to the ITRF

This first section is intended to provide insight into the concrete nature of the GNSS contribution to the ITRF. The various GNSS currently operating or developing, their operating principles and some of their technical characteristics are first described in Sect. 2.1.1. Sect. 2.1.2 details how the Analysis Centres of the International GNSS Service form, from GNSS observations, solutions that constitute the elementary contribution of GNSS to the ITRF. Sect. 2.1.3 then presents the contribution of GNSS to the ITRF2008 and their expected contribution to the ITRF2013. The primordial role of GNSS in the elaboration and dissemination of the ITRF is finally stressed in Sect. 2.1.4.

2.1.1 Description of current GNSS

Nowadays, several Global Navigation Satellite Systems (GNSS) are jointly either operating or developing. All rely on same basic principle: the broadcast of microwave signals by a constellation of satellites. The different GNSS listed below mainly differ by the characteristics of their satellite constellations, but also in some technical aspects.

The American Global Positioning System (GPS), operational since 1994, pioneered the GNSS adventure. The nominal GPS constellation consists of 24 satellites spread over 6 orbital planes. But more or less 6 backup satellites have also been constantly operating since 1994. The nominal GPS orbital planes have an inclination of 55° and are separated by 60° in the equatorial plane. The GPS satellites have quasi-circular orbits with a radius of about 26560 km (i.e. an altitude of about 20200 km) and a revolution period of about 11 hours 58 minutes. Their ground tracks approximately repeat with a period of 23 hours 56 minutes, but slightly shift each day due to the precession of the ascending nodes induced by the oblateness of the Earth. Each GPS satellite broadcasts microwave signals in at least both the L1 and L2 frequency bands. The latest generation of GPS satellites broadcasts an additional signal in the L5 frequency band. The different GPS satellites can be identified by a receiver thanks to satellite-specific C/A-codes which modulate the broadcast signals. This signal separation technique is known as Code Division Multiple Access or CDMA.

The Russian counterpart of GPS is the GLONASS system, which first became operational in 1995. After falling into disrepair until 2003, the GLONASS constellation was then progressively reconstructed until it became operational again in 2008. The nominal GLONASS constellation consists of 24 satellites equally spread over 3 orbital planes. The nominal GLONASS orbital planes have an inclination of 64.8° and are separated by 120° in the equatorial plane. The GLONASS satellites have quasi-circular orbits with a radius of about 25510 km (i.e. an altitude of about 19140 km) and a revolution period of about 11 hours 15 minutes. Their ground tracks approximately repeat every 8 days. Each GLONASS satellite broadcasts L1 and L2 signals, but unlike with GPS, the exact frequencies of the broadcast signals are slightly different for each GLONASS satellite, which allows a receiver to identify the emitting satellite. Compared with the CDMA technique used by GPS, this signal separation technique, known as Frequency Division Multiple Access (FDMA), raises specific issues in the geodetic analysis of GLONASS data (Sect. 2.1.2).

The European Union is currently developing a third GNSS called Galileo. In addition to the two validation satellites GIOVE-A and GIOVE-B, four Galileo satellites are now in orbit. The nominal Galileo constellation will eventually consist of

27 satellites equally spread over 3 orbital planes. The nominal Galileo orbital planes have an inclination of 56° and are separated by 120° in the equatorial plane. The Galileo satellites have quasi-circular orbits with a radius of about 29600 km (i.e. an altitude of about 23200 km) and a revolution period of about 14 hours 5 minutes. Their ground tracks approximately repeat every 10 days. Each Galileo satellite will broadcast signals in the L1, E5 and E6 frequency bands. Like GPS, Galileo uses the CDMA signal separation technique.

China is also currently developing its own GNSS known as Beidou or Compass. The Beidou constellation, now composed of 15 satellites, will eventually comprise 5 geostationary (GEO) satellites, 27 medium Earth orbit (MEO) satellites and 3 inclined geosynchronous orbit (IGSO) satellites. Let us finally mention the Japanese Quasi-Zenith Satellite System (QZSS) composed of 4 satellites in slightly elliptical, geosynchronous orbits, which aims at improving GNSS positioning over Japan.

2.1.2 Global GNSS data analysis

As mentioned in Sect. 1.2.1, the analysis of a global set of GNSS data collected by ground stations allows the simultaneous estimation of the GNSS satellite orbits, of the ground station coordinates and of a subset of EOPs together with other nuisance parameters. The different Analysis Centers (ACs) of the International GNSS Service (IGS) regularly perform such analyses and their solutions compose the elementary contribution of GNSS to the ITRF. This subsection therefore gives an overview of the global GNSS analyses performed by the IGS ACs.

Thousands of permanent geodetic GNSS stations are nowadays operating worldwide and continuously track the signals emitted by the satellites from one or more GNSS. Data collected by such stations are made publicly available by different organizations such as the IGS in the form of RINEX files. RINEX files concretely contain so-called code and phase pseudo-ranges, usually sampled at 30 seconds, which constitute the basic observations used by the IGS ACs. A code pseudo-range is a measure of the travel time (converted into a distance) of a GNSS signal from a satellite to a station which is based on the C/A code or P code that modulates the signal. Pseudo-ranges are biased, among other error sources, by the satellite and station clock errors, hence the prefix "pseudo". Once corrected for different errors, their precision is roughly at the order of 1 m. A phase pseudo-range is a measure (converted into a distance) of the phase difference of a GNSS signal between its emission by a satellite and its reception by a station. Like code pseudo-ranges, phase pseudo-ranges are affected by several error sources, including the satellite and station clock errors. But phase pseudo-ranges are additionally ambiguous by an integer number of cycles. They are however much more precise than code pseudo-ranges (roughly at the order of 1 cm) and thus constitute the basis of the IGS AC analyses.

One of the error sources affecting phase pseudo-ranges is the ionospheric refraction of GNSS signals. However, the advance of the GNSS signal phases due to ionospheric refraction is frequency-dependent, so that if phase pseudo-ranges are measured by a station for two signals with different frequencies, it is possible to cancel (at least at first order) the ionosphere-induced error by forming a linear combination of both phase pseudo-ranges. The IGS ACs thus use either undifferenced ionosphere-free linear combinations of L1- and L2-based phase pseudo-ranges, or double differences of such ionosphere-free linear combinations as observations in their GPS and GLONASS analyses.

GPS undifferenced observation equation The observation equation for a GPS undifferenced ionosphere-free phase pseudo-range $(L_3)_k^i$ measured by a station k on a satellite i can be written as follows:

$$(L_3)_k^i = \rho_k^i + c\delta t_k - c\delta t^i + T_k^i + \lambda n_k^i + \lambda\delta\phi_k - \lambda\delta\phi^i + (\epsilon_{mod})_k^i + (\epsilon_{err})_k^i \tag{2.1}$$

where:

- ρ_k^i is the geometric station-satellite distance;
- δt_k and δt^i are respectively the unknown station and satellite clock errors;
- T_k^i is the error due to the tropospheric refraction of the GNSS signal (tropospheric delay);
- λ is the wavelength of the ionosphere-free linear combination (approximately 11 cm);
- n_k^i is the so-called phase cycle ambiguity;
- $\delta\phi^j$ and $\delta\phi_i$ are respectively station and satellite biases known as *uncalibrated phase delays* (UPD; Ge et al., 2008);
- $(\epsilon_{mod})_k^i$ groups a number of different modelled effects such as the phase wind-up bias, the station and satellite antenna phase center corrections, the second and third order ionospheric effects, relativistic effects...
- $(\epsilon_{err})_k^i$ groups all remaining, non-modelled errors.

GPS double-differenced observation equation In their analyses, some IGS ACs do not directly use undifferenced ionosphere-free phase pseudo-ranges as observations, but rather double differences between the ionosphere-free phase pseudo-ranges observed at the same time by pairs of stations on pairs of satellites. The observation equation for such a GPS double-differenced observation involving the stations k, l

and the satellites i, j can be written:

$$\begin{aligned}(L_3)^{ij}_{kl} &= ((L_3)^i_k - (L_3)^i_l) - ((L_3)^j_k - (L_3)^j_l) \\ &= \rho^{ij}_{kl} + T^{ij}_{kl} + \lambda n^{ij}_{kl} + (\epsilon_{mod})^{ij}_{kl} + (\epsilon_{err})^{ij}_{kl}\end{aligned} \tag{2.2}$$

where each term in the second line is the double-difference of the corresponding term in Eq. 2.1. An obvious advantage of forming double-differenced observations is that both station and satellite clock errors and uncalibrated phase delays are cancelled.

Station-satellite distance parameterization The geometric distance ρ^i_k can itself be expressed, at a given time t, as:

$$\rho^i_k(t) = \|\boldsymbol{X}^i(t-\tau) - \boldsymbol{Q}(t)\boldsymbol{R}(t)\boldsymbol{W}(t)(\boldsymbol{X}^R_k + \boldsymbol{\delta X}_k(t))\| \tag{2.3}$$

where:

- τ denotes the signal travel time;
- $\boldsymbol{X}^i(t-\tau)$ are the satellite coordinates, in the GCRS, at time $t-\tau$;
- $\boldsymbol{Q}(t)$, $\boldsymbol{R}(t)$ and $\boldsymbol{W}(t)$ are the three rotation matrices that describe the transformation from the ITRS to the GCRS (see Sect. 1.1.5) and depend on unknown EOPs;
- $\boldsymbol{X}^R_k + \boldsymbol{\delta X}_k(t)$ represents the station coordinates in the ITRS as the sum of conventionally modelled corrections $\boldsymbol{\delta X}_k(t)$ (see Sect. 1.1.2) and of unknown regularized coordinates $\boldsymbol{X}^R_k$.

The partial derivatives of phase pseudo-ranges with respect to station coordinates and EOPs can be straightforwardly obtained from Eq. 2.3. Computing their partial derivatives with respect to the satellite orbit parameters is more complicated.

The orbit of a satellite is indeed not represented by an explicit time-dependent function like station coordinates, but rather as the solution of a differential motion equation:

$$\left\{\begin{aligned}\ddot{\boldsymbol{X}}^i(t) &= \boldsymbol{a}^i(t, \boldsymbol{X}^i(t), \dot{\boldsymbol{X}}^i(t), p^i_1, \ldots, p^i_m) \\ \boldsymbol{X}^i(t_0) &= \boldsymbol{X}^i_0 \\ \dot{\boldsymbol{X}}^i(t_0) &= \dot{\boldsymbol{X}}^i_0\end{aligned}\right. \tag{2.4}$$

where the function $\boldsymbol{a}^i$ is the sum of conventionally modelled accelerations (e.g. gravitational accelerations, Earth-reflected radiation pressure, antenna thrust) and of empirical accelerations depending on unknown parameters $p^i_1, \ldots, p^i_m$. The satellite orbit parameters estimated by an IGS AC consist of the satellite initial position $\boldsymbol{X}^i_0$, the satellite initial velocity $\dot{\boldsymbol{X}}^i_0$ and those empirical parameters $p^i_1, \ldots, p^i_m$. The partial derivatives of $\boldsymbol{X}^i(t)$ (hence of $\rho^i_k(t)$ and of $(L_3)^i_k$) with respect to the satellite orbit parameters are obtained by numerically integrating so-called *variational equations* (see, e.g., Springer, 2000).

To parameterize empirical satellite accelerations, most IGS ACs use variants of the Extended CODE Orbit Model (ECOM; Beutler et al., 1994; Springer et al., 1999). The empirical parameters $p_1^i, \dots, p_m^i$ are in this case the amplitudes of constant and once-per-revolution periodic accelerations along the axes D, Y and B of a satellite-Sun oriented frame[1]. With this parameterization, the empirical acceleration acting on a satellite can be written:

$$\begin{aligned}\boldsymbol{a}_{ECOM}(u) = &\left(D_0 + D_c \cos(u) + D_s \sin(u)\right) \boldsymbol{e}_D \\ &+ \left(Y_0 + Y_c \cos(u) + Y_s \sin(u)\right) \boldsymbol{e}_Y \\ &+ \left(B_0 + B_c \cos(u) + B_s \sin(u)\right) \boldsymbol{e}_B\end{aligned} \tag{2.5}$$

where u denotes the satellite's argument of latitude. Note that a majority of IGS ACs only estimates a subset of five ECOM parameters: D_0, Y_0, B_0, B_c and B_s.

Tropospheric delay parameterization The IERS Conventions (Petit and Luzum, 2010) recommend that the tropospheric delay affecting a GNSS observation be modelled as follows:

$$T_k^i = m_h(e) D_{hz} + m_w(e) D_{wz} + m_g(e) \left(G_N \cos(a) + G_E \sin(a)\right) \tag{2.6}$$

where:

- e and a respectively denote the elevation and the azimuth of the satellite above the station;
- the zenith hydrostatic delay D_{hz} is computed a priori from surface pressure data or numerical weather models;
- the zenith wet delay D_{wz} is a priori unknown. It is usually parameterized, for each station, as a step function or a continuous piecewise linear function with a time step of one or two hours;
- the North/South and East/West tropospheric gradients G_N and G_E are the sums of a priori modelled gradients and of additional unknown gradient parameters usually parameterized, for each station, as daily linear functions;
- the hydrostatic and wet mapping functions, $m_h(e)$ and $m_w(e)$, that map the zenith tropospheric delay to the observation elevation, should either be the Vienna Mapping Functions (VMF1; Boehm et al., 2006b) or the Global Mapping Functions (GMF; Boehm et al., 2006a);
- the gradient mapping function $m_g(e)$ is given by Chen and Herring (1997).

Handling phase cycle ambiguities Due to the ionosphere-free linear combination, the phase cycle ambiguity n_k^i of an ionosphere-free phase pseudo-range is not an integer. It can nevertheless be expressed as a linear combination of two integers: the phase cycle ambiguities of the L1 and L2 phase pseudo-ranges. L1 and L2 ambiguities

---

[1] The D axis is the normal to the satellite solar panels, i.e. the satellite-Sun direction. Y is the rotation axis of the satellite solar panels. B completes the right-handed system.

remain constant during the pass of each satellite over each station as long as no loss of signal lock (cycle slip) occurs. In case of such cycle slips, several L1 and L2 ambiguities need to be considered for the same satellite pass.

The positive impact of ambiguity fixing (i.e. the fixation of L1 and L2 ambiguities to integer values so that the ionosphere-free ambiguities n_k^i are *known* and do not have to be estimated as unknown parameters) in global GNSS analyses has long been recognized. In their analyses, the IGS ACs thus strive to fix as many ambiguities as possible. However, due to the presence of station and satellite uncalibrated phase delays, ambiguity fixing cannot be performed at the level of undifferenced phase pseudo-ranges. The IGS ACs using double-differenced observations are not affected by this issue and can directly fix double-differenced ambiguities. On the other hand, the IGS ACs using undifferenced observations need to introduce the ambiguity fixing information as relative constraints between undifferenced ambiguities.

With modern geodetic receivers and ambiguity fixation techniques, ACs are nowadays able to fix about 90% of the double-differenced ambiguities in a GPS analysis. As discussed below, the situation is more complicated with GLONASS.

Clock and UPD parameterization Clock errors are currently estimated by the IGS ACs using undifferenced observations as epoch-wise parameters for each station and each satellite. Uncalibrated phase delays are currently not estimated and become as a matter of fact part of the estimated station and satellite clock offsets.

By looking at Eq. 2.1, it is clear that adding one constant offset to the clock offsets of all stations and all satellites has virtually no impact on a set of GNSS observations. In other words, it is important to bring all station and satellite clocks to a common time reference, but the choice of this reference is of no importance. As a consequence, if epoch-wise clock offsets are estimated for all stations and all satellite in a GNSS analysis, then one singularity arises at each observation epoch. These singularities are usually cancelled by either choosing one particular station clock as time reference, or by imposing epoch-wise constraints on the mean of all estimated clock offsets.

Finally note that, due to their large numbers, station and satellite clock offsets are usually *reduced* (see Sect. B.3.1) by the IGS ACs using undifferenced observations.

Global GPS data analysis: summary Table 2.1 summarizes all the parameters estimated and the constraints applied in a simulated undifferenced GPS-only analysis. To obtain the numerical values in Table 2.1, we assumed:

- 300-s sampled observations over one day;

- an elevation cut-off angle of 10° (i.e. all observations made below an elevation of 10° were not considered);
- a nominal constellation of 24 GPS satellites;
- a fictive network of 100 well-distributed stations;
- 5 empirical orbit parameters per satellite (D_0, Y_0, B_0, B_c and B_s);
- a parameterization of tropospheric zenith wet delays as step functions with one hour time steps;
- a parameterization of tropospheric gradients as linear functions over the day;
- no cycle slip (i.e. only one ambiguity per pass);
- all double-differenced ambiguities fixed;
- the orientation and *DUT1* singularities (see Sect. 1.2.2) respectively cancelled by no-net-rotation constraints and by fixing *DUT1* to its a priori value.

Table 2.1 Numbers of observations, parameters, constraints and degrees of freedom in a simulated undifferenced GPS analysis

	Type	Count	Number
Obs.	**Total**		**207289**
Parameters	Station coordinates	3 per station	300
	EOPs	6	6
	Satellite orbit parameters	$(6+5)$ per satellite	264
	Zenith wet delays	1 per station and hour	2400
	Tropospheric gradients	2 per station and component	400
	Phase cycle ambiguities	1 per pass	4129
	Station clock offsets	1 per station and epoch	28800
	Satellite clock offsets	1 per satellite and epoch	6912
	Total		**43211**
Constraints	Double differenced ambiguity fixing constraints	(1 per pass) - (1 reference ambiguity per station and satellite)	4005
	Time reference constraints	1 per epoch	288
	No-net-rotation constraint	3	3
	DUT1 constraint	1	1
	Total		**4297**
DOF	**Total**		**168375**

Most IGS ACs use the generalized least-squares estimation method (Sect. B.1), while some others use sequential adjustment methods. ACs using undifferenced observations usually assume that they are independent and thus use diagonal observation weight matrices. Undifferenced observations are generally given elevation-dependent weights (e.g. proportional to $\sin(e)$ or $\sin^2(e)$). ACs using double-differenced observations should in principle propagate the (diagonal) covariance matrix of undifferenced observations to their chosen set of double-differenced observations so as to obtain the corresponding weight matrix.

GLONASS specificities As mentioned in Sect. 2.1.1, the exact frequencies of the L1 and L2 signals broadcast by the GLONASS satellites are slightly different for each satellite (except that pairs antipodal GLONASS satellites use the same frequencies). Since it is frequency-dependent, the uncalibrated phase delay of a GLONASS receiver can therefore not be represented by a single term $\delta\phi_k$ as in the GPS case. Consequently, when GLONASS double-differenced observations are formed, the receiver UPDs do not cancel, which prevents a straightforward fixation of double-differenced GLONASS ambiguities to integer values.

There exist GLONASS ambiguity resolution techniques that involve the estimation of so-called inter-frequency biases (one parameter per station and GLONASS frequency channel). Another (lazier) solution consists in simply not attempting to fix GLONASS ambiguities and estimating them as floats.

2.1.3 GNSS contribution to the ITRF2008 and ITRF2013

In 2008, eleven ACs (Table 2.2) reanalyzed the full history of GPS data collected by the IGS tracking network back to 1994 using the latest models and methodology available at that time. This unprecedented effort, known as first IGS reprocessing campaign or *repro1* (see `http://acc.igs.org/reprocess.html`), constituted the basis of the GNSS contribution to the ITRF2008. Major quality improvements from the operational IGS products used for the previous ITRF2005 to the repro1 products were noted by, e.g., Griffiths et al. (2009) and Collilieux et al. (2011). The eleven ACs contributing to repro1 performed weekly GPS-only analyses over the period 1994-2008, that resulted in weekly SINEX files including station coordinate, EOPs and, for some ACs, satellite antenna phase center offset estimates. The AC SINEX files were combined on a weekly basis into so-called *ig1* SINEX files by Remi Ferland at NRCan (IGS Mail 6136). Those, supplemented with operational combined SINEX files over the period 2008-2009.5, constituted the IGS contribution to ITRF2008.

The IGS is currently undertaking a second reprocessing campaign (repro2) that will provide the IGS input to the ITRF2013. Apart from covering a longer period and involving less ACs, repro2 will differ from repro1 in the following respects:

Table 2.2 IGS Analysis Centers having contributed to repro1

Operational acronym	Repro1 acronym	Description	Country
cod	co1	Center for Orbit Determination in Europe	Switzerland
emr	em1	Natural Resources Canada	Canada
esa	es1	European Space Operation Centre	Germany
gfz	gf1	GeoForschungZentrum	Germany
	gt1	GeoForschungZentrum - TIGA contribution	Germany
jpl	jp1	Jet Propulsion Laboratory	USA
mit	mi1	Massachusetts Institute of Technology	USA
ngs	ng1	National Geodetic Survey	USA
	pd1	Potsdam-Dresden Reprocessing	Germany
sio	si1	Scripps Institution of Oceanography	USA
	ul1	Université de la Rochelle	France

- Updated models and conventions will be used (see a list at `http://acc.igs.org/reprocess2.html`).
- Like in their operational analyses since GPS week 1702 (IGS Mail 6613), the ACs will provide daily instead of weekly SINEX files.
- Some of the participating ACs will provide combined GPS-GLONASS solutions, whereas all AC contributions to repro1 were GPS-only solutions.

2.1.4 A primordial contribution to the ITRF

The GNSS contribution to the ITRF is fundamental in several respects. First of all, GNSS are by far the cheapest and most widespread technique via which a vast majority of users access the ITRF, either by positioning a GNSS receiver relatively to ITRF GNSS stations, or by absolute Precise Point Positioning (PPP) using ITRF-consistent satellite orbits and clocks. A first primordial role of GNSS is thus that they allow the ITRF dissemination.

Besides that, GNSS also play a primordial role in the elaboration of the ITRF, as the link between the three other techniques. Most of the co-location sites in the ITRF2008 are indeed composed of one VLBI, SLR or DORIS station and of one GNSS station. If the 137 local ties involving GNSS stations had not been used, the ITRF2008 would thus have relied on only 8 VLBI-SLR, 10 VLBI-DORIS and 10 SLR-DORIS ties (Altamimi et al., 2011).

The definition of the ITRF orientation (and its continuity between the successive ITRF realizations) is also ensured by GNSS. The no-net-rotation and no-net-rotation-rate constraints used to define the ITRF orientation are indeed applied via a subset of high quality GNSS stations.

Except for *DUT1* to which they are insensitive and *LOD* of which they give biased estimates (Ray, 1996, 2009), GNSS are additionally the major contributing technique to the ITRF EOPs. According to the ITRF2008 inter-technique weighting, the GPS-derived pole coordinates used in the ITRF2008 combination were for instance more than ten times more precise than the pole coordinates from any of the three other techniques (Altamimi et al., 2011).

Finally, GNSS also provide more precise station coordinates than any of the three other techniques. As an example, Fig. 2.1 shows residual times series from the ITRF2008 technique-specific long-term stacking for four co-located stations (one of each technique). In the East and North components, the residual time series of the GPS station (shown in red) are clearly much less scattered than those of the three other stations. In the Up component, the preeminence of GPS is less pronounced (in particular over SLR), but still noticeable. Considering in addition that they have the denser network of stations, GNSS thus clearly have a particularly robust contribution to the terrestrial part of the ITRF.

However, GNSS-derived station coordinates are known to be affected by various systematic errors, so that even if the contribution of GNSS to the ITRF is fundamental, it remains perfectible. Moreover, as mentioned in Sect. 1.2.6, GNSS did not contribute to defining the origin, neither the scale of ITRF2008: the origin and terrestrial scale information stemming from the input GPS solutions was indeed not considered reliable enough. For now, GNSS alone could thus not suffice to completely define a Terrestrial Reference Frame. The next sections of this chapter will describe in more detail the above mentioned issues and their current understanding.

2.2 Systematic errors in GNSS station position estimates

In this section, various known sources of systematic errors in GNSS-derived station coordinates are first reviewed (Sect. 2.2.1). The consequences of these systematic errors on the ITRF and on the geophysical interpretation of GNSS station position time series are then discussed in Sect. 2.2.2. Sect. 2.2.3 finally summarizes the results from a study of the IGS SINEX combination residuals (i.e. of the discrepancies between station positions estimated by the various IGS ACs) presented at the IGS Workshop 2012 (Rebischung et al., 2012).

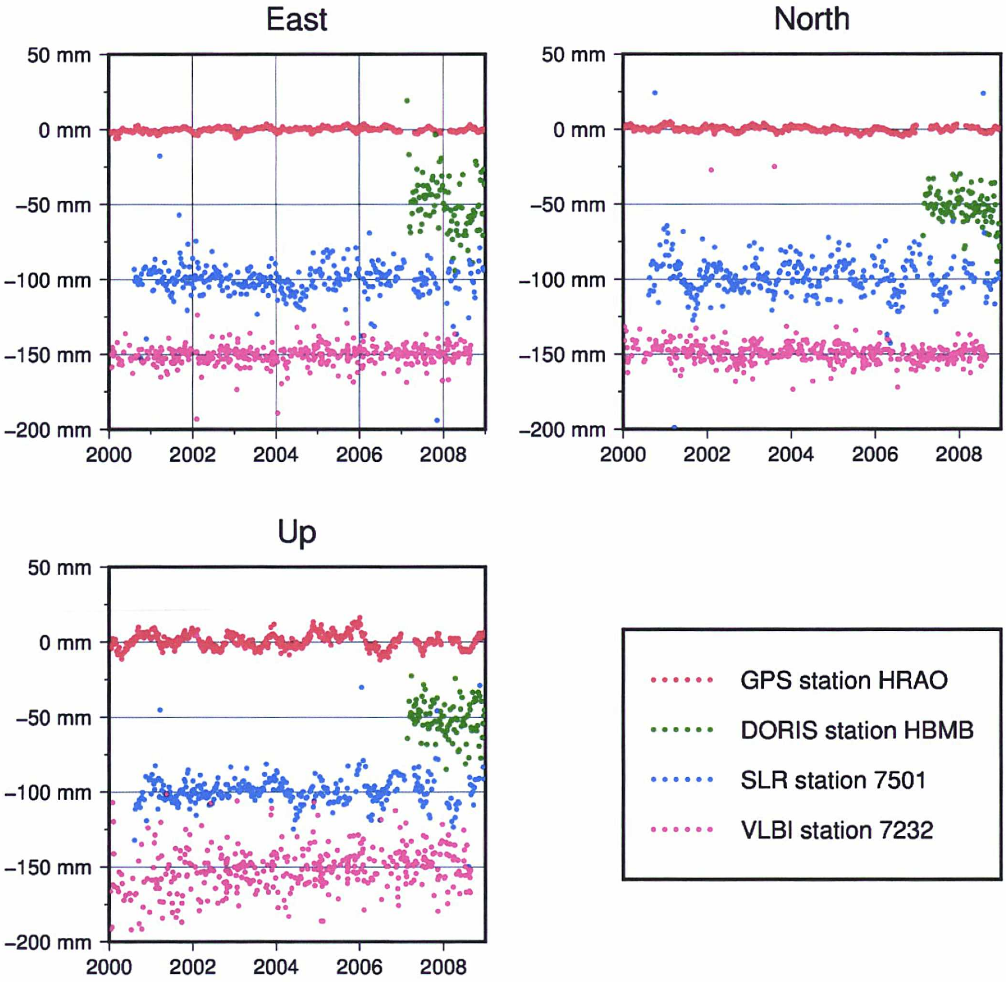

Figure 2.1 Examples of residual times series from the ITRF2008 technique-specific long-term stacking for one station of each technique. The four selected stations are all co-located at the Hartebeesthoek Radio Astronomy Observatory (South Africa). The DORIS, SLR and VLBI series are respectively shifted by -50, -100 and -150 mm.

2.2.1 Sources

Tide mis-modelling Errors in the modelling of Earth tides, ocean tidal loading deformations or EOP tidal variations can introduce artificial signals at various tidal periods in GPS station position time series. Moreover, tide modelling errors, combined with either the repeat period of the GPS constellation or the usual 24 hour period used to process GPS data, can potentially result into aliased periodic signals in GPS station position time series, in particular at near annual and near semi-annual periods (Penna and Stewart, 2003; Watson et al., 2006; King et al., 2008). Ray et al.

(2013) evidenced fortnightly signals in most recent IGS station position time series, indicating that tide modelling errors are currently still contaminating GNSS station position estimates.

Higher order ionospheric effects Following Kedar et al. (2003) and Hernández-Pajares et al. (2007), Petrie et al. (2010) investigated the impact of higher order ionospheric effects on GPS station position estimates. They demonstrate that ignoring the second and third order ionospheric effects is primarily responsible for spurious global Z translations of the GPS-derived terrestrial frames, with amplitudes reaching ~10 mm during periods of maximal solar activity. But spurious distortions of the station network are also induced at the order of ~1 mm during periods of maximal solar activity. These slowly varying errors may in particular be responsible for biases in the estimated velocities of GPS stations. The second-order ionospheric effects will be taken into account in the IGS repro2 campaign. However, small residual systematic errors will have to be expected due to ignoring the third-order ionospheric effects (Petrie et al., 2010) and to imperfections of the second-order ionospheric corrections (Garcia-Fernandez et al., 2012).

Orbit mis-modelling There exist several evidences that imperfectly modelling the GNSS satellite orbits is responsible for systematic errors in GNSS-derived terrestrial frames. For instance, by improving the orbit modelling employed at the CODE AC, Springer (2000) could eliminate a ~7 cm bias that was previously affecting the Y component of the origin of the CODE terrestrial frames. More recently, Rodriguez-Solano et al. (2011) showed that not modelling the Earth-reflected radiation pressure acting on GPS satellites was responsible for millimetric periodic errors in GPS station position estimates. But the main evidence that GPS station position estimates are contaminated by mis-modelling of the GPS satellite orbits resides in the so-called *draconitic* signals found in GPS station position time series.

In the stacked periodogram of GPS station position time series, Ray et al. (2008) indeed observed spurious spectral peaks at harmonics of the GPS draconitic year (i.e. the period at which the orientation of the GPS constellation with respect to the Sun repeats, approximately 351.4 d), that no geophysical process could explain. Systematic errors at harmonics of the GPS draconitic year were later found in other GPS-derived geodetic products such as EOPs (Ray et al., 2011), satellite orbits (Griffiths and Ray, 2013) and satellite phase center offsets (Schmid et al., 2007). Ray et al. (2008) proposed two possible mechanisms that could explain these draconitic errors: long-period satellite orbit modelling errors and/or the aliasing of station-specific errors (e.g. antenna mis-calibration or multipath) repeating with the satellite constellation geometry. The geographical coherence of the draconitic errors observed in GPS station position time series seems to imply a main orbit-related origin, but smaller local contributions exist as well, as evidenced in the differential position time series between pairs of nearby stations Ray et al. (2011). The predominance of an orbital origin tends to be confirmed by the results of Rodriguez-Solano et al. (2014) who achieved a significant reduction of the draconitic errors in various geodetic products with an improved modelling of satellite dynamics.

Troposphere mis-modelling Imperfections in the modelling of tropospheric delays of the GNSS observations may also be responsible for systematic errors in GNSS station position estimates. For instance, the non-estimation of horizontal tropospheric gradients is known to cause global North-South distortions of GNSS-derived terrestrial frames due to the equatorial tropospheric bulge (MacMillan and Ma, 1997). Similarly, not using accurate surface pressure data to compute a priori zenith hydrostatic delays can lead to biases and spurious annual variations in GNSS station height estimates (Tregoning and Herring, 2006). However, with the current state of troposphere modelling, station height biases and annual variations are expected not to exceed 1 mm (Steigenberger et al., 2009).

Multipath Following Elósegui et al. (1995), King and Watson (2010) investigated the effect of not modelling *multipath* (i.e. the reception of reflected signals by GPS antennas) on GPS station position estimates. They demonstrate that multipath may be responsible of station-specific height biases up to 7 mm, but also of height velocity biases up to 2.6 mm/yr and of aliased periodic signals at harmonics of the GPS draconitic year.

PCC mis-modelling Mis-modelling the phase center corrections (PCCs) of GNSS station antennas is, like multipath, another possible source of biases and aliased periodic errors in GNSS station position estimates. Biases induced by PCC mis-modelling can be evidenced by using different antenna calibration models. For instance, when the IGS switched from the igs05.atx set of antenna calibrations to the igs08.atx set (IGS Mail 6355), Rebischung et al. (2012) assessed the impact of the calibration switch on individual IGS station positions. The obtained position offsets reached up to 4 mm, 3 mm and 11 mm in the East, North and Up components respectively. Such offsets do of course not give access to the actual biases in the estimated station positions, but they constitute at least a demonstration that such biases exist and are far from negligible.

The set of antenna calibrations currently employed by the IGS (igs08.atx) groups calibrations from two different categories: calibrations obtained using a robot rotating and tilting the antenna (Wübbena et al., 1997) and field calibrations relative to a reference antenna then converted into absolute calibrations (Rothacher, 2001). Some IGS stations are additionally equipped with antennas covered by radomes for which no calibration is available. In such a case, the effect of the radome on PCCs is ignored and the calibration of the antenna without radome is used. igs08.atx contains *type* *mean* calibrations, i.e. averages of the individual calibrations of several antennas of the same type.

Position biases due to mis-modelling of GNSS antenna PCCs are expected to be the smallest in case of robot-calibrated antennas. However, by comparatively using igs08.atx type mean calibrations and individual antenna calibrations, Baire et al. (2013) obtained vertical position offsets reaching up to 10 mm and horizontal position offsets up to 4 mm. Even with robot calibrations, significant biases thus appear to affect the station positions derived by the IGS, due to using type mean calibrations. The use of antenna-specific calibrations, when available, could help in reducing those biases, but would likely not solve the problem entirely. By comparatively using antenna-specific calibrations from different facilities, Baire et al. (2013) indeed still obtained a vertical position offset of 5 mm.

Other instrumental effects Ray (2006) noticed that the observed seasonal displacements of several IGS stations was seriously altered by changes of the station receivers. Along the same lines, he observed striking correlations between the position time series and various data quality metrics of several IGS stations. These observations imply that part of the observed GPS station displacements have an instrumental basis, although the underlying instrumental mechanisms are mostly unknown.

2.2.2 Implications

Biases While constant biases in GNSS station position estimates are of no consequences for geophysical applications, they are a serious issue in the ITRF inter-technique combination as they limit the accuracy with which local ties can be introduced. Among the error sources listed in Sect. 2.2.1, multipath and PCC mis-modelling are likely the main contributors to such biases nowadays, with potential effects of several millimetres.

By inspecting the ITRF2008 local tie residuals, Altamimi et al. (2011) thus suspected large discrepancies found at several co-location sites to be due to non-calibrated radomes covering the GNSS antennas. The IGS therefore undertook a campaign to measure the position biases due to non-calibrated radomes at several co-located GNSS stations (Romero et al., 2013). The radomes of these stations were removed for several months and then put back in their initial positions. We investigated different time series of station positions estimated around the radome experiment periods, but this analysis was unfortunately mostly inconclusive. Only two radome-induced biases could indeed be evidenced: a vertical bias of about 13 mm at the TSKB station (Tsukuba, Japan) and an East bias of about 5 mm at the MDO1 station (Mc Donald Observatory, Texas, USA). Additional short baseline analyses are planned and may help in better determining the radome-induced position biases. But more generally, an effective reduction of the GNSS station position biases could only be expected from a progressive rebuilding of the IGS network with low multipath, individually calibrated antennas.

Velocity errors GNSS station velocities are of direct interest to the observation of long-term geophysical processes such as tectonic motions and post-glacial rebound, but also serve to correct vertical land motions at tide gauges in order to observe sea-level rise (Wöppelmann et al., 2007). As sea-level rises at rates of a few mm/yr, this latter application requires especially precise vertical GNSS station velocities.

If averaged over sufficiently long time spans, the seasonal and sub-seasonal signals found in GNSS station time series cause negligible velocity biases (Blewitt and Lavallée, 2002). Slowly varying spurious signals induced by ignoring higher-order ionospheric effects must have been responsible for vertical velocity biases of a few tenths of mm (Petrie et al., 2010). But the residual velocity biases due to ionosphere mis-modelling should become negligible as the second-order ionospheric effects become conventionally modelled. Nowadays, instrumental effects must therefore likely be expected as the main cause of velocity biases, via at least three possible mechanisms:

- trends in the impact of multipath on station positions due to the time-evolution of the satellite constellations (King and Watson, 2010);
- the non-detection of small offsets due to, e.g., equipment changes in GNSS station position time series (Williams, 2003);
- the progressive quality degradation of the data acquired by some stations because of antenna and/or receiver ageing.

Spurious seasonal signals GNSS station position time series, conveniently expressed in a given TRF, are expected to reflect geophysical ground motions. Apart from the long-term motions induced by plate tectonics and post-glacial rebound and from the conventionally modelled tides and ocean tide loading deformations, the main global source of crustal deformations is the permanent redistribution of masses within the oceans, atmosphere and continental hydrology (i.e. non-tidal loading deformations). Ignoring GNSS stations affected by post-seismic relaxation, de-trended GNSS station position time series are thus expected to mainly reflect such non-tidal loading deformations.

Various authors have compared de-trended GPS station position time series with geophysical loading deformation models (van Dam et al., 1994, 2001; Dong et al., 2002; Collilieux et al., 2010; van Dam et al., 2012; Collilieux et al., 2012) or with loading deformation models derived from GRACE gravity fields (Davis et al., 2004;

van Dam et al., 2007; Tregoning et al., 2009; Tesmer et al., 2011). All found that loading deformation models were able to reduce the global scatter of GPS time series to some extent, but could not explain all of the non-linear variations seen in GPS time series. Ray et al. (2011) recently repeated such a comparison using the GPS time series of 706 stations extracted from homogeneously reprocessed IGS combined solutions (the so-called *igb* dataset; see IGS Mail 6401) and a loading deformation model based on NCEP atmosphere pressure data, ECCO ocean bottom pressure data and LDAS continental hydrology data. With this up-to-date dataset, loading corrections were able to reduce the WRMS of GPS time series by only 1.6%, 3.8% and 15.2% in the East, North and Up components respectively. The annual signals in the GPS time series, for which loading corrections are expected to have the main impact, had their amplitudes globally reduced by roughly 10%, 20% and 50% respectively. A significant gap thus remains to be bridged between GPS time series and loading deformation models.

Other sources of "real" GPS station displacements first contribute to this gap, including:

- the thermal expansion of bedrock and GPS monuments (Dong et al., 2002; Yan et al., 2009);
- local loading effects not captured by the geophysical loading models nor by GRACE due to, e.g., water level variations in lakes or water tables (Meertens et al., 2012);
- non-loading geophysical processes such as clay swelling (Nahmani et al., 2012) or poroelastic effects in sediments (Meertens et al., 2012).

But "apparent" seasonal displacements induced by the error sources listed in Sect. 2.2.1 most certainly contribute to a large extent to the GPS-loading gap and thus limit the interpretation of observed GPS station seasonal displacements in terms of geophysical ground motions. Moreover, such spurious seasonal signals will become an issue for the ITRF as it evolves towards more complicated time representations of station coordinates.

2.2.3 Analysis of the IGS SINEX combination residuals

The IGS contribution to the ITRF is obtained by combining the solutions derived by different ACs with different analysis strategies (Sect. 1.2.3 and 2.1.3). The primary aim of this combination is to form weighted averaged products that potentially maximize the benefits from the AC solutions while minimizing their weaknesses. But it also allows an intrinsic inter-comparison of the AC solutions that offers valuable insight into the impact of the various AC analysis strategies on their solutions (Rebischung and Garayt, 2013). In the residuals of the IGS SINEX combinations (i.e. the differences between the AC and IGS combined station positions), common geophysical signals should indeed cancel out, leaving only analysis-related effects for investigation (i.e. differences in the modelling, selection or weighting of observations, metadata errors or differences in the impact of common modelling errors).

In 2012, a detailed study of the IGS SINEX combination residuals was initiated (Rebischung et al., 2012). Similarly to what Ray (2006) observed in position time series, instrumental effects could first be observed in the IGS SINEX combination residual time series of several stations. A first extreme case is the VENE station (Venezia, Italy; see Fig. 2.2), for which large AC-specific height biases were observed until the station's antenna was changed in 2001. Before this change, a metallic ring was in fact mounted around the antenna, which probably caused spurious phase center variations. Another interesting case is the MCM4 station (McMurdo, Antarctica; see Fig. 2.3). Again, AC-specific height biases can be observed. The fact that changes in the AC biases correspond to changes of the station's equipment tends to indicate an instrumental origin. Moreover, changes in the seasonal signals present in the AC residual time series appear likely due to changes of the station's multipath behaviour. Both these examples show that instrumental effects can have noticeably different impacts on the station positions estimated by the various IGS ACs. A more detailed analysis of the instrumental effects in the IGS SINEX combination residuals nevertheless remains to be done.

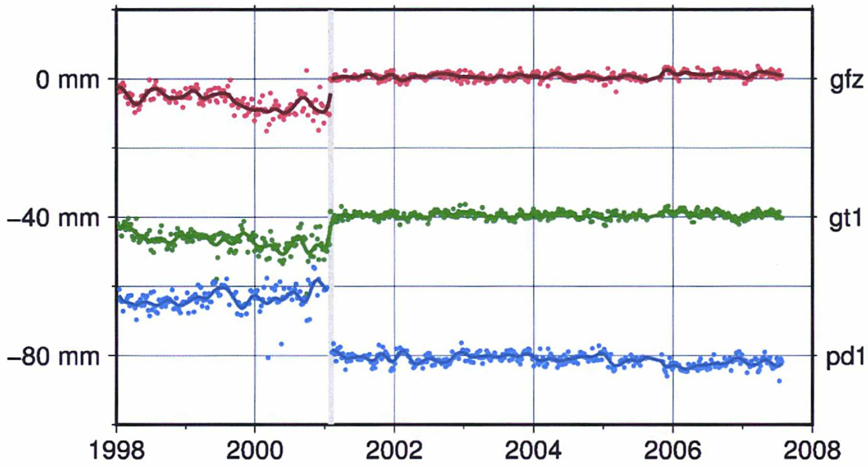

Figure 2.2 IGS SINEX combination residual time series of three selected ACs (GFZ, GT1, PD1) for the height component of station VENE. The GT1 and PD1 residual time series are respectively shifted by -40 mm and -80 mm for clarity. The residuals, represented by color dots, are extracted from the weekly *igb* combinations. The vertical grey line corresponds to an antenna change on Feb 1, 2001. The solid color lines were obtained by Vondrak-filtering the residual time series with a cut-off frequency of 3 cpy, separately before and after the 2001 antenna change.

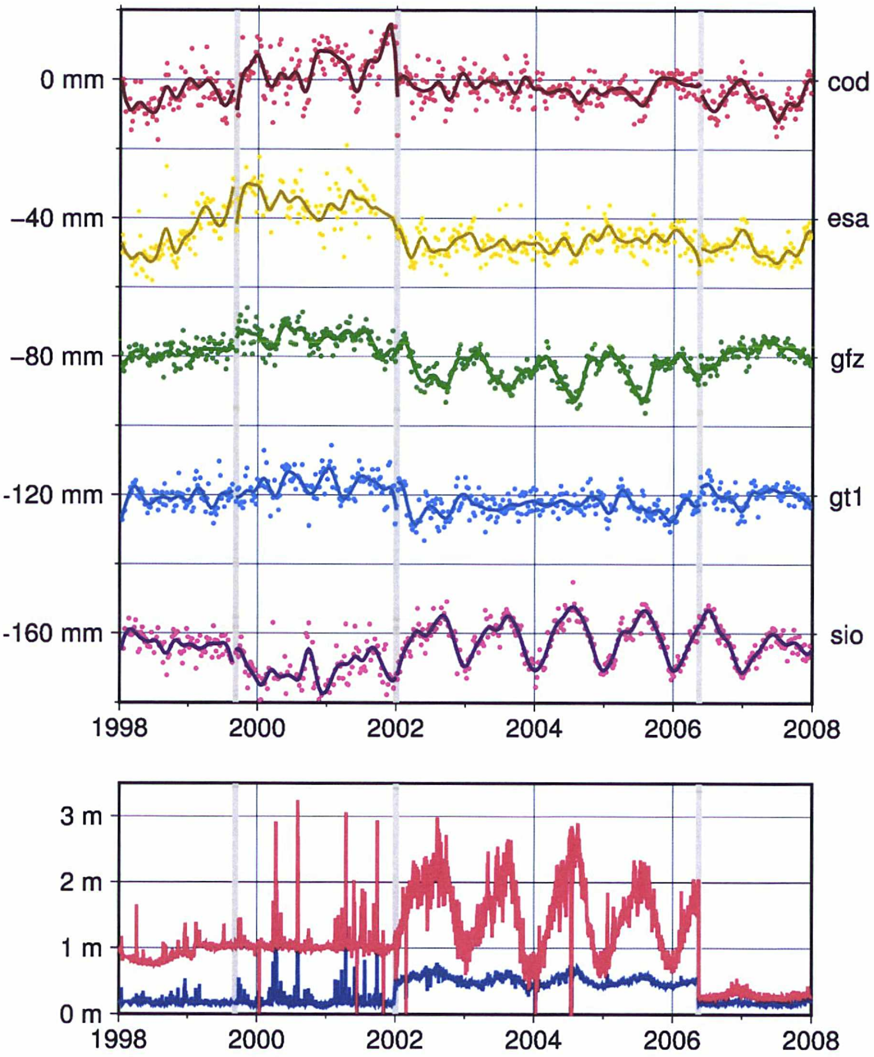

Figure 2.3 *Top:* IGS SINEX combination residual time series of five selected ACs (COD, ESA, GFZ, PD1, SIO) for the height component of station MCM4. The AC residual time series are shifted by multiples of -40 mm for clarity. The residuals, represented by color dots, are extracted from the weekly *igb* combinations. The vertical grey lines correspond to a receiver firmware upgrade on September 7, 1999, a receiver change on January 3, 2002 and a receiver firmware upgrade on May 19, 2006. The solid color lines were obtained by Vondrak-filtering the residual time series with a cut-off frequency of 3 cpy, separately before and after each event. *Bottom:* Daily RMS of L1 (blue) and L2 (red) multipath at station MCM4. Data are extracted from the daily TEQC quality checks performed by the IGS Central Bureau.

Rebischung et al. (2012) also analysed the IGS SINEX combination residuals on a global scale, so as to answer the following questions:

- How large are AC-specific analysis artefacts compared to the GPS-loading gap?

- How much are the draconitic signals found in GPS station position time series dependent on the analysis strategy?

A frequency analysis of the *igb* combination residuals was thus performed for each AC, station and component using a modified version of the FAMOUS software (Mignard, 2005; Collilieux, 2008). Statistically significant frequencies were extracted from each of the series and identified, when possible, to the annual frequency, the semi-annual frequency or to a harmonic of the GPS draconitic frequency. Amplitude/phase maps of the extracted signals were finally drawn for each AC, component and frequency class. A similar analysis was repeated and similar maps were drawn for the set of load-corrected IGS position time series used by Ray et al. (2011) (see Sect. 2.2.1), hereafter denoted as *igb-load* time series.

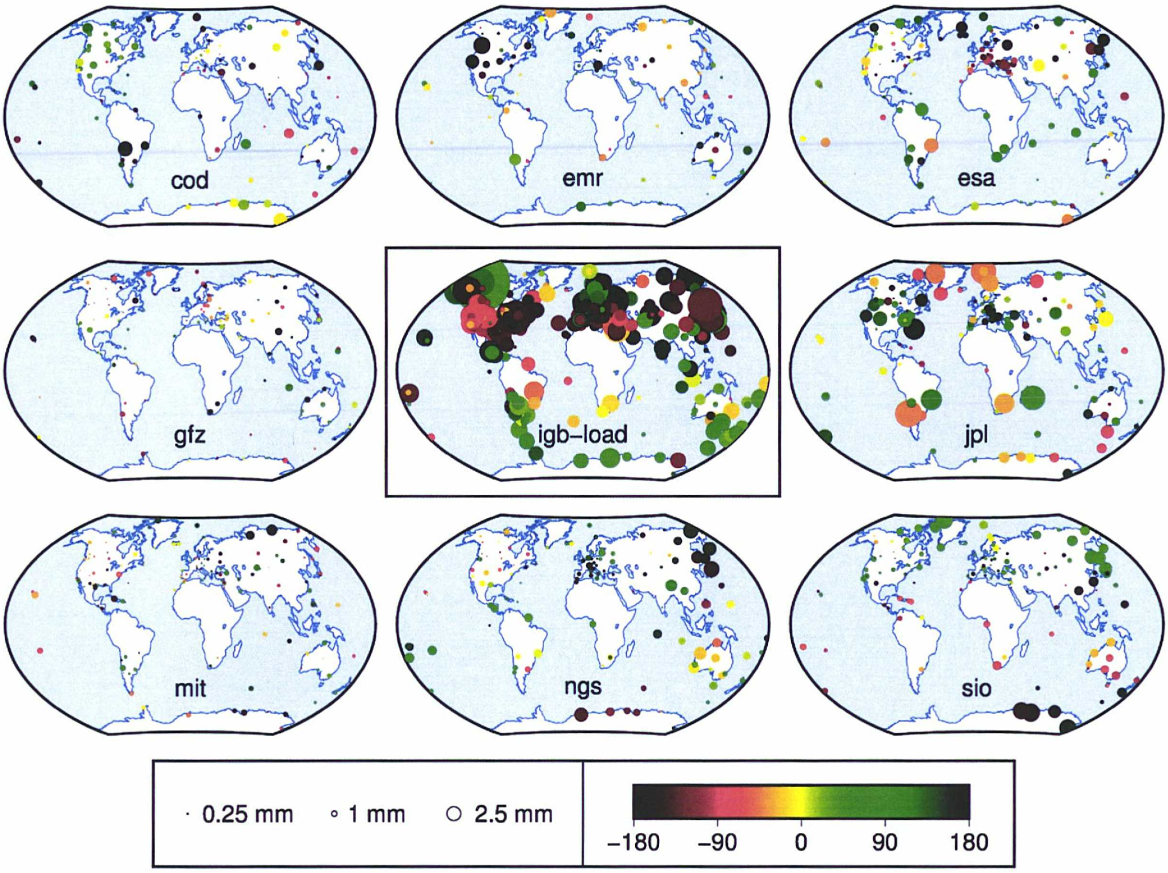

Figure 2.4 Amplitude/phase maps of the annual signals extracted from the height residual time series of eight selected ACs, as well as from the *igb-load* height time series. Amplitudes and phases correspond to the model $A\cos((t-2000.0)-\phi)$, with t in decimal year, and are respectively represented by the size and color of the dots.

Fig. 2.4 shows for instance maps of the annual signals extracted from the height residual time series of eight selected ACs, as well as from the *igb-load* height time series. From Fig. 2.4, it is clear that the vertical annual signals found in the AC residual time series are globally smaller than those found in the *igb-load* time series. In other words, the vertical annual GPS-loading gap is mostly due to signals commonly observed by all ACs, while AC specificities play a secondary role. Similar conclusions can be drawn for the horizontal annual signals as well as for the vertical and horizontal semi-annual signals. A noticeable exception in Fig. 2.4 is the JPL AC, whose residuals seem to show larger annual signals than the other ACs. But this may be due to the fact that JPL uses disjoint station networks from one week to the next, so that the JPL residual time series are especially sparse and that their frequency analysis is subject to caution.

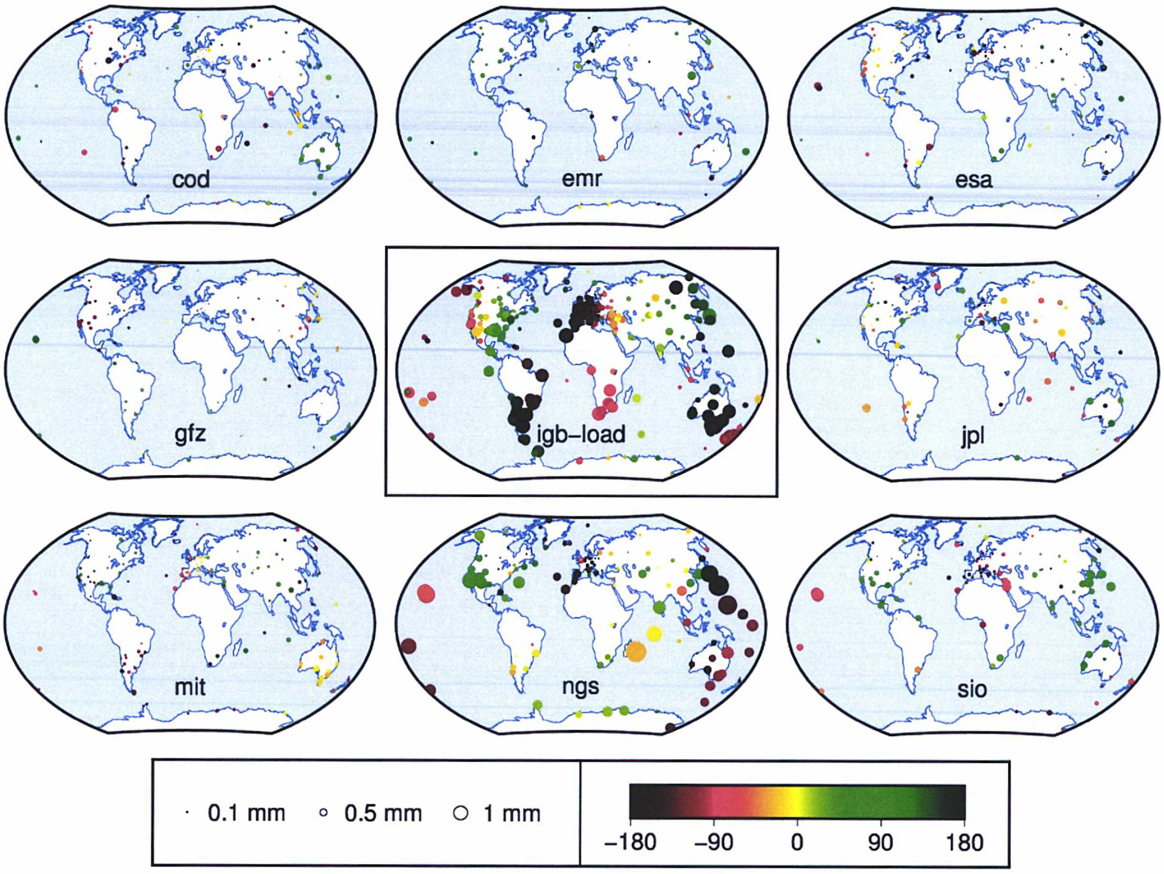

Figure 2.5 Amplitude/phase maps of the second draconitic harmonic signals extracted from the East residual time series of eight selected ACs, as well as from the *igb-load* East time series. Amplitudes and phases correspond to the model $A\cos((t - 2000.0) - \phi)$, with t in decimal year, and are respectively represented by the size and color of the dots.

Fig. 2.5 similarly shows maps of the second draconitic harmonic signals extracted from the East residual time series of eight selected ACs, as well as from the *igb-load*

East time series. The strong spatial coherence of the second draconitic harmonic signals extracted from the *igb-load* time series is first striking and corroborates the predominance of an orbit-related origin. Secondly, apart from NGS, the second draconitic harmonic signals extracted from the AC residual time series are globally smaller than those found in the *igb-load* time series. Similar conclusions can be drawn for the North and Up components, as well as for other draconitic harmonics. In other words, it seems that the spurious draconitic signals found in the AC station position time series are induced by common modelling errors, while AC specificities play again a secondary role. The NGS exception is specific to the second draconitic harmonic and remains unexplained.

In summary, it appears that the impact of the various analysis strategies used by the IGS ACs is secondary compared to both the GPS-loading gap and the draconitic signals found in GPS station position time series. This situation is quite unfortunate as it implies that all ACs have somehow converged to common modelling errors, while AC-specific modelling errors could have been much easier to track down.

2.3 GNSS and the terrestrial scale

The fundamental issue concerning the determination of the terrestrial scale with GNSS was first documented by Springer (2000) and Zhu et al. (2003). They indeed demonstrated that GNSS observations were weakly sensitive to the mean of the radial component of the GNSS satellite antenna phase center offsets (z-PCOs) because of correlations with satellite clock offsets, zenith wet delays and station heights. (The mechanism of these correlations will be detailed in Sect. 4.2.) Zhu et al. (2003) showed in particular that a mean error δz (in m) of the satellite z-PCOs would induce a net scale change of the GNSS-derived terrestrial frames by approximately $\delta s = 7.8\, \delta z$ (in ppb).

The second aspect of the problem is that pre-launch antenna calibrations are not available for any of the GPS and GLONASS satellites launched so far. The "true" mean of the satellite z-PCOs is thus unknown and can hardly be estimated from GNSS observations. Current GNSS are therefore considered unable to provide reliable intrinsic terrestrial scale information. On the contrary, the IGS currently relies on the ITRF scale to determine conventional GPS and GLONASS satellite z-PCOs (Rebischung et al., 2012; Ray et al., 2013). In their analyses, the IGS ACs then fix or tightly constrain the satellite z-PCOs to their conventional IGS values, so that, unless these constraints are removed, the scales of the IGS AC solutions are in turn conventionally determined.

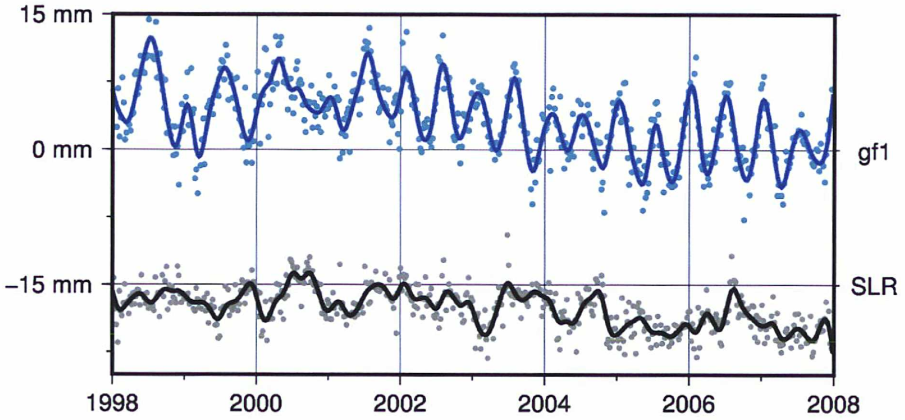

Figure 2.6 *Cyan dots*: Scale factors estimated between the weekly *gf1* solutions processed as described in the text and the ITRF2008. *Grey dots*: Scale factors estimated between the SLR input solutions to the ITRF2008 and the ITRF2008, shifted by -15 mm. The solid lines were obtained by Vondrak-filtering each of the scale factor time series with a cut-off frequency of 3 cpy.

As an illustration, Fig. 2.6 shows how the intrinsic scale of GPS terrestrial frames actually compares with the scale of SLR frames. VLBI is not considered in this comparison since VLBI frames are computed on a session-wise basis rather than on a weekly basis like GPS and SLR frames. The SLR time series shown in Fig. 2.6 consists of the scale factors estimated between the SLR input solutions to the ITRF2008 and the ITRF2008 (see Fig. 6 in Altamimi et al. (2011)). The GPS time series shown in Fig. 2.6 was derived from the weekly reprocessed solutions of the GFZ AC (*gf1*) as follows. The original, non-constrained normal equations, in which the GPS satellite z-PCOs were included, were first recovered using Eq. 1.9. The normal equations were then inverted using no-net-rotation constraints only, while letting free both the satellite z-PCOs and the terrestrial scale. Seven transformation parameters were finally iteratively estimated between each of the obtained solutions and the ITRF2008.

The intrinsic scale factors of the *gf1* solutions are not only globally more scattered than the SLR scale factors, but also show significant long-term biases and trends. A particularly pronounced semi-annual signal is also visible, much too large to be attributed to some network effect (i.e. the aliasing of loading deformations into the estimated scale parameters). What rather happens is that, when the satellite z-PCOs are let free, (unidentified) modelling errors tend to spread into the weakly determined terrestrial scale. It appears anyway justified not to use such intrinsic GPS scale information in the definition of the ITRF scale.

2.4 GNSS and geocenter motion

As highlighted in Sect. 1.3, several approaches can be used to estimate geocenter motion from GNSS observations. We will focus in this section on the realization of CM via the GNSS satellite orbit dynamics only (i.e. on the network shift approach), as it is the way by which GNSS could potentially contribute to defining the ITRF origin.

2.4.1 Current status

GPS network shift estimations of geocenter motion have been carried out by several authors for more than twenty years (e.g. Vigue et al., 1992; Ray, 1999; Heflin et al., 2002; Dong et al., 2003; Altamimi and Collilieux, 2009; Collilieux et al., 2011). But although tremendous improvements have been achieved during that time, GPS geocenter motion estimates are still far from competing with SLR ones. By analysing the translation time series between reprocessed weekly solutions from four IGS ACs and a preliminary version of ITRF2008, Collilieux et al. (2011) indeed found significant long-term biases with respect to the SLR translations, as well AC-dependent trends in the Z component. Moreover, the annual signals present in the X and Z components of the IGS AC translation time series were in poor agreement with SLR.

In 2012, a deeper analysis of the IGS AC geocenter motion estimates was conducted (Rebischung et al., 2012). The inputs of this study were the reprocessed weekly solutions of seven selected ACs for the period 1998.0-2008.0, supplemented with their operational solutions for the period 2008.0-2011.3. When necessary, non-constrained normal equations were first recovered from the original AC solutions and inverted under no-net-rotation constraints. A long-term stacking was then performed for each AC as described in Sect. 1.2.4. Finally, three rotation and three translation parameters were iteratively estimated between each weekly AC solution and the corresponding long-term solution. The obtained translations correspond to network shift estimates of non-linear geocenter motion (Sect. 1.3.1). Note that AC-specific, well-distributed station sub-networks were used so as to mitigate potential network effects.

As an example, Fig. 2.7 compares the translation time series derived from the GPS solutions of the ESA AC with SLR geocenter motion estimates from Altamimi et al. (2012). While the GPS and SLR translation time series have comparable high-frequency scatter levels, the GPS translations show much stronger sub-annual signals, especially in the Z component. A frequency analysis of the time series indeed reveals the presence of unexpected spectral peaks at various harmonics of the GPS draconitic year (see Fig. 2.8). As can be seen in Fig. C.1-C.6, this situation is not specific to the ESA AC, although the draconitic harmonic spectral peaks have various amplitudes in the translation time series of the different ACs.

As non-linear geocenter motion is expected to mostly consist of an annual signal, a question raised by Rebischung et al. (2012) was the following: despite the spurious sub-annual draconitic signals present in the IGS AC translation time series, do the underlying seasonal signals constitute reasonable estimates of annual geocenter motion? To answer this question, the IGS AC translation time series were first Vondrak-filtered with a cut-off frequency of 1.25 cpy, so as to retain their seasonal (and lower frequency) part only, and compared to similarly smoothed SLR translation time series (Fig. 2.9-2.11). Periodic signals at the annual and semi-annual frequencies and at the seven first harmonics of the GPS draconitic year were then simultaneously fitted to each of the AC translation time series. The amplitudes and phases of the extracted annual signals were finally compared to reasonable estimates of annual geocenter motion selected by Ries (2011) (Fig. 2.12).

As regards the Y component of geocenter motion, the annual signals of all IGS AC translation time series show a remarkably good agreement in phase with each other, with SLR (Fig. 2.10) and with Ries (2011)'s selection (Fig. 2.12 (Y)). The amplitudes of the IGS AC annual signals are however quite disparate, ranging from 2 to 5 mm.

The situation is notably different for the Z component of geocenter motion. The seasonal signals found in the AC Z translation time series indeed show long-term amplitude variations as well as progressive phase shifts with respect to the SLR seasonal signal (Fig. 2.11). (Note that, except JPL and EMR since 2006, the AC seasonal signals are rather consistent in phase with each other.) As illustrated in Fig. 2.13, this behaviour may be partly explained by the interference of annual signals with spurious draconitic signals with a near annual period of $\sim$351.4 days. However, the simultaneous fit of annual and draconitic signals to the AC Z translation time series did not allow to uncover reliable annual signals (Fig. 2.12 (Z)). At least two possible reasons could explain this fact. First, the annual signals present in the AC Z translation time series might actually not correspond to "real" geocenter motion. But it is also possible that the AC Z translation time series contain non-stationary draconitic errors that would prevent a reliable isolation of the underlying annual signals.

Finally, similarly as in the Z component, the seasonal signals of the IGS AC X translation time series are alternatively in phase and out-of-phase with the SLR seasonal signal. But the most striking feature in Fig. 2.9 is the small amplitude of the IGS AC seasonal signals compared to SLR. This can also be observed in

Fig. C.4 where a lack of spectral power is visible for all ACs at the annual frequency. This behaviour might again be explained by an overall destructive interference of annual signals with spurious draconitic signals during the considered period. The simultaneous fit of annual and draconitic signals to the AC X translation time series indeed enabled to uncover realistic annual signals for some ACs (COD, NGS, GFZ; see Fig. 2.12 (X)). However, the possibility of non-stationary draconitic errors prevents a definitive interpretation of this result.

In summary, the network shift estimation of geocenter motion with GPS currently remains prone to significant errors, from sub-seasonal to secular time scales, and thus far from competing with SLR geocenter motion estimation. In the X and Z components, the main annual component of geocenter motion can in particular not be retrieved from GPS network shift estimates. As shown by Meindl et al. (2013), the situation is even much worse with GLONASS-only or combined GPS+GLONASS network shift estimates. These observations explain why the origin information stemming from GNSS solutions has so far not been considered reliable enough to contribute to the definition of the ITRF origin.

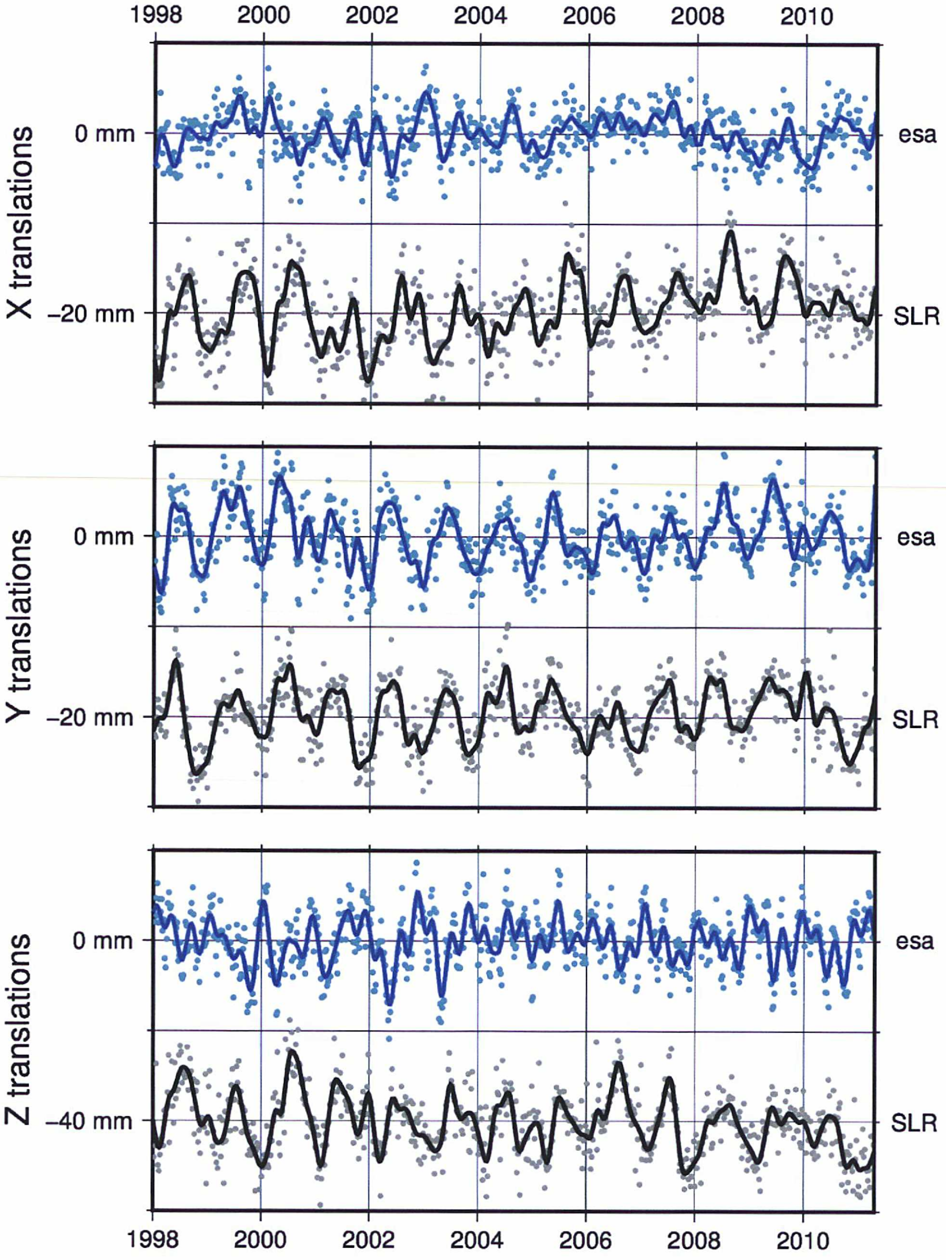

Figure 2.7 *Cyan dots*: Translations derived from the weekly ESA solutions. *Grey dots*: SLR-derived translations from Altamimi et al. (2012) shifted by -20 mm, -20 mm and -40 mm respectively for the X, Y and Z components. The solid lines were obtained by Vondrak-filtering each of the translation time series with a cut-off frequency of 3 cpy.

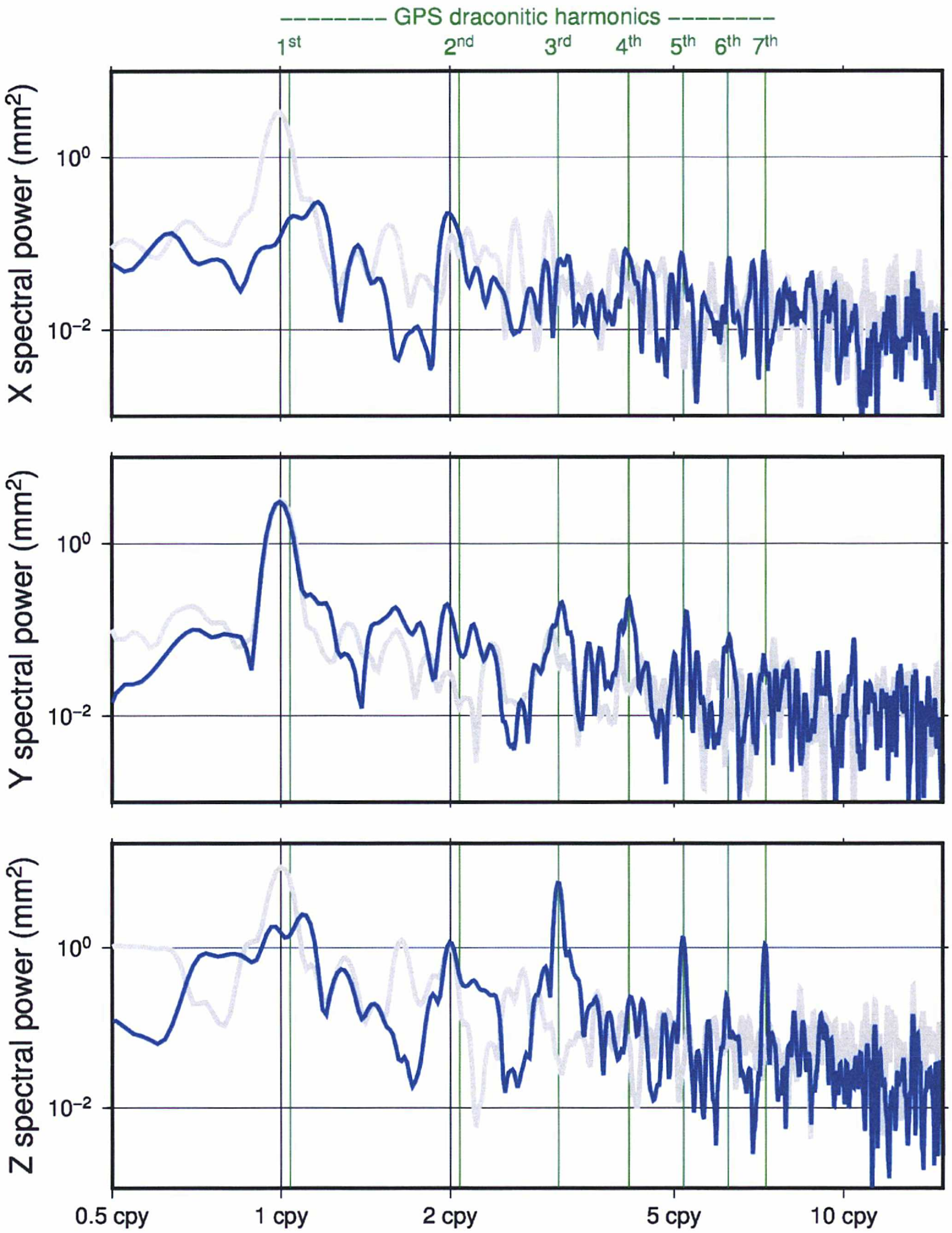

Figure 2.8 Lomb-Scargle periodograms of the ESA GPS (blue) and SLR (grey) translation time series shown in Fig. 2.7. For better legibility, the periodograms were computed over a 4 times oversampled frequency set and boxcar smoothed over 5 adjacent frequencies.

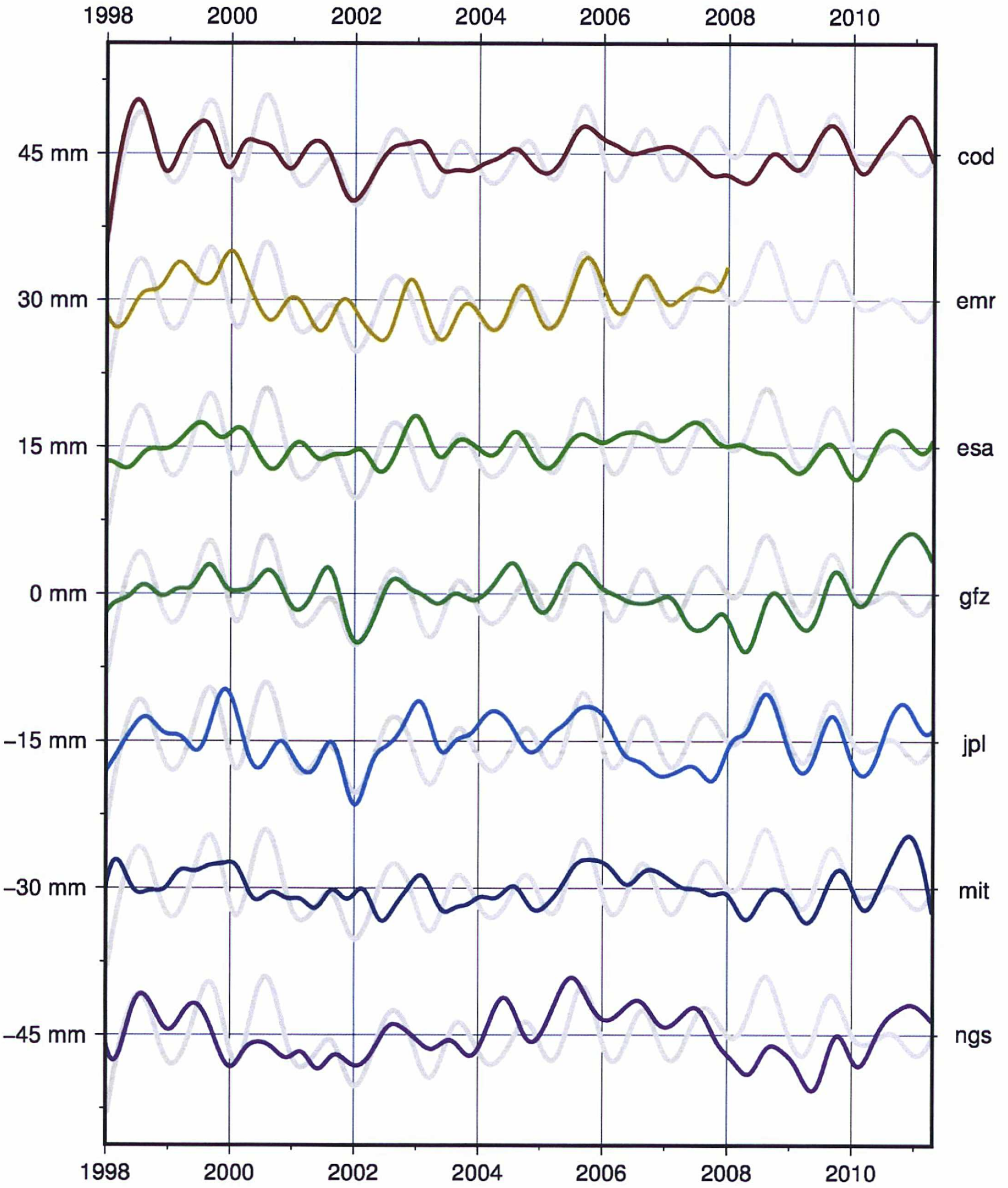

Figure 2.9 X translation time series derived from the reprocessed solutions of seven IGS ACs, Vondrak-filtered with a cut-off frequency of 1.25 cpy and shifted by multiples of 15 mm. The background grey lines correspond to the similarly filtered SLR X translation time series from Altamimi et al. (2012).

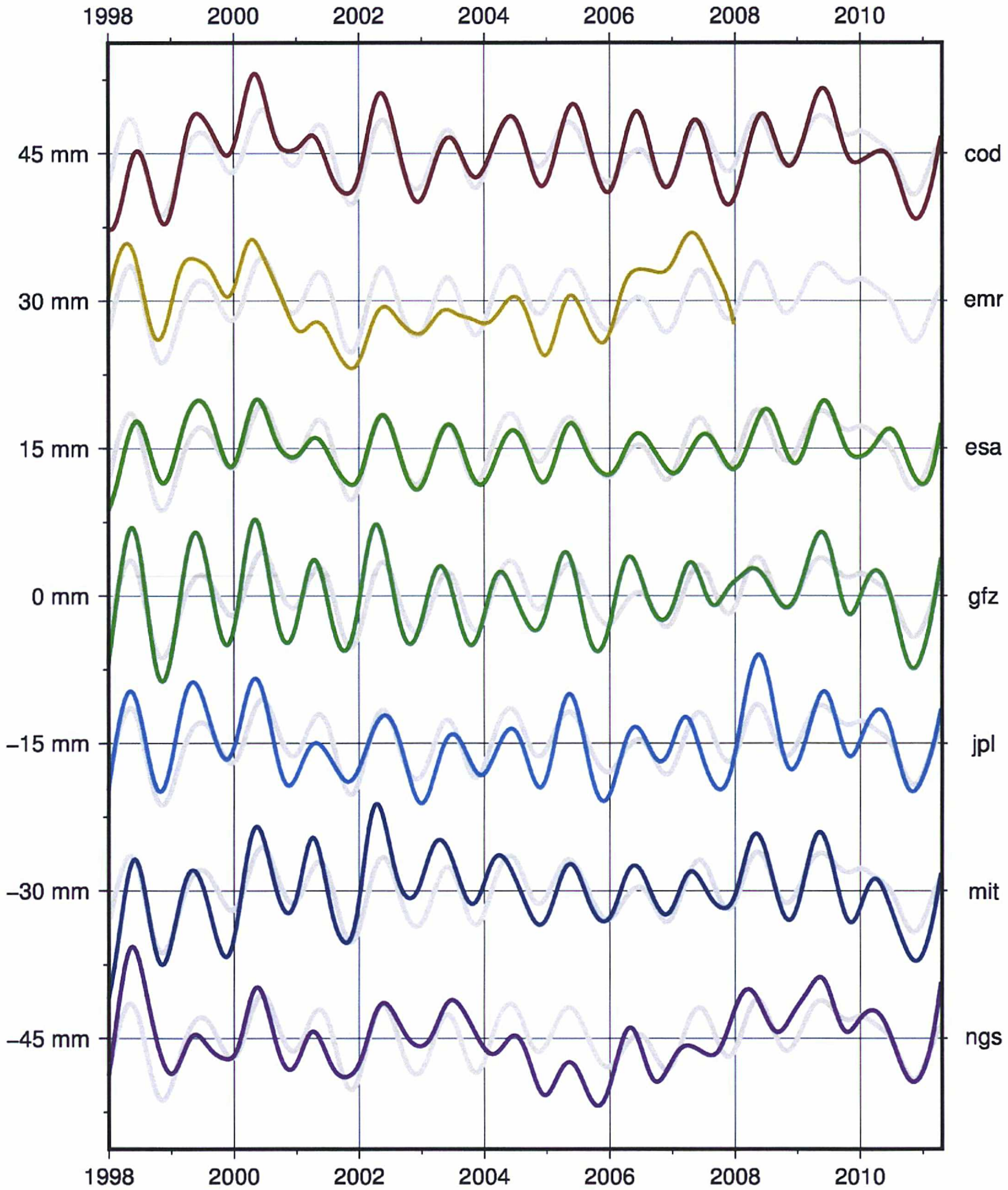

Figure 2.10 Y translation time series derived from the reprocessed solutions of seven IGS ACs, Vondrak-filtered with a cut-off frequency of 1.25 cpy and shifted by multiples of 15 mm. The background grey lines correspond to the similarly filtered SLR Y translation time series from Altamimi et al. (2012).

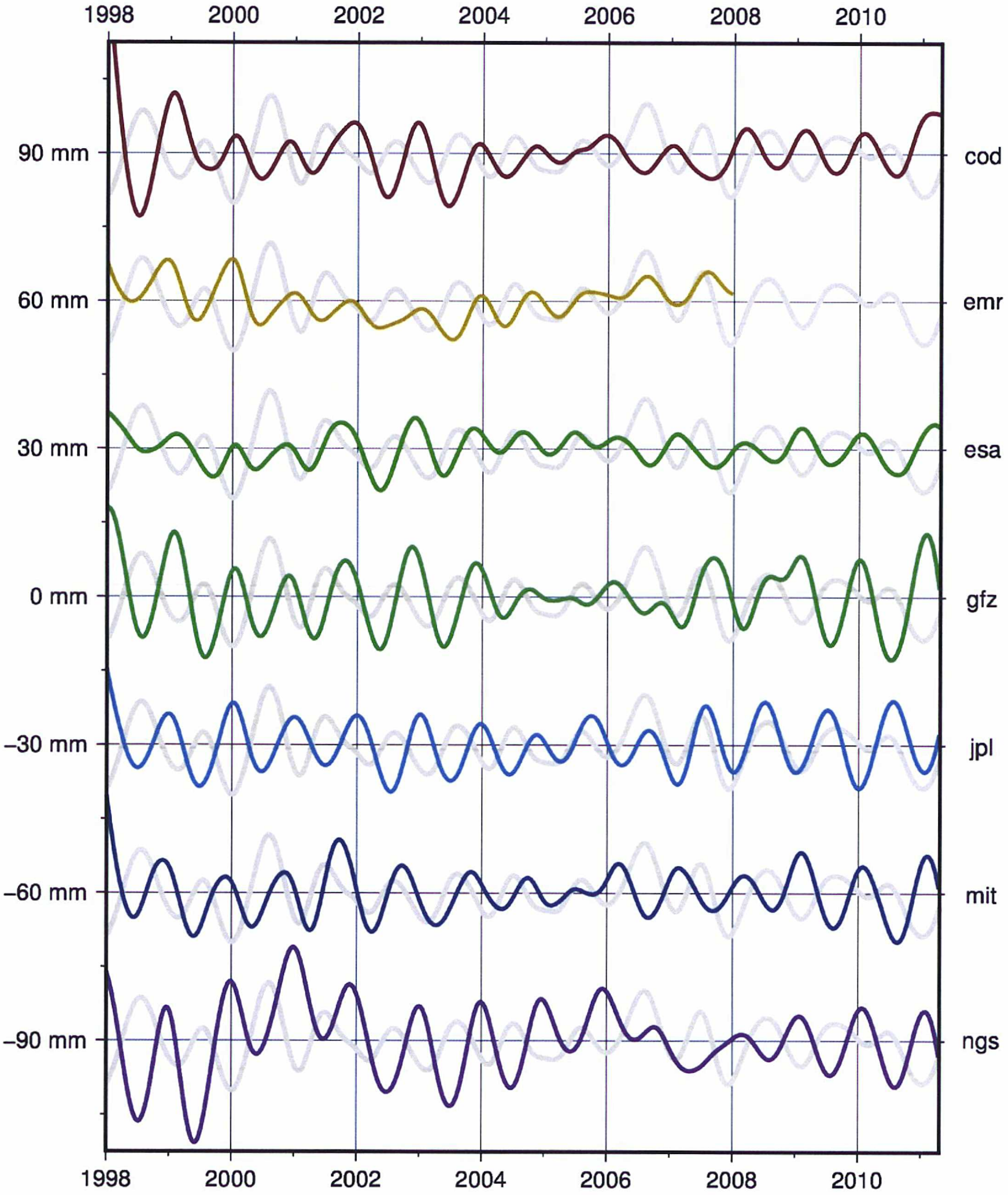

Figure 2.11 Z translation time series derived from the reprocessed solutions of seven IGS ACs, Vondrak-filtered with a cut-off frequency of 1.25 cpy and shifted by multiples of 15 mm. The background grey lines correspond to the similarly filtered SLR Z translation time series from Altamimi et al. (2012).

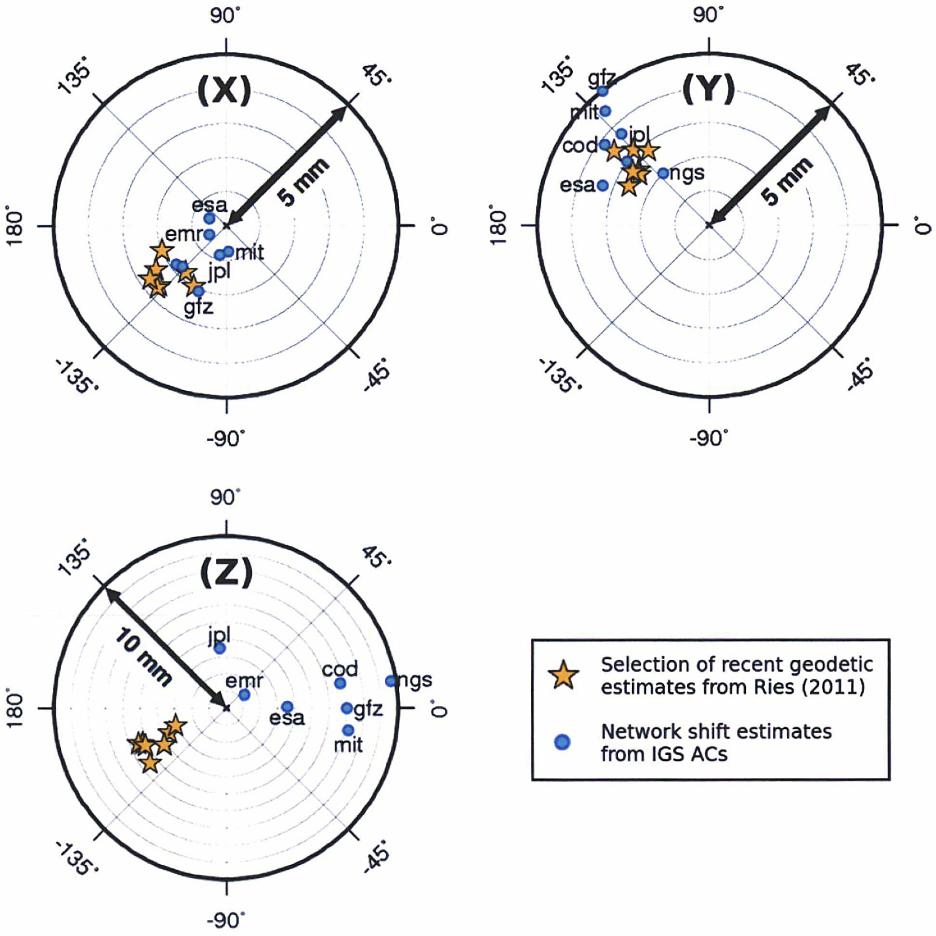

Figure 2.12 Amplitude/phase diagrams of the annual signals extracted from the IGS AC translation time series (blue dots) and of Ries (2011)'s selection of reasonable annual geocenter motion estimates (yellow stars).

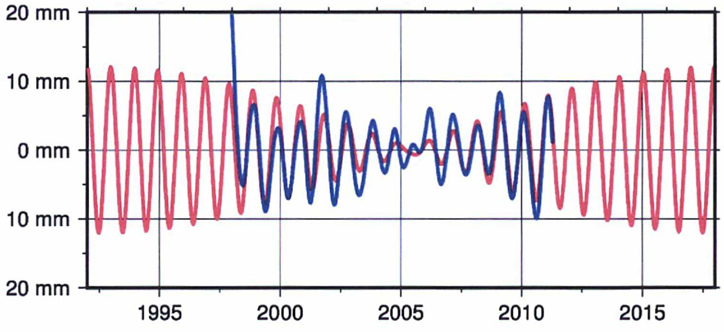

Figure 2.13 *Blue:* Z translation time series from the MIT AC, Vondrak-filtered with a cut-off frequency of 1.25 cpy. *Red:* Result from the simultaneous fit of an annual and a draconitic signal to this time series.

2.4.2 An unresolved issue

As they benefit from many more satellites and a much denser tracking network than SLR, the fact that GNSS are still far from competing with SLR for the network shift estimation of geocenter motion may seem rather counterintuitive. Moreover, until recently, no precise correlation mechanism had been described which could have explained a weak sensitivity of GNSS to geocenter motion. When this thesis started, the question of why GNSS were performing so poorly, compared to SLR, through the network shift approach was thus remaining unresolved.

Observations had nevertheless been made by several authors that the modelling of the GNSS satellite orbits had a particular importance for GNSS geocenter motion estimates. Firstly, the parameterization of the empirical accelerations set up to account for the non-modelled forces acting on GPS satellites was shown to be of great influence by Springer (2000) and, more recently, Herring (2011). By fixing some of the usually set up empirical acceleration parameters, they indeed observed a clear degradation of GPS geocenter motion estimates, especially via a ~7 cm bias in the Y component and a ~4 cm spurious seasonal signal in the Z component. On the other hand, by setting up empirical acceleration parameters usually not considered, Meindl et al. (2013) obtained an even stronger degradation of GPS Z geocenter motion estimates.

Secondly, besides the empirical parameterization of satellite orbits, the a priori modelling of non-gravitational forces acting on GPS satellites was also shown to influence GPS geocenter estimates. In the differences between GPS Z geocenter estimates obtained using different a priori solar radiation pressure models, Hugentobler et al. (2006) thus observed clear patterns repeating at the period of the GPS draconitic year. The a priori modelling of Earth-reflected radiation pressure was similarly shown to have a millimetric influence on GPS geocenter estimates (Rodriguez-Solano et al., 2011).

All these observations point to a particularly high sensitivity of GNSS geocenter motion estimates to orbit modelling deficiencies. But the cause of this sensitivity had so far remained unclear. Meindl et al. (2013) recently attempted to shed light on this question. On the basis of orbit perturbation theory considerations, they incriminated correlations between the Z geocenter coordinates and particular empirical acceleration parameters set up by most IGS ACs. But, as will be explained in Sect. 4.5, we find Meindl et al. (2013)'s conclusions questionable.

2.5 Summary

Although the contribution of GNSS to the ITRF is fundamental in several respects (Sect. 2.1.4), it is nevertheless subject to potential improvements in various areas. A progressive rebuilding of the IGS network with stable monuments and low-multipath, individually calibrated antennas would first be highly desirable. This would likely be the most effective way to mitigate the biases affecting GNSS station position estimates and would also allow a partial reduction of spurious trends and seasonal signals. However, this objective does not only appear practically unattainable in the near term, but would also not concern the historical IGS network and data. Instrumental errors will therefore likely remain an important limiting factor in the GNSS contribution to at least the few next ITRF realizations.

A second area of potential improvements for the contribution of GNSS to the ITRF is the global modelling of GNSS observations. In this respect, a primordial objective is the understanding and mitigation of the draconitic errors found in GNSS station position estimates, which will likely require important progress in the modelling of GNSS satellite orbit dynamics. But progress in other global modelling aspects (tidal effects, ionosphere, troposphere) remain necessary as well.

The work done during this thesis falls within a last objective: improving the determination of the terrestrial scale and of geocenter motion with GNSS, so that they could eventually contribute to defining the ITRF scale and origin. The weak ability of current GNSS to determine the terrestrial scale is well understood (Sect. 2.3 and 4.2). But, as will be detailed in 5.1, there nevertheless exist prospects for a future contribution of GNSS to defining the ITRF scale, or at least its scale rate.

On the other hand, the poor performance of GNSS in determining geocenter motion through the network shift approach was remaining unresolved when this thesis started (Sect. 2.4.2). In view of a future possible contribution of GNSS to defining the ITRF origin, a first necessary step was therefore to understand why GNSS geocenter motion estimates were so unreliable. This question is actually the main thread of the next chapters.

Chapter 3

Mathematical tools and developments

This chapter presents the mathematical concepts that were used and developed during this thesis so as to investigate the poor performance of GNSS for determining geocenter motion with the network shift approach. In Sect. 3.1, the notion of collinearity in least-squares regression is first introduced as well as several possible approaches for diagnosing collinearity issues. In Sect. 3.2, we introduce the notion of *implicit parameters* that will be used to represent quantities which are, like geocenter coordinates in GNSS data analyses, not explicitly estimated as model parameters, but nevertheless implicitly realized through the model parameters (i.e. through station coordinates). Sect. 3.3 presents a generalized collinearity diagnosis, adapted to several peculiarities of geodetic data analyses, which will be applied to different problems in the next chapter. Sect. 3.4 finally discusses the question of whether using double-differenced observations rather than undifferenced observations in global GNSS analyses has an impact or not on collinearity issues and their diagnosis.

3.1 Collinearity in generalized least-squares regression

Throughout this section, the linear regression model $\boldsymbol{l} = \boldsymbol{A}\boldsymbol{x} + \boldsymbol{v}$ will be considered, where:

- $\boldsymbol{l}$ is a vector of n observations associated with a given covariance matrix $\boldsymbol{Q}_l = \boldsymbol{P}_l^{-1}$;
- $\boldsymbol{x}$ a vector of p unknown parameters;

- $\boldsymbol{A} = \partial \boldsymbol{l} / \partial \boldsymbol{x}$ is the so-called design matrix;
- $\boldsymbol{Ax}$ is the vector of observations predicted by the parameters $\boldsymbol{x}$ (model prediction);
- $\boldsymbol{v}$ is a vector of unknown observational and model errors (residuals).

Specifying a weight matrix $\boldsymbol{P_l}$ for the observations corresponds to the choice of a particular metric in the observation space $\mathbb{R}^n$, i.e. of an inner product $< \boldsymbol{l}, \boldsymbol{l}' >= \boldsymbol{l}^T \boldsymbol{P_l} \boldsymbol{l}'$ and of the associated norm $||\boldsymbol{l}|| = \sqrt{\boldsymbol{l}^T \boldsymbol{P_l} \boldsymbol{l}}$. Let E denote the Hilbert observation space $\mathbb{R}^n$ equipped with this metric. The row space of the design matrix, $\mathrm{Im}(\boldsymbol{A}) = \{\boldsymbol{Ax}, \boldsymbol{x} \in \mathbb{R}^p\}$, is a subspace of E which spans all possible model predictions. It will therefore be called the model space.

The objective of generalized least-squares regression is to minimize the norm $||\boldsymbol{v}|| = ||\boldsymbol{l} - \boldsymbol{Ax}||$ of the residual vector. It is achieved when the vector of predicted observations $\boldsymbol{Ax}$ is the orthogonal projection of the observation vector $\boldsymbol{l}$ onto the model space $\mathrm{Im}(\boldsymbol{A})$. This condition leads to the well-known normal equation:

$$\boldsymbol{Nx} = \boldsymbol{b} \tag{3.1}$$

where $\boldsymbol{N} = \boldsymbol{A}^T \boldsymbol{P_l} \boldsymbol{A}$ is called the normal matrix and $\boldsymbol{b} = \boldsymbol{A}^T \boldsymbol{P_l} \boldsymbol{l}$. Unless stated otherwise, $\boldsymbol{A}$ will be assumed of full rank in this section. Under this condition, $\boldsymbol{N}$ is invertible and the normal equation has a unique solution:

$$\hat{\boldsymbol{x}} = \boldsymbol{N}^{-1} \boldsymbol{b} = (\boldsymbol{A}^T \boldsymbol{P_l} \boldsymbol{A})^{-1} \boldsymbol{A}^T \boldsymbol{P_l} \boldsymbol{l} \tag{3.2}$$

The covariance matrix of the estimated parameters is in this case the inverse of the normal matrix $\boldsymbol{Q} = \boldsymbol{N}^{-1}$. The goodness of fit can be measured by the coefficient of determination:

$$R^2 = \frac{||\boldsymbol{A}\hat{\boldsymbol{x}}||^2}{||\boldsymbol{l}||^2} = \cos^2 \theta \tag{3.3}$$

where θ is the angle between the observation vector $\boldsymbol{l}$ and the model space $\mathrm{Im}(\boldsymbol{A})$.

We refer the reader to Sect. B.1 for a less abrupt derivation of these results.

3.1.1 Conditioning and parameter scaling

When $\boldsymbol{A}$ is of full rank but $\boldsymbol{N}$ is however close to singularity, small perturbations in the observations may cause relatively large variations in the estimated parameters: the least-squares regression is ill-conditioned. The closeness of $\boldsymbol{N}$ to singularity can be measured by its condition number $\kappa(\boldsymbol{N})$, i.e. the ratio of its largest to its smallest singular value.

Because $\boldsymbol{N}$ is symmetric, the ideal case $\kappa(\boldsymbol{N}) = 1$ is achieved only when:

$$\boldsymbol{N} = k\boldsymbol{I} \Leftrightarrow \begin{cases} \forall i, & \boldsymbol{N}_{i,i} = \|\boldsymbol{A}_i\|^2 = k \\ \forall i \neq j, & \boldsymbol{N}_{i,j} =< \boldsymbol{A}_i, \boldsymbol{A}_j >= 0 \end{cases} \tag{3.4}$$

i.e. when the columns of $\boldsymbol{A}$ form an orthogonal basis of the model space $\mathrm{Im}(\boldsymbol{A})$ and all have the same norm. $\boldsymbol{N}$ can thus be ill-conditioned for two non-exclusive reasons: either because the columns of $\boldsymbol{A}$ have disparate norms (scaling problem), or because they are far from being orthogonal to each other (collinearity problem).

The first possible reason for ill-conditioning can be circumvented by solving for an auxiliary set of scaled parameters $\tilde{\boldsymbol{x}}$ such that $\tilde{\boldsymbol{x}}_i = \|\boldsymbol{A}_i\|\boldsymbol{x}_i = \sqrt{\boldsymbol{N}_{i,i}}\boldsymbol{x}_i$. In matrix notations, $\tilde{\boldsymbol{x}} = \tilde{\boldsymbol{D}}^{-1}\boldsymbol{x}$ where $\tilde{\boldsymbol{D}}$ denotes the diagonal matrix with elements $\tilde{\boldsymbol{D}}_{i,i} = 1/\sqrt{\boldsymbol{N}_{i,i}}$. This leads to the design matrix $\tilde{\boldsymbol{A}} = \boldsymbol{A}\tilde{\boldsymbol{D}}$ whose columns all have unit norms, and to the scaled normal equation $\tilde{\boldsymbol{N}}\tilde{\boldsymbol{x}} = \tilde{\boldsymbol{b}}$, where $\tilde{\boldsymbol{N}} = \tilde{\boldsymbol{D}}\boldsymbol{N}\tilde{\boldsymbol{D}}$ has the form of a correlation matrix and $\tilde{\boldsymbol{b}} = \tilde{\boldsymbol{D}}\boldsymbol{b}$.

In terms of condition number, this particular scaling of the parameters may not be optimal: there may exist other matrices $\boldsymbol{D}$ in the set $\mathcal{D}_p$ of all non-singular $p \times p$ diagonal matrices such that $\kappa(\boldsymbol{DND}) < \kappa(\tilde{\boldsymbol{N}})$. Nevertheless, a theorem by van der Sluis (1969) states that:

$$\kappa(\tilde{\boldsymbol{N}}) \leq p \min_{\boldsymbol{D} \in \mathcal{D}_p} \kappa(\boldsymbol{DND}) \tag{3.5}$$

i.e. that even if the scaling by $\tilde{\boldsymbol{D}}$ is not optimal, it is not far from being optimal. But the main justification for this particular scaling is that it isolates the second possible source for ill-conditioning: collinearity.

3.1.2 Introduction to collinearity

When the design matrix $\boldsymbol{A}$ is rank deficient and the normal matrix $\boldsymbol{N}$ is consequently singular, there exists one or more linear dependencies among the columns of $\boldsymbol{A}$. One or more linear combinations of the model parameters do not influence the predicted observations. In other words, the regression model does not provide information about specific linear combinations of parameters, which can therefore not be inferred from the observations. This situation, well-known in geodetic problems, will be referred to as *perfect collinearity*. For instance, in a global GNSS data analysis, any net rotation of the station network can be compensated by variations of the EOPs without any impact on the observations (Sect. 1.2.2). Three independent linear combinations of station positions and EOPs are thus not estimable. The design matrix $\boldsymbol{A}$ and the normal matrix $\boldsymbol{N}$ have three orientation singularities.

More subtly, the columns of $\boldsymbol{A}$ may be, not exactly, but nearly linearly dependent, a situation known as *collinearity* or *multicollinearity*. In such a case, specific linear combinations of parameters have only few influence on the observations and may therefore hardly be inferred from them. The harm caused by collinearity to the estimability of specific linear combinations of parameters is thus described as follows by Belsley et al. (1980): "The essential harm due to collinearity arises from the fact that a collinear relation can readily result in a situation in which some of the observed systematic influence of the explanatory variables on the response variable is swamped by the model's random error term - or in the familiar terminology of electrical engineering, the signal is swamped by the noise. It is intuitively clear that, under these circumstances, estimation can be hindered." In other words, if the influence of some linear combination of parameters is actually below the level of observation and model errors, its estimation is likely to be unreliable.

For better insight, let us introduce a geometric interpretation of collinearity. The resolution of a least-squares problem can be conceptually decomposed into two steps:

- finding the best-fitting model prediction $\boldsymbol{A}\hat{\boldsymbol{x}}$ by projecting the observations $\boldsymbol{l}$ onto the model space $\mathrm{Im}(\boldsymbol{A})$ (Fig. B.1);
- finding the parameters $\hat{\boldsymbol{x}}$ that predict the projected observations $\boldsymbol{A}\hat{\boldsymbol{x}}$, i.e. decomposing the projected observations onto the basis of $\mathrm{Im}(\boldsymbol{A})$ formed by the columns of $\boldsymbol{A}$ (Fig. 3.1).

Collinearity is not a concern for the first step: it does not affect how well the model predicts the observations, i.e. the coefficient of determination R^2. But collinearity may become an issue during the second step, when attempting to separate the contribution of each parameter to the predicted observations. If linear quasi-dependencies exist among the columns of $\boldsymbol{A}$, the basis they form indeed tends to be squashed, so that the decomposition of the predicted observations onto this basis becomes an ill-posed problem. Collinearity can in fact be geometrically defined as a severe departure of the basis formed by the columns of the *scaled* design matrix $\tilde{\boldsymbol{A}}$ from orthogonality (Farrar and Glauber, 1967) or as its closeness to singularity (Haitovsky, 1969).

Fig. 3.1 gives an illustration of this geometric interpretation in the simplest possible case of a two-parameter regression. In the left part of the figure, both columns of $\boldsymbol{A}$ are orthogonal: there exists no linear dependency between $\boldsymbol{A}_1$ and $\boldsymbol{A}_2$. On the other hand, the angle between $\boldsymbol{A}_1$ and $\boldsymbol{A}_2$ has been decreased in the right part of the figure, so that $\boldsymbol{A}_1$ and $\boldsymbol{A}_2$ become very approximately collinear ($\boldsymbol{A}_1 - \boldsymbol{A}_2$ is relatively close to zero). The consequence of this poorer geometry on the determination of the model parameters x_1 and x_2 is nevertheless visible: with the same uncertainty on the predicted observations, the error bars of the parameters are clearly longer in the right case. Fig. 3.1 thus points out another consequence of collinearity. The existence of linear quasi-dependencies among the columns of $\boldsymbol{A}$ does not only hinder the estimation of the corresponding linear combinations of parameters, but also inflates the uncertainties all involved individual model parameters.

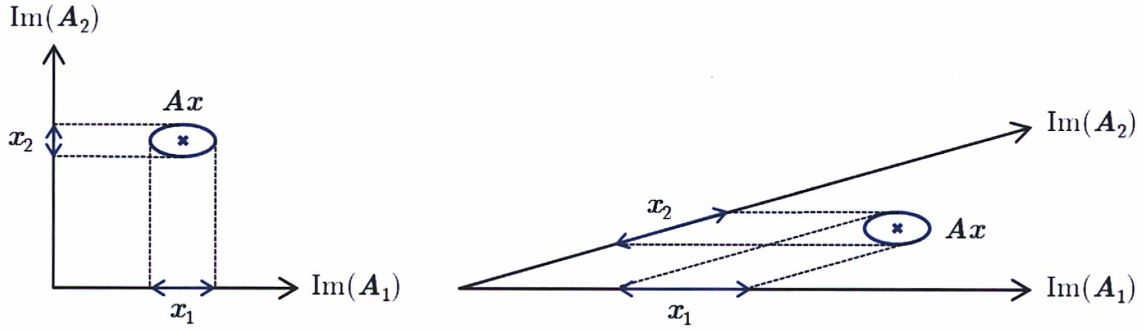

Figure 3.1 Decomposition of predicted observations $\boldsymbol{A}x$ onto orthogonal (left) and roughly collinear (right) two-dimensional bases

3.1.3 Global measures of collinearity

Given the geometric definition of collinearity introduced in Sect. 3.1.2, a first possible indicator of the overall collinearity degree of a least-squares problem is the determinant of the scaled normal matrix, $\det(\tilde{\boldsymbol{N}})$, which indeed measures the volume of the parallelotope formed by the columns of $\tilde{\boldsymbol{A}}$ in E^1. $\det(\tilde{\boldsymbol{N}})$ necessarily lies between 0 and 1^2. $\det(\tilde{\boldsymbol{N}}) = 1$ only if the columns of $\tilde{\boldsymbol{A}}$ form an orthonormal basis (hypercube), while $\det(\tilde{\boldsymbol{N}})$ tends to zero as the parallelotope formed by the columns of $\tilde{\boldsymbol{A}}$ tends to be squashed. $\det(\tilde{\boldsymbol{N}})$ was thus proposed by Farrar and Glauber (1967) as a global measure of collinearity.

For the same purpose, Belsley et al. (1980) prefer using the condition number $\kappa(\tilde{\boldsymbol{N}})$ which ranges from 1 when the columns of $\tilde{\boldsymbol{A}}$ form an orthonormal basis to infinity as $\tilde{\boldsymbol{N}}$ approaches singularity. An indicative scale relating $\kappa(\tilde{\boldsymbol{N}})$ to the severity of collinearity issues is thus given by Montgomery et al. (2012), but it is likely not suited to problems with thousands of parameters like GNSS data analyses.

Global measures of collinearity such as $\det(\tilde{\boldsymbol{N}})$ and $\kappa(\tilde{\boldsymbol{N}})$ may in fact be useful to compare the relative level of collinearity between different problems, but seem hardly interpretable in an absolute sense. Moreover, they do not provide information about the causes of potential collinearity issues, i.e. about which linear quasi-dependencies may exist among the columns of $\tilde{\boldsymbol{A}}$.

---

[1] $\det(\tilde{N})$ is in fact the *Gram determinant* of $\tilde{A}$ in E.

[2] Let $(\lambda_i)_{1\leq i\leq p}$ denote the singular values of $\tilde{N}$. As $\tilde{N}$ is positive-semidefinite, each λ_i is positive or zero, so that: $0 \leq \det(\tilde{N})^{1/p} = (\prod \lambda_i)^{1/p} \leq \sum \lambda_i / p = \mathrm{trace}(\tilde{N})/p = 1$

3.1.4 Belsley et al. (1980)'s procedure

When possible, the singular value decomposition of the scaled normal matrix $\tilde{\boldsymbol{N}}$ can be a useful tool to diagnose and understand collinearity issues. $\tilde{\boldsymbol{N}}$, as a symmetric positive-semidefinite matrix, can indeed be decomposed into $\tilde{\boldsymbol{N}} = \boldsymbol{V}\boldsymbol{\Lambda}\boldsymbol{V}^T$, where:

- $\boldsymbol{V}$ is an orthogonal matrix whose columns are the eigenvectors of $\tilde{\boldsymbol{N}}$;
- $\boldsymbol{\Lambda} = \mathrm{diag}(\lambda_1, \ldots, \lambda_p)$ is the diagonal matrix whose elements are the eigenvalues of $\tilde{\boldsymbol{N}}$.

In the ideal case where the columns of $\tilde{\boldsymbol{A}}$ form an orthonormal basis of $\mathrm{Im}(\boldsymbol{A})$, all eigenvalues of $\tilde{\boldsymbol{N}}$ are equal to 1. On the other hand, when $\tilde{\boldsymbol{N}}$ approaches singularity, at least one of its eigenvalues approaches zero, and the corresponding eigenvector(s) indicate linear combination(s) of the columns of $\tilde{\boldsymbol{A}}$ which is (are) nearly dependent. Note that the arithmetic mean of the λ_i's is 1 in any case.

Belsley et al. (1980) therefore proposed a procedure based on the singular value decomposition of $\tilde{\boldsymbol{N}}$ for diagnosing potential collinearity issues. The first step of Belsley et al. (1980)'s procedure consists in identifying potentially harmful linear quasi-dependencies among the columns of $\tilde{\boldsymbol{A}}$ by means of the *condition indices*:

$$\eta_i = \frac{\lambda_{max}}{\lambda_i} \tag{3.6}$$

where λ_{max} denotes the largest eigenvalue of $\tilde{\boldsymbol{N}}$. Linear quasi-dependencies among the columns of $\tilde{\boldsymbol{A}}$ are indeed indicated by large condition indices (small eigenvalues). Each eigenvector associated with such a large condition index corresponds to a hardly estimable linear combination of parameters, potential source of collinearity issues.

An absolute scale for condition indices is proposed by Belsley (1991) who notes that "the relative strengths of the scaled condition indices are determined by their approximate position along the progression 1, 3, 10, 30, 100, 300, 1000, and so on." From his experience, if the largest condition indices are below 10, then "collinearity is not really a major problem" while if the largest condition indices are in the range 30-100, then "there are collinearity problems". He finally considers the range 1000-3000 as "immense". But again, such an absolute scale might not be very well suited to huge problems like GNSS data analyses.

Another suggestion from Belsley (1991), applicable to any problem, is to plot the progression of the condition indices. If a gap of several orders of magnitude can be observed near the end of this progression, it is likely to indicate a separation between the really problematic eigenvectors and the others. But if the progression of the condition indices is wholly smooth, it becomes of course much more difficult to isolate nearly dependent eigenvectors.

After having identified potentially harmful linear quasi-dependencies among the columns of $\tilde{\boldsymbol{A}}$, the second step in Belsley et al. (1980)'s procedure is to assess how they may degrade the estimation of each individual model parameter. For that purpose, the variance of each scaled parameter is decomposed into a sum of components, each associated with one of the eigenvectors of $\tilde{\boldsymbol{N}}$. The covariance matrix of the scaled parameters is indeed $\tilde{\boldsymbol{Q}} = \tilde{\boldsymbol{N}}^{-1} = \boldsymbol{V}\boldsymbol{\Lambda}^{-1}\boldsymbol{V}^T$, so that the variance of $\tilde{\boldsymbol{x}}_i$ can be expressed as:

$$\mathrm{var}(\tilde{\boldsymbol{x}}_i) = \tilde{\boldsymbol{Q}}_{i,i} = \sum_{k=1}^{p} \frac{\boldsymbol{V}_{i,k}^2}{\lambda_k} \tag{3.7}$$

The ratio:

$$\pi_{i,k} = \frac{1}{\tilde{\boldsymbol{Q}}_{i,i}} \frac{\boldsymbol{V}_{i,k}^2}{\lambda_k} \tag{3.8}$$

represents the proportion of $\mathrm{var}(\tilde{\boldsymbol{x}}_i)$ associated with the k$^{\mathrm{th}}$ eigenvector of $\tilde{\boldsymbol{N}}$. If a large proportion of $\mathrm{var}(\tilde{\boldsymbol{x}}_i)$ is associated with one or more eigenvectors previously identified as problematic, it is indication that the estimation of $\tilde{\boldsymbol{x}}_i$ may be degraded by collinearity issues.

3.1.5 Collinearity diagnosis for a specific parameter

The singular value decomposition of $\tilde{\boldsymbol{N}}$ is an indubitably precious tool to diagnose and understand collinearity issues and its application to GNSS data analyses would certainly be rich of lessons. However, it is unfortunately hardly applicable to realistic GNSS data analyses with several ten thousand parameters. Moreover, as any parameter is generally involved in several eigenvectors of $\tilde{\boldsymbol{N}}$, Belsley et al. (1980)'s procedure does not appear as the most appropriate tool for the particular purpose of understanding whether and why the estimation of a particular parameter may be affected by collinearity issues. This subsection therefore introduces a collinearity diagnosis applicable to specific parameters of interest. This will be the basis for the generalized collinearity diagnosis developed in Sect. 3.3 and used in Chapter 4.

Signature of a parameter Each column $\boldsymbol{A}_i = \partial \boldsymbol{l} / \partial \boldsymbol{x}_i$ of $\boldsymbol{A}$ is a vector of the model space, which represents the impact on the observations predicted by the model of a unit variation of the i$^{\mathrm{th}}$ parameter $\boldsymbol{x}_i$. It can be thought as the signal which characterizes the influence of $\boldsymbol{x}_i$ on the observations. In the following, $\boldsymbol{A}_i$ will thus be called the *signature* of $\boldsymbol{x}_i$ on the observations.

Decomposition of A_i Each parameter $\boldsymbol{x}_i$ can also be associated with a particular hyperplane of the model space. Let $\boldsymbol{e}_i = [\delta_{i,1}, \delta_{i,2}, ..., \delta_{i,p}]^T$ (vector with all zero elements, except a unit i$^{\text{th}}$ element) be the coordinates of $\boldsymbol{x}_i$ in the canonical basis of the parameter space $\mathbb{R}^p$. And let $\boldsymbol{K}_i$ be any $p \times p-1$ matrix whose columns form a basis of $\text{Ker}(\boldsymbol{e}_i^T) = \{\boldsymbol{x} \in \mathbb{R}^p / \boldsymbol{e}_i^T \boldsymbol{x} = 0\}$. One could choose for instance:

$$\boldsymbol{K}_i = [\boldsymbol{e}_1, \ldots, \boldsymbol{e}_{i-1}, \boldsymbol{e}_{i+1}, \ldots, \boldsymbol{e}_p] \tag{3.9}$$

Under the assumption that $\boldsymbol{A}$ is of full rank, $\text{Im}(\boldsymbol{AK}_i)$ is a $p-1$ dimensional subspace (hyperplane) of the model space (proposition A.6), which contains the signatures of all parameters except $\boldsymbol{x}_i$.

Let us now decompose the signature $\boldsymbol{A}_i$ of $\boldsymbol{x}_i$ into the sum of its orthogonal projection $\boldsymbol{A}_i^u$ onto $\text{Im}(\boldsymbol{AK}_i)$ and of its orthogonal projection $\boldsymbol{A}_i^p$ onto $\text{Im}(\boldsymbol{AK}_i)^\perp$ (Fig. 3.2). $\boldsymbol{A}_i^u$, as it lies in $\text{Im}(\boldsymbol{AK}_i)$, is strictly collinear with the signatures of $\boldsymbol{x}_1, \ldots, \boldsymbol{x}_{i-1}, \boldsymbol{x}_{i+1}, \ldots \boldsymbol{x}_p$. This part of the signature of $\boldsymbol{x}_i$ is consequently indistinguishable from the signatures of the other parameters. Because of the simultaneous estimation of the other parameters, the estimation of $\boldsymbol{x}_i$ can therefore only rely on $\boldsymbol{A}_i^p$, i.e. the part of $\boldsymbol{A}_i$ which is orthogonal to each of the signatures of $\boldsymbol{x}_1, \ldots, \boldsymbol{x}_{i-1}, \boldsymbol{x}_{i+1}, \ldots \boldsymbol{x}_p$. In the following, $\boldsymbol{A}_i^p$ will be called the *proper signature* of $\boldsymbol{x}_i$. As proven below, it can be expressed as:

$$\boldsymbol{A}_i^p = \frac{\boldsymbol{AQe}_i}{\boldsymbol{Q}_{i,i}} \tag{3.10}$$

Proof. The columns of the $n \times p-1$ matrix $\boldsymbol{AK}_i$ form a basis of $\text{Im}(\boldsymbol{AK}_i)$, so that, according to proposition A.16, the matrix form of the orthogonal projection onto $\text{Im}(\boldsymbol{AK}_i)^\perp$ is:

$$\begin{aligned}\boldsymbol{\Pi} &= \boldsymbol{I} - (\boldsymbol{AK}_i)\left((\boldsymbol{AK}_i)^{-1}\boldsymbol{P}_l(\boldsymbol{AK}_i)^T)\right)^{-1}(\boldsymbol{AK}_i)^T\boldsymbol{P}_l \\ &= \boldsymbol{I} - \boldsymbol{AK}_i(\boldsymbol{K}_i^T\boldsymbol{NK}_i)^{-1}\boldsymbol{K}_i^T\boldsymbol{A}^T\boldsymbol{P}_l\end{aligned}$$

The proper signature of $\boldsymbol{x}_i$, defined as the orthogonal projection of $\boldsymbol{A}_i$ onto $\text{Im}(\boldsymbol{AK}_i)^\perp$ can therefore be expressed as:

$$\boldsymbol{A}_i^p = \boldsymbol{\Pi A}_i = \boldsymbol{\Pi Ae}_i = \boldsymbol{Ae}_i - \boldsymbol{AK}_i(\boldsymbol{K}_i^T\boldsymbol{NK}_i)^{-1}\boldsymbol{K}_i^T\boldsymbol{Ne}_i$$

According to proposition A.19, $\boldsymbol{K}_i(\boldsymbol{K}_i^T\boldsymbol{NK}_i)^{-1}\boldsymbol{K}_i^T$ can be replaced by $\boldsymbol{Q} - \boldsymbol{Qe}_i(\boldsymbol{e}_i^T\boldsymbol{Qe}_i)^{-1}\boldsymbol{e}_i^T\boldsymbol{Q}$ in the previous equation, which leads, after simplification, to Eq. 3.10. □

Variance inflation factor Let us associate to each parameter $\boldsymbol{x}_i$ the angle θ_i between its signature $\boldsymbol{A}_i$ and the hyperplane $\text{Im}(\boldsymbol{AK}_i)$ (Fig. 3.2). $R_i^2 = \cos^2\theta_i$ is the coefficient of determination obtained from the regression of $\boldsymbol{A}_i$ on the other columns of $\boldsymbol{A}$. The variance inflation factor (VIF) of $\boldsymbol{x}_i$ is defined from the angle θ_i, or from R_i^2, by:

$$V_i = \frac{1}{\sin^2\theta_i} = \frac{1}{1-R_i^2} \tag{3.11}$$

$V_i = 1$ ($\theta_i = \pi/2$; $R_i^2 = 0$) means that $\boldsymbol{A}_i$ is orthogonal to all other columns of $\boldsymbol{A}$, i.e. that $\boldsymbol{x}_i$ is uncorrelated with any other parameter. On the other hand, V_i

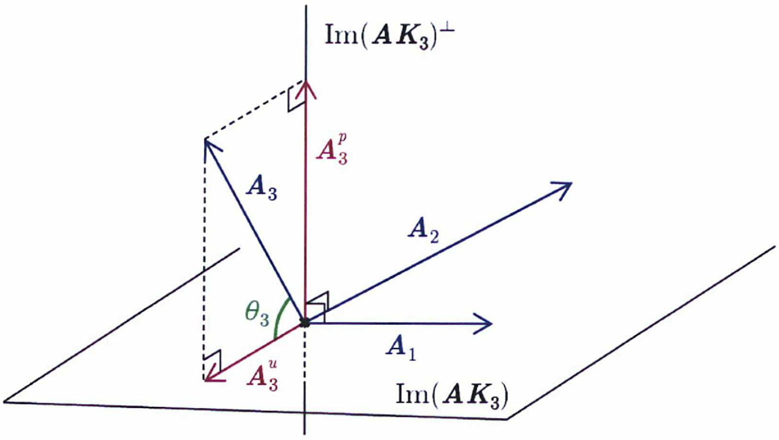

Figure 3.2 Decomposition of the signature of x_3 in a 3-parameter problem. $\mathrm{Im}(\boldsymbol{A}\boldsymbol{K}_3)$ is the plane containing $\boldsymbol{A}_1$ and $\boldsymbol{A}_2$. $\boldsymbol{A}_3^u$ is the orthogonal projection of $\boldsymbol{A}_3$ onto this plane. $\boldsymbol{A}_3^p$ is the orthogonal projection of $\boldsymbol{A}_3$ onto the line orthogonal to this plane. θ_3 is the angle between $\boldsymbol{A}_3$ and this plane.

tends to infinity ($\theta_i \to 0$; $R_i^2 \to 1$) when $\boldsymbol{A}_i$ tends to lie in $\mathrm{Im}(\boldsymbol{A}\boldsymbol{K}_i)$ and $\boldsymbol{x}_i$ tends to be indistinguishable from the other parameters. V_i thus measures the degree of collinearity of $\boldsymbol{x}_i$ with all other parameters.

VIFs are a widespread tool for diagnosing whether the estimation of specific parameters may be harmed by collinearity (see, e.g., Farrar and Glauber, 1967; Belsley et al., 1980; Draper and Smith, 1998; Montgomery et al., 2012). The term "variance inflation factor", introduced by Marquardt (1970), derives from the fact that the variance of a parameter $\boldsymbol{x}_i$ obeys the relation:

$$\mathrm{var}(\boldsymbol{x}_i) = \boldsymbol{Q}_{i,i} = \frac{1}{\boldsymbol{N}_{i,i}}.V_i \tag{3.12}$$

The first factor, $1/\boldsymbol{N}_{i,i}$, would be the variance of $\boldsymbol{x}_i$ if all other parameters were known and held fixed. V_i is thus the factor by which the simultaneous estimation of the other parameters inflates the variance of $\boldsymbol{x}_i$. Eq. 3.12 can be demonstrated by noting that:

$$\cos\theta_i = \frac{<\boldsymbol{A}_i, \boldsymbol{A}_i^u>}{||\boldsymbol{A}_i||\,||\boldsymbol{A}_i^u||} = \frac{<\boldsymbol{A}_i, \boldsymbol{A}_i - \boldsymbol{A}_i^p>}{||\boldsymbol{A}_i||\,||\boldsymbol{A}_i - \boldsymbol{A}_i^p||} \tag{3.13}$$

Replacing $\boldsymbol{A}_i^p$ by its expression in Eq. 3.10 leads to:

$$\cos\theta_i = \sqrt{1 - \frac{1}{\boldsymbol{N}_{i,i}\boldsymbol{Q}_{i,i}}} \tag{3.14}$$

which is equivalent to Eq. 3.12.

Let us mention another interpretation of VIFs. Noting that $\|\boldsymbol{A}_i\|^2 = \boldsymbol{N}_{i,i}$ and that, according to Eq. 3.10, $\|\boldsymbol{A}_i^p\|^2 = 1/\boldsymbol{Q}_{i,i}$, Eq. 3.12 can indeed be rewritten as:

$$V_i = \boldsymbol{N}_{i,i}\boldsymbol{Q}_{i,i} = \frac{\|\boldsymbol{A}_i\|^2}{\|\boldsymbol{A}_i^p\|^2} \tag{3.15}$$

The numerator in Eq. 3.15 is the squared norm of the signature of $\boldsymbol{x}_i$ on the observations, i.e. of the signal on which the estimation of $\boldsymbol{x}_i$ would rely if all other parameters were held fixed. On the other hand, the denominator in Eq. 3.15 is the squared norm of the *proper* signature of $\boldsymbol{x}_i$, i.e. of the signal on which the estimation of $\boldsymbol{x}_i$ actually relies. V_i thus measures how the magnitude of the signal on which the estimation of $\boldsymbol{x}_i$ relies is reduced because of the simultaneous estimation of the other parameters.

Like for other measures of collinearity, the questions arise again of what are large and what are small VIFs. Numerical thresholds may be found in the literature, commonly seen values being 5 and 10 (see, e.g., Montgomery et al., 2012). However, as pointed out by Smith and Campbell (1980) or Belsley (1982), VIFs are in fact not interpretable in an absolute sense. For instance, a parameter may be satisfactorily estimated if, even despite a strong collinearity with the other parameters (large VIF), its proper influence on the observations remains significantly larger than the observation and model errors. What eventually matters to the estimability of some parameter is how its variance $\text{var}(\boldsymbol{x}_i) = \boldsymbol{Q}_{i,i} = 1/\|\boldsymbol{A}_i^p\|^2$ compares to the required level of precision. The fact nevertheless remains that:

- if the estimation of some parameter is manifestly subject to errors,
- if its variance is near or larger than the required level of precision,
- and if it has a large VIF (i.e. if its variance is large because of a strong collinearity with the other parameters),

then collinearity constributes to the poor estimability of this parameter.

Even if VIFs have no absolute meaning, it can be useful to make relative comparisons between, e.g., the VIFs obtained for the same parameter with different analysis settings. For such relative comparisons, it should be noted that, because of their quotient nature, VIFs should be considered as varying on a logarithmic scale rather than on a linear scale. Finally note that, for the ease of interpretation, numerical VIF values will always be accompanied, in the rest of the thesis, by bracketed percentage values corresponding to:

$$\cos\theta_i = R_i = \sqrt{1 - \frac{1}{V_i}} \tag{3.16}$$

By its nature, this quantity is indeed interpretable in the same way as a correlation coefficient[3]

---

[3] R_i is sometimes called ***multiple correlation coefficient*** between x_i and the other parameters.

Coordinates of A_i^u When analysing the collinearity of $\boldsymbol{x}_i$ with the other parameters, not only the values of θ_i, R_i^2 and V_i are of interest, but also the coordinates of $\boldsymbol{A}_i^u$ in the basis formed by the columns of $\boldsymbol{A}$. If $\boldsymbol{x}_i$ has a large VIF (small θ_i), $\boldsymbol{A}_i^u$ is indeed a linear combination of $\boldsymbol{A}_1, \ldots, \boldsymbol{A}_{i-1}, \boldsymbol{A}_{i+1}, \ldots \boldsymbol{A}_p$ which closely matches $\boldsymbol{A}_i$. In other words, the coordinates of $\boldsymbol{A}_i^u$ in the basis formed by the columns of $\boldsymbol{A}$ are the coefficients of a linear combination of $\boldsymbol{x}_1, \ldots, \boldsymbol{x}_{i-1}, \boldsymbol{x}_{i+1}, \ldots \boldsymbol{x}_p$ which is almost indistinguishable from $\boldsymbol{x}_i$. The coordinates of $\boldsymbol{A}_i^u$ are thus the answer to the question of why $\boldsymbol{x}_i$ may be hardly estimable.

According to Eq. 3.10,

$$\boldsymbol{A}_i^u = \boldsymbol{A}_i - \boldsymbol{A}_i^p = \boldsymbol{A}\left(\boldsymbol{e}_i - \frac{\boldsymbol{Q}\boldsymbol{e}_i}{\boldsymbol{Q}_{i,i}}\right) \tag{3.17}$$

so that the coordinates $\boldsymbol{\mu}_i$ of $\boldsymbol{A}_i^u$ in the basis formed by the columns of $\boldsymbol{A}$ are:

$$\boldsymbol{\mu}_i = \boldsymbol{e}_i - \frac{\boldsymbol{Q}\boldsymbol{e}_i}{\boldsymbol{Q}_{i,i}} = -\left[\frac{\boldsymbol{Q}_{1,i}}{\boldsymbol{Q}_{i,i}}, \ldots, \frac{\boldsymbol{Q}_{i-1,i}}{\boldsymbol{Q}_{i,i}}, 0, \frac{\boldsymbol{Q}_{i+1,i}}{\boldsymbol{Q}_{i,i}}, \ldots, \frac{\boldsymbol{Q}_{p,i}}{\boldsymbol{Q}_{i,i}}\right]^T \tag{3.18}$$

3.1.6 Correlation coefficients

A common practice in the field of global geodetic analyses is the analysis of pairwise correlation coefficients between the estimated parameters (see, e.g., Gobinddass et al., 2009b; Rodriguez-Solano et al., 2012; Meindl et al., 2013; Haines et al., 2013). This subsection aims at replacing this practice in the framework of collinearity and presenting some of its shortcomings. But let us first point out that the notion of correlation coefficients can have two different meanings.

In the terminology of Belsley et al. (1980), the correlation matrix of the estimated parameters is the scaled normal matrix $\tilde{\boldsymbol{N}}$. In this case, the correlation coefficient between two parameters $\boldsymbol{x}_i$ and $\boldsymbol{x}_j$ is:

$$c_{i,j} = \tilde{\boldsymbol{N}}_{i,j} = \frac{\boldsymbol{N}_{i,j}}{\sqrt{\boldsymbol{N}_{i,i}\boldsymbol{N}_{j,j}}} = \frac{< \boldsymbol{A}_i, \boldsymbol{A}_j >}{\|\boldsymbol{A}_i\|\|\boldsymbol{A}_j\|} = \cos\theta_{i,j} \tag{3.19}$$

where $\theta_{i,j}$ denotes the angle between the signatures $\boldsymbol{A}_i$ and $\boldsymbol{A}_j$ of both parameters. While $|c_{i,j}|$'s close to 1 clearly indicate pairs of redundant parameters, low $|c_{i,j}|$'s do not imply the absence of collinearity issues, for problematic linear quasi-dependencies generally involve more than two parameters[4]. The $c_{i,j}$ coefficients are therefore inadequate for diagnosing and understanding potential collinearity issues.

---

[4] A limit case is obtained when the scaled parameter signatures $(\tilde{A}_i)_{1\leq i\leq p}$ tend to form a $p-1$-simplex. In this case, the problem tends to perfect collinearity while all $c_{i,j}$'s stay as low as $1/(p-1)$.

On the other hand, in the geodetic community, the correlation coefficient between $\boldsymbol{x}_i$ and $\boldsymbol{x}_j$ is rather usually defined from the elements of the parameter covariance matrix $\boldsymbol{Q}$ by:

$$c^p_{i,j} = \frac{\operatorname{cov}(\boldsymbol{x}_i, \boldsymbol{x}_j)}{\sqrt{\operatorname{var}(\boldsymbol{x}_i)\operatorname{var}(\boldsymbol{x}_j)}} = \frac{\boldsymbol{Q}_{i,j}}{\sqrt{\boldsymbol{Q}_{i,i}\boldsymbol{Q}_{j,j}}} \tag{3.20}$$

From Eq. 3.10, it can be shown that:

$$c^p_{i,j} = \frac{< \boldsymbol{A}^p_i, \boldsymbol{A}^p_j >}{||\boldsymbol{A}^p_i||\,||\boldsymbol{A}^p_j||} = \cos\theta^p_{i,j} \tag{3.21}$$

which allows a geometric interpretation of $c^p_{i,j}$ as the cosine of the angle $\theta^p_{i,j}$ between the proper signatures of $\boldsymbol{x}_i$ and $\boldsymbol{x}_j$.

As shown by Belsley et al. (1980), if the columns of $\boldsymbol{A}$ tend to be linearly dependent, then the $c^p_{i,j}$ coefficients between *all* parameters more or less involved in linear quasi-dependencies tend to ±1. Large $|c^p_{i,j}|$'s are thus an indication of potential collinearity issues. However, as a strong linear quasi-dependency may contaminate the whole correlation matrix, the $c^p_{i,j}$'s are not well suited to understand the causes of potential collinearity issues.

3.2 Implicit parameters

In global geodetic analyses, some physically meaningful quantities may not be explicitly estimated as model parameters, but nevertheless implicitly realized through the model parameters. For instance, the net translations between a quasi-instantaneous GNSS terrestrial frame and the ITRF represent in principle the coordinates of CM in the ITRF and should thus reflect non-linear geocenter motion (Sect. 1.3.1). The coordinates of CM in the ITRF are generally not explicitly estimated in global GNSS analyses, for the corresponding parameters would be fully redundant with station coordinates. They are rather implicitly realized through the estimated station coordinates. Likewise, other quantities implicitly realized through the station coordinates estimated in a global GNSS analysis are the surface load coefficients $\sigma^C_{lm}, \sigma^S_{lm}$ (Sect. 1.3.2).

Such quantities, implicitly realized through the parameters of a generalized least-squares regression, are termed here *implicit parameters*. After a formal definition of implicit parameters is given in Sect. 3.2.1, a method to estimate such quantities and their uncertainties is presented in Sect. 3.2.2 and 3.2.3. The link between implicit parameters and the notion of *reference system effect* developed by Sillard and Boucher (2001) is finally highlighted in Sect. 3.2.4.

3.2.1 Definitions

Implicit parameter Let us define an implicit parameter as a quantity y with respect to which the partial derivatives of the explicit model parameters $\boldsymbol{x}$ are a known vector $\boldsymbol{\lambda} = \partial\boldsymbol{x}/\partial y$ of $\mathbb{R}^p$. As an example, consider the implicit parameter y corresponding to the X coordinate of CM in a global GNSS analysis, i.e. to an X origin shift from the a priori terrestrial frame to the estimated terrestrial frame. In this case,

$$\boldsymbol{\lambda} = \frac{\partial \boldsymbol{x}}{\partial y} = [\underbrace{1,0,0,1,0,0,\ldots,1,0,0}_{\text{station coordinates}},\underbrace{0,0,0,0,\ldots,0}_{\text{other parameters}}]^T \tag{3.22}$$

Explicit model parameters are obviously encompassed by the notion of implicit parameter. The partial derivatives of $\boldsymbol{x}$ with respect to a given $\boldsymbol{x}_i$ are indeed a known vector $\boldsymbol{e}_i$ of $\mathbb{R}^p$.

Independence of two implicit parameters Two implicit parameters y and z respectively characterized by $\partial\boldsymbol{x}/\partial y = \boldsymbol{\lambda}$ and $\partial\boldsymbol{x}/\partial z = \boldsymbol{\mu}$ will be said independent if $\boldsymbol{\lambda}^T\boldsymbol{\mu} = 0$, i.e. if $\boldsymbol{\lambda}$ and $\boldsymbol{\mu}$ are orthogonal in the parameter space $\mathbb{R}^p$. Orthogonality in the parameter space may be thought in terms of degrees of freedom allowed within the model. For example, two explicit parameters $\boldsymbol{x}_i$ and $\boldsymbol{x}_j$ are clearly allowed to vary independently from each other within the model: $\boldsymbol{e}_i^T\boldsymbol{e}_j = 0$. On the other hand, a quantity like $\boldsymbol{x}_i+\boldsymbol{x}_j$ cannot vary independently from $\boldsymbol{x}_i$: $\boldsymbol{e}_i^T(\boldsymbol{e}_i+\boldsymbol{e}_j) \neq 0$. More generally, $\boldsymbol{\lambda}^T\boldsymbol{\mu} = 0$ means that the implicit parameters y and z can vary independently from each other within the model.

3.2.2 Estimating implicit parameters in a non-constrained problem

This goal of this subsection is to introduce a method to estimate the values and uncertainties of implicit parameters. For simplicity, it is first assumed in this subsection that $\boldsymbol{A}$ is of full rank, so that $\boldsymbol{N}$ is invertible ($\boldsymbol{N}^{-1} = \boldsymbol{Q}$) and that no particular constraints are required to estimate the explicit model parameters $\boldsymbol{x}$. In this case, a unique set $\hat{\boldsymbol{x}} = \boldsymbol{Qb}$ of explicit model parameters satisfies the normal equation $\boldsymbol{Nx} = \boldsymbol{b}$ and has $\boldsymbol{Q}$ as covariance matrix. The case where constraints are additionally considered will be separately discussed in Sect. 3.2.3.

Recommended approach Let us consider a vector $\boldsymbol{y} = [\boldsymbol{y}_1,\ldots,\boldsymbol{y}_q]$ of q implicit parameters characterized by the partial derivatives:

$$\boldsymbol{\Lambda} = \frac{\partial \boldsymbol{x}}{\partial \boldsymbol{y}} = \left[\frac{\partial \boldsymbol{x}}{\partial \boldsymbol{y}_1}\cdots\frac{\partial \boldsymbol{x}}{\partial \boldsymbol{y}_q}\right] \tag{3.23}$$

For instance, $\boldsymbol{y}$ could consist of the coordinates of CM in the ITRF, while $\boldsymbol{x}$ would be the parameters estimated in a hypothetical full-rank global GNSS analysis. In this example, the partial derivative matrix would be:

$$\boldsymbol{\Lambda} = [\underbrace{\boldsymbol{I}_3, \boldsymbol{I}_3, \boldsymbol{I}_3, \ldots, \boldsymbol{I}_3}_{\text{station coordinates}}, \underbrace{0, 0, 0, 0, \ldots, 0}_{\text{other parameters}}]^T \tag{3.24}$$

Provided that $\boldsymbol{\Lambda}$ is of full rank (i.e. that there is no redundancy between the y_i's), $\boldsymbol{y}$ can be associated with a q-dimensional subspace of the parameter space $\mathbb{R}^p$: $\text{Im}(\boldsymbol{\Lambda}) = \{\boldsymbol{x} \in \mathbb{R}^p / \boldsymbol{x} = \boldsymbol{\Lambda y}\}$. This subspace spans the variations of the model parameters $\boldsymbol{x}$ that are fully explainable by some set $\boldsymbol{y}$ of implicit parameters. On the other hand, its orthogonal complement, $\text{Im}(\boldsymbol{\Lambda})^{\perp} = \text{Ker}(\boldsymbol{\Lambda}^T)$, spans the variations of the model parameters $\boldsymbol{x}$ that are independent from any of the y_i's. In the above example, $\text{Im}(\boldsymbol{\Lambda})$ spans net translations of the station network, while $\text{Ker}(\boldsymbol{\Lambda}^T)$ spans non-translational network distortions and variations of the non-station-position parameters. The decomposition of the parameter space $\mathbb{R}^p$ into $\text{Im}(\boldsymbol{\Lambda}) \oplus \text{Ker}(\boldsymbol{\Lambda}^T)$ allows a unique decomposition of the explicit model parameters $\boldsymbol{x}$ into:

$$\boldsymbol{x} = \boldsymbol{\Lambda y} + \boldsymbol{x}' \text{ , with } \boldsymbol{x}' \in \text{Ker}(\boldsymbol{\Lambda}^T) \tag{3.25}$$

In Eq. 3.25, the explicit model parameters $\boldsymbol{x}$ are thus split into a part $\boldsymbol{\Lambda y}$ explained by a set $\boldsymbol{y}$ of implicit parameters $\boldsymbol{y}$ and another part $\boldsymbol{x}'$, independent of any of the considered implicit parameters.

This decomposition of the explicit model parameters allows to rewrite the observation equations $\boldsymbol{l} = \boldsymbol{Ax} + \boldsymbol{v}$ as:

$$\boldsymbol{l} = \boldsymbol{A\Lambda y} + \boldsymbol{Ax}' + \boldsymbol{v} \tag{3.26}$$

Eq. 3.26 defines a re-parameterized model with $\boldsymbol{y}$ and $\boldsymbol{x}'$ as unknown parameters, while the fact that $\boldsymbol{x}' \in \text{Ker}(\boldsymbol{\Lambda}^T)$ can be translated into the condition equation $\boldsymbol{\Lambda}^T \boldsymbol{x}' = 0$. According to Sect. B.2.2, the solution of this re-parameterized problem can be obtained from the following constrained normal equation:

$$\begin{bmatrix} \boldsymbol{\Lambda}^T \boldsymbol{N\Lambda} & \boldsymbol{\Lambda}^T \boldsymbol{N} & 0 \\ \boldsymbol{N\Lambda} & \boldsymbol{N} & \boldsymbol{\Lambda} \\ 0 & \boldsymbol{\Lambda}^T & 0 \end{bmatrix} \begin{bmatrix} \boldsymbol{y} \\ \boldsymbol{x}' \\ \boldsymbol{k} \end{bmatrix} = \begin{bmatrix} \boldsymbol{\Lambda}^T \boldsymbol{b} \\ \boldsymbol{b} \\ 0 \end{bmatrix} \tag{3.27}$$

where $\boldsymbol{k}$ denotes a vector of q Lagrange multipliers.

As proven below, a unique set $\hat{\boldsymbol{y}}$ of implicit parameters satisfies Eq. 3.27. $\hat{\boldsymbol{y}}$ and its covariance matrix $\boldsymbol{Q}_{\hat{y}}$ can be expressed in function of the estimated model parameters $\hat{\boldsymbol{x}}$ and of their covariance matrix $\boldsymbol{Q}$ as:

$$\hat{\boldsymbol{y}} = (\boldsymbol{\Lambda}^T \boldsymbol{\Lambda})^{-1} \boldsymbol{\Lambda}^T \hat{\boldsymbol{x}} \tag{3.28}$$

$$Q_{\hat{y}} = (\Lambda^T\Lambda)^{-1}\Lambda^T Q\Lambda(\Lambda^T\Lambda)^{-1} \tag{3.29}$$

Eq. 3.28 and 3.29 provide a practical way to infer the values and uncertainties of implicit parameters from the values and uncertainties of the explicit model parameters. Note that, if these equations are used for the trivial purpose of inferring the value and uncertainty of an explicit model parameter x_i from $\hat{x}$ (i.e. with $\Lambda = e_i$), it leads to the expected results $\hat{x}_i$ and $Q_{i,i}$. But recall that these equations are only valid when A and N are of full rank and no constraints are considered.

Proof. A block-decomposition of Eq. 3.27 leads to:

$$\Lambda^T N\Lambda y + \Lambda^T N x' = \Lambda^T b \tag{3.30}$$

$$\begin{bmatrix} N & \Lambda \\ \Lambda^T & 0 \end{bmatrix} \begin{bmatrix} y \\ k \end{bmatrix} = \begin{bmatrix} b - N\Lambda y \\ 0 \end{bmatrix} \tag{3.31}$$

According to Eq. B.17, the solution of Eq. 3.31 can be expressed as:

$$x' = K(K^T N K)^{-1} K^T (b - N\Lambda y) \tag{3.32}$$

where K denotes any matrix whose columns form a basis of $\text{Ker}(\Lambda^T)$. Since N is assumed of full rank, proposition A.19 allows to express x' as:

$$x' = \left(Q - Q\Lambda(\Lambda^T Q\Lambda)^{-1}\Lambda^T Q\right)(b - N\Lambda y) \tag{3.33}$$

Inserting this expression of x' into Eq. 3.30 leads, after simplification, to the following reduced normal equation:

$$\Lambda^T\Lambda(\Lambda^T Q\Lambda)^{-1}\Lambda^T\Lambda y = \Lambda^T\Lambda(\Lambda^T Q\Lambda)^{-1}\Lambda^T Q b = \Lambda^T\Lambda(\Lambda^T Q\Lambda)^{-1}\Lambda^T\hat{x} \tag{3.34}$$

which clearly has as solution the values of $\hat{y}$ and $Q_{\hat{y}}$ given in Eq. 3.28 and 3.29. □

Traditional approach The method described above, based on a re-parameterization of the explicit model parameters x into $\Lambda y + x'$ with $x' \in \text{Ker}(\Lambda^T)$, constitutes our recommended approach for estimating the values and uncertainties of implicit parameters y. However, another commonly employed approach consists in treating the explicit model parameters x as pseudo-observations and estimating y via a least-squares regression based on the model:

$$x = \Lambda y + w \tag{3.35}$$

If the covariance matrix $Q = N^{-1}$ of the model parameters is considered, this approach leads to an estimate:

$$\hat{y} = (\Lambda^T N\Lambda)^{-1}\Lambda^T N\hat{x} \tag{3.36}$$

of the implicit parameters and to the covariance matrix:

$$Q_{\hat{y}} = (\Lambda^T N\Lambda)^{-1} \tag{3.37}$$

which is generally scaled by a variance factor function of the regression residuals. However, the covariance matrix of the model parameters is sometimes discarded, in which case the estimated implicit parameters and their covariance matrix are:

$$\hat{y} = (\Lambda^T\Lambda)^{-1}\Lambda^T\hat{x} \tag{3.38}$$

$$Q_{\hat{y}} \propto (\Lambda^T \Lambda)^{-1} \tag{3.39}$$

Treating the explicit model parameters x as pseudo-observations is the approach traditionally used when inferring, for instance, the coordinates of CM or surface load coefficients from the results of a global GNSS analysis. There is however no consensus on the questions of whether the covariance matrix Q of the model parameters should be considered or not, and why. On one hand, Lavallée et al. (2006) state that the full covariance matrix Q needs to be considered in their unified geocenter motion estimation approach (Sect. 1.3.3). But on the other hand, considering the full covariance matrix Q in the network shift approach leads to unrealistic results (Rebischung et al., 2012), so that an identity weight matrix is generally used.

We believe in fact that the traditional approach of treating the explicit model parameters x as pseudo-observations is misleading. When the covariance matrix of the model parameters is considered, the results from the traditional approach (Eq. 3.36 and 3.37) can indeed easily be identified to those who would be obtained, directly from the observations l, via the regression model:

$$l = (A\Lambda)y + v \tag{3.40}$$

and the associated normal equation:

$$\Lambda^T N \Lambda y = \Lambda^T b \tag{3.41}$$

In this case, the traditional approach is therefore equivalent to estimating the implicit parameters y directly from the observations, *after having fixed* all independent variations of the (non-reduced) model parameters to their a priori values. In the example given above, the coordinates of CM and their uncertainties obtained from Eq. 3.36 and 3.37 can thus be thought as resulting from a global GNSS analysis in which non-translational network distortions and (non-reduced) non-station-position parameters would have been fixed to their a priori values. This interpretation illustrates why we think that the traditional way of inferring implicit parameters using Eq. 3.36 and 3.37 is misleading.

In contrast, our recommended approach comes down to estimating the implicit parameters y from the observations, *simultaneously with* independent variations x' of the model parameters. In the example, the coordinates of CM and their uncertainties obtained from Eq. 3.28 and 3.29 can thus be thought as resulting from a global GNSS analysis in which they would have been estimated together with non-translational network distortions and all other non-station-position parameters.

Finally, an interpretation may hardly be given to the traditional approach when the covariance matrix of the model parameters is discarded (Eq. 3.38 and 3.39), except that it is a wrong way to obtain a correct result. The implicit parameters obtained from Eq. 3.38 are indeed the same as obtained with our recommended approach (Eq. 3.28). However, the covariance matrix from Eq. 3.39 has obviously little meaning, as it does not depend at all on the uncertainty of the explicit model parameters.

3.2.3 Estimating implicit parameters in a constrained problem

In this subsection, the approach introduced in Sect. 3.2.2 for estimating the values and uncertainties of implicit parameters is extended to the case where constraints are imposed on the parameters, in order to supplement possible rank deficiencies of $\boldsymbol{A}$ and $\boldsymbol{N}$, or for any other purpose. Like previously, our proposed method is based on the decomposition of the explicit model parameters $\boldsymbol{x}$ into:

$$\boldsymbol{x} = \Lambda \boldsymbol{y} + \boldsymbol{x}' \text{ , with } \boldsymbol{x}' \in \operatorname{Ker}(\Lambda^T) \tag{3.42}$$

which leads to the re-parameterized observation equations:

$$\boldsymbol{l} = \boldsymbol{A}\Lambda\boldsymbol{y} + \boldsymbol{A}\boldsymbol{x}' + \boldsymbol{v} \tag{3.43}$$

But we will now consider that $\boldsymbol{x}'$ is subject to the additional constraint $\boldsymbol{C}^T\boldsymbol{x}' = \boldsymbol{0}$, where $\boldsymbol{C}$ denotes a $p \times c$ full-rank matrix. It will be assumed that $\boldsymbol{C}$ properly supplements the possible rank deficiencies of $\boldsymbol{A}$ and $\boldsymbol{N}$, i.e. that $\operatorname{rank}([\boldsymbol{A}^T\ \boldsymbol{C}]) = p$. $\boldsymbol{C}$ could for instance correspond to no-net-rotation constraints in a global GNSS analysis. We will finally assume that $[\Lambda\ \boldsymbol{C}]$ is of full rank, i.e. that there is no redundancy between the considered implicit parameters and the applied constraints.

Considering this additional constraint leads to extend the normal equation 3.27 into:

$$\begin{bmatrix} \Lambda^T\boldsymbol{N}\Lambda & \Lambda^T\boldsymbol{N} & 0 & 0 \\ \boldsymbol{N}\Lambda & \boldsymbol{N} & \Lambda & \boldsymbol{C} \\ 0 & \Lambda^T & 0 & 0 \\ 0 & \boldsymbol{C}^T & 0 & 0 \end{bmatrix} \begin{bmatrix} \boldsymbol{y} \\ \boldsymbol{x}' \\ \boldsymbol{k} \\ \boldsymbol{k}' \end{bmatrix} = \begin{bmatrix} \Lambda^T\boldsymbol{b} \\ \boldsymbol{b} \\ 0 \\ 0 \end{bmatrix} \tag{3.44}$$

where $\boldsymbol{k}'$ denotes a vector of c Lagrange multipliers. As proven below, Eq. 3.44 admits a unique set $\hat{\boldsymbol{y}}_c$ of implicit parameters as solution. If $\boldsymbol{K}$ denotes any matrix whose columns form a basis of $\operatorname{Ker}([\Lambda\ \boldsymbol{C}]^T)$, then $\hat{\boldsymbol{y}}_c$ and its covariance matrix $\boldsymbol{Q}_{\hat{\boldsymbol{y}}_c}$ can be expressed as:

$$\boldsymbol{Q}_{\hat{\boldsymbol{y}}_c} = \left(\Lambda^T\boldsymbol{N}\Lambda - \Lambda^T\boldsymbol{N}\boldsymbol{K}(\boldsymbol{K}^T\boldsymbol{N}\boldsymbol{K})^{-1}\boldsymbol{K}^T\boldsymbol{N}\Lambda\right)^{-1} \tag{3.45}$$

$$\hat{\boldsymbol{y}}_c = \boldsymbol{Q}_{\hat{\boldsymbol{y}}_c}\left(\Lambda^T\boldsymbol{b} - \Lambda^T\boldsymbol{N}\boldsymbol{K}(\boldsymbol{K}^T\boldsymbol{N}\boldsymbol{K})^{-1}\boldsymbol{K}^T\boldsymbol{b}\right) \tag{3.46}$$

As such a matrix $\boldsymbol{K}$ is generally not available, Eq. 3.45 and 3.46 are of no practical use. To practically estimate the values and uncertainties of implicit parameters in case where constraints are used, the full normal equation 3.44 needs in fact to be solved. Alternatively, one could also solve the following equation:

$$\begin{bmatrix} \boldsymbol{N} & \boldsymbol{C}' \\ \boldsymbol{C}'^T & 0 \end{bmatrix} \begin{bmatrix} \boldsymbol{x} \\ \boldsymbol{k} \end{bmatrix} = \begin{bmatrix} \boldsymbol{b} \\ 0 \end{bmatrix} \tag{3.47}$$

where $\boldsymbol{C}' = \left(\boldsymbol{I} - \boldsymbol{\Lambda}(\boldsymbol{\Lambda}^T\boldsymbol{\Lambda})^{-1}\boldsymbol{\Lambda}^T\right)\boldsymbol{C}$. It can indeed be shown that $\hat{\boldsymbol{y}}_c$ and $\boldsymbol{Q}_{\hat{\boldsymbol{y}}_c}$ can be inferred from the solution $(\hat{\boldsymbol{x}}_{c'}, \boldsymbol{Q}_{\hat{\boldsymbol{x}}_{c'}})$ of Eq. 3.47 by:

$$\hat{\boldsymbol{y}}_c = (\boldsymbol{\Lambda}^T\boldsymbol{\Lambda})^{-1}\boldsymbol{\Lambda}^T\hat{\boldsymbol{x}}_{c'} \tag{3.48}$$

$$\boldsymbol{Q}_{\hat{\boldsymbol{y}}_c} = (\boldsymbol{\Lambda}^T\boldsymbol{\Lambda})^{-1}\boldsymbol{\Lambda}^T\boldsymbol{Q}_{\hat{\boldsymbol{x}}_{c'}}\boldsymbol{\Lambda}(\boldsymbol{\Lambda}^T\boldsymbol{\Lambda})^{-1} \tag{3.49}$$

Proof. A block-decomposition of Eq. 3.44 leads to:

$$\boldsymbol{\Lambda}^T\boldsymbol{N}\boldsymbol{\Lambda}\boldsymbol{y} + \boldsymbol{\Lambda}^T\boldsymbol{N}\boldsymbol{x}' = \boldsymbol{\Lambda}^T\boldsymbol{b} \tag{3.50}$$

$$\begin{bmatrix} \boldsymbol{N} & \boldsymbol{\Lambda} & \boldsymbol{C} \\ \boldsymbol{\Lambda}^T & 0 & 0 \\ \boldsymbol{C}^T & 0 & 0 \end{bmatrix} \begin{bmatrix} \boldsymbol{y} \\ \boldsymbol{k} \\ \boldsymbol{k}' \end{bmatrix} = \begin{bmatrix} \boldsymbol{b} - \boldsymbol{N}\boldsymbol{\Lambda}\boldsymbol{y} \\ 0 \\ 0 \end{bmatrix} \tag{3.51}$$

Since $[\boldsymbol{\Lambda}\ \boldsymbol{C}]$ is assumed of full rank, the solution of Eq. 3.51 can be expressed, according to Eq. B.17, as:

$$\boldsymbol{x}' = \boldsymbol{K}(\boldsymbol{K}^T\boldsymbol{N}\boldsymbol{K})^{-1}\boldsymbol{K}^T(\boldsymbol{b} - \boldsymbol{N}\boldsymbol{\Lambda}\boldsymbol{y}) \tag{3.52}$$

where $\boldsymbol{K}$ denotes any matrix whose columns form a basis of $\mathrm{Ker}([\boldsymbol{\Lambda}\ \boldsymbol{C}]^T)$. Inserting this expression of $\boldsymbol{x}'$ into Eq. 3.50 leads to the following reduced normal equation:

$$\left(\boldsymbol{\Lambda}^T\boldsymbol{N}\boldsymbol{\Lambda} - \boldsymbol{\Lambda}^T\boldsymbol{N}\boldsymbol{K}(\boldsymbol{K}^T\boldsymbol{N}\boldsymbol{K})^{-1}\boldsymbol{K}^T\boldsymbol{N}\boldsymbol{\Lambda}\right)\boldsymbol{y} = \boldsymbol{\Lambda}^T\boldsymbol{b} - \boldsymbol{\Lambda}^T\boldsymbol{N}\boldsymbol{K}(\boldsymbol{K}^T\boldsymbol{N}\boldsymbol{K})^{-1}\boldsymbol{K}^T\boldsymbol{b} \tag{3.53}$$

which has as solution the values of $\hat{\boldsymbol{y}}_c$ and $\boldsymbol{Q}_{\hat{\boldsymbol{y}}_c}$ given in Eq. 3.45 and 3.46. ☐

3.2.4 Link with Sillard and Boucher (2001)'s reference system effect

The decomposition of the model parameters $\boldsymbol{x}$ into $\boldsymbol{\Lambda}\boldsymbol{y} + \boldsymbol{x}'$, with $\boldsymbol{x}' \in \mathrm{Ker}(\boldsymbol{\Lambda}^T)$, used in the previous subsections is somehow arbitrary as it depends on the choice of a particular direct complementary subspace of $\mathrm{Im}(\boldsymbol{\Lambda})$, in this case, $\mathrm{Ker}(\boldsymbol{\Lambda}^T)$. The particular choice of $\mathrm{Ker}(\boldsymbol{\Lambda}^T)$ was in fact made in accordance with the notion of *independence* between implicit parameters defined in Sect. 3.2.1. But in principle, any direct complementary subspace $\mathcal{M}$ of $\mathrm{Im}(\boldsymbol{\Lambda})$ could allow a unique decomposition of the model parameters $\boldsymbol{x}$ into:

$$\boldsymbol{x} = \boldsymbol{\Lambda}\boldsymbol{y}_{\mathcal{M}} + \boldsymbol{x}'_{\mathcal{M}}\ ,\ \text{with } \boldsymbol{x}'_{\mathcal{M}} \in \mathcal{M} \tag{3.54}$$

and thus lead to a specific estimate $\hat{\boldsymbol{y}}_{\mathcal{M}}$ of the implicit parameters $\boldsymbol{y}$. In case where no constraints are considered, this estimate can be expressed as:

$$\hat{\boldsymbol{y}}_{\mathcal{M}} = (\boldsymbol{K}_{\mathcal{M}}^T\boldsymbol{\Lambda})^{-1}\boldsymbol{K}_{\mathcal{M}}^T\hat{\boldsymbol{x}} \tag{3.55}$$

and has as covariance matrix:

$$\boldsymbol{Q}_{\hat{\boldsymbol{y}}_{\mathcal{M}}} = (\boldsymbol{K}_{\mathcal{M}}^T\boldsymbol{\Lambda})^{-1}\boldsymbol{K}_{\mathcal{M}}^T\boldsymbol{Q}\boldsymbol{K}_{\mathcal{M}}(\boldsymbol{\Lambda}^T\boldsymbol{K}_{\mathcal{M}})^{-1} \tag{3.56}$$

where $\boldsymbol{K}_{\mathcal{M}}$ denotes any matrix whose columns form a basis of $\mathcal{M}^{\perp}$.

Sillard and Boucher (2001) propose a different, but equivalent view of the same problem: they associate the various possible decompositions of $\boldsymbol{x}$ with different metrics of $\mathbb{R}^p$. Each $p \times p$ symmetric positive definite matrix $\boldsymbol{W}$ indeed defines a scalar product $< \boldsymbol{x}, \boldsymbol{x}' >_{\boldsymbol{W}} = \boldsymbol{x}^T\boldsymbol{W}\boldsymbol{x}'$ in $\mathbb{R}^p$, from which a particular notion of independence (i.e. orthogonality) between implicit parameters can be derived. Each $\boldsymbol{W}$ thus allows a unique decomposition of the model parameters $\boldsymbol{x}$ into:

$$\boldsymbol{x} = \boldsymbol{\Lambda}\boldsymbol{y}_{\boldsymbol{W}} + \boldsymbol{x}'_{\boldsymbol{W}} \text{ , with } \boldsymbol{\Lambda}^T\boldsymbol{W}\boldsymbol{x}'_{\boldsymbol{W}} = \boldsymbol{0} \tag{3.57}$$

In case where no constraints are considered, this decomposition of the model parameters leads to a specific estimate

$$\hat{\boldsymbol{y}}_{\boldsymbol{W}} = (\boldsymbol{\Lambda}^T\boldsymbol{W}\boldsymbol{\Lambda})^{-1}\boldsymbol{\Lambda}^T\boldsymbol{W}\hat{\boldsymbol{x}} \tag{3.58}$$

of the implicit parameters $\boldsymbol{y}$ and to the associated covariance matrix

$$\boldsymbol{Q}_{\hat{\boldsymbol{y}}_{\boldsymbol{W}}} = (\boldsymbol{\Lambda}^T\boldsymbol{W}\boldsymbol{\Lambda})^{-1}\boldsymbol{\Lambda}^T\boldsymbol{W}\boldsymbol{Q}\boldsymbol{W}\boldsymbol{\Lambda}(\boldsymbol{\Lambda}^T\boldsymbol{W}\boldsymbol{\Lambda})^{-1} \tag{3.59}$$

Sillard and Boucher (2001)'s developments were made for the particular purpose of assessing the uncertainty of the origin, scale and orientation (i.e. the *reference system effect* or *datum definition*) of terrestrial frames derived from space geodesy observations. They therefore consider as implicit parameters $\boldsymbol{y}$ differential translations, scale factor and rotations and estimate their uncertainties using Eq. 3.59.

The question of how to make a meaningful choice of $\boldsymbol{W}$ (or equivalently $\mathcal{M}$) is unfortunately not fully addressed by Sillard and Boucher (2001). They recommend using $\boldsymbol{W} = \boldsymbol{N}$, but without clear justification. $\boldsymbol{W} = \boldsymbol{N}$ is also the choice made by Blewitt (1998) for the particular purpose of removing artificial reference frame definition from GPS solution covariance matrices. But Sillard and Boucher (2001) also mention that choosing $\boldsymbol{W} = \boldsymbol{I}$ leads to interesting properties.

Some light can be shed on this question by identifying the choice of $\boldsymbol{W} = \boldsymbol{I}$ with our recommended approach to estimate the values and uncertainties of implicit parameters with Eq. 3.28 and 3.29 (i.e. simultaneously with independent variations of the model parameters). On the other hand, the choice of $\boldsymbol{W} = \boldsymbol{N}$ can be identified with Eq. 3.36 and 3.37, i.e. with the so-called traditional approach to estimate implicit parameters, in which independent variations of the (non-reduced) model parameters are fixed. In other words, if the choice $\boldsymbol{W} = \boldsymbol{I}$ is made for estimating the reference system effect of a terrestrial frame, then the correlations between datum parameters, network geometry and all non-station-position parameters are kept into consideration. On the other hand, choosing $\boldsymbol{W} = \boldsymbol{N}$ discards these correlations and results in a tighter, meaningless estimate of the datum definition.

3.3 A generalized collinearity diagnosis

In this section, the method introduced in Sect. 3.1.5 for diagnosing the collinearity of specific parameters is generalized so as to handle several peculiarities of geodetic data analyses. In Sect. 3.3.1, it is first extended to implicit parameters in the case where $\boldsymbol{A}$ is of full rank and no constraints are imposed on the model parameters. Sect. 3.3.2 provides a further generalization to the case where constraints are applied. In Sect. 3.3.3, a practical method to perform such generalized collinearity diagnoses is finally exposed.

3.3.1 Generalization to implicit parameters

This goal of this subsection is to extend the collinearity diagnosis introduced in Sect. 3.1.5 to implicit parameters. For simplicity, it is first assumed in this subsection that $\boldsymbol{A}$ and $\boldsymbol{N}$ are of full rank and that no constraints are imposed on the parameters. The case where constraints are additionally considered will be separately discussed in Sect. 3.3.2.

Let us consider an implicit parameter y characterized by the partial derivatives $\partial \boldsymbol{x}/\partial y = \boldsymbol{\lambda}$. Similarly as in Sect. 3.2.2, our developments are based on the decomposition of the explicit model parameters $\boldsymbol{x}$ into:

$$\boldsymbol{x} = \boldsymbol{\lambda} y + \boldsymbol{x}' \text{ , with } \boldsymbol{x}' \in \text{Ker}(\boldsymbol{\lambda}^T) \tag{3.60}$$

where $\boldsymbol{x}'$ represents parameter variations independent of y.

Signature of an implicit parameter The impact of a unit variation of y on the observations predicted by the model will be called the *signature* of y on the observations. It can be expressed as:

$$\boldsymbol{S}_y = \frac{\partial \boldsymbol{l}}{\partial y} = \frac{\partial \boldsymbol{l}}{\partial \boldsymbol{x}} \frac{\partial \boldsymbol{x}}{\partial y} = \boldsymbol{A}\boldsymbol{\lambda} \tag{3.61}$$

$\boldsymbol{S}_y$ can be thought as the signal which characterizes the influence of y on the observations.

Decomposition of $\boldsymbol{S}_y$ Let $\boldsymbol{K}_y$ denote any $p \times p - 1$ matrix whose columns form a basis of $\text{Ker}(\boldsymbol{\lambda}^T)$. Provided that $\boldsymbol{A}$ is of full rank, $\text{Im}(\boldsymbol{A}\boldsymbol{K}_y)$ is a $p-1$-dimensional subspace (hyperplane) of the model space $\text{Im}(\boldsymbol{A})$ which spans the signatures of all parameter variations independent of y. Let us now decompose the signature $\boldsymbol{S}_y$ of y into the sum of its orthogonal projection $\boldsymbol{S}_y^u$ onto $\mathrm{Im}(\boldsymbol{A}\boldsymbol{K}_y)$ and of its orthogonal projection $\boldsymbol{S}_y^p$ onto $\mathrm{Im}(\boldsymbol{A}\boldsymbol{K}_y)^\perp$. $\boldsymbol{S}_y^u$, as it lies in $\mathrm{Im}(\boldsymbol{A}\boldsymbol{K}_y)$, is strictly collinear with the signatures of parameter variations independent of y. The estimation of y can therefore only rely on $\boldsymbol{S}_y^p$, which will be called the *proper signature* of y. As proven below, $\boldsymbol{S}_y^p$ can be expressed as:

$$\boldsymbol{S}_y^p = \frac{\boldsymbol{\lambda}^T\boldsymbol{\lambda}}{\boldsymbol{\lambda}^T\boldsymbol{Q}\boldsymbol{\lambda}}\boldsymbol{A}\boldsymbol{Q}\boldsymbol{\lambda} \tag{3.62}$$

Proof. Since $\boldsymbol{A}$ is assumed of full rank, proposition A.6 implies that $\mathrm{rank}(\boldsymbol{A}\boldsymbol{K}_y) = \mathrm{rank}(\boldsymbol{K}_y) = p-1$. The columns of $\boldsymbol{A}\boldsymbol{K}_y$ therefore form a basis of the $p-1$-dimensional subspace $\mathrm{Im}(\boldsymbol{A}\boldsymbol{K}_y)$. According to proposition A.16, the matrix form of the orthogonal projection onto $\mathrm{Im}(\boldsymbol{A}\boldsymbol{K}_y)^\perp$ is thus:

$$\begin{aligned}\boldsymbol{\Pi} &= \boldsymbol{I} - \boldsymbol{A}\boldsymbol{K}_y\left((\boldsymbol{A}\boldsymbol{K}_y)^T\boldsymbol{P}_l\boldsymbol{A}\boldsymbol{K}_y\right)^{-1}(\boldsymbol{A}\boldsymbol{K}_y)^T\boldsymbol{P}_l\\ &= \boldsymbol{I} - \boldsymbol{A}\boldsymbol{K}_y(\boldsymbol{K}_y^T\boldsymbol{N}\boldsymbol{K}_y)^{-1}\boldsymbol{K}_y^T\boldsymbol{A}^T\boldsymbol{P}_l\end{aligned}$$

Therefore,

$$\boldsymbol{S}_y^p = \boldsymbol{\Pi}\boldsymbol{S}_y = \boldsymbol{\Pi}\boldsymbol{A}\boldsymbol{\lambda} = \boldsymbol{A}\boldsymbol{\lambda} - \boldsymbol{A}\boldsymbol{K}_y(\boldsymbol{K}_y^T\boldsymbol{N}\boldsymbol{K}_y)^{-1}\boldsymbol{K}_y^T\boldsymbol{N}\boldsymbol{\lambda}$$

Since $\boldsymbol{N}$ is assumed of full rank, $\boldsymbol{K}_y(\boldsymbol{K}_y^T\boldsymbol{N}\boldsymbol{K}_y)^{-1}\boldsymbol{K}_y^T$ can be replaced, according to proposition A.19, by $\boldsymbol{Q} - \boldsymbol{Q}\boldsymbol{\lambda}(\boldsymbol{\lambda}^T\boldsymbol{Q}\boldsymbol{\lambda})^{-1}\boldsymbol{\lambda}^T\boldsymbol{Q}$ in the previous equation, which leads after simplification to the expression of $\boldsymbol{S}_y^p$ given in Eq. 3.62. ☐

VIF of an implicit parameter Let θ_y denote the angle between the signature $\boldsymbol{S}_y$ of y and the hyperplane $\mathrm{Im}(\boldsymbol{A}\boldsymbol{K}_y)$. Using Eq. 3.62, it can be shown that:

$$\begin{aligned}\cos\theta_y &= \frac{<\boldsymbol{S}_y, \boldsymbol{S}_y^u>}{\|\boldsymbol{S}_y\|\|\boldsymbol{S}_y^u\|} = \frac{<\boldsymbol{S}_y, \boldsymbol{S}_y - \boldsymbol{S}_y^p>}{\|\boldsymbol{S}_y\|\|\boldsymbol{S}_y - \boldsymbol{S}_y^p\|}\\ &= \sqrt{1 - \frac{(\boldsymbol{\lambda}^T\boldsymbol{\lambda})^2}{(\boldsymbol{\lambda}^T\boldsymbol{N}\boldsymbol{\lambda})(\boldsymbol{\lambda}^T\boldsymbol{Q}\boldsymbol{\lambda})}}\end{aligned} \tag{3.63}$$

One can also show that, if a regression of $\boldsymbol{S}_y$ on the columns of $\boldsymbol{A}\boldsymbol{K}_y$ was made, the obtained coefficient of determination would be $R_y^2 = \cos^2\theta_y$.

The variance inflation factor V_y of an implicit parameter y can be defined from θ_y or R_y^2 by:

$$V_y = \frac{1}{\sin^2\theta_y} = \frac{1}{1 - R_y^2} \tag{3.64}$$

Inserting Eq. 3.63 into Eq. 3.64 leads to a formula from which V_y can be practically computed when disposing of the normal matrix $\boldsymbol{N}$ and of its inverse $\boldsymbol{Q}$:

$$V_y = \frac{(\boldsymbol{\lambda}^T\boldsymbol{N}\boldsymbol{\lambda})(\boldsymbol{\lambda}^T\boldsymbol{Q}\boldsymbol{\lambda})}{(\boldsymbol{\lambda}^T\boldsymbol{\lambda})^2} \tag{3.65}$$

Replacing $\boldsymbol{\lambda}$ by $\boldsymbol{e}_i$ in the preceding developments leads back to the equations of Sect. 3.1.5, which proves that this extension of VIFs to implicit parameters encompasses usual VIFs.

The interpretation of such generalized VIFs remains unchanged. $V_y = 1$ when $\boldsymbol{S}_y$ is orthogonal to $\mathrm{Im}(\boldsymbol{A}\boldsymbol{K}_y)$, i.e. when y is uncorrelated with any independent parameter variation. On the other hand, V_y tends to infinity when $\boldsymbol{S}_y$ tends to lie in $\mathrm{Im}(\boldsymbol{A}\boldsymbol{K}_y)$ and y tends to be indistinguishable from independent parameter variations. Note that V_y also remains interpretable as a "variance inflation factor". According to Eq. 3.29, the variance of y, when simultaneously estimated with independent parameter variations, is indeed $(\boldsymbol{\lambda}^T\boldsymbol{Q}\boldsymbol{\lambda})/(\boldsymbol{\lambda}^T\boldsymbol{\lambda})^2$. On the other hand, if all independent parameter variations were known and held fixed, the variance of y would be $1/(\boldsymbol{\lambda}^T\boldsymbol{N}\boldsymbol{\lambda})$. Let us finally mention that V_y can still be interpreted as the ratio of the squared norm of the signature of y on the observations to the squared norm of its proper signature ($V_y = \|\boldsymbol{S}_y\|^2/\|\boldsymbol{S}_y^p\|^2$).

Coordinates of $\boldsymbol{S}_y^u$ Like the coordinates of $\boldsymbol{A}_i^u$ in the basis formed by the columns of $\boldsymbol{A}$ can enlighten why a parameter $\boldsymbol{x}_i$ may be hardly distinguishable from the other parameters, the coordinates of $\boldsymbol{S}_y^u$ in this basis can similarly explain why an implicit parameter y may be hardly distinguishable from independent parameter variations. These coordinates can now be interpreted as $\partial\boldsymbol{x}/\partial z$ where z is the implicit parameter independent of y whose signature $\boldsymbol{S}_z = \boldsymbol{S}_y^u$ most closely matches $\boldsymbol{S}_y$.

According to Eq. 3.61 and 3.62,

$$\boldsymbol{S}_y^u = \boldsymbol{S}_y - \boldsymbol{S}_y^p = \boldsymbol{A}\left(\boldsymbol{\lambda} - \frac{\boldsymbol{\lambda}^T\boldsymbol{\lambda}}{\boldsymbol{\lambda}^T\boldsymbol{Q}\boldsymbol{\lambda}}\boldsymbol{Q}\boldsymbol{\lambda}\right) \tag{3.66}$$

so that the coordinates $\boldsymbol{\mu}_y$ of $\boldsymbol{S}_y^u$ in the basis formed by the columns of $\boldsymbol{A}$ are:

$$\boldsymbol{\mu}_y = \boldsymbol{\lambda} - \frac{\boldsymbol{\lambda}^T\boldsymbol{\lambda}}{\boldsymbol{\lambda}^T\boldsymbol{Q}\boldsymbol{\lambda}}\boldsymbol{Q}\boldsymbol{\lambda} \tag{3.67}$$

3.3.2 Generalization to constrained problems

In this subsection, the generalized collinearity diagnosis developed in Sect. 3.3.1 is further extended to the case where constraints are imposed on the parameters, in order to supplement possible rank deficiencies of $\boldsymbol{A}$ and $\boldsymbol{N}$, or for any other purpose. Like in Sect. 3.2.3, we will now assume that the parameter variations independent of y are subject to the constraint $\boldsymbol{C}^T\boldsymbol{x}' = \boldsymbol{0}$, where the $p \times c$ matrix $\boldsymbol{C}$ is of full rank and properly supplements the possible rank deficiencies of $\boldsymbol{A}$ and $\boldsymbol{N}$. It will also be assumed that $\lambda \notin \mathrm{Im}(\boldsymbol{C})$, i.e. that $\mathrm{rank}([\boldsymbol{\lambda}\,\boldsymbol{C}]) = c + 1$.

Decomposition of S_y Let $\boldsymbol{K}_{y,c}$ denote any matrix whose columns form a basis of $\mathrm{Ker}([\boldsymbol{\lambda}\ \boldsymbol{C}]^T)$. $\mathrm{Im}(\boldsymbol{A}\boldsymbol{K}_{y,c})$ is a subspace of the model space $\mathrm{Im}(\boldsymbol{A})$ which spans the signatures of all parameter variations independent of y and allowed by the constraints. Like previously, the signature $\boldsymbol{S}_y$ of y can be decomposed into the sum of its orthogonal projection $\boldsymbol{S}^u_{y,c}$ onto $\mathrm{Im}(\boldsymbol{A}\boldsymbol{K}_{y,c})$ and of its orthogonal projection $\boldsymbol{S}^p_{y,c}$ onto $\mathrm{Im}(\boldsymbol{A}\boldsymbol{K}_{y,c})^{\perp}$. $\boldsymbol{S}^u_{y,c}$ is indistinguishable from the signatures of parameter variations independent of y and allowed by the constraints. The estimation of y can therefore only rely on its proper signature $\boldsymbol{S}^p_{y,c}$. As proven below, $\boldsymbol{S}^p_{y,c}$ can be expressed as:

$$\boldsymbol{S}^p_{y,c} = \boldsymbol{A}\boldsymbol{\lambda} - \boldsymbol{A}\boldsymbol{K}_{y,c}(\boldsymbol{K}^T_{y,c}\boldsymbol{N}\boldsymbol{K}_{y,c})^{-1}\boldsymbol{K}^T_{y,c}\boldsymbol{N}\boldsymbol{\lambda} \tag{3.68}$$

Proof. Since $\mathrm{rank}([\boldsymbol{\lambda}\ \boldsymbol{C}]) = c+1$, $\dim(\mathrm{Ker}([\boldsymbol{\lambda}\ \boldsymbol{C}]^T)) = p-c-1$. $\boldsymbol{K}_{y,c}$, whose columns form a basis of $\mathrm{Ker}([\boldsymbol{\lambda}\ \boldsymbol{C}]^T)$ is therefore a $p \times (p-c-1)$ matrix. Moreover, the columns of the $p \times p$ matrix $[\boldsymbol{\lambda}\ \boldsymbol{C}\ \boldsymbol{K}_{y,c}]$ form a basis of $\mathbb{R}^p$. The hypothesis that $\boldsymbol{C}$ properly supplements the rank deficiencies of $\boldsymbol{A}$ is equivalent to $\mathrm{rank}\left(\begin{bmatrix} \boldsymbol{A} \\ \boldsymbol{C}^T \end{bmatrix}\right) = p$. Proposition A.6 consequently implies that the $(n+c) \times p$ matrix:

$$\begin{bmatrix} \boldsymbol{A} \\ \boldsymbol{C}^T \end{bmatrix} [\boldsymbol{\lambda}\ \boldsymbol{C}\ \boldsymbol{K}_{y,c}] = \begin{bmatrix} \boldsymbol{A}\boldsymbol{\lambda} & \boldsymbol{A}\boldsymbol{C} & \boldsymbol{A}\boldsymbol{K}_{y,c} \\ \boldsymbol{C}^T\boldsymbol{\lambda} & \boldsymbol{C}^T\boldsymbol{C} & \boldsymbol{0} \end{bmatrix}$$

is of full rank. The $n \times (p-c-1)$ matrix $\boldsymbol{A}\boldsymbol{K}_{y,c}$ is therefore necessarily of full rank itself. In other words, the columns of $\boldsymbol{A}\boldsymbol{K}_{y,c}$ form a basis of $\mathrm{Im}(\boldsymbol{A}\boldsymbol{K}_{y,c})$. According to proposition A.16, the matrix form of the orthogonal projection onto $\mathrm{Im}(\boldsymbol{A}\boldsymbol{K}_{y,c})^{\perp}$ is thus:

$$\begin{aligned} \boldsymbol{\Pi} &= \boldsymbol{I} - \boldsymbol{A}\boldsymbol{K}_{y,c}\left((\boldsymbol{A}\boldsymbol{K}_{y,c})^T\boldsymbol{P_l}\boldsymbol{A}\boldsymbol{K}_{y,c}\right)^{-1}(\boldsymbol{A}\boldsymbol{K}_{y,c})^T\boldsymbol{P_l} \\ &= \boldsymbol{I} - \boldsymbol{A}\boldsymbol{K}_{y,c}(\boldsymbol{K}^T_{y,c}\boldsymbol{N}\boldsymbol{K}_{y,c})^{-1}\boldsymbol{K}^T_{y,c}\boldsymbol{A}^T\boldsymbol{P_l} \end{aligned}$$

Therefore,

$$\boldsymbol{S}^p_{y,c} = \boldsymbol{\Pi}\boldsymbol{S}_{y,c} = \boldsymbol{\Pi}\boldsymbol{A}\boldsymbol{\lambda} = \boldsymbol{A}\boldsymbol{\lambda} - \boldsymbol{A}\boldsymbol{K}_{y,c}(\boldsymbol{K}^T_{y,c}\boldsymbol{N}\boldsymbol{K}_{y,c})^{-1}\boldsymbol{K}^T_{y,c}\boldsymbol{N}\boldsymbol{\lambda}$$

□

Variance inflation factor Let $\theta_{y,c}$ denote the angle between the signature $\boldsymbol{S}_y$ of y and the hyperplane $\mathrm{Im}(\boldsymbol{A}\boldsymbol{K}_{y,c})$. Using Eq. 3.68, it can be shown that:

$$\begin{aligned} \cos\theta_{y,c} &= \frac{<\boldsymbol{S}_y, \boldsymbol{S}^u_{y,c}>}{||\boldsymbol{S}_y||\,||\boldsymbol{S}^u_{y,c}||} = \frac{<\boldsymbol{S}_y, \boldsymbol{S}_y - \boldsymbol{S}^p_{y,c}>}{||\boldsymbol{S}_y||\,||\boldsymbol{S}_y - \boldsymbol{S}^p_{y,c}||} \\ &= \sqrt{\frac{\boldsymbol{\lambda}^T\boldsymbol{N}\boldsymbol{K}_{y,c}(\boldsymbol{K}^T_{y,c}\boldsymbol{N}\boldsymbol{K}_{y,c})^{-1}\boldsymbol{K}^T_{y,c}\boldsymbol{N}\boldsymbol{\lambda}}{\boldsymbol{\lambda}^T\boldsymbol{N}\boldsymbol{\lambda}}} \end{aligned} \tag{3.69}$$

One can also show that, if a regression of $\boldsymbol{S}_{y,c}$ on the columns of $\boldsymbol{A}\boldsymbol{K}_{y,c}$ was made, the obtained coefficient of determination would be $R^2_{y,c} = \cos^2\theta_{y,c}$.

In case where constraints are imposed on the parameters, the variance inflation factor $V_{y,c}$ of an implicit parameter y can be defined from $\theta_{y,c}$ or $R^2_{y,c}$ by:

$$V_{y,c} = \frac{1}{\sin^2\theta_{y,c}} = \frac{1}{1 - R^2_{y,c}} \tag{3.70}$$

Inserting Eq. 3.69 into Eq. 3.70 leads to the following expression of $V_{y,c}$:

$$V_{y,c} = \frac{\boldsymbol{\lambda}^T \boldsymbol{N} \boldsymbol{\lambda}}{\boldsymbol{\lambda}^T \boldsymbol{N} \boldsymbol{\lambda} - \boldsymbol{\lambda}^T \boldsymbol{N} \boldsymbol{K}_{y,c} (\boldsymbol{K}_{y,c}^T \boldsymbol{N} \boldsymbol{K}_{y,c})^{-1} \boldsymbol{K}_{y,c}^T \boldsymbol{N} \boldsymbol{\lambda}} \tag{3.71}$$

Like previously, $V_{y,c} = 1$ means that y is uncorrelated with any independent parameter variation allowed by the constraints. On the other hand, $V_{y,c}$ tends to infinity when $\boldsymbol{S}_y$ tends to lie in $\mathrm{Im}(\boldsymbol{A}\boldsymbol{K}_{y,c})$ and y tends to be indistinguishable from independent parameter variations allowed by the constraints. $V_{y,c}$ also remains interpretable as a "variance inflation factor". In case where constraints are applied, the variance of y, when simultaneously estimated with independent parameter variations, is indeed $\left(\boldsymbol{\lambda}^T \boldsymbol{N} \boldsymbol{\lambda} - \boldsymbol{\lambda}^T \boldsymbol{N} \boldsymbol{K}_{y,c} (\boldsymbol{K}_{y,c}^T \boldsymbol{N} \boldsymbol{K}_{y,c})^{-1} \boldsymbol{K}_{y,c}^T \boldsymbol{N} \boldsymbol{\lambda}\right)^{-1}$ according to Eq. 3.45. On the other hand, if all independent parameter variations were known and held fixed, the variance of y would be $1/(\boldsymbol{\lambda}^T \boldsymbol{N} \boldsymbol{\lambda})$. $V_{y,c}$ can finally still be interpreted as the ratio of the squared norm of the signature of y on the observations to the squared norm of its proper signature ($V_{y,c} = \|\boldsymbol{S}_y\|^2 / \|\boldsymbol{S}_{y,c}^p\|^2$).

Coordinates of $\boldsymbol{S}_y^u$ According to Eq. 3.68,

$$\boldsymbol{S}_{y,c}^u = \boldsymbol{S}_y - \boldsymbol{S}_{y,c}^p = \boldsymbol{A} \boldsymbol{K}_{y,c} (\boldsymbol{K}_{y,c}^T \boldsymbol{N} \boldsymbol{K}_{y,c})^{-1} \boldsymbol{K}_{y,c}^T \boldsymbol{N} \boldsymbol{\lambda} \tag{3.72}$$

The vector

$$\boldsymbol{\mu}_{y,c} = \boldsymbol{K}_{y,c} (\boldsymbol{K}_{y,c}^T \boldsymbol{N} \boldsymbol{K}_{y,c})^{-1} \boldsymbol{K}_{y,c}^T \boldsymbol{N} \boldsymbol{\lambda} \tag{3.73}$$

can therefore be interpreted as $\partial \boldsymbol{x} / \partial z$ where z is the implicit parameter independent of y and allowed by the constraints whose signature $\boldsymbol{S}_z = \boldsymbol{S}_y^u$ most closely matches $\boldsymbol{S}_y$. It can therefore explain why y may be hardly distinguishable from independent parameter variations allowed by the constraints.

3.3.3 Practical collinearity diagnosis

As a matrix $\boldsymbol{K}_{y,c}$ is generally not available, Eq. 3.71 and 3.73 are of no practical use. A practical method to perform collinearity diagnoses in case where constraints are applied is therefore exposed in this subsection.

Computing $\boldsymbol{\mu}_{y,c}$ Given an implicit parameter y such that $\partial \boldsymbol{x} / \partial y = \boldsymbol{\lambda}$, finding the parameter variation $\boldsymbol{\mu}_{y,c}$ independent of y and allowed by the constraints whose signature most closely matches $\boldsymbol{S}_y = \boldsymbol{A}\boldsymbol{\lambda}$ clearly comes to solving the following problem:

$$\hat{\boldsymbol{\mu}} = \operatorname*{argmin}_{\boldsymbol{\mu} \in \mathbb{R}^p, \boldsymbol{\lambda}^T \boldsymbol{\mu} = 0, \boldsymbol{C}^T \boldsymbol{\mu} = 0} \left(\|\boldsymbol{A}(\boldsymbol{\mu} - \boldsymbol{\lambda})\|^2\right) \tag{3.74}$$

According to Sect. B.2.2, this problem can be solved through the following constrained normal equation:

$$\begin{bmatrix} \boldsymbol{N} & \boldsymbol{\lambda} & \boldsymbol{C} \\ \boldsymbol{\lambda}^T & 0 & 0 \\ \boldsymbol{C}^T & 0 & 0 \end{bmatrix} \begin{bmatrix} \boldsymbol{\mu} \\ k \\ \boldsymbol{k}' \end{bmatrix} = \begin{bmatrix} \boldsymbol{N\lambda} \\ 0 \\ \boldsymbol{0} \end{bmatrix} \tag{3.75}$$

where k and $\boldsymbol{k}'$ denote $c+1$ Lagrange multipliers. Eq. B.17 indeed confirms that the solution of Eq. 3.75 is nothing but:

$$\boldsymbol{\mu}_{y,c} = \boldsymbol{K}_{y,c}(\boldsymbol{K}_{y,c}^T \boldsymbol{N} \boldsymbol{K}_{y,c})^{-1} \boldsymbol{K}_{y,c}^T \boldsymbol{N\lambda} \tag{3.76}$$

Solving Eq. 3.75 thus constitutes the first step of our practical collinearity diagnosis.

Note that to avoid computing $\boldsymbol{N\lambda}$, the variable change $\boldsymbol{\gamma} = \boldsymbol{\lambda} - \boldsymbol{\mu}$ can be made, leading to:

$$\begin{bmatrix} \boldsymbol{N} & \boldsymbol{\lambda} & \boldsymbol{C} \\ \boldsymbol{\lambda}^T & 0 & 0 \\ \boldsymbol{C}^T & 0 & 0 \end{bmatrix} \begin{bmatrix} \boldsymbol{\gamma} \\ k \\ \boldsymbol{k}' \end{bmatrix} = \begin{bmatrix} \boldsymbol{0} \\ \boldsymbol{\lambda}^T\boldsymbol{\lambda} \\ \boldsymbol{C}^T\boldsymbol{\lambda} \end{bmatrix} \tag{3.77}$$

Computing $V_{y,c}$ Once $\boldsymbol{\mu}_{y,c}$ has been obtained, the second step of our practical collinearity diagnosis is the computation of the variance inflation factor $V_{y,c}$ of y. This step requires the availability of the design matrix $\boldsymbol{A}$. From $\boldsymbol{A}$, $\boldsymbol{\lambda}$, and $\boldsymbol{\mu}_{y,c}$, the signature $\boldsymbol{S}_y = \boldsymbol{A\lambda}$ and the proper signature $\boldsymbol{S}_{y,c}^p = \boldsymbol{A}(\boldsymbol{\lambda} - \boldsymbol{\mu}_{y,c})$ of y can be computed. $V_{y,c}$ can then be obtained by:

$$V_{y,c} = \frac{||\boldsymbol{S}_y||^2}{||\boldsymbol{S}_{y,c}^p||^2} \tag{3.78}$$

Note that the quantities $1/||\boldsymbol{S}_y||$ and $1/||\boldsymbol{S}_{y,c}^p||$ are of interest as well. According to Eq. 3.45, $1/||\boldsymbol{S}_{y,c}^p||$ is nothing but the formal error of the implicit parameter y. On the other hand, $1/||\boldsymbol{S}_y||$ would be the formal error of y in case where all independent parameter variations were known and held fixed.

3.4 Impact of double-differencing

As mentioned in Sect. 2.1.2, some Analysis Centers of the IGS make use of double-differenced GNSS observations while other process undifferenced observations. In the next chapter, we will consider undifferenced observations only, because of their simpler geometric interpretation. The collinearity diagnosis developed above could nevertheless be performed in double-differenced analyses and would lead to different variance inflation factors than in undifferenced analyses. We therefore deem important to explain how the results of collinearity diagnoses performed in double-differenced analyses and undifferenced analyses relate to each other. This section starts by demonstrating that, under certain conditions, processing double-differenced observations is equivalent to reducing clock parameters from an undifferenced system (Sect. 3.4.1). A relationship between "undifferenced VIFs" and "double-differenced VIFs" is then derived and discussed in Sect. 3.4.2.

3.4.1 Equivalence of double-differencing and clock parameter reduction

Clock parameter reduction Consider a global GNSS analysis based on undifferenced observations $\boldsymbol{l}$ and suppose that the model parameters are organized in such a way that $\boldsymbol{x}^T = [\boldsymbol{x}_1^T \, \boldsymbol{x}_2^T]$ where $\boldsymbol{x}_2$ groups the station and satellite clock parameters and $\boldsymbol{x}_1$ all other parameters. The design matrix $\boldsymbol{A}$ can be accordingly split into two column blocks: $\boldsymbol{A} = [\boldsymbol{A}_1 \, \boldsymbol{A}_2]$, and the full normal equation can be block-decomposed into:

$$\begin{bmatrix} \boldsymbol{N}_{11} & \boldsymbol{N}_{12} \\ \boldsymbol{N}_{21} & \boldsymbol{N}_{22} \end{bmatrix} \begin{bmatrix} \boldsymbol{x}_1 \\ \boldsymbol{x}_2 \end{bmatrix} = \begin{bmatrix} \boldsymbol{b}_1 \\ \boldsymbol{b}_2 \end{bmatrix} \tag{3.79}$$

The reduction of the clock parameters $\boldsymbol{x}_2$ (Sect. B.3.1) leads to the reduced normal equation $\boldsymbol{N}_r \boldsymbol{x}_1 = \boldsymbol{b}_r$ with:

$$\begin{aligned} \boldsymbol{N}_r &= \boldsymbol{N}_{1,1} - \boldsymbol{N}_{1,2} \boldsymbol{N}_{2,2}^{-1} \boldsymbol{N}_{2,1} \\ &= \boldsymbol{A}_1^T \boldsymbol{P}_l \boldsymbol{A}_1 - \boldsymbol{A}_1^T \boldsymbol{P}_l \boldsymbol{A}_2 (\boldsymbol{A}_2^T \boldsymbol{P}_l \boldsymbol{A}_2)^{-1} \boldsymbol{A}_2^T \boldsymbol{P}_l \boldsymbol{A}_1 \\ &= \boldsymbol{A}_1^T \left(\boldsymbol{P}_l - \boldsymbol{P}_l \boldsymbol{A}_2 (\boldsymbol{A}_2^T \boldsymbol{P}_l \boldsymbol{A}_2)^{-1} \boldsymbol{A}_2^T \boldsymbol{P}_l \right) \boldsymbol{A}_1 \end{aligned} \tag{3.80}$$

and:

$$\begin{aligned} \boldsymbol{b}_r &= \boldsymbol{b}_1 - \boldsymbol{N}_{1,2} \boldsymbol{N}_{2,2}^{-1} \boldsymbol{b}_2 \\ &= \boldsymbol{A}_1^T \boldsymbol{P}_l \boldsymbol{l} - \boldsymbol{A}_1^T \boldsymbol{P}_l \boldsymbol{A}_2 (\boldsymbol{A}_2^T \boldsymbol{P}_l \boldsymbol{A}_2)^{-1} \boldsymbol{A}_2^T \boldsymbol{P}_l \boldsymbol{l} \\ &= \boldsymbol{A}_1^T \left(\boldsymbol{P}_l - \boldsymbol{P}_l \boldsymbol{A}_2 (\boldsymbol{A}_2^T \boldsymbol{P}_l \boldsymbol{A}_2)^{-1} \boldsymbol{A}_2^T \boldsymbol{P}_l \right) \boldsymbol{l} \end{aligned} \tag{3.81}$$

Double-differencing Double-differenced observations $\boldsymbol{l}_d$ are obtained from the undifferenced observations $\boldsymbol{l}$ by the application of a $n_d \times n$ "differencing operator" $\boldsymbol{D}$: $\boldsymbol{l}_d = \boldsymbol{D}\boldsymbol{l}$. According to the variance propagation law, the covariance matrix of the double-differenced observations is: $\boldsymbol{Q}_{l_d} = \boldsymbol{D}\boldsymbol{Q}_l\boldsymbol{D}^T$. Note that using $\boldsymbol{P}_{l_d} = \boldsymbol{Q}_{l_d}^{-1}$ as a weight matrix for the double-differenced observations requires that $\boldsymbol{D}$ be of full rank, i.e. that the double differences be linearly independent.

The double-differenced observation equations can be written as:

$$\boldsymbol{l}_d = \boldsymbol{D}\boldsymbol{l} = \boldsymbol{D}[\boldsymbol{A}_1 \boldsymbol{A}_2] \begin{bmatrix} \boldsymbol{x}_1 \\ \boldsymbol{x}_2 \end{bmatrix} + \boldsymbol{D}\boldsymbol{v} \tag{3.82}$$

But all the interest of double differencing resides in the fact that double differenced observations are insensitive to the clock parameters $\boldsymbol{x}_2$. Mathematically, this means that the partial derivatives $\partial \boldsymbol{l}_d / \partial \boldsymbol{x}_2 = \boldsymbol{D}\boldsymbol{A}_2 = \boldsymbol{0}$ so that the observation equations simplify to:

$$\boldsymbol{l}_d = \boldsymbol{D}\boldsymbol{A}_1 \boldsymbol{x}_1 + \boldsymbol{D}\boldsymbol{v} \tag{3.83}$$

The corresponding design matrix is $\boldsymbol{A}_d = \boldsymbol{D}\boldsymbol{A}_1$, and the double-differenced normal equation can be written as $\boldsymbol{N}_d \boldsymbol{x}_1 = \boldsymbol{b}_d$ with:

$$\boldsymbol{N}_d = \boldsymbol{A}_d^T \boldsymbol{Q}_{l_d}^{-1} \boldsymbol{A}_d = \boldsymbol{A}_1^T \boldsymbol{D}^T (\boldsymbol{D}\boldsymbol{Q}_l \boldsymbol{D}^T)^{-1} \boldsymbol{D}\boldsymbol{A}_1 \tag{3.84}$$

and:

$$\boldsymbol{b}_d = \boldsymbol{A}_d^T \boldsymbol{Q}_{l_d}^{-1} \boldsymbol{l}_d = \boldsymbol{A}_1^T \boldsymbol{D}^T (\boldsymbol{D}\boldsymbol{Q}_l \boldsymbol{D}^T)^{-1} \boldsymbol{D}\boldsymbol{l} \tag{3.85}$$

Equivalence By comparing Eq. 3.80 and 3.81 with Eq. 3.84 and 3.85, it is clear that if $\boldsymbol{P}_l - \boldsymbol{P}_l \boldsymbol{A}_2 (\boldsymbol{A}_2^T \boldsymbol{P}_l \boldsymbol{A}_2)^{-1} \boldsymbol{A}_2^T \boldsymbol{P}_l = \boldsymbol{D}^T (\boldsymbol{D}\boldsymbol{Q}_l \boldsymbol{D}^T)^{-1} \boldsymbol{D}$, then the clock parameter reduction and the double differencing approaches lead to identical normal equations. According to proposition A.19, this condition is fulfilled when the columns of $\boldsymbol{D}^T$ form a basis of $\mathrm{Ker}(\boldsymbol{A}_2^T)$, i.e. if:

$$\begin{cases} \boldsymbol{D}\boldsymbol{A}_2 = 0 \\ \boldsymbol{D} \text{ is of full rank} \\ \mathrm{rank}(\boldsymbol{D}) = \dim(\mathrm{Ker}(\boldsymbol{A}_2^T)) \end{cases} \tag{3.86}$$

The first condition ($\boldsymbol{D}\boldsymbol{A}_2 = 0$) is "naturally" fulfilled by any double-differencing operator. The second condition (linear independence of the double differences) was already assumed, otherwise, the covariance matrix of the double-differenced observations would not be invertible. Only the last condition remains to be met. It basically means that, under both previous conditions, $\boldsymbol{D}$ should have the maximal possible size, i.e. that as many independent double differences as possible should be formed.

In conclusion, when a maximal set of independent double-differenced observations is used, processing double-differenced observations leads to the same normal equation as reducing clock parameters from the full undifferenced normal equation. Under these conditions, processing double-differenced observations therefore leads to identical values and uncertainties for all non-clock parameters as processing undifferenced observations.

3.4.2 Relationship between undifferenced and double-differenced VIFs

Consider, in a global undifferenced GNSS analysis, an implicit parameter y characterized by the partial derivatives $\partial \boldsymbol{x}/\partial y = \boldsymbol{\lambda}$. Assume that the parameters $\boldsymbol{x}$ are organized in the same way as in Sect. 3.4.1, and suppose that $\boldsymbol{\lambda}$ has the form:

$$\boldsymbol{\lambda} = \begin{bmatrix} \boldsymbol{\lambda}_1 \\ 0 \end{bmatrix} \tag{3.87}$$

This hypothesis concretely requires that y be independent of any clock parameter. For the simplicity of the demonstration, finally suppose that the design matrix $\boldsymbol{A}$ is of full rank so that the normal matrix $\boldsymbol{N}$ can be inverted into $\boldsymbol{Q} = \boldsymbol{N}^{-1}$. The squared norm of the signature of y on the undifferenced observations is:

$$||\boldsymbol{S_y}||^2 = ||\boldsymbol{A\lambda}||^2 = \boldsymbol{\lambda}^T\boldsymbol{N\lambda} \tag{3.88}$$

On the other hand, the squared norm of the proper signature of y is, according to Eq. 3.62:

$$||\boldsymbol{S_y^p}||^2 = \frac{(\boldsymbol{\lambda}^T\boldsymbol{\lambda})^2}{\boldsymbol{\lambda}^T\boldsymbol{Q\lambda}} \tag{3.89}$$

Because of the assumed form of $\boldsymbol{\lambda}$, Eq. 3.89 can be re-arranged, using proposition A.18, into:

$$||\boldsymbol{S_y^p}||^2 = \frac{(\boldsymbol{\lambda}_1^T\boldsymbol{\lambda}_1)^2}{(\boldsymbol{\lambda}_1^T(\boldsymbol{N}_{11} - \boldsymbol{N}_{12}\boldsymbol{N}_{22}^{-1}\boldsymbol{N}_{21})^{-1}\boldsymbol{\lambda}_1)} \tag{3.90}$$

Suppose now that a set of n_d independent double-differenced observations $\boldsymbol{l}_d = \boldsymbol{Dl}$ is formed. The weight matrix of the double-differenced observations:

$$\boldsymbol{P}_{\boldsymbol{l}_d} = \boldsymbol{Q}_{\boldsymbol{l}_d}^{-1} = (\boldsymbol{DQ}_l\boldsymbol{D}^T)^{-1} \tag{3.91}$$

induces the norm $||\boldsymbol{l}_d||_d = \sqrt{\boldsymbol{l}_d^T\boldsymbol{P}_{\boldsymbol{l}_d}\boldsymbol{l}_d}$ in the space of double-differenced observations $\mathbb{R}^{n_d}$. The signature of y on the double-differenced observations is:

$$\boldsymbol{S}_{y,d} = \boldsymbol{DS}_y = \boldsymbol{DA\lambda} = \boldsymbol{DA}_1\boldsymbol{\lambda}_1 = \boldsymbol{A}_d\boldsymbol{\lambda}_1 \tag{3.92}$$

and its squared norm is:

$$\begin{aligned} ||\boldsymbol{S}_{y,d}||_d^2 &= (\boldsymbol{A}_d\boldsymbol{\lambda}_1)^T\boldsymbol{P}_{\boldsymbol{l}_d}(\boldsymbol{A}_d\boldsymbol{\lambda}_1) = (\boldsymbol{DA\lambda})^T\boldsymbol{P}_{\boldsymbol{l}_d}(\boldsymbol{DA\lambda}) \\ &= (\boldsymbol{A\lambda})^T\boldsymbol{D}^T(\boldsymbol{DQ}_l\boldsymbol{D}^T)^{-1}\boldsymbol{D}(\boldsymbol{A\lambda}) \end{aligned} \tag{3.93}$$

If a maximal set of independent double-differenced observations is used, then, according to Sect. 3.4.1,

$$\boldsymbol{D}^T(\boldsymbol{DQ}_l\boldsymbol{D}^T)^{-1}\boldsymbol{D} = \boldsymbol{P}_l - \boldsymbol{P}_l\boldsymbol{A}_2(\boldsymbol{A}_2^T\boldsymbol{P}_l\boldsymbol{A}_2)^{-1}\boldsymbol{A}_2^T\boldsymbol{P}_l = \Pi_{\boldsymbol{A}_2^\perp}^T\boldsymbol{P}_l\Pi_{\boldsymbol{A}_2^\perp} \tag{3.94}$$

where $\Pi_{\boldsymbol{A}_2^\perp} = \boldsymbol{I} - \boldsymbol{A}_2(\boldsymbol{A}_2^T\boldsymbol{P}_l\boldsymbol{A}_2)^{-1}\boldsymbol{A}_2^T\boldsymbol{P}_l$ is the matrix form of the orthogonal projection onto $\mathrm{Im}(\boldsymbol{A}_2)^\perp = \mathrm{Ker}(\boldsymbol{A}_2^T)$. Eq. 3.93 can consequently be re-written as:

$$||\boldsymbol{S}_{y,d}||_d^2 = (\boldsymbol{\Pi}_{\boldsymbol{A}_2^\perp}\boldsymbol{A}\boldsymbol{\lambda})^T\boldsymbol{P}_l(\boldsymbol{\Pi}_{\boldsymbol{A}_2^\perp}\boldsymbol{A}\boldsymbol{\lambda}) = ||\boldsymbol{\Pi}_{\boldsymbol{A}_2^\perp}\boldsymbol{S}_y||^2 \tag{3.95}$$

Eq. 3.95 clearly implies that:

$$||\boldsymbol{S}_{y,d}||_d^2 < ||\boldsymbol{S}_y||^2 \tag{3.96}$$

This inequality concretely represents a loss of sensitivity to y due to double-differencing the observations. If all independent parameter variations were known and held fixed, the estimation of y from double-differenced observations would thus lead to a larger variance $(1/||\boldsymbol{S}_{y,d}||_d^2)$ than its estimation from undifferenced observations $(1/||\boldsymbol{S}_y||^2)$.

If we still assume, for the simplicity of the demonstration, that $\boldsymbol{A}$ is of full rank, then the normal matrix $\boldsymbol{N}_d$ of the double-differenced system can be inverted into $\boldsymbol{Q}_d = \boldsymbol{N}_d^{-1}$. According to Eq. 3.62, the squared norm of the proper signature of y on the double-differenced observations can thus be expressed as:

$$||\boldsymbol{S}_y^p||_d^2 = \frac{(\boldsymbol{\lambda}_1^T\boldsymbol{\lambda}_1)^2}{\boldsymbol{\lambda}_1^T\boldsymbol{Q}_d\boldsymbol{\lambda}_1} \tag{3.97}$$

But, according to Sect. 3.4.1, if a maximal set of independent double-differenced observations is used, then:

$$\boldsymbol{Q}_d = \boldsymbol{N}_d^{-1} = \boldsymbol{N}_r^{-1} = (\boldsymbol{N}_{11} - \boldsymbol{N}_{12}\boldsymbol{N}_{22}^{-1}\boldsymbol{N}_{21})^{-1} \tag{3.98}$$

so that comparing Eq. 3.90 and 3.97 yields:

$$||\boldsymbol{S}_{y,d}^p||_d^2 = ||\boldsymbol{S}_y^p||^2 \tag{3.99}$$

In other words, double-differencing the observations has no impact on the squared norm of the proper signature of y, i.e. on the variance of y when estimated simultaneously with independent parameter variations. This is a particular consequence of the equivalence between the double-differenced and undifferenced approaches proven in Sect. 3.4.1.

Let us finally compare the VIFs obtained for y in the undifferenced case ($V_y = ||\boldsymbol{S}_y||^2/||\boldsymbol{S}_y^p||^2$) and in the double-differenced case ($V_{y,d} = ||\boldsymbol{S}_{y,d}||_d^2/||\boldsymbol{S}_{y,d}^p||_d^2$). According to Eq. 3.96 and Eq. 3.99, the ratio between both VIFs is:

$$\frac{V_{y,d}}{V_y} = \frac{||\boldsymbol{S}_{y,d}||_d^2}{||\boldsymbol{S}_y||^2} < 1 \tag{3.100}$$

The left term in Eq. 3.100 represents a reduction of the collinearity of y with the other parameters in the double-differenced case, which naturally stems from the fact that a double-differenced system has less parameters than an undifferenced system. On the other hand, the right term in Eq. 3.100 represents, as discussed above, a loss of sensitivity to y due to double-differencing the observations. As proven in Sect. 3.4.1, processing double-differenced rather than undifferenced observations has in the end no impact on the values and uncertainties of the estimated parameters.

One can therefore conclude that the formation of double differences has the apparent advantage of reducing collinearity among parameters, but that this advantage is in fact strictly offset by a reduction of the sensitivity of the observations.

Eq. 3.100 can in particular be used to quantify the sensitivity reduction to geocenter coordinates qualitatively observed by Meindl et al. (2013) when forming double-differences. This sensitivity reduction can equivalently be thought in terms of collinearity of the geocenter coordinates with satellite and station clock parameters. As already mentioned, we will prefer undifferenced observations in the following for their simpler geometric interpretation and thus adopt the latter point of view.

Chapter 4

Terrestrial scale and geocenter determination with GNSS: the collinearity perspective

In this chapter, the problems of determining the terrestrial scale and geocenter motion with GNSS are examined from the perspective of collinearity. The weak ability of current GNSS to determine the terrestrial scale is already well understood (Sect. 2.3). On the other hand, the question of why the network shift estimation of geocenter motion with GNSS performs so poorly was remaining unresolved when this thesis started (Sect. 2.4.2). The main purpose of this chapter is actually to answer this question by means of the tools developed in Chapter 3.

As an introduction to this chapter, the singular value decomposition of a GNSS-derived terrestrial frame is first presented in Sect. 4.1. The weak sensitivity of GNSS to terrestrial scale and geocenter is thus evidenced. In Sect. 4.2, the generalized collinearity diagnosis developed in Sect. 3.3 is then applied to the GNSS terrestrial scale determination problem. The next three sections are devoted to understand the poor performance of the GNSS geocenter determination. In Sect. 4.3, the signatures of the geocenter coordinates on station-satellite range observations are first described in detail. In Sect. 4.4 and Sect. 4.5, the generalized collinearity diagnosis developed in Sect. 3.3 is then respectively applied to the geocenter determination with SLR and GNSS.

4.1 Singular value decomposition of a GPS terrestrial frame

In Sect. 3.1.4, Belsley et al. (1980)'s procedure to diagnose and understand potential collinearity issues, based on the singular value decomposition (SVD) of the normal matrix, was described. This procedure is unfortunately hardly applicable to realistic global GNSS analyses, as they involve several ten thousand parameters. SVDs can however be performed for *reduced* normal matrices from global GNSS analyses. As they do not involve *all* estimated parameters, such reduced SVDs cannot help in understanding the causes of potential collinearity issues, but they nevertheless turn out to be instructive. This section therefore presents and discusses the results of the SVD of such a reduced normal matrix.

As a starting point, a normal matrix provided by ESA was used, resulting from the analysis of GPS data collected by 150 stations on July 11, 2008. All parameters except station coordinates were reduced from this normal matrix. Except satellite z-PCOs, all reduced parameters had previously been constrained in the same way as in ESA's operational analyses. In ESA's operational analyses, satellite z-PCOs are usually tightly constrained to conventional IGS values, so that the scales of the obtained terrestrial frames are in turn conventionally determined (see Sect. 2.3). However, satellite z-PCOs were intentionally left free of constraints in this experiment, with the purpose of studying how GPS can intrinsically determine the terrestrial scale.

An SVD of the reduced normal matrix was then performed. The progression of the obtained singular values is shown in Fig. 4.1. Let us recall that eigenvectors associated with large singular values correspond to well determined linear combinations of parameters (here station coordinates), while eigenvectors associated with small singular values correspond to loosely determined linear combinations of parameters. As visible in the right part of Fig. 4.1, the progression of the obtained singular values shows a clear gap between the 7th and 8th singular values. The first three singular values can in fact be considered as numerically zero. The next four singular values lie between 346.6 and 793.3, while the 8th singular value is 11768.6, i.e. almost 15 times larger than the previous one. This gap in the progression of the singular values translates the fact that seven linear combinations of the estimated station coordinates (i.e. the eigenvectors associated with the seven smallest singular values) are especially loosely determined.

In order to give a concrete interpretation of these seven loosely determined linear combinations, each of the eigenvectors associated with the seven smallest eigenvalues was regressed onto normalized rotations, translations and scale offset of the station network. The 6th eigenvector is for instance shown in Fig. 4.2 (in blue), together with the corresponding regression results (in green) and regression residuals (in red). The regression coefficients obtained for each of the seven eigenvectors, as well as the coefficients of determination R^2 of the seven regressions are given in Table 4.1.

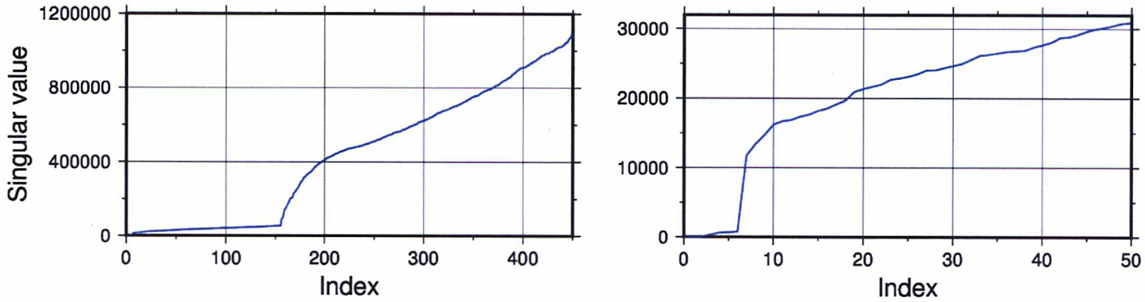

Figure 4.1 *Left*: Singular values of the reduced normal matrix described in the text, sorted in ascending order. *Right*: Zoom on the 50 smallest singular values.

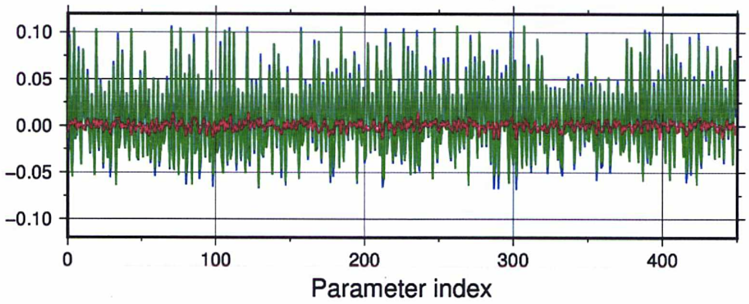

Figure 4.2 *Blue*: 6th eigenvector of the reduced normal matrix described in the text. *Green*: Result of the regression of this eigenvector onto normalized rotations, translations and scale offset of the station network. *Red*: Residuals of the regression.

Table 4.1 Regression coefficients and coefficients of determination R^2 obtained from the regression of the seven first eigenvectors of the reduced normal matrix described in the text onto normalized rotations, translations and scale offset of the station network.

	RX	RY	RZ	TX	TY	TZ	SC	R^2
1st eigenvector	0.99	0.07	0.02	0.00	0.00	0.00	0.00	1.0000
2nd eigenvector	-0.06	1.00	0.03	0.00	0.00	0.00	0.00	1.0000
3rd eigenvector	0.05	-0.07	1.00	0.00	0.00	0.00	0.00	1.0000
4th eigenvector	0.02	-0.03	-0.00	-0.09	0.03	-0.74	-0.50	0.9960
5th eigenvector	0.05	0.13	-0.03	-0.28	0.26	0.68	-0.80	0.9943
6th eigenvector	0.23	0.09	-0.06	-0.43	0.87	-0.20	0.36	0.9871
7th eigenvector	0.16	-0.28	-0.01	0.91	0.50	0.03	-0.20	0.9908

Unsurprisingly, the three first eigenvectors, associated with numerically zero eigenvalues, correspond to pure rotations of the station network. This simply illustrates the fact that GPS observations do not allow to estimate the orientation of a station network simultaneously with (reduced) EOPs (Sect. 1.2.2), so that the reduced normal matrix has three orientation singularities.

More interestingly, the next four eigenvectors quasi-perfectly correspond to linear combinations of rotations, translations and scale offset of the station network. This concretely means the origin and the scale of the station network are more loosely determined by the observations than any other distortion of the station network. One could conclude without much exaggeration that the origin and the scale of the station network correspond to quasi-singularities of GNSS data analyses. Once again, the reason why the terrestrial scale corresponds to a quasi-singularity in GNSS data analyses (in case where satellite z-PCOs are left free) is well understood (Sect. 2.3). On the other hand, the reason why the origin of the station network similarly corresponds to quasi-singularities had so far remained unclear (Sect. 2.4.2). In the next sections, light will be shed on this question by means the generalized collinearity diagnosis developed in Chapter 3.

Note that the existence of four quasi-singularities corresponding to the origin and the scale of the station network are not specific to ESA's normal matrices, but can be evidenced in the SINEX solutions of all IGS ACs that include satellite phase center offsets. Also note that, if the satellite z-PCOs are tightly constrained, then three quasi-singularities corresponding to the origin of the station network remain in the reduced normal matrix.

4.2 Collinearity diagnosis of the GNSS terrestrial scale determination

In this section, the generalized collinearity diagnosis developed in Chapter 3 is applied to the GNSS terrestrial scale determination problem, mainly with an illustrative purpose. The signature of the terrestrial scale on station-satellite ranges is first described in Sect. 4.2.1. The settings we used to simulate a global GPS analysis are then given in Sect. 4.2.2. The application of our collinearity diagnosis to the GNSS terrestrial scale determination problem is detailed in Sect. 4.2.3. Sect. 4.2.4 finally presents the results of some complementary experiments.

4.2.1 Signature of the terrestrial scale on station-satellite ranges

In a global geodetic analysis represented by the linear regression model $\boldsymbol{l} = \boldsymbol{A}\boldsymbol{x} + \boldsymbol{v}$, let us consider the implicit parameter y corresponding to a variation $\delta s = 1$ ppb of the terrestrial scale. The partial derivatives of the explicit model parameters with respect to y are:

$$\boldsymbol{\lambda} = \frac{\partial \boldsymbol{x}}{\partial y} = \delta s \, [\underbrace{\ldots, X_i, Y_i, Z_i, \ldots}_{\text{station coordinates}}, \underbrace{0, 0, 0, 0, \ldots, 0}_{\text{other parameters}}]^T \tag{4.1}$$

y corresponds to a change of the geocentric radius (height) of any station by $\delta r \simeq a_E \delta s \simeq 6.4$ mm, where a_E denotes the mean Earth radius. The impact of such a height change on any station-satellite range observation l made at an elevation angle e is $\delta l = -\delta r \sin e \simeq -a_E \delta s \sin e$. If $\boldsymbol{l}$ consists of station-satellite (pseudo-)range observations, then the elements of the signature $\boldsymbol{S}_y = \boldsymbol{A}\boldsymbol{\lambda}$ of a unit terrestrial scale change on $\boldsymbol{l}$ are nothing but such δl's.

4.2.2 Simulation

Using the options listed in Table 4.2, a series of 207289 station-satellite range observations $\boldsymbol{l}$ was simulated and a design matrix $\boldsymbol{A}$ including the parameters listed in Table 4.3 was set up. The considered satellite empirical accelerations are the five ECOM parameters estimated by most of the IGS Analysis Centers: D_0, Y_0, B_0, B_c and B_s (Sect. 2.1.2). The considered EOPs are the pole coordinates x_p and y_p at noon, their rates $\dot{x}_p$ and $\dot{y}_p$, the $DUT1$ offset at noon and the length of day LOD. Note that simple mapping functions have been used for ZWDs $(1/\sin e)$ and tropospheric gradients (from Chen and Herring, 1997).

Table 4.2 Simulation options

Aspect	Option
Station network	Fictive network of 100 well-distributed stations
Satellite constellation	24 GPS-like satellites equally spread over 6 orbital planes (semi-major axis: $a = 26560$ km; eccentricity: $e = 0$; inclination: $i = 55°$)
Data span	24 h
Observation sampling	5 min
Cut-off angle	10°
Observation weighting	All observations equally weighted with an a priori sigma of 1 cm ($\boldsymbol{P_l} = 10^4 m^{-2} \boldsymbol{I}$)

Table 4.3 List of simulated parameters

Type	Count	Number
Station coordinates	3 per station	300
Zenithal wet delays (ZWDs)	1 per station and hour	2400
Tropospheric gradients	2 per station	200
Station clock offsets	1 per station and epoch	28800
Satellite initial state vectors	6 per satellite	144
Satellite empirical accelerations	5 per satellite	120
Satellite clock offsets	1 per satellite and epoch	6912
Satellite z-PCOs	1 per satellite	24
EOPs	6	6

Except satellite z-PCOs, the list of parameters in Table 4.3 is the minimal common set of parameters freely estimated by a majority of IGS ACs. It could in fact be the list of parameters set up by a slightly sub-standard AC. The collinearity diagnoses exposed in the following will be based on this particular sub-standard list of parameters. But note that the estimation of additional parameters (e.g. satellite velocity pulses, additional empirical accelerations, but also unfixed phase cycle ambiguities) by the real ACs can only increase collinearity issues.

The satellite z-PCOs are usually set up, but tightly constrained by the IGS ACs. In the simulations of this section, they are however freely estimated for the particular purpose of studying their collinearity with the terrestrial scale.

Except the fictive station network and constellation, the options listed in Table 4.2 could also be those used by an IGS AC. The choice of a perfectly distributed network and constellation was made in order to avoid that the obtained results be perturbed by some "network effect". But additional simulations with real network and constellation will also be performed for comparison in Sect. 4.2.4. The influence of the cut-off angle and of the observation weighting will similarly be investigated through additional simulations in Sect. 4.2.4.

Besides the design matrix $\boldsymbol{A}$, a minimal constraint matrix $\boldsymbol{C}$ was also set up, including:

- three no-net-rotation constraints on the station network, in order to compensate the orientation singularities of $\boldsymbol{A}$ (Sect. 1.2.2);
- one constraint on the $DUT1$ offset, in order to compensate its perfect correlation with the satellite orbit parameters (Sect. 1.2.2);
- 288 epoch-wise zero-mean constraints on all (station and satellite) clock offsets,

in order to compensate the time reference singularities of $\boldsymbol{A}$ (Sect. 2.1.2).

4.2.3 Collinearity diagnosis

Given the design matrix $\boldsymbol{A}$, the observation weight matrix $\boldsymbol{P_l}$, the constraint matrix $\boldsymbol{C}$ and the partial derivatives $\boldsymbol{\lambda} = \partial \boldsymbol{x}/\partial y$ described above, Eq. 3.75 was set up and solved. Its solution $\boldsymbol{\mu}_{y,c}$ represents the linear combination of the estimated parameters, independent of any scale change of the station network and allowed by the constraints, whose signature most closely matches $\boldsymbol{S}_y$. This independent variation of the estimated parameters turned out to be mainly composed of:

- a mean variation of the satellite z-PCOs by 137.37 mm, plus small satellite-specific z-PCO variations below 0.19 mm,
- a mean variation of the satellite clock offsets by -105.16 mm (-350.78 ps), plus small satellite- and epoch-specific variations below 0.23 mm (0.75 ps),
- a mean variation of the station clock offsets by 25.24 mm (84.19 ps), plus small station- and epoch-specific variations below 0.37 mm (1.24 ps),
- a mean variation of the ZWDs by 0.39 mm, plus small station- and hour-specific variations below 0.11 mm.

All other estimated parameters (EOPs, station coordinates, tropospheric gradients and satellite orbit parameters) were not found to significantly contribute to $\boldsymbol{\mu}_{y,c}$.

The obtained mean variation of the satellite and station clock offsets has for effect to lengthen the predicted observations by $25.24 + 105.16 = 130.40$ mm. The impact of the obtained mean ZWD variation is to lengthen any observation made at an elevation e by $0.39/\sin e$ mm. Finally, according to Cardellach et al. (2007), the impact of the obtained mean z-PCO variation is to shorten any observation made at an elevation e by $-137.37\sqrt{1 - a_E^2 \cos^2 e/a^2}$ mm. The sum of these three effects is compared in Fig. 4.3 with the signature $\boldsymbol{S}_y$ of a 1 ppb terrestrial scale change.

Fig. 4.3 shows that the signature of a terrestrial scale change can be almost perfectly reproduced by variations of independent parameters (clock offsets, ZWDs and z-PCOs), which indicates a severe collinearity of the terrestrial scale with those parameters. Another view of the same result is given in Fig. 4.4, where the signature $\boldsymbol{S}_y = \boldsymbol{A\lambda}$ of a 1 ppb terrestrial scale change on the observations made by a particular station is compared with the corresponding proper signature $\boldsymbol{S}^p_{y,c} = \boldsymbol{A}(\boldsymbol{\lambda} - \boldsymbol{\mu}_{y,c})$. There is a reduction by almost 2 orders of magnitude from the signature to the proper signature of the terrestrial scale change, which also points to a severe collinearity issue.

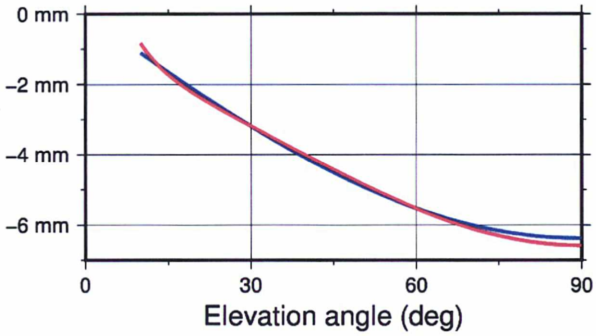

Figure 4.3 *Blue*: Signature S_y of a 1 ppb terrestrial scale change, plotted as a function of the observation elevation angle ($-a_E \delta s \sin e$). ***Red***: Sum of the impacts of the obtained clock, ZWD and z-PCO mean variations ($130.40 + 0.39/\sin e - 137.37\sqrt{1 - a_E^2 \cos^2 e/a^2}$).

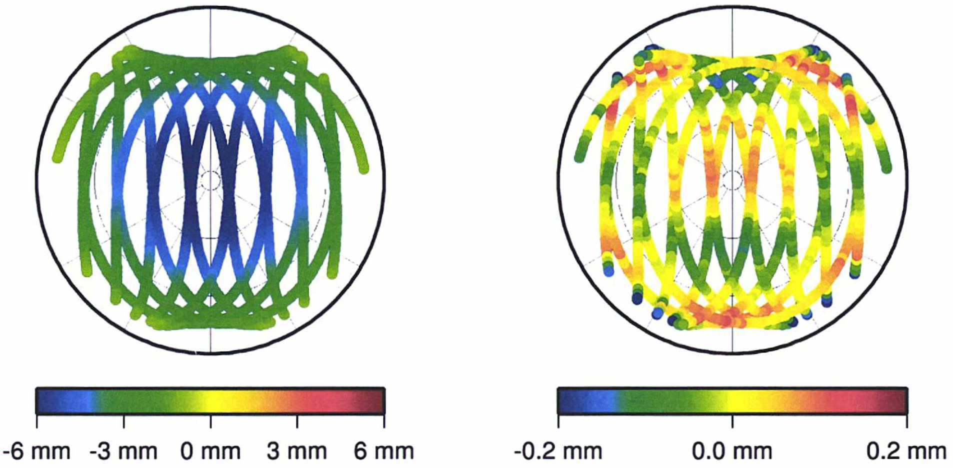

Figure 4.4 *Left*: Signature a 1 ppb terrestrial scale change on simulated observations made by a particular station, represented as a skyplot. Each dot represents an element of $\boldsymbol{S}_y = \boldsymbol{A\lambda}$. ***Right***: Corresponding proper signature. Each dot represents an element of $\boldsymbol{S}^p_{y,c} = \boldsymbol{A}(\boldsymbol{\lambda} - \boldsymbol{\mu}_{y,c})$. Note the different color scales.

The VIF obtained for the terrestrial scale in this simulation (i.e. $||\boldsymbol{S}_y||^2/||\boldsymbol{S}^p_{y,c}||^2$) was in fact 3069.7 ($\sqrt{1 - 1/\text{VIF}} = 99.984\%$), far beyond the commonly seen thresholds of 5 (89.443%) and 10 (94.868%). If the terrestrial scale had been estimated from the simulated observations, independently of any other parameter variation, its formal error (i.e. $1/||\boldsymbol{S}_y||$) would have been 0.0057 ppb (0.036 mm). But the simultaneous estimation of independent parameter variations made the actual formal error of the terrestrial scale (i.e. $1/||\boldsymbol{S}^p_{y,c}||$) as large as 0.3152 ppb (2.010 mm). Note that this formal error should be interpreted with extreme caution as it is based, not only on the settings described in Sect. 4.2.2, but also on the assumption that the observations are statistically independent and have normally distributed errors. It does not account for the temporal correlations that exist between GNSS observations, neither for systematic observation and modelling errors, and should therefore be considered as a very optimistic lower bound of the actual scale uncertainty of a GNSS frame derived with the settings described in Sect. 4.2.2.

In summary, the strong correlation already observed by Springer (2000) and Zhu et al. (2003) between the terrestrial scale on one hand, satellite z-PCOs, ZWDs and clock offsets on the other, was evidenced by means of our generalized collinearity diagnosis. As long as satellite z-PCOs are estimated, this severe collinearity results, to paraphrase Belsley et al. (1980), in a situation in which the systematic influence of the terrestrial scale on GNSS observations is swamped by observation and modelling errors. In other words, this severe collinearity explains why the intrinsic scale of GNSS solutions, such as illustrated in Fig. 2.6, appears unreliable and, consequently, why GNSS have so far not contributed to defining the ITRF scale.

4.2.4 Complementary simulations

Cut-off angle and observation weighting The collinearity diagnosis described in Sect. 4.2.3 was repeated with different cut-off angles and observation weighting functions. The obtained VIFs are given in Table 4.4. The collinearity of the terrestrial scale with the other parameters clearly increases when higher cut-off angles are used. This translates the fact that the more the signature of the terrestrial scale change ($-a_E \delta s \sin e$; blue curve in Fig. 4.3) is truncated, the more accurately it can be matched by linear combinations of the partial derivatives of clock offsets, z-PCOs and ZWDs. Downweighting low elevation observations similarly increases the collinearity of the terrestrial scale with the other parameters.

Table 4.4 VIFs obtained for the terrestrial scale with different cut-off angles and observation weighting functions. The other simulation options were as described in Sect. 4.2.2.

Weighting function	Cut-off angle			
	0°	5°	10°	20°
1	85.7 (99.415%)	704.7 (99.929%)	3069.7 (99.984%)	46512.7 (99.999%)
$\sin e$	316.3 (99.842%)	1519.0 (99.967%)	5200.4 (99.990%)	58905.2 (99.999%)
$\sin^2 e$	1463.2 (99.966%)	3649.1 (99.986%)	9600.7 (99.995%)	79274.9 (99.999%)

Real network and constellation The experiment described in Sect. 4.2.3 was repeated with a real network of 150 stations and a real constellation of 30 GPS satellites (both extracted from a solution provided by ESA for July 11, 2008), all other simulation options being kept unchanged. The obtained VIF was 3115.1 (99.984%), just slightly above the VIF obtained with perfectly distributed station network and constellation.

The mechanism described in Sect. 4.2.3 holds in fact for any network and constellation. As long as satellite z-PCOs are estimated, the distribution of the station network and of the constellation does thus not seem to have a significant impact on the collinearity of the terrestrial scale with the other parameters.

Multi-GNSS The impact of considering multiple GNSS constellations on the GNSS terrestrial scale determination was then investigated through a simulation in which a second constellation of 27 Galileo-like satellites (a = 23222 km, $e = 0$, $i = 56°$) equally spread over 3 orbital planes was included. All of the 100 considered stations were assumed to be multi-GNSS stations, i.e. to provide observations for all GPS and Galileo satellites in view. The list of simulated parameters was the same as in Table 4.3, except that orbit parameters, clock offsets and z-PCOs were estimated for all 51 considered satellites, instead of only the 24 GPS-like satellites.

The VIF obtained for the terrestrial scale was 2520.0 (99.980%), i.e. about 1.2 times smaller than in the GPS-only case. This slight collinearity reduction can be explained as follows. Due to the slightly different radii of the GPS and Galileo orbits, the partial derivatives of the GPS and Galileo satellite z-PCOs ($\sqrt{1 - a_E^2 \cos^2 e / a^2}$) are themselves slightly different. On the other hand, the station ZWDs are jointly determined from GPS and Galileo observations. Reproducing the terrestrial scale signature ($-a_E \delta s \sin e$) with the partial derivatives of clock offsets, ZWDs and satellite z-PCOs thus comes down to finding five coefficients $(\alpha_i)_{1 \leq i \leq 5}$ such that both following functions simultaneously best match $-a_E \delta s \sin e$:

$$\begin{cases} \alpha_1 + \alpha_2 / \sin e + \alpha_3 \sqrt{1 - a_E^2 \cos^2 e / a_{GPS}^2} \\ \alpha_4 + \alpha_2 / \sin e + \alpha_5 \sqrt{1 - a_E^2 \cos^2 e / a_{Galileo}^2} \end{cases} \tag{4.2}$$

Because the coefficient α_2 is common to both functions, this problem is slightly harder to solve than the corresponding single-GNSS problem, which explains the slight collinearity reduction observed for the terrestrial scale.

Fixed satellite z-PCOs Another simulation was finally run, with the same options as described in Sect. 4.2.2, except that the satellite z-PCOs were held fixed. The VIF obtained for the terrestrial scale was in this case 47.3 (98.938%) and its formal error 0.0391 ppb (0.250 mm). When the satellite z-PCOs are not estimated, clock offsets and ZWDs become much less able to reproduce the signature of a terrestrial scale change. The collinearity of the terrestrial scale with the other parameters is thus greatly reduced.

The impact of this collinearity reduction on actual GPS terrestrial scale estimates is illustrated in Fig. 4.5. The time series shown in blue in Fig. 4.5 is the same as in Fig. 2.6 and represents the scale factors estimated between weekly GPS solutions obtained without constraining the satellite z-PCOs and the ITRF2008, i.e. intrinsic

GPS terrestrial scale estimates. The time series shown in black in Fig. 4.5 is also the same as in Fig. 2.6 and represents scale factors estimated between weekly SLR solutions and the ITRF2008. Finally, the time series shown in red in Fig. 4.5 represents scale factors estimated between weekly GPS solutions in which the satellite z-PCOs were fixed to conventional values and the ITRF2008.

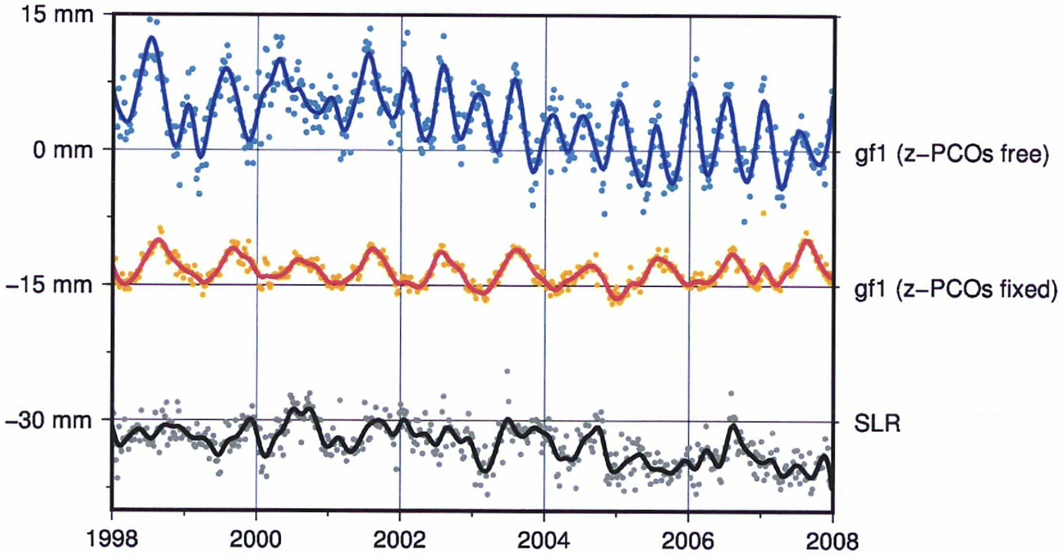

Figure 4.5 *Cyan dots*: Scale factors estimated between the weekly *gf1* solutions processed as described in Sect. 2.3 and the ITRF2008. *Orange dots*: Scale factors estimated between the weekly *gf1* solutions processed as described in Sect. 2.3 - except that satellite z-PCOs were fixed to conventional values - and the ITRF2008, shifted by -15 mm. *Grey dots*: Scale factors estimated between the SLR input solutions to the ITRF2008 and the ITRF2008, shifted by -30 mm. The solid lines were obtained by Vondrak-filtering each of the time series with a cut-off frequency of 3 cpy.

While the GPS terrestrial scale estimates obtained with free satellite z-PCOs show a comparatively large scatter, a strong spurious semi-annual signal, as well as long-term biases and trends, those obtained with fixed satellite z-PCOs show a remarkable stability and are dominated, as expected, by an annual signal presumably due to some network effect (i.e. the aliasing of loading deformation into the estimated scale parameters). From Fig. 4.5, one can conclude that, if the z-PCOs of the GPS satellite were known, then GPS would certainly provide better estimates of the terrestrial scale than SLR and could clearly contribute to defining the ITRF scale. Pre-launch antenna calibrations are unfortunately not available for any of the GPS satellites launched so far, nor for any GLONASS satellite...

4.3 Signatures of geocenter coordinates on station-satellite ranges

As a preliminary step before investigating the collinearity of the geocenter coordinates with the other GNSS parameters, this section describes their signatures on station-satellite range observations. The signature of the Z geocenter coordinate is first studied in Sect. 4.3.1, followed by the signatures of the X and Y geocenter coordinates (Sect. 4.3.2).

4.3.1 Signature of the Z geocenter coordinate

In a global geodetic analysis represented by the linear regression model $\boldsymbol{l} = \boldsymbol{A}\boldsymbol{x} + \boldsymbol{v}$, let us consider the implicit parameter y corresponding to a variation $\delta t = 1$ cm of the Z geocenter coordinate. The partial derivatives of the explicit model parameters with respect to y are:

$$\boldsymbol{\lambda} = \frac{\partial \boldsymbol{x}}{\partial y} = [\underbrace{0, 0, \delta t, \ldots, 0, 0, \delta t}_{\text{station coordinates}}, \underbrace{0, 0, 0, 0, \ldots, 0}_{\text{other parameters}}]^T \tag{4.3}$$

The signature $\boldsymbol{S}_y = \boldsymbol{A}\boldsymbol{\lambda}$ of y was computed for the particular set of observations described in Sect. 4.2.2. It is represented in Fig. 4.6 from the point of view of a particular satellite.

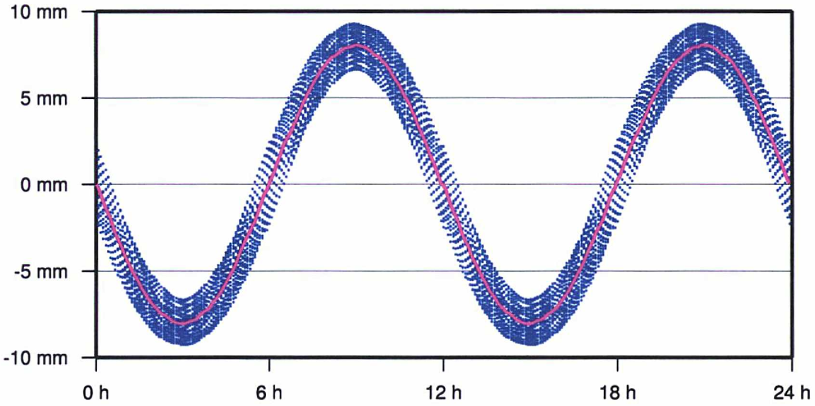

Figure 4.6 Signature of a 1 cm variation of the Z geocenter coordinate on simulated observations made on a particular GPS-like satellite by the whole station network. Each blue dot represents an element of $\boldsymbol{S}_y$. The magenta line corresponds to an epoch mean signature.

The impact of a positive Z geocenter shift is basically to shorten the observations made when the satellite is in the Northern hemisphere and to lengthen the observa-

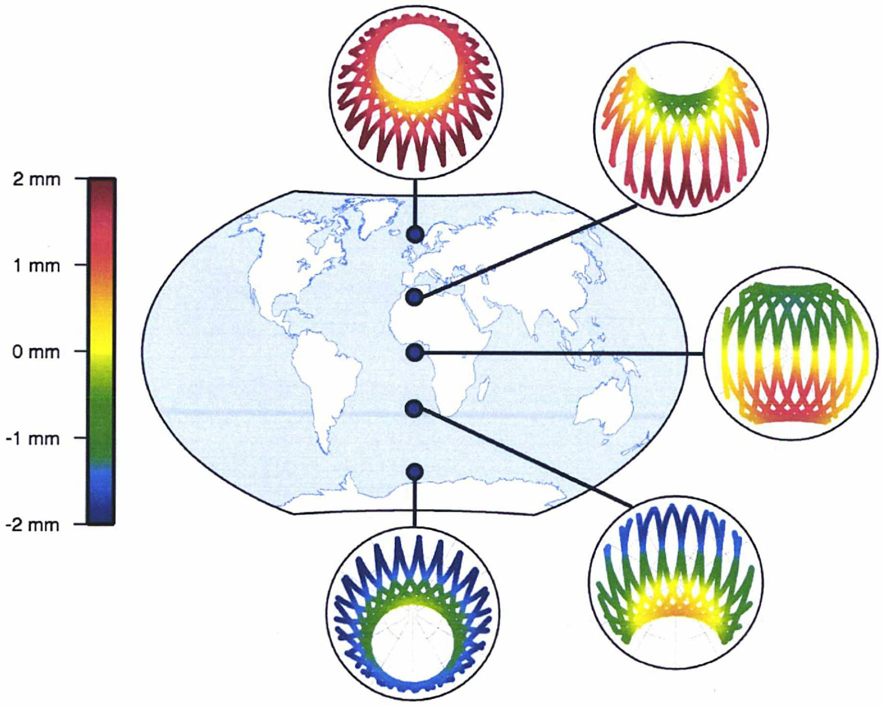

Figure 4.7 Signature of a 1 cm variation of the Z geocenter coordinate on simulated observations made by five particular stations. An epoch mean signature was first removed for each satellite.

tions made when the satellite is in the Southern hemisphere. That is why, at first order, the signature the Z geocenter coordinate follows the opposite of the satellite Z coordinate. For a circular orbit, this results in a sinusoid with an amplitude $\delta t \sin i$, where i denotes the inclination of the satellite orbit.

The "width" of the blue sinusoid in Fig. 4.6 stems from the fact that, at a given epoch, observations are made on the same satellite by several stations under different angles, and are thus slightly differently affected by the geocenter shift. This width mainly depends on the radius of the satellite orbit, but also of the employed cut-off angle.

With slight anticipation over Sect. 4.5, let us mention that the epoch mean signature shown in magenta in Fig. 4.6 can be strictly reproduced by variations of the satellite clock offsets and is therefore unobservable in a standard GNSS analysis. The determination of the Z geocenter coordinate with GNSS can consequently only rely on the difference between its signature and this epoch mean signature (i.e. on the signal around the magenta line in Fig. 4.6). This second order signature is represented in Fig. 4.7 from the points of view of five particular stations.

4.3.2 Signatures of the X and Y geocenter coordinates

Similarly, the impact of a positive X geocenter shift is to shorten the observations made on satellites lying in the positive X hemisphere of the terrestrial frame and to lengthen the observations made on satellites lying in the negative X hemisphere. At first order, the signature of a positive X geocenter shift on the observations of a particular satellite thus follows the opposite of the satellite X coordinate in the terrestrial frame. For a circular orbit, this results in the product of two sinusoids, one at the satellite revolution period, the other at the Earth rotation period. The signature of a 1 cm variation of the X geocenter coordinate on the set of observations described in Sect. 4.2.2 is represented in Fig. 4.8 from the point of view of a particular satellite.

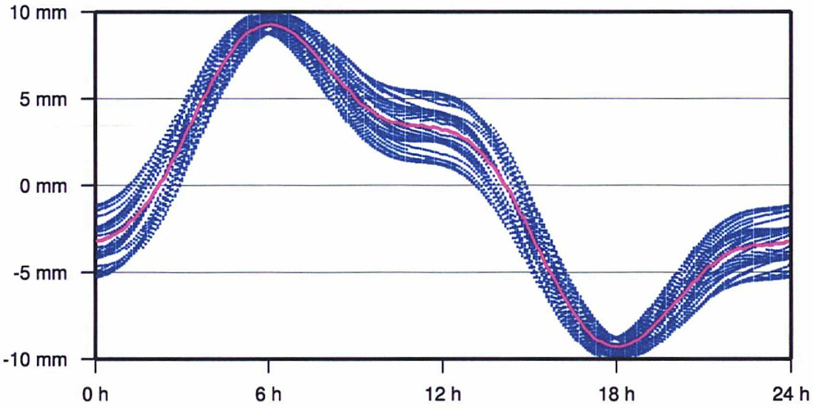

Figure 4.8 Signature of a 1 cm variation of the X geocenter coordinate on simulated observations made on a particular GPS-like satellite by the whole station network. Each blue dot represents an element of S_y. The magenta line corresponds to an epoch mean signature.

Like for the Z geocenter coordinate, the epoch mean signature shown in magenta in Fig. 4.8 can be strictly reproduced by variations of the satellite clock offsets and is therefore unobservable in a standard GNSS analysis. The determination of the X geocenter coordinate with GNSS can consequently only rely on the difference between its signature and this epoch mean signature (i.e. on the signal around the magenta line in Fig. 4.8). This second order signature is represented in Fig. 4.9 from the points of view of seven particular stations.

The signature of the Y geocenter coordinate on station-satellite ranges is similar in all respects to the signature of the X geocenter coordinate.

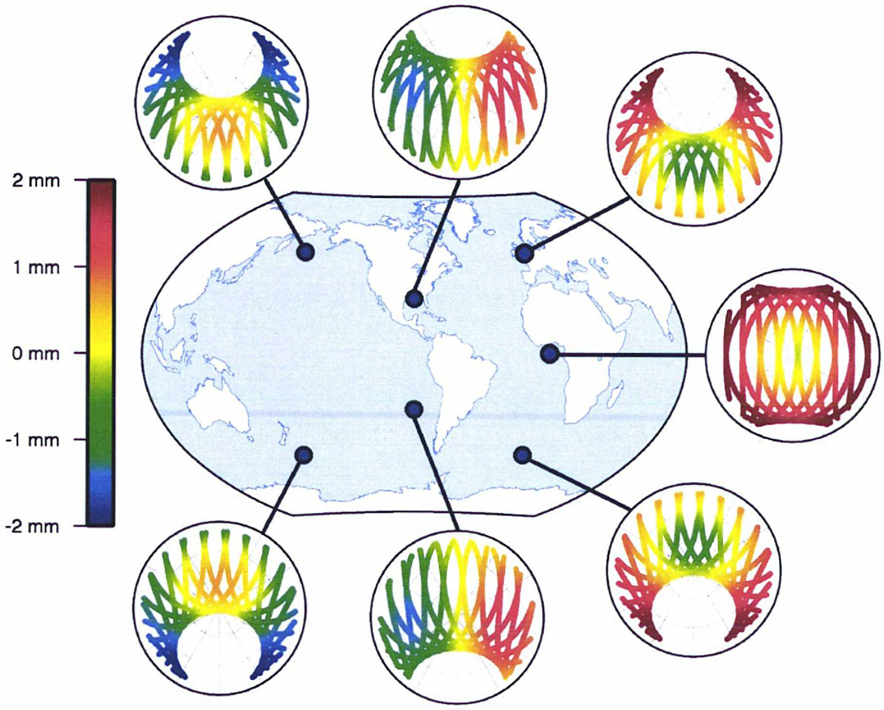

Figure 4.9 Signature of a 1 cm variation of the X geocenter coordinate on simulated observations made by seven particular stations. An epoch mean signature was first removed for each satellite.

4.4 Collinearity diagnosis of the SLR geocenter determination

The generalized collinearity diagnosis developed in Sect. 3.3 is applied in this section to the SLR geocenter determination problem. This interlude will help in understanding why the SLR technique is much more able to retrieve geocenter motion than GNSS. Sect. 4.4.1 first details the settings that were used to simulate a global SLR analysis. The collinearity of the geocenter coordinates with the other parameters set up in global SLR analyses is then studied in Sect. 4.4.2 and Sect. 4.4.3.

4.4.1 Simulation

A series of 9896 station-satellite range observations $\boldsymbol{l}$ was simulated with the options listed in Table 4.2, except that a constellation of two LAGEOS-like satellites (a = 12200 km, $e = 0$, $i_1 = 110°$, $i_2 = 53°$) was used. A design matrix $\boldsymbol{A}$ was set up, including the parameters listed in Table 4.5. The considered empirical accelerations were constant along-track accelerations and once-per-revolution periodic accelerations in the along-track and cross-track directions: S_0, S_c, S_s, W_c and W_s in the notations of Rodriguez-Solano et al. (2012). The main differences with the GNSS case is that neither clock offsets nor tropospheric parameters needed to be set up. Finally, a minimal constraint matrix $\boldsymbol{C}$ was built, including three no-net-rotation constraints on the station network and one constraint on the $DUT1$ offset.

Table 4.5 List of simulated parameters

Type	Count	Number
Station coordinates	3 per station	300
Satellite initial state vectors	6 per satellite	12
Satellite empirical accelerations	5 per satellite	10
EOPs	6	6

The choice of a perfectly distributed network of 100 stations providing observations at a 5 min rate is rather unrealistic for an SLR simulation. But like in the GNSS case, this choice avoids that the obtained results be perturbed by some network effect. This will also facilitate the comparison with the GNSS results obtained in Sect. 4.5.

The choice of a 24 h data span is also questionable, as seven day data batches are usually processed in SLR. 24 h data batches were used for comparison with GNSS. But the results of additional simulations using seven day data batches will also be presented in Sect. 4.4.2 and Sect. 4.4.3.

4.4.2 Collinearity diagnosis of the X and Y geocenter coordinates

The implicit parameter y corresponding to a variation $\delta t = 1$ cm of the X geocenter coordinate, i.e. characterized by

$$\boldsymbol{\lambda} = \frac{\partial \boldsymbol{x}}{\partial y} = [\underbrace{\delta t, 0, 0, \ldots, \delta t, 0, 0}_{\text{station coordinates}}, \underbrace{0, 0, 0, 0, \ldots, 0}_{\text{other parameters}}]^T \tag{4.4}$$

was then considered. Given the design matrix $\boldsymbol{A}$, the observation weight matrix $\boldsymbol{P}_l$, the constraint matrix $\boldsymbol{C}$ described above and $\boldsymbol{\lambda}$, Eq. 3.75 was set up and solved. This led to the linear combination $\boldsymbol{\mu}_{y,c}$ of the estimated parameters, independent of any X translation of the station network and allowed by the constraints, whose signature most closely matches $\boldsymbol{S}_y = \boldsymbol{A\lambda}$. The VIF of the X geocenter coordinate was then computed using Eq. 3.78. The obtained value was 1.82 (67.040%), which clearly indicates the absence of collinearity issues. This result is illustrated in Fig. 4.10, where it is shown that the signature of the X geocenter coordinate on the observations made on a particular LAGEOS-like satellite and the corresponding proper signature have similar magnitudes. In other words, the signature of the X geocenter coordinate could hardly be reproduced by independent parameter variations.

The same experiment was repeated for the Y geocenter coordinate. An even lower VIF of 1.22 (42.799%) was obtained. Additional simulations were carried out using a seven day data batch. The obtained VIFs were respectively 1.04 (20.553%) and 1.04 (19.115%) for the X and Y geocenter coordinates. In conclusion, the determination of the X and Y geocenter coordinates with SLR does manifestly not suffer from collinearity issues.

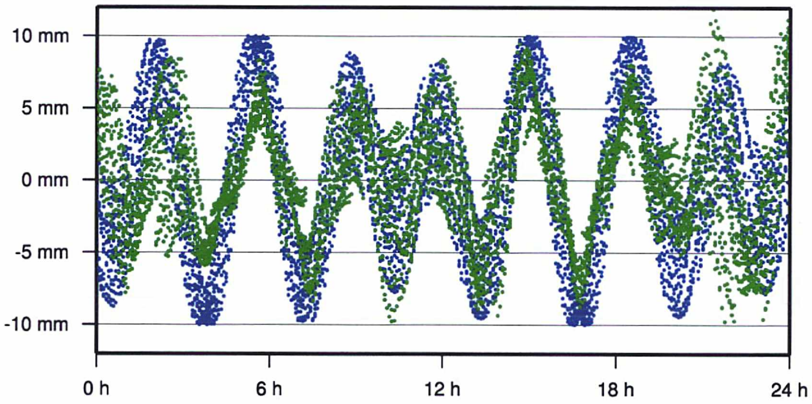

Figure 4.10 *Blue*: Signature of a 1 cm variation of the X geocenter coordinate on simulated observations made on a particular LAGEOS-like satellite. Each blue dot represents an element of $\boldsymbol{S}_y = \boldsymbol{A\lambda}$. *Green*: Corresponding proper signature. Each green dot represents an element of $\boldsymbol{S}^p_{y,c} = \boldsymbol{A}(\boldsymbol{\lambda} - \boldsymbol{\mu}_{y,c})$.

4.4.3 Collinearity diagnosis of the Z geocenter coordinate

For the Z coordinate of the geocenter and a 24 h data batch, a larger VIF of 9.03 (94.298%) was obtained. This result is illustrated in Fig. 4.11: the proper signature of the Z geocenter coordinate is clearly smaller than its signature. The first order sinusoidal signal could in particular be reproduced by independent parameter variations.

Those independent parameter variations, i.e. $\boldsymbol{\mu}_{y,c}$, turned out to be mainly composed of variations of the satellite initial state vectors. We therefore investigated how variations of the satellite initial state vectors could have reproduced the first order sinusoidal signature of the Z geocenter coordinate. It is straightforwardly seen that this first order signature can be reproduced by a periodic variation of the orbit radius with:

- an amplitude of $\delta t \sin i$,

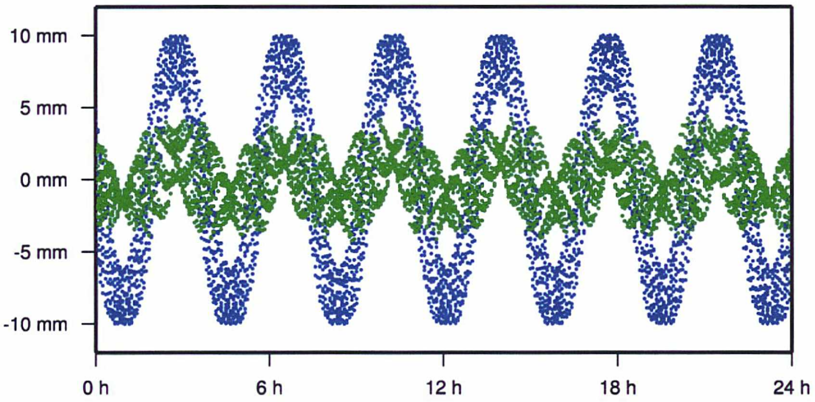

Figure 4.11 *Blue*: Signature of a 1 cm variation of the Z geocenter coordinate on simulated observations made on a particular LAGEOS-like satellite. Each blue dot represents an element of $\boldsymbol{S}_y = \boldsymbol{A}\boldsymbol{\lambda}$. *Green*: Corresponding proper signature. Each green dot represents an element of $\boldsymbol{S}^p_{y,c} = \boldsymbol{A}(\boldsymbol{\lambda} - \boldsymbol{\mu}_{y,c})$.

- its maximum when the satellite reaches the southernmost point of its orbit,
- its minimum when the satellite reaches the northernmost point of its orbit.

Starting from a circular orbit, such a periodic variation of the orbit radius can in fact simply be obtained through a slight "ellipticization". Let us arbitrarily place the perigee of the starting circular orbit at $\omega = \pi/2$ (i.e. at its northernmost point) and consider the perturbed orbit with an eccentricity $\delta e = \delta t \sin i / a$. The radial difference between both orbits is, at first order in δe:

$$\delta r = -a\delta e \cos \nu = -\delta t \sin i \cos \nu \tag{4.5}$$

where ν denotes the satellite true anomaly. It clearly meets the requirements listed above.

In summary, the first order signature of the Z geocenter coordinate can be reproduced, in case of circular orbits, by variations of the satellite osculating elements, or equivalently by variations of their initial state vectors. The parameter variation $\boldsymbol{\mu}_{y,c}$ obtained from our simulation was indeed corresponding to such ellipticizations of both LAGEOS orbits. It is worth mentioning that this problem is not restricted to circular orbits. Appendix D shows that the first order signature of the Z geocenter coordinate can similarly be reproduced by variations of the satellite osculating elements in case of elliptical orbits.

The same experiment was repeated with a seven day data batch. The VIF obtained for the Z geocenter coordinate was 8.60 (94.009%), only slightly lower than for the 24 h case. The mechanism described above, which explains the collinearity of the Z geocenter coordinate with the satellite osculating elements, holds in fact for any data batch and orbital arc lengths. In addition to the uneven distribution of the SLR network, this slight collinearity issue may partly explain why the Z component of SLR-derived geocenter motion is of lower quality than its X and Y components (see, e.g., Fig. 4 in Altamimi et al., 2011).

4.5 Collinearity diagnosis of the GNSS geocenter determination

The collinearity diagnosis developed in Sect. 3.3 is eventually applied in this section to the GNSS geocenter determination problem. The collinearity of the three geocenter coordinates with the other parameters of a standard single-GNSS global analysis is investigated in Sect. 4.5.1 and Sect. 4.5.2. The results of some complementary experiments are then presented in Sect. 4.5.3. Sect. 4.5.4 studies in detail the role played by the satellite empirical accelerations estimated by most IGS ACs in the collinearity of the geocenter coordinates. Since our results concerning this role enter in contradiction with conclusions drawn by Meindl et al. (2013), a critical review of their arguments is given in Sect. 4.5.5. Sect. 4.5.6 finally summarizes the results obtained in this section.

4.5.1 Collinearity diagnosis of the X and Y geocenter coordinates

A series of 207289 station-satellite range observations $\boldsymbol{l}$ was simulated using the options listed in Table 4.2, and a design matrix including the parameters listed in Table 4.3 except satellite z-PCOs was set up. The implicit parameter y corresponding to a 1 cm variation of the X geocenter coordinate was considered and Eq. 3.75 was solved. The obtained VIF was 2355.6 (99.979%). As illustrated from the point of view of a satellite in Fig. 4.12 and from the point of view of a station in Fig. 4.13, the proper signature $\boldsymbol{S}^p_{y,c}$ of the X geocenter coordinate is indeed smaller than its signature $\boldsymbol{S}_y$ by almost two orders of magnitude. If the X geocenter coordinate had been estimated from the simulated observations, independently of any other parameter variation, its formal error (i.e. $1/||\boldsymbol{S}_y||$) would have been 0.038 mm. But the simultaneous estimation of independent parameter variations made its actual formal error (i.e. $1/||\boldsymbol{S}^p_{y,c}||$) as large as 2.129 mm.

We then examined the independent parameter variations $\boldsymbol{\mu}_{y,c}$ by which the signature of the X geocenter coordinate could be almost perfectly reproduced. As anticipated in Sect. 4.3, the epoch mean signature of the X geocenter coordinate on the observations of each satellite (magenta line in Fig. 4.8) was reproduced by

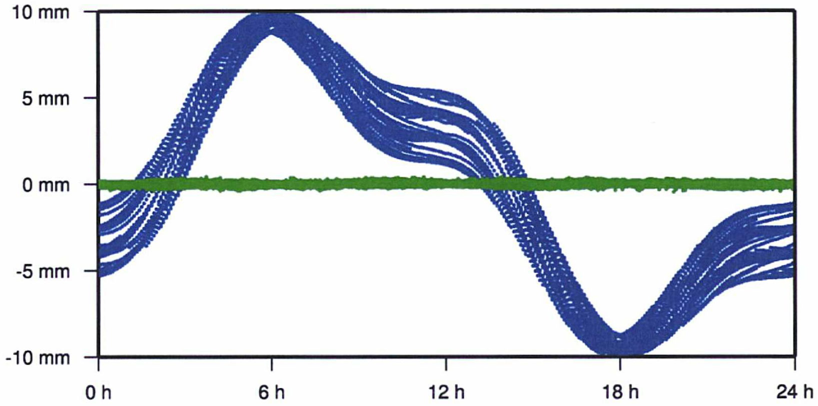

Figure 4.12 *Blue*: Signature of a 1 cm variation of the X geocenter coordinate on simulated observations made on a particular GPS-like satellite. Each blue dot represents an element of $\boldsymbol{S}_y = \boldsymbol{A\lambda}$. *Green*: Corresponding proper signature. Each green dot represents an element of $\boldsymbol{S}^p_{y,c} = \boldsymbol{A}(\boldsymbol{\lambda} - \boldsymbol{\mu}_{y,c})$.

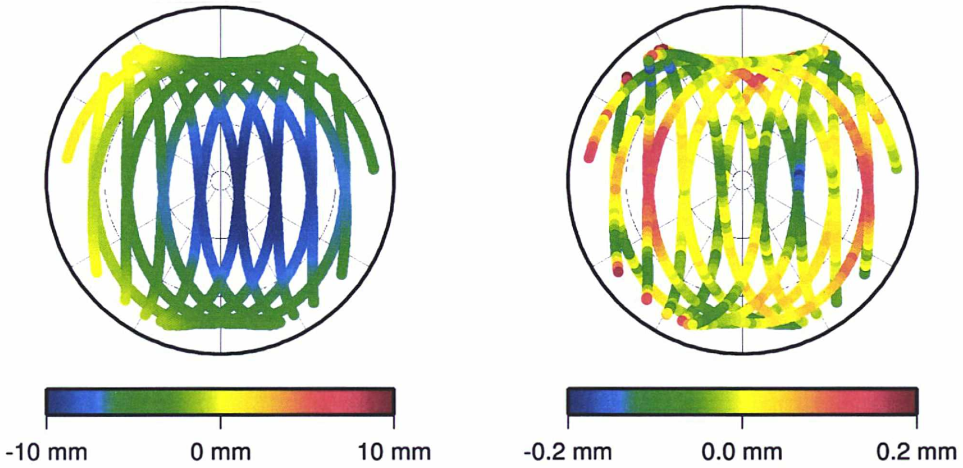

Figure 4.13 *Left*: Signature a 1 cm variation of the X geocenter coordinate on simulated observations made by a particular station, represented as a skyplot. Each dot represents an element of $\boldsymbol{S}_y = \boldsymbol{A\lambda}$. *Right*: Corresponding proper signature. Each dot represents an element of $\boldsymbol{S}^p_{y,c} = \boldsymbol{A}(\boldsymbol{\lambda} - \boldsymbol{\mu}_{y,c})$. Note the different color scales.

variations of the respective satellite clock offsets. And as one could have expected, the second order signatures represented in Fig. 4.9 could be reproduced to a great extent by the station-related parameters (positions, clock offsets, ZWDs and tropospheric gradients). On the other hand, neither the satellite initial state vectors nor the empirical accelerations did substantially contribute to $\boldsymbol{\mu}_{y,c}$. (The corresponding 3-dimensional orbit differences have an overall RMS of 0.3 mm.)

Fig. 4.14 illustrates the part of $\boldsymbol{\mu}_{y,c}$ corresponding to station coordinate variations, i.e. the distortion of the station network which contributed to reproduce the signature of the X geocenter coordinate. The distortion pattern visible in Fig. 4.14 resembles the deformation pattern associated the surface load coefficient $\sigma_{1,1}^{C}$. (Fitting such a load deformation pattern to the network distortion shown in Fig. 4.14 leads to a coefficient of determination of 94.5%.) This resemblance explains the significant correlation observed by G. Blewitt (personal communication, 2012) in the solutions of various IGS ACs between the X component of their origins and the deformation pattern associated with the surface load coefficient $\sigma_{1,1}^{C}$.

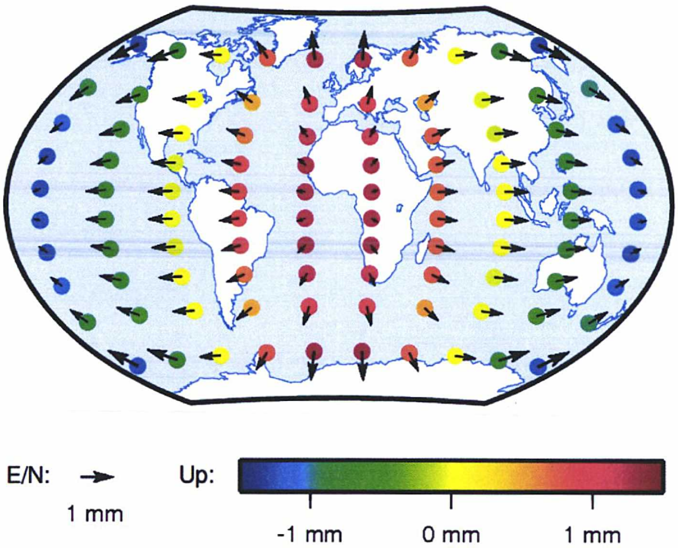

Figure 4.14 Part of $\boldsymbol{\mu}_{y,c}$ corresponding to station coordinate variations. The horizontal variations are represented by the black arrows; the vertical variations by the color dots.

The same experiment was repeated for the Y geocenter coordinate. The obtained VIF was 2353.1 (99.979%). While the formal error of the Y geocenter coordinate would have been 0.038 mm if estimated independently of any other parameter variation, its actual formal error was 1.850 mm. The independent parameter variation $\boldsymbol{\mu}_{y,c}$ whose signature most closely matches that of the Y geocenter coordinate is similar to the one obtained for the X geocenter coordinate. In particular, the obtained network distortion pattern resembles the deformation pattern associated with the surface load coefficient $\sigma_{1,1}^{S}$.

In conclusion, the X and Y coordinates of the geocenter are hardly distinguishable from independent variations of the parameters estimated in a standard GNSS analysis. Their epoch mean signatures can indeed be strictly reproduced by variations of the satellite clock parameters, while their second order signatures can be reproduced to a great extent by all station-related parameters. The determination of the X and

Y geocenter coordinates with GNSS can therefore only rely on tiny proper signatures (of the order of a few tenths of millimeters for 1 cm geocenter shifts). Note that the VIFs and formal errors obtained for the X and Y geocenter coordinates are of the same order as those obtained for the terrestrial scale in Sect. 4.2.

4.5.2 Collinearity diagnosis of the Z geocenter coordinate

Using a fictive network of 100 stations and a fictive constellation of 24 satellites, a VIF of 3157.3 (99.984%) was obtained for the Z geocenter coordinate. While its formal error would have been 0.038 mm if estimated independently of any other parameter variation, its actual formal error was 2.129 mm. The examination of $\boldsymbol{\mu}_{y,c}$ revealed that both the clock offsets (like for the X and Y geocenter coordinates) and the initial state vector of each satellite (like in the SLR case) "combined their strengths" to reproduce the main part of the signature of the Z geocenter coordinate. Like for the X and Y coordinates, the remaining second order signature could be largely absorbed by variations of the station-related parameters, leaving a proper signature of the order of a few tenths of millimeters. The part of $\boldsymbol{\mu}_{y,c}$ corresponding to station coordinate variations resembles the deformation pattern associated the surface load coefficient $\sigma^C_{1,0}$.

As will be shown in Sect. 4.5.4, the larger VIFs of the Z geocenter coordinate compared to those of the X and Y geocenter coordinates stem from a particular role played by the estimated satellite empirical accelerations. The VIF and formal error obtained for the Z geocenter coordinate are of the same order as those obtained in Sect. 4.2 for the terrestrial scale. This concretely means that, in a standard GNSS analysis, the Z geocenter coordinate is as weakly determined as is the terrestrial scale when satellite z-PCOs are estimated.

4.5.3 Complementary simulations

Cut-off angle and observation weighting For completeness, the VIFs of the three geocenter coordinates were computed for different cut-off angles and observation weighting functions. Results are summarized in Table 4.6. Like for the terrestrial scale, using higher cut-off angles or downweighting low-elevation observations has the effect of increasing collinearity issues. With reasonable cut-off angles and observation weighting functions, the VIFs obtained for the geocenter coordinate are roughly of the same order as those obtained for the terrestrial scale in Sect. 4.2.

Table 4.6 VIFs obtained for the three geocenter coordinates with different cut-off angles and observation weighting functions. The other simulation options were as described in Sect. 4.2.2, except that satellite z-PCOs were not estimated.

	Cut-off angle			
	0°	5°	10°	20°
1	X: 450.1 (99.889%)	X: 1066.9 (99.953%)	X: 2355.6 (99.979%)	X: 12409.1 (99.996%)
	Y: 452.3 (99.889%)	Y: 1069.3 (99.953%)	Y: 2353.1 (99.979%)	Y: 12431.8 (99.996%)
	Z: 932.3 (99.946%)	Z: 1673.5 (99.970%)	Z: 3157.3 (99.984%)	Z: 13884.9 (99.996%)
$\sin e$	X: 654.7 (99.924%)	X: 1273.9 (99.961%)	X: 2643.1 (99.981%)	X: 13507.6 (99.996%)
	Y: 654.7 (99.924%)	Y: 1278.5 (99.961%)	Y: 2644.8 (99.981%)	Y: 13520.2 (99.996%)
	Z: 1306.5 (99.962%)	Z: 2022.4 (99.975%)	Z: 3583.8 (99.986%)	Z: 15133.2 (99.997%)
$\sin^2 e$	X: 1126.1 (99.956%)	X: 1944.7 (99.974%)	X: 3582.3 (99.986%)	X: 16115.0 (99.997%)
	Y: 1123.0 (99.955%)	Y: 1951.5 (99.974%)	Y: 3585.3 (99.986%)	Y: 16118.0 (99.997%)
	Z: 2026.1 (99.975%)	Z: 2942.4 (99.983%)	Z: 4815.1 (99.990%)	Z: 18123.9 (99.997%)

Real network and constellation Another round of simulations was run using a real network of 150 stations and a real constellation of 30 GPS satellites (both extracted from a solution provided by ESA for July 11, 2008), all other simulation options being kept unchanged. The VIFs obtained for the X, Y and Z geocenter coordinates were respectively 2233.2 (99.978%), 2431.5 (99.979%) and 3585.2 (99.986%), i.e. at the same level as the VIFs obtained with perfectly distributed network and constellation.

Float ambiguities If not fixed to integer values, but estimated as unknown parameters, phase cycle ambiguities constitute a large set of additional parameters which may further increase the collinearity of the geocenter coordinates in a global GNSS analysis. Ambiguities indeed correspond to constant biases per pass of each satellite over each station, and may therefore clearly contribute to masking the second order geocenter signatures shown in Fig. 4.7 and 4.9.

In order to assess the impact of not fixing phase cycle ambiguities, simulations were run in which one float ambiguity was estimated per pass of each satellite over each station (4129 additional parameters in total). The other simulation options were as described in Sect. 4.2.2, except that satellite z-PCOs were not estimated. The VIFs obtained for the X, Y and Z geocenter coordinates were respectively 4462.1 (99.989%), 4310.6 (99.989%) and 13995.1 (99.996%), i.e. 1.9, 1.8 and 4.4 times larger than in the case where all ambiguities were assumed to be fixed. Exacerbated systematic errors are thus to be expected in GNSS geocenter motion estimates, and especially their Z component, in case where phase cycle ambiguities are not fixed.

An illustration of the impact of ambiguity fixation on the Z component of actual

GPS geocenter motion estimates can in fact be found in Springer (2000). In the early part of his figure 5.7 (b), when GPS ambiguities were not fixed, a strong artificial periodic signal with an amplitude of about 20 cm is visible. This spurious signal then vanished as soon as ambiguity fixation was introduced in the processing.

As evoked in Sect. 2.1.2, fixing phase cycle ambiguities to integer values in a GLONASS analysis is a complicated task. In his GLONASS analyses, Meindl (2011) could for instance fix less than 50% of ambiguities to integer values, against 90% for GPS. In addition to larger modelling deficiencies than in the case of GPS, the fact that a large fraction of GLONASS ambiguities cannot be fixed may thus partly contribute to the poorer quality of GLONASS-derived geocenter motion estimates observed by Meindl (2011).

Multi-GNSS The impact of considering multiple GNSS constellations was finally investigated through simulations in which 27 Galileo-like satellites were considered in addition to the previous 24 GPS-like satellites. The VIFs obtained for the X, Y and Z geocenter coordinates were respectively 1386.5 (99.964%), 1403.8 (99.964%) and 2460.5 (99.980%), i.e. 1.7, 1.7 and 1.3 times smaller than in the GPS-only case. Similarly to the mechanism described for the terrestrial scale in Sect. 4.2.4, this slight collinearity reduction is due to the combination of both following facts.

- Due to the slightly different radii of the GPS and Galileo orbits, the second order signatures of the geocenter coordinates (i.e. parts of their signatures that are distinguishable from the satellite clock offsets) on GPS and Galileo observations are slightly different.
- All station-related parameters are common to both GNSS and are therefore less able to reproduce the second order signatures of geocenter coordinates in the multi-GNSS case than in the single-GNSS case.

4.5.4 Role of the empirical accelerations

Meindl et al. (2013), on the basis of orbital perturbation considerations, concluded that the estimation of constant empirical accelerations in the Sun-satellite directions (i.e. the D_0 parameter of the ECOM model) was an important limiting factor in the determination of the Z geocenter coordinate with GNSS. To investigate the role effectively played by the ECOM parameters in the collinearity of the Z geocenter coordinate, a series of simulations was run in which different subsets of ECOM parameters were estimated. The results are summarized in Table 4.7.

The purpose here was to assess the individual and combined contributions of the five usually estimated ECOM parameters to the collinearity of the Z geocenter coor-

Table 4.7 VIFs obtained for the Z geocenter coordinate when estimating different subsets of ECOM parameters. The other simulation options were as described in Sect. 4.2.2, except that satellite z-PCOs were not estimated.

ECOM parameters	VIF	$\sqrt{1-1/\text{VIF}}$
None	2556.6	99.980%
D_0	2558.2	99.980%
Y_0	2556.8	99.980%
B_0	2560.7	99.980%
B_c, B_s	2609.9	99.981%
D_0, B_c, B_s	3147.8	99.984%
D_0, Y_0, B_0, B_c, B_s	3157.3	99.984%

dinate. It is clear that, when individually estimated, each of these five parameters, in particular D_0, has little impact. When the five parameters are simultaneously estimated, the VIF of the Z geocenter coordinate increases from about 2550 (99.980%) to 3157.3 (99.984%). This increase by a factor of about 1.2 can in fact be quasi-fully explained by the simultaneous estimation of three of the five parameters: D_0, B_c and B_s. It is nevertheless rather minor.

The results in Table 4.7 were however obtained with a particular configuration of the orbital planes with respect to the Sun. The β_s angles (elevations of the Sun above the orbital planes) were in this case ranging from $-30°$ to $68°$. Another series of simulations was thus run using a configuration considered by Meindl et al. (2013) as a worst case scenario. A constellation of 24 GLONASS-like satellites ($a = 25520$ km, $e = 0$, $i = 65°$) equally spread over three orbital planes was used. The β_s angles were respectively $87°$, $-15°$ and $-15°$ for the three orbital planes. Results are summarized in Table 4.8. The VIF of the Z geocenter coordinate is this time increased by a factor of about 1.9 when estimating the five ECOM parameters. Like previously, this collinearity increase can be explained by the simultaneous estimation of only three ECOM parameters: D_0, B_c and B_s.

These experiments demonstrate that:

- the Z geocenter coordinate is highly collinear with the other parameters of a global GNSS analysis, even when no ECOM parameter is estimated;
- estimating the five usual ECOM parameters further increases this collinearity, but to a very moderate extent;
- this further increase is attributable to the simultaneous estimation of D_0, B_c and B_s, while the estimation of D_0 alone causes a marginal increase of collinearity.

From these observations, we think it justified to conclude, in opposition with Meindl

Table 4.8 VIFs obtained for the Z geocenter coordinate when estimating different subsets of ECOM parameters and using the GLONASS-like constellation described in the text. The other simulation options were as described in Sect. 4.2.2, except that satellite z-PCOs were not estimated.

ECOM parameters	VIF	$\sqrt{1-1/\text{VIF}}$
None	2577.1	99.981%
D_0	2813.5	99.982%
Y_0	2577.9	99.981%
B_0	2586.9	99.981%
B_c, B_s	2616.6	99.981%
D_0, B_c, B_s	4776.6	99.989%
D_0, Y_0, B_0, B_c, B_s	4802.7	99.990%

et al. (2013), that the estimation of the ECOM parameters, and especially of D_0 alone, does not play a predominant role in the insensitivity of GNSS to the Z component of geocenter motion.

A last experiment was carried out to consolidate this view. The parameters estimated in GNSS analyses, but not in SLR analyses were grouped into three categories:

- the five usually estimated ECOM parameters ("ECOM" in Table 4.9),
- tropospheric parameters (ZWDs and tropospheric gradients; "tropo" in Table 4.9),
- station and satellite clock offsets ("clocks" in Table 4.9).

And different simulations were run to assess the individual and combined contributions of these parameter categories to the collinearity of the three geocenter coordinates. The obtained VIFs are summarized in Table 4.9.

The GNSS parameter category with the largest individual impact is the clock offset category: a hypothetical GNSS that could dispense with the estimation of clock offsets would most certainly allow an accurate determination of geocenter motion. The combination of clock offsets with tropospheric parameters has a devastating effect. It concretely makes the second order signatures shown in Fig. 4.7 and Fig. 4.9 quasi-unobservable. In case of the Z geocenter coordinate, estimating the five ECOM parameters has an additional, but relatively small impact. That is why we assert that the inability of GNSS, as opposed to SLR, to properly sense the Z component of geocenter motion is mostly due to the simultaneous estimation of clock offsets and tropospheric parameters. For the X and Y components of geocenter motion, this inability is quasi-entirely due to the simultaneous estimation of clock offsets and tropospheric parameters.

Table 4.9 VIFs obtained for the three geocenter coordinates when estimating different subsets of GNSS-specific parameters. The other simulation options were as described in Sect. 4.2.2, except that satellite z-PCOs were not estimated.

GNSS parameters	Axis	VIF	$\sqrt{1-1/\text{VIF}}$
None	X	1.0	16.263%
	Y	1.0	16.523%
	Z	33.4	98.489%
ECOM	X	4.0	86.529%
	Y	4.0	86.504%
	Z	44.5	98.869%
tropo	X	2.4	76.094%
	Y	2.4	76.085%
	Z	36.4	98.617%
clocks	X	675.6	99.926%
	Y	679.8	99.926%
	Z	770.2	99.935%
ECOM, tropo	X	6.6	92.051%
	Y	6.6	92.067%
	Z	55.8	99.101%
ECOM, clocks	X	718.1	99.930%
	Y	719.3	99.930%
	Z	1304.9	99.962%
tropo, clocks	X	2296.9	99.978%
	Y	2293.5	99.978%
	Z	2556.6	99.980%
ECOM, tropo, clocks	X	2355.6	99.979%
	Y	2353.1	99.979%
	Z	3157.3	99.984%

4.5.5 Comments to Meindl et al. (2013)

The conclusion of Sect. 4.5.4 contradicts the one drawn by Meindl et al. (2013), according to whom the inability of GNSS to properly sense the Z component of geocenter motion stems from the correlation between the Z geocenter coordinate and the ECOM D_0 parameters. This subsection therefore gives a critical review of Meindl et al. (2013)'s arguments.

The reasoning of Meindl et al. (2013) relies on two main arguments. The first one can be summarized as follows. According to the orbital perturbation theory, a constant cross-track acceleration W_0 has the effect of translating the satellite orbit orthogonally to the orbital plane. Consequently,

- if all satellites of a GNSS were lying on a single orbital plane,
- if the Sun was standing perpendicular to this orbital plane ($\beta_s = 90°$ so that $D_0 \equiv W_0$),
- and if the Earth was not rotating,

then a new singularity would appear in the analysis of such GNSS data. Under these conditions, a mean variation of the D_0 parameters (causing a common translation of all satellite orbits) could indeed be strictly compensated by a translation of the station network. This is undeniable. However:

- The Earth rotates, so that a translation of the orbital plane is actually not compensable by a translation of the station network. Meindl et al. (2013) nevertheless note that, even if the Earth rotates, a strong correlation remains between the mean of the D_0 parameters and the Z geocenter coordinate in the case of a single orbital plane (-91.2% for $\beta_s = 90°$, a value which actually also depends on the inclination of the orbital plane).
- This correlation decreases very rapidly with β_s (only -54.4% for $\beta_s = 80°$). It therefore seems that, even with two orbital planes and $\beta_s = 90°$ for one of both, the overall correlation between the D_0 parameters and the geocenter Z coordinate should not be particularly problematic.

The second argument of Meindl et al. (2013) relies on the comparison of two series of GNSS solutions obtained with and without constraining the Z geocenter coordinate, i.e. with and without introducing artificial δz geocenter shifts. They observed that the variations of the estimated D_0 parameters in response to the introduction of δz geocenter shifts were approximately obeying:

$$\delta z = -\frac{\sum\limits_{k=1}^{P} \delta D_0^k \sin \beta_s^k}{n^2 \cos i} \tag{4.6}$$

where

- P denotes the number of orbital planes,
- δD_0^k is the mean variation of the D_0 parameters observed for the satellites of plane k,
- β_s^k is the elevation of the Sun above the orbital plane k,
- n denotes the mean motion of the satellites.

Meindl et al. (2013) justify Eq. 4.6 by the fact that a variation δD_0 has the effect, among others, of translating the orbit of a satellite by $\delta D_0 \sin \beta_s / (n^2 \cos i)$ along the

Z axis. From Eq. 4.6, they conclude that the geocenter differences δz between their two solution series are "explained by the differences of the $[D_0]$ parameters in both solution series".

We were however unable to reproduce Meindl et al. (2013)'s result. We introduced for instance artificial 1 cm Z geocenter shifts into two simulated solutions that were only differing by the employed cut-off angles (0° in the first, 10° in the second). The obtained right-hand sides of Eq. 4.6 were respectively 2.3 mm and 5.3 mm, both far from 1 cm, and also very different from each other. Repeating the same experiment with one year of real daily solutions provided by ESA led to right-hand sides that were rather constant (mean: 4.6 mm; standard deviation: 1.0 mm), but again far from 1 cm. We therefore think that Eq. 4.6 does probably only hold for the particular analysis settings used by Meindl et al. (2013).

In fact, the point where the reasoning of Meindl et al. (2013) fails is that their δz geocenter differences are not *explained* by the δD_0 variations. On the contrary, these δD_0 variations are only one particular consequence of the introduction of the δz geocenter shifts (i.e. of the application or not of no-net-Z-translation constraints). Introducing an artificial Z geocenter shift into a solution admittedly induces variations of the D_0 parameters. But all other parameter categories are affected as well. With given analysis settings, formulas like Eq. 4.6 could in fact be derived for any parameter category like, e.g., tropospheric gradients. But each would only give a partial view of the problem.

4.5.6 Summary

The generalized collinearity diagnosis developed in Sect. 3.3 was applied in Sect. 4.5.1 and 4.5.2 to the problem of determining geocenter coordinates in a standard single-GNSS global analysis. The fact, already evidenced in Sect. 4.1, that the three geocenter coordinates correspond to quasi-singularities in such a global GNSS analysis was confirmed their huge VIFs. With reasonable analysis settings, the VIFs and formal errors obtained for the three geocenter coordinates are roughly of the same order as those obtained for the terrestrial scale in Sect. 4.2.3. One can therefore consider that, in a standard single-GNSS analysis, the three geocenter coordinates are as weakly determined as is the terrestrial scale when satellite z-PCOs are estimated.

The various tests performed in Sect. 4.5.4 proved that, among the parameters of a GNSS analysis, two specific categories quasi-fully explain the insensitivity of GNSS to the X and Y geocenter coordinates: epoch-wise clock offsets and tropospheric parameters. These two parameter categories also explain most of the insensitivity of GNSS to the Z geocenter coordinate, which is in addition slightly amplified by the simultaneous estimation of three ECOM parameters: D_0, B_c and B_s. We therefore conclude that the inability of GNSS, as opposed to SLR, to properly sense geocenter motion, including its Z component, is mainly due to the simultaneous estimation of clock offsets and tropospheric parameters.

This collinearity diagnosis explains *why* the translation time series derived from IGS AC solutions are far from reflecting a realistic geocenter motion (Sect. 2.4.1). To paraphrase Belsley et al. (1980), the extreme collinearity of the three geocenter coordinates with the other parameters of a GNSS analysis indeed results in a situation in which the systematic influence of geocenter motion on GNSS observations is swamped by observation and modelling errors. A different problem, not answered by this collinearity diagnosis, is to understand *what* the IGS AC translation time series do actually reflect, i.e. what are the modelling deficiencies which contaminate GNSS geocenter motion estimates.

Chapter 5

Perspectives

In Chapter 4, the weak sensitivity of current GNSS to the terrestrial scale and to geocenter motion was explained by means of the generalized collinearity diagnosis developed in Chapter 3. In both cases, this weak sensitivity results from situations of extreme collinearity with the other parameters set up in global GNSS analyses. The mechanisms at the origin of this extreme collinearity were also detailed. In other words, the question of why current GNSS are quasi-insensitive to the terrestrial scale and to geocenter motion has been answered. The consequence of this quasi-insensitivity is that intrinsic GNSS estimates of the terrestrial scale (Sect. 2.3) and of geocenter motion (Sect. 2.4.1) are currently extremely sensitive to modelling errors and therefore not reliable enough to allow a contribution of GNSS to the definition of the ITRF scale and origin. In this last chapter, several prospects are investigated, that could improve the determination of the terrestrial scale (Sect. 5.1) and of geocenter motion (Sect. 5.2) with GNSS, and therefore lead to future potential contributions of GNSS to the definition of the ITRF scale and origin.

5.1 Prospects for a contribution of GNSS to the ITRF scale

When the satellite z-PCOs are estimated in a global GNSS analysis, a quasi-singularity arises due to a quasi-perfect correlation between terrestrial scale, ZWDs, station and satellite clock offsets and satellite z-PCOs (Sect. 4.2.3). On the other hand, when the satellite z-PCOs are fixed, this quasi-singularity vanishes and the terrestrial scale becomes in particular well determined (Sect. 4.2.4). It was therefore concluded in Sect. 4.2 that, if the z-PCOs of the GNSS satellites were known (independently of any conventional TRF scale), then GNSS could most likely contribute to defining the ITRF scale. In Sect. 5.1.1 and Sect. 5.1.2, two paths are thus considered that could lead to such an absolute calibration of the GNSS satellite z-PCOs, hence to a future contribution of GNSS to the ITRF scale definition.

But, before such absolute z-PCO calibrations become available, the long-term stability of the GNSS satellite z-PCOs might already be used for a GNSS contribution to the ITRF scale *rate*. This is the topic of Sect. 5.1.3.

5.1.1 z-PCO calibrations relative to a reference GNSS satellite

Pre-launch antenna calibrations are unfortunately not available for any GNSS satellite launched so far. However, Springer (2000) noted that, if the z-PCO of one single GNSS satellite was known, then the z-PCOs of the other GNSS satellites may be determined relative to this reference satellite:

> We conclude that it is not feasible to accurately solve for the satellite antenna offsets in an absolute sense due to the correlation with the terrestrial scale, the tropospheric delays, the receiver antenna phase center offsets, and elevation-dependent variations. However, we are able to solve for these offsets in a relative way, e.g., by adopting a specific value for a single satellite. The offsets of the other satellites may then be determined relative to this adopted value.

Via such relative calibrations, the availability of a pre-launch calibration for a *single* GNSS satellite might consequently be enough to allow a GNSS contribution to the ITRF scale.

The goal of this subsection is to demonstrate the feasibility of the relative z-PCO calibrations suggested by Springer (2000). From the reprocessed weekly solutions of the GFZ AC (*gf1*), two different sets of GPS satellite z-PCOs are therefore derived and compared. The first set is obtained in a similar way as the conventional IGS z-PCO values, i.e., relative to the ITRF2008 scale. On the other hand, the second set is derived under the assumption that one particular satellite has a known, i.e. pre-launch calibrated, z-PCO.

z-PCO estimation relative to the ITRF2008 scale From the *gf1* SINEX solutions of the period 1998.0-2008.0, a first set of GPS satellite z-PCOs was derived as follows. The original, non-constrained weekly normal equations were first recovered using Eq. 1.9. The weekly normal equations were then inverted under no-net-rotation, no-net-scale and no-net-translation constraints with respect to the ITRF2008. No-net-scale constraints were applied in order to remove the quasi-perfect correlation that would otherwise exist between the terrestrial scale and the mean of the satellite z-PCOs (see Sect. 2.3 and 4.2). This allows to obtain robust estimates of the satellite z-PCOs, which however conventionally rely on the ITRF2008 scale. The choice to additionally apply non-mandatory no-net-translation constraints was made in accordance with Collilieux and Schmid (2012), who observed that they had a positive impact on the determination of the satellite z-PCOs.

From the obtained solutions, weekly estimates of the satellite z-PCOs were extracted, as well as their covariance matrices. Those weekly estimates were finally rigorously stacked into long-term z-PCO estimates. Except for the last step, this procedure is the same that was used to generate the conventional z-PCO values, consistent with the ITRF2008 scale, currently in use within the IGS.

For the record, the differences between the obtained z-PCO estimates and their conventional IGS values (mean: 1.7 cm; standard deviation: 1.6 cm) are shown in Fig. 5.1. Those differences are mostly due to the facts that:

- the conventional IGS values were obtained by averaging weekly z-PCO estimates derived from the solutions of five different ACs, whereas only the *gf1* solutions were used here;
- the conventional IGS values were obtained using a longer data span (1994.0-2010.0).

They are however irrelevant to the present discussion.

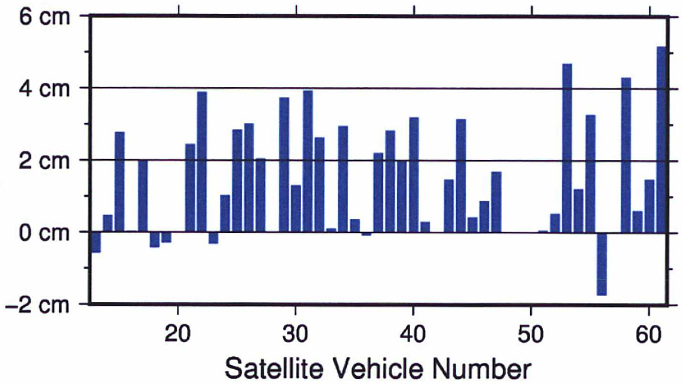

Figure 5.1 Differences between the long-term z-PCO estimates derived from the *gf1* solutions relative to the ITRF2008 scale and the conventional IGS z-PCO values currently in use.

z-PCO estimation relative to a reference satellite From the same set of weekly *gf1* SINEX solutions, a second set of satellite z-PCOs was derived as follows. The weekly unconstrained normal equations were this time inverted under no-net-rotation and no-net-translation constraints only. From the obtained solutions, weekly estimates of the satellite z-PCOs were extracted, as well as their covariance matrices. Because no-net-scale constraints were *not* applied, these weekly z-PCO estimates were independent of any conventional TRF scale. However, due to their quasi-perfect correlation with the terrestrial scale, the means of these weekly z-PCO estimates were unreliably determined.

Like previously, the obtained weekly z-PCO estimates were then stacked into long-term z-PCO estimates. But during this stacking, the z-PCO of one particular reference satellite was fixed (Satellite Vehicle Number G061), so as to simulate relative calibrations of the other satellites to a hypothetical ground-calibrated satellite. Moreover, weekly mean z-PCO bias parameters were additionally estimated in order to discard information about the unreliably determined weekly z-PCO means.

Comparison Fig. 5.2 shows the differences between the long-term z-PCO estimates thus obtained relative to G061 and those previously obtained relative to the ITRF2008 scale. These differences have a mean of 0.3 mm, which, according to Zhu et al. (2003), corresponds to a negligible terrestrial scale bias of about 0.002 ppb (0.015 mm). They have a standard deviation of 1.2 mm and all lie between ±4 mm around their mean. According to Cardellach et al. (2007), this millimetric scatter is also of negligible consequence for the terrestrial frame. By assuming that the z-PCO of a particular satellite was known, we were thus able to calibrate the other satellites, independently of any conventional TRF scale, with negligible differences compared with the calibrations obtained relative to the ITRF2008 scale.

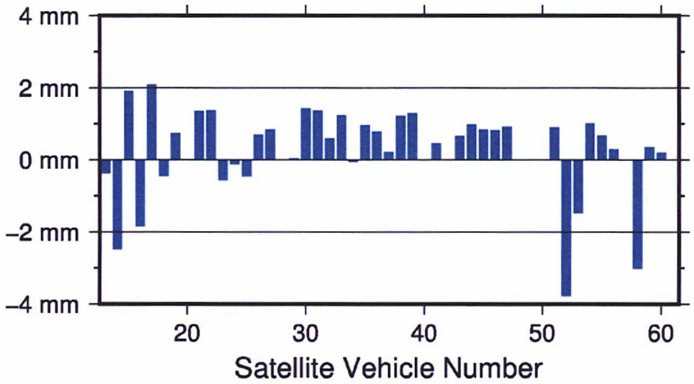

Figure 5.2 Differences between the long-term z-PCO estimates derived from the *gf1* solutions (a) relative to G061 and (b) relative to the ITRF2008 scale

Fig. 5.3 shows the same z-PCO differences as Fig. 5.2, plotted in function of the number of weekly z-PCO estimates available for each satellite. It illustrates the fact that the scatter of these differences is imputable for a large part to satellites with less than 3 years of data. The z-PCO differences of satellites with more than 3 years of data indeed have a standard deviation of only 0.6 mm and all lie within ±1.5 mm around their mean.

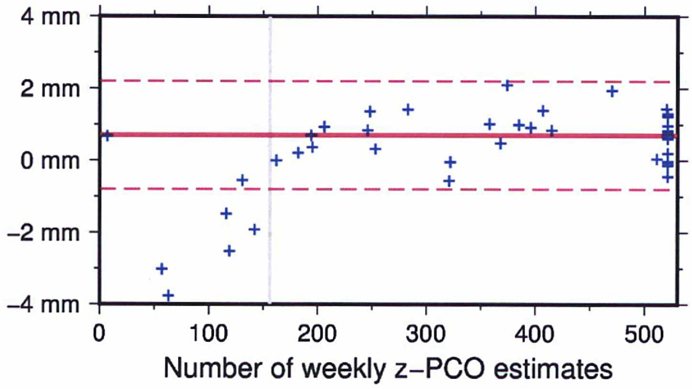

Figure 5.3 Differences between the long-term z-PCO estimates derived from the *gf1* solutions (a) relative to G061 and (b) relative to the ITRF2008 scale, plotted in function of the number of weekly z-PCO estimates available for each satellite. Each blue cross corresponds to one satellite. The vertical grey line marks the limit of 156 weekly estimates (i.e. 3 years). The solid red line indicates the mean of the z-PCO differences of satellites with more than 156 weekly estimates. The dashed red lines are 1.5 mm above and below this mean.

Choice of the reference satellite The differences shown in Fig. 5.2 and Fig. 5.3 were however obtained after a particular reference satellite (G061) was arbitrarily chosen. To assess the impact of choosing different reference satellites, the previous steps were repeated with each available satellite successively taken as reference satellite. The mean and standard deviation of the differences between the long-term z-PCO estimates obtained relative to each satellite and those obtained relative to the ITRF2008 scale were thus computed. It turned out that the scatter of those z-PCO differences was independent of the chosen reference satellite. (This scatter seems in fact mostly linked to the overall number of weekly z-PCO estimates available per satellite.)

On the other hand, as illustrated in Fig. 5.4, the mean of those z-PCO differences is dependent on the chosen reference satellite, and seems more specifically linked to the data span available for the chosen reference satellite. In particular, if any satellite with more than 3 years of data is taken as reference satellite, then the obtained mean z-PCO difference systematically lies within ±2 mm, corresponding to a terrestrial scale bias within ±0.1 mm.

Summary With the experiments carried out in this section, it was demonstrated that calibrations of the GPS satellite z-PCOs relative to a reference satellite could

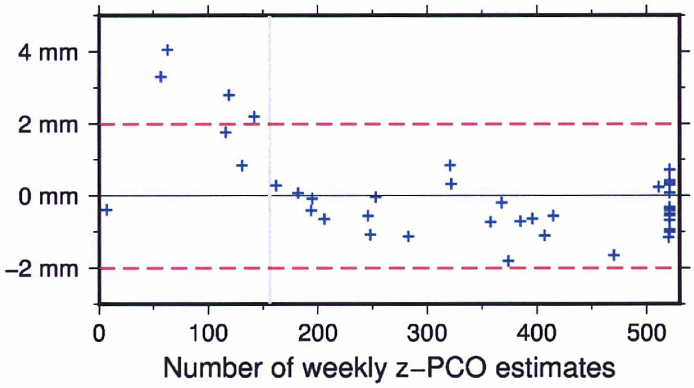

Figure 5.4 Means of the differences between the long-term z-PCO estimates obtained relative to each satellite and those obtained relative to the ITRF2008 scale, plotted in function of the number of weekly z-PCO estimates available for the chosen reference satellite. Each blue cross corresponds to the choice of a particular reference satellite. The vertical grey line marks the limit of 156 weekly estimates (i.e. 3 years). The dashed red lines mark the limits of ±2 mm.

reproduce calibrations relative to a given TRF scale at the level of a few mm. Provided that at least 3 years of data are available for the chosen reference satellite, the mean bias observed between both sets of calibrations was below 2 mm, corresponding to a terrestrial scale bias below 0.1 mm.

In the hypothetical scenario where a pre-launch calibration becomes available for some future GPS satellite, the relative calibration method described above could be used to obtain absolute (i.e. independent of any conventional TRF scale) z-PCO calibrations for all GPS satellites. Subsequently fixing those absolute satellite z-PCOs in GPS data analyses would allow an absolute determination of the terrestrial scale by GPS, with a better precision than SLR (see Sect. 4.2). The accuracy of this hypothetical absolute determination of the terrestrial scale by GPS is however hard to assess, as it depends on multiple factors. The maximum expected bias of 0.1 mm after 3 years of flight of the reference satellite is only one particular aspect of this problem. It does not take into account possible systematic errors that would have cancelled in the z-PCO differences studied above, nor a possible error in the pre-launch calibration of the reference satellite. In this scenario, GPS would nevertheless become at least candidate to the definition of the ITRF scale, and may help in resolving the discrepancy between the SLR and VLBI estimates of the terrestrial scale (Altamimi et al., 2011).

In the tests carried out and the conclusions drawn in this section, a single GNSS, namely GPS, was considered. The question was not addressed whether cross-GNSS relative z-PCO calibrations would be feasible, i.e. whether, for instance, a ground-calibrated GLONASS or Galileo satellite would allow relative calibrations of the

GPS satellites. Experiments similar to the GPS-only tests described above were in fact carried out using combined GPS+GLONASS solutions. But because no homogeneous, long enough GPS+GLONASS dataset was available, any definitive conclusion could not be reached. The question of cross-GNSS relative z-PCO calibrations thus remains open for the moment, but may be answered soon, by means of the AC solutions from the second IGS reprocessing campaign.

5.1.2 z-PCO calibrations relative to a reference LEO satellite

An alternative strategy to obtain z-PCO calibrations of the GPS satellites independently of any conventional TRF scale was proposed by Haines et al. (2004). They used the GPS data collected by different low Earth orbiting (LEO) satellites equipped with ground-calibrated, low-multipath GPS antennas to estimate antenna phase center corrections for the GPS satellites. Haines et al. (2011) then used such LEO-based calibrations of the GPS satellites to compute long-term GPS terrestrial frames. The scales of these frames however showed large biases with respect to the ITRF2008 (-18 mm using TOPEX-based phase center corrections; +17 mm using GRACE-based phase center corrections), indicating that their mean LEO-based GPS satellite z-PCOs were affected by significant errors.

Unlike the calibrations relative to a hypothetical reference GNSS satellite evoked in Sect. 5.1.1, LEO-based calibrations of the GNSS satellites have the advantage of being readily feasible and thus deserve consideration. However, the large mean z-PCO errors observed in Haines et al. (2011)'s results will have to be understood and mitigated before LEO-based calibrations can allow a GNSS contribution to the ITRF scale definition.

5.1.3 Contribution of GNSS to the ITRF scale rate

When the satellite z-PCOs are fixed in a *time series* of GNSS analyses, two different pieces of information are in fact introduced:

- the fact that the satellite z-PCOs are equal to reference values (at some given date);
- the time invariability of the satellite z-PCOs.

If the terrestrial frames resulting from such GNSS analyses are stacked into a long-term linear frame (such as done for the ITRF computation - see Sect. 1.2.4), each of these two pieces of information will impact particular aspects of the long-term stacked frame. In particular, the scale of the long-term stacked frame will be controlled by the adopted reference z-PCO values, while the scale *rate* of the long-term stacked frame will be controlled by the assumed time invariability of the satellite z-PCOs.

In their contribution to the ITRF2013, the IGS ACs will fix the satellite z-PCOs to conventional values. The scale rate of the long-term GNSS frame that will enter the ITRF2013 computation will thus be controlled by the assumed time invariability of the satellite z-PCOs. Depending on the actual validity of this assumption, a contribution of GNSS to the definition of the ITRF2013 scale rate may therefore be considered.

This possibility of a GNSS contribution to the ITRF scale rate definition was in fact studied by Collilieux and Schmid (2012) from a reverse perspective. From the reprocessed solutions of five IGS ACs, they derived time series of satellite z-PCO estimates, relatively to various TRFs obtained from ITRF2008 by only changing its scale rate. They then searched the scale rate offsets with respect to ITRF2008 for which the resulting satellite z-PCO estimates were as constant as possible over time, i.e. for which the z-PCO time invariability assumption was best met. Those offsets represent intrinsic GPS scale rate estimates with respect to ITRF2008, based on the z-PCO time invariability assumption. Depending on the considered AC, the obtained offsets were ranging from -0.27 mm/yr to -0.06 mm/yr, consistently closer to the SLR scale rate offset with respect to ITRF2008 (-0.15 mm/yr) than to the VLBI scale rate offset (+0.15 mm/yr).

Collilieux and Schmid (2012) globally optimized the time invariability of their z-PCO time series over an ensemble of several satellites. But their optimized z-PCO time series nevertheless showed residual satellite-specific trends, with a scatter of about 5 mm/yr. This scatter can be considered as an estimate of the precision with which the z-PCO time invariability assumption is actually met. It corresponds to a precision of about 0.25 mm/yr for the intrinsic GPS terrestrial scale rate, which is quite consistent with the scatter of the AC scale rate offsets with respect to ITRF2008.

From Collilieux and Schmid (2012)'s study, it can be concluded that the IGS AC contributions to ITRF2008 allow a determination of the terrestrial scale rate, based on the z-PCO time invariability assumption, with a precision of about 0.25 mm/yr. A similar analysis will be conducted over the IGS AC contributions to ITRF2013. Depending on the obtained precision estimate of the intrinsic GNSS scale rate, and on its agreement with the SLR and VLBI scale rates, a contribution of GNSS to the definition of the ITRF2013 scale rate could actually be considered.

5.2 Prospects for improving the geocenter determination with GNSS

The collinearity diagnosis performed in Sect. 4.5 clarified why GNSS could so far not contribute to define the ITRF origin. The three components of the origin of GNSS-derived terrestrial frames are indeed quasi-perfectly correlated (collinear) with the other parameters set up in standard GNSS analyses. The determination of geocenter motion with GNSS is thus a nearly singular problem, which explains why GNSS geocenter motion estimates have so far been unreliable and particularly sensitive to modelling errors (Sect. 2.4.1). In view of a reliable observation of geocenter motion with GNSS and a future possible contribution of GNSS to the ITRF origin, two complementary paths can consequently be considered: the reduction of collinearity issues and the mitigation of modelling errors.

To reduce the collinearity of the geocenter coordinates in GNSS analyses, two different paths can again be considered:

- the inclusion of additional decorrelating observations;
- a reduction of the number of parameters to estimate, or equivalently, the addition of constraints on some estimated parameters.

As regards the first path, two possibilities are examined in the following, namely the joint analysis of observations from several GNSS (Sect. 5.2.1) and the inclusion of GNSS observations collected by LEO satellites (Sect. 5.2.2).

As regards the second path towards collinearity reduction, one should bear in mind that the GNSS parameter categories that mostly explain the extreme collinearity of the geocenter coordinates are epoch-wise clock offsets and tropospheric parameters (Sect. 4.5.4). Consequently, a collinearity reduction is to be expected from this second path principally if the number of clock and/or tropospheric parameters to estimate can be reduced, or if these parameters can be sufficiently constrained. An improvement of global meteorological models up to a point where GNSS analyses could dispense with the estimation of tropospheric parameters seems rather unfeasible in the near term. The main remaining prospect within this second path is therefore the modelling of station and/or satellite clocks by other means than non-constrained epoch-wise offsets. In this respect, the modelling of satellite clocks appears especially attractive: if the time evolution of satellite clock offsets could be tightly enough constrained, then the epoch mean signatures of the geocenter coordinates (magenta lines in Fig. 4.6 and 4.8) could indeed become observable. This possibility is investigated in Sect. 5.2.3.

Finally, besides the reduction of collinearity issues, improvements of the geocenter determination with GNSS could also be expected from a reduction of modelling errors. From the fact that the IGS AC translation time series contain strong spurious signals at harmonics of the GPS draconitic year (Sect. 2.4.1), and from various experiments showing that changes in orbit modelling have significant impacts on GPS-derived geocenter motion (see Sect. 2.4.2 and, e.g., Springer, 2000; Hugentobler et al., 2006; Herring, 2011; Rodriguez-Solano et al., 2011; Meindl et al., 2013), it seems clear that orbit modelling deficiencies are a major source of geocenter contamination. Sect. 5.2.4 will therefore discuss several prospects towards orbit modelling improvements.

5.2.1 Multi-GNSS geocenter determination

As shown in Sect. 4.5.3, the collinearity of the three geocenter coordinates is slightly reduced when observations from several GNSS are simultaneously analysed, rather than observations from a single GNSS. One could therefore expect better geocenter motion estimates from multi-GNSS analyses than from GPS-only analyses. For the time being, this is however not the case.

At present, only two fully deployed GNSS indeed allow the estimation of geocenter motion time series: GPS and GLONASS. A comparative study of GPS-only, GLONASS-only and combined GPS+GLONASS geocenter estimates can be found in Meindl (2011) and Meindl et al. (2013). In the X and Y components, their GPS and GLONASS geocenter time series are quite consistent, although the GLONASS time series are clearly noisier. Hardly any difference can be observed between the combined GPS+GLONASS and the GPS-only time series. In the Z component however, the GLONASS-only geocenter time series is of much lower quality than the GPS-only time series and contains in particular a strong spurious periodic signal with an amplitude of about 20 cm. The combined GPS+GLONASS time series is close to the GPS-only time series, but nevertheless shows traces of the spurious GLONASS signal. In summary, the overall effect of adding GLONASS observations is a degradation of the GPS-only geocenter estimates, rather than the expected improvement.

The much lower quality of Meindl (2011)'s GLONASS-only geocenter estimates is likely due for a large part to larger (orbit) modelling errors than in the GPS case. In their combined GPS+GLONASS analyses, the gain in collinearity compared to the GPS-only case was thus probably offset by the introduction of those larger GLONASS modelling errors, resulting in an overall degradation of the geocenter estimation. An actual improvement over GPS-only geocenter estimates via the inclusion of GLONASS observations would in fact likely require that the GLONASS satellite orbits are modelled with a similar precision as the GPS orbits, which is still far from being the case (Rodriguez-Solano et al., 2014).

For the moment, it is hardly assessable whether the inclusion of Galileo observations will improve or degrade GPS-only geocenter estimates. It will first depend on the precision with which the Galileo satellite orbits can be modelled when the full Galileo constellation is deployed. But, even if a similar precision as for the GPS orbits is reached, the slight collinearity reduction resulting from the inclusion of Galileo observations may still not be enough to obtain reliable GNSS geocenter motion estimates.

5.2.2 Inclusion of LEO observations

In all the preceding, only observations collected by ground GNSS stations have been considered. However, many LEO satellites are equipped with GNSS antennas. This subsection therefore investigates how the simultaneous analysis of GNSS observations collected by ground stations and LEO satellites may reduce the collinearity of the geocenter coordinates in a global GNSS analysis.

Several simulations were thus run in which GNSS observations collected by a GRACE-like satellite ($a = 6811.5$ km, $e = 0$, $i = 89°$) were considered. In addition to the parameters listed in Table 4.3 (except the GNSS satellite z-PCOs), an initial state vector, empirical accelerations and epoch-wise clock offsets were estimated for the GRACE-like satellite. The considered empirical accelerations were, following Kang et al. (2006), constant along-track accelerations and once-per-revolution periodic accelerations in the along-track and cross-track directions (S_0, S_c, S_s, W_c and W_s in the notations of Rodriguez-Solano et al. (2012)), each estimated once per orbital revolution.

In a first round of simulations, the GRACE observations were given the same weight as the ground observations, i.e. an a priori sigma of 1 cm. The VIFs obtained for the three geocenter coordinates were 137.7 (99.636%), 138.5 (99.638%) and 1853.4 (99.973%), i.e. 17.1, 17.0 and 1.7 times smaller than in the case where no GRACE observations were used. Like in the case where no GRACE observations were used, the epoch mean signatures of the three geocenter coordinates on the ground observations (magenta lines in Fig. 4.6 and 4.8) could be reproduced by variations of the GNSS satellite clock offsets. These variations of the GNSS satellite clock offsets however had undesirable impacts on the GRACE observations. In case of the X and Y geocenter coordinates, these side effects could hardly be accommodated by variations of the GRACE parameters. The inclusion of GRACE observations thus enabled a partial decorrelation of the X and Y geocenter coordinates from the GNSS satellite clock offsets. On the other hand, in case of the Z geocenter coordinate, the undesirable impact of the GNSS satellite clock offset variations on the GRACE observations could be accommodated to a great extent by variations of the GRACE parameters, which is why the collinearity of the Z geocenter coordinate was much less reduced.

In a second run of simulations, the GRACE observations were given an a priori sigma of 1 mm, while an a priori sigma of 1 cm was kept for the ground observations. The VIFs obtained for the three geocenter coordinates were 23.4 (97.843%), 22.8 (97.780%) and 220.7 (99.773%), i.e. 100.7, 103.2 and 14.3 times smaller than in the case where no GRACE observations were used. Compared to the previous simulations, a greater importance was given to the minimization of any undesirable impact on the heavily weighted GRACE observations. The collinearity between the three geocenter coordinates and the GNSS satellite clock offsets was thus further reduced. Further collinearity reductions were similarly observed in simulations where observations collected by several LEO satellites were considered.

In conclusion, depending on their relative weight to the ground observations, the inclusion of LEO observations in a global GNSS analysis can lead to a drastic collinearity reduction for the three geocenter coordinates, hence to a potentially improved determination of geocenter motion with GNSS.

Haines et al. (2011) actually compared geocenter motion time series derived from global GPS analyses including (a) ground observations only and (b) additional GPS observations collected by GRACE. They noted a beneficial impact of the inclusion of GRACE observations on the three components of geocenter motion, via an overall noise decrease and a dramatic reduction of the draconitic errors in their Z geocenter time series. But, even with GRACE observations included, Haines et al. (2011)'s geocenter time series were still showing some disagreement with SLR-derived and global-inversion-derived geocenter motion estimates (under-estimation of the annual signals in the X and Z components; presence of residual draconitic errors in the Z component). For the moment, the question remains open whether giving more weight to the GRACE observations or including more LEO observations would allow GNSS to eventually provide competitive geocenter estimates.

5.2.3 Satellite clock modelling

The passive hydrogen maser of the Galileo validation satellite GIOVE-B and the latest generation of rubidium clocks of the GPS Block IIF satellites have both demonstrated unprecedented stability (Montenbruck et al., 2012b). The stability of these new generation clocks opens the way for modelling satellite clocks by other means than non-constrained epoch-wise offsets, hence for an increased robustness of global GNSS analyses. Hugentobler et al. (2012) and Hackel et al. (2014) showed for instance that constraining the clock offsets of the GIOVE-B satellite towards a linear model could improve its orbit determination. In this subsection, we investigate how such modelling of the satellite clocks may reduce the collinearity of the geocenter coordinates in global GNSS analyses.

The stability of a clock over a specified time interval τ is usually measured by its Allan deviation $\sigma_y(\tau)$. For τ up to several thousands of seconds, the Allan deviations of the new generation Galileo and GPS satellite clocks approximately vary as $1/\sqrt{\tau}$. The stability specification for GIOVE-B's passive hydrogen maser was for instance $10^{-12}/\sqrt{\tau}$. Ground tests demonstrated a stability of $6 \times 10^{-13}/\sqrt{\tau}$. However, the actual in-flight stability of GIOVE-B's passive hydrogen maser is rather at the order of $1.5 \times 10^{-12}/\sqrt{\tau}$ (Montenbruck et al., 2012b). The rubidium clock of the GPS IIF satellite G062 shows a comparable in-flight stability level (Montenbruck et al., 2012a).

Assuming a given stability $\sigma/\sqrt{\tau}$ for a satellite clock is equivalent to assuming that the satellite epoch-wise clock offsets are normally distributed with a standard deviation σ. This assumption can be introduced into a GNSS analysis via simple weighted pseudo-observations (constraints) on the epoch-wise satellite clock offsets (Hugentobler et al., 2012; Hackel et al., 2014). We will use this approach in the following simulations, with different σ's and different numbers of stable satellite clocks. When several stable clocks are simultaneously considered, it is however necessary to account for relative frequency biases between them (i.e. for their inaccuracy). This will be done in the following simulations by freely estimating one bias and one rate for all but one of the considered stable clocks.

Before coming to the simulation results, it should finally be noted that at least two stable satellite clocks need to be simultaneously considered. Constraining the epoch-wise clock offsets of a single satellite indeed has for only effect to compensate the time reference singularities of a global GNSS analysis (Sect. 2.1.2), but does not bring any additional information.

Two stable satellite clocks In a first round of simulations, it was assumed that two GPS-like satellites were equipped with stable clocks. The epoch-wise clock offsets of those two satellites were therefore constrained with different σ's. Moreover, a constant clock bias and a constant clock rate were estimated for one of both satellites. All other simulation options were as described in Sect. 4.2.2 except that satellite z-PCOs were not estimated.

Fig. 5.5 shows the VIFs of the three geocenter coordinates thus obtained for different assumed clock stabilities (i.e. different σ's). For σ down to 3×10^{-10} s, the clock constraints have no impact on the collinearity of the geocenter coordinates. Tighter and tighter clock constraints result in a progressive collinearity decrease, until asymptotic VIFs are reached. Interestingly, these asymptotic VIFs are almost reached for $\sigma = 1.5 \times 10^{-12}$ s, i.e. for the actual in-flight stability of GIOVE-B's and G062's clocks. The asymptotic VIFs of the three geocenter coordinates are 262.6 (99.809%), 285.2 (99.825%) and 954.9 (99.948%), i.e. 9.0, 8.3 and 3.3 times smaller than without clock constraints. By sufficiently constraining the clock offsets of two satellites towards a linear model, a modest, but still noticeable collinearity reduction could thus be achieved.

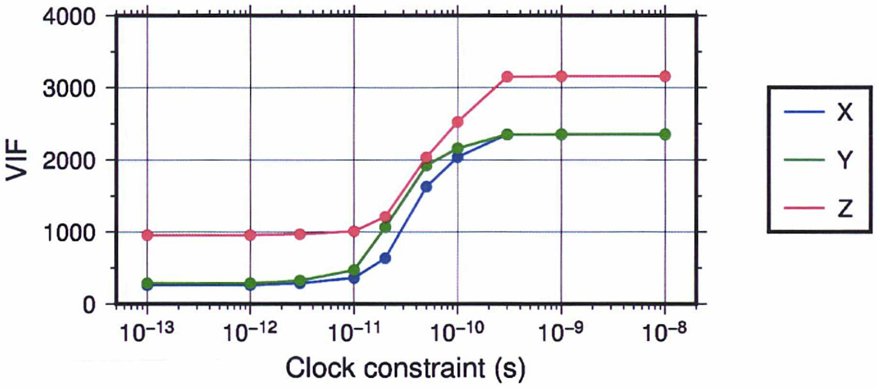

Figure 5.5 VIFs of the three geocenter coordinates obtained when applying different constraints to the epoch-wise clock offsets of two GPS-like satellites

Whole constellation of stable clocks In a second round of simulations, all 24 considered GPS-like satellites were assumed to be equipped with stable clocks. All epoch-wise satellite clock offsets were therefore constrained with different σ's. Moreover, constant clock biases and constant clock rates were estimated for all but one satellites. All other simulation options were as described in Sect. 4.2.2 except that satellite z-PCOs were not estimated.

Fig. 5.6 shows the VIFs of the three geocenter coordinates thus obtained for different assumed clock stabilities (i.e. different σ's). The overall pattern is similar as in Fig. 5.5, although a steeper collinearity decrease and much lower asymptotic VIFs can be observed. The asymptotic VIFs of the three geocenter coordinates are in this case practically reached for $\sigma = 3 \times 10^{-12}$ s. Their respective values are 22.0 (97.697%), 22.2 (97.724%) and 82.3 (99.390%), i.e. 107.0, 106.0 and 38.4 times smaller than without clock constraints. By sufficiently constraining the satellite clock offsets of a whole GNSS constellation towards a linear model, a drastic collinearity reduction could thus be achieved for the three geocenter coordinates.

This drastic collinearity reduction is explained by the fact that sufficiently constrained satellite clock offsets become unable to reproduce the epoch-mean signatures of the geocenter coordinates (magenta lines in Fig. 4.6 and 4.8). In other words, the introduced constraints allow a decorrelation of the geocenter coordinates from the

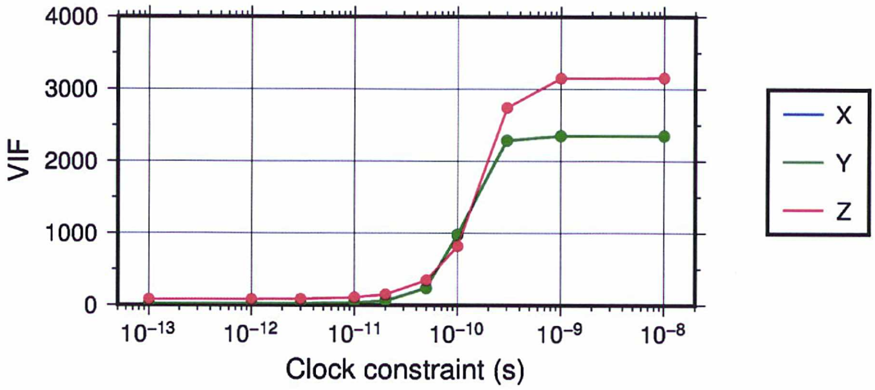

Figure 5.6 VIFs of the three geocenter coordinates obtained when applying different constraints to the epoch-wise clock offsets of the 24 considered GPS-like satellites. The VIFs of the X and Y geocenter coordinates are actually overlapping.

satellite clock offsets. Correlations with the station clock offsets and the tropospheric parameters however remain, which explains why the asymptotic VIFs of the geocenter coordinates are still larger than in an SLR analysis (Sect. 4.4).

Periodic clock variations In the preceding simulations, it was implicitly assumed that the Allan deviations of the satellite clocks were varying as $1/\sqrt{\tau}$ for τ up to one day. The analysis of actual estimates of GIOVE-B's or G062's clock offsets however reveals that this assumption is only valid for τ up to about 2000 s (Hugentobler et al., 2012; Montenbruck et al., 2012b,a; Hackel et al., 2014). The Allan deviations of such GIOVE-B or G062 clock estimates then show a pronounced bump, approximately centered around $\tau = 20000$ s, caused by periodic variations of the clock estimates (mainly once-per-revolution and twice-per-revolution variations with amplitudes of several cm).

According to Montenbruck et al. (2012a), three mechanisms could be at the origin of these apparent periodic clock variations:

- coupling with orbit determination uncertainties, via the strong correlation between clock offsets and the satellite radial position;
- frequency variations of the clock oscillator, induced, e.g., by temperature variations;
- line bias variations, induced, e.g., by temperature variations.

As evidenced by Svehla (2010) by means of SLR observations, the apparent periodic clock variations of GIOVE-B appear mostly induced by orbit modelling errors. Additional temperature-induced variations can however not be ruled out. On the other hand, as regards G062, the availability of triple-frequency observations allowed

Montenbruck et al. (2012a) to unambiguously evidence temperature-induced line bias variations.

Apparent clock variations induced by orbit modelling errors, such as observed for GIOVE-B, can provide insight into the underlying orbit modelling deficiencies and thus help in overcoming them (Svehla et al., 2013). One can therefore expect that such orbit-induced apparent clock variations will eventually vanish as progress is made in orbit modelling. On the other hand, "real" temperature-induced (frequency and/or line bias) clock variations cannot be modelled *a priori* without a detailed knowledge of the internal structure and thermal characteristics of the satellites.

As such detailed knowledge is not publicly available, temperature-induced periodic clock variations will likely need to be accounted for *empirically* in future global GNSS analyses, e.g. by freely estimating once-per-revolution and twice-per-revolution clock variations. In a last run of simulations, we therefore investigated how the estimation of such parameters would impact the collinearity of the geocenter coordinates. Like previously, all 24 considered GPS-like satellites were assumed to be equipped with stable clocks. All epoch-wise satellite clock offsets were constrained with $\sigma = 10^{-12}$ s. Clock biases, clock rates and once-per-revolution clock variations were additionally estimated for all but one satellites. (The impact of estimating or not twice-per-revolution clock variations on the collinearity of the geocenter coordinates was found to be negligible.)

The VIFs thus obtained for the three geocenter coordinates were 22.2 (97.721%), 22.4 (97.744%) and 2680.4 (99.981%). Obviously, estimating or not once-per-revolution clock variations has little impact on the collinearity of the X and Y geocenter coordinates. On the other hand, the VIF of the Z geocenter coordinate is almost as large as in the case where no stable satellite clocks were considered. This can be explained by the fact that once-per-revolution clock variations can reproduce the epoch-mean signature of the Z geocenter coordinate (magenta line in Fig. 4.6) almost as efficiently as freely estimated epoch-wise clock offsets.

Summary Sufficiently constraining the clock offsets of at least two GNSS satellites towards a linear model allows a decorrelation of the three geocenter coordinates from the satellite clock offsets. This decorrelation is all the more effective as the clock offsets of more satellites are constrained. If the clock offsets of a whole GNSS constellation could be constrained towards a linear model at a level of 3×10^{-12} s, then a drastic collinearity reduction could be achieved and would likely lead to competitive GNSS geocenter motion estimates. This could be the case of the future Galileo constellation, whose satellites will carry similar passive hydrogen masers as GIOVE-B. However, if once-per-revolution clock variations need to be estimated in order to account for non-modelled thermal effects, then stable satellite clocks do not allow any significant collinearity reduction for the Z geocenter coordinate.

5.2.4 Orbit modelling improvements

As mentioned in the introduction of Sect. 5.2, improvements of the geocenter determination with GNSS can be expected, not only from a reduction of collinearity issues, but also from a mitigation of orbit modelling errors, which are likely the main contributor to systematic errors in current GNSS geocenter motion estimates. This subsection therefore gives an overview of several prospects towards orbit modelling improvements.

Systematic errors in GNSS satellite orbits are currently mostly due to mis-modelling of the non-gravitational forces acting on GNSS satellites: Earth radiation pressure, thermal re-radiation, antenna thrust and, above all, direct solar radiation pressure. Several evidences, like:

- the systematic Sun-dependent patterns observed by Urschl et al. (2007) in SLR range residuals to GPS orbits,
- similar patterns observed by Svehla et al. (2013) in the apparent clock variations of GIOVE-B,

indeed indicate that neither the a priori modelling of solar radiation pressure by the IGS ACs, nor the empirical orbit parameters they set up are able to completely account for the effects of solar radiation pressure. In view of an improved consideration of the non-gravitational forces, and especially solar radiation pressure, in global GNSS analyses, three different ways can be considered.

Alternative orbit parameterizations A first possible way would be the estimation by the IGS ACs of empirical orbit parameters more able to account for the effects of non-gravitational forces than those currently estimated. In this respect, Rodriguez-Solano et al. (2012) proposed to estimate the optical properties of simple satellite box-wing models, together with additional empirical parameters, rather than the purely empirical accelerations of the ECOM model. This alternative parameterization of the GNSS satellite orbits, based on the physical interaction between solar radiation pressure and the satellite's surfaces, shows a comparable performance as the ECOM parameterization in terms of orbit overlap and prediction errors. However, systematic differences can be observed between the orbits derived with each parameterization.

Rodriguez-Solano et al. (2014) then studied the impact of this alternative parameterization on various GNSS-derived geodetic parameters and in particular geocenter motion. Compared to the ECOM parameterization, they observed a drastic reduction of the draconitic errors in the Z component of geocenter motion. The expected annual signals are however surprisingly not detected in their improved geocenter time series. For the time being, the possibility that alternative orbit parameterizations may lead to competitive GNSS geocenter estimates thus remains to be demonstrated.

A priori solar radiation pressure modelling The second possible way in view of an improved consideration of non-gravitational forces in global GNSS analyses would be to dispose of accurate *a priori* models of these forces. Analytical solar radiation pressure models have been developed for the GLONASS-IIv (Ziebart and Dare, 2001) and GPS-IIR (Ziebart et al., 2003) satellites, by computing the effects of the solar photon flux on a computer simulation of the spacecraft structures using ray-tracing algorithms. Analytical models now also exist for the GPS-IIA and GLONASS-IIM satellites and additionally account for Earth radiation pressure, thermal re-radiation and antenna thrust (Ziebart et al., 2012). Their accuracy is however limited by the ignorance of the actual optical and thermal properties of the satellite materials, and it is currently unsure whether such analytical models will eventually reach the accuracy required for precise GNSS orbit determination.

Accelerometers Finally, a last possible prospect towards improvements of the GNSS satellite orbits would be to *measure* the non-conservative forces acting on GNSS satellites rather than imperfectly modelling them. Equipping future GNSS satellites with 3-dimensional accelerometers would in fact likely be the best way to improve GNSS orbits. This might moreover help in understanding and mitigating orbit modelling deficiencies for current unequipped satellites.

Conclusion

Although fundamental in several respects, the GNSS contribution to the ITRF remains subject to various potential improvements. In particular, the origin and scale information stemming from global GNSS solutions has so far not been considered reliable enough to contribute to the definition of the ITRF origin and scale. In view of a possible future contribution of GNSS to the ITRF origin and scale, a first necessary step was to provide a detailed understanding of the weak ability of GNSS to determine the terrestrial scale and geocenter motion. This was actually the core purpose of this thesis.

The fundamental issue concerning the determination of the terrestrial scale with GNSS had in fact already been identified by Springer (2000) and Zhu et al. (2003). In global GNSS analyses, there indeed exists a quasi-perfect correlation between the terrestrial scale, the satellite z-PCOs, the zenith wet delays and the station and satellite clock offsets. Since pre-launch antenna calibrations are not available for any of the GNSS satellites launched so far, this quasi-perfect correlation prevents a reliable estimation of the terrestrial scale with GNSS apart from conventional satellite z-PCOs.

On the other hand, the weak ability of GNSS to determine geocenter motion through the network shift approach was remaining unresolved when this thesis started. In order to gain insight into this question, we addressed it from the perspective of collinearity among the parameters of a least-squares regression. Several peculiarities of global GNSS analyses required particular mathematical developments. A generalized collinearity diagnosis was therefore developed, based on the notion of variance inflation factor. It allows to assess and explain the collinearity of any explicit or implicit parameter of a generalized least-squares problem in presence of constraints.

This generalized collinearity diagnosis was then applied to the SLR geocenter determination problem. It turned out that the determination of the X and Y geocenter coordinates with SLR does not suffer from any collinearity issue. On the other hand, the Z geocenter coordinate has a VIF of about 9 in our simulated SLR analyses due to correlations with the satellite osculating elements. In addition to the uneven distribution of the SLR network, this slight collinearity issue may partly explain why the Z component of SLR-derived geocenter motion is of lower quality than its X and Y components.

On the other hand, all three geocenter coordinates were shown to be highly collinear with the other parameters set up in global GNSS analyses. This severe collinearity explains why the three components of their origin correspond to quasi-singularities of GNSS-derived terrestrial frames and why standard GNSS analyses are hardly sensitive to geocenter motion. Among the parameters set up in GNSS analyses, two specific categories quasi-fully explain the severe collinearity of the geocenter coordinates: epoch-wise clock offsets and tropospheric parameters. One can therefore conclude that the inability of GNSS, as opposed to SLR, to properly sense geocenter motion is due to the simultaneous estimation of epoch-wise clock offsets and tropospheric parameters.

Once the weak ability of GNSS to determine the terrestrial scale and geocenter motion was understood, several prospects were investigated, that could lead to a possible future contribution of GNSS to the definition of the ITRF scale and origin. The entire terrestrial scale issue could be solved if z-PCO calibrations, independent of any conventional terrestrial scale, were available for one or more GNSS satellites. This could be the case if the ground antenna calibrations of one or more Galileo satellites were made publicly available. Another possibility would consist in calibrating the GNSS satellite antennas with respect to reference LEO satellites (Haines et al., 2004). This method is however currently prone to large systematic errors that remain to be understood and mitigated.

Before absolute z-PCO calibrations become available, the long-term stability of the GNSS satellite z-PCOs may however already be used for a GNSS contribution to the ITRF scale rate. By assuming the time invariability of the GPS satellite z-PCOs, Collilieux and Schmid (2012) indeed showed that the IGS AC contributions to ITRF2008 could provide intrinsic estimates of the terrestrial scale rate with a precision of about 0.25 mm/yr. The way for a contribution of GNSS to defining the scale rate of the next ITRF2013 is thus open.

In view of an improved determination of geocenter motion with GNSS and a possible future contribution of GNSS to the ITRF origin, two complementary paths can finally be considered. The first one would be to improve the sensitivity of GNSS analyses to the geocenter coordinates by reducing their collinearity. In this respect, a first promising way is the simultaneous analysis of GNSS data collected by ground stations and LEO satellites. The inclusion of LEO observations in global GNSS analyses indeed allows a decorrelation of the geocenter coordinates from the GNSS satellite clock offsets. This method does however not yet provide competitive geocenter estimates.

A second promising way toward reducing the collinearity of the geocenter coordinates in GNSS analyses is the modelling of satellite clock offsets by other means than non-constrained epoch-wise clock offsets. Such clock modelling is already possible for specific satellites equipped with latest generation clocks (G062, GIOVE-B) and will become feasible for the whole future Galileo constellation. Non-modelled once-per-revolution clock variations (e.g. due to thermal effects) may however prevent any significant collinearity reduction for the Z geocenter coordinate in this way.

Besides the reduction of collinearity issues, improvements of the geocenter determination with GNSS can also be expected from improvements in the modelling of the GNSS satellite orbits, and especially of the non-gravitational forces acting on GNSS satellites. In this respect, alternative orbit parameterizations or accurate analytical modelling of non-gravitational forces might eventually help in leading to competitive GNSS geocenter estimates. But the best way to overcome the difficult modelling of non-gravitational forces would likely be to equip future GNSS satellites with 3-dimensional accelerometers.

Several possible paths thus exist towards a reliable observation of geocenter motion with GNSS. At the moment, it is however hardly predictable whether any of these paths will succeed, which path(s) will possibly succeed and in how much time. One can nevertheless anticipate that GNSS will likely not become able to complement SLR for the definition of the ITRF origin in the near term.

Bibliography

Altamimi Z, Collilieux X (2009) IGS contribution to the ITRF. Journal of Geodesy 83(3-4):375–383, DOI 10.1007/s00190-008-0294-x

Altamimi Z, Collilieux X (2010) Quality assessment of the IDS contribution to ITRF2008. Advances in Space Research 45(12):1500–1509, DOI 10.1016/j.asr.2010.03.010

Altamimi Z, Sillard P, Boucher C (2002) ITRF2000: a new release of the International Terrestrial Reference Frame for Earth science applications. Journal of Geophysical Research 107(B10):ETG 2–1 – ETG 2–19, DOI 10.1029/2001JB000561

Altamimi Z, Sillard P, Boucher C (2004) Combination and analysis of terrestrial reference frames. Tech. Rep. SP04, Institut Géographique National / LAREG

Altamimi Z, Collilieux X, Boucher C (2006) Accuracy assessment of the ITRF datum definition. In: Xu P, Liu J, Dermanis A (eds) VI Hotine-Marussi Symposium on Theoretical and Computational Geodesy, Springer Berlin Heidelberg, International Association of Geodesy Symposia, vol 132, pp 101–110, DOI 10.1007/978-3-540-74584-6_16

Altamimi Z, Collilieux X, Legrand J, Garayt B, Boucher C (2007) ITRF2005: a new release of the International Terrestrial Reference Frame based on time series of station positions and Earth Orientation Parameters. Journal of Geophysical Research 112(B9):B09,401, DOI 10.1029/2007JB004949

Altamimi Z, Collilieux X, Métivier L (2011) ITRF2008: an improved solution of the International Terrestrial Reference Frame. Journal of Geodesy 85(8):457–473, DOI 10.1007/s00190-011-0444-4

Altamimi Z, Collilieux X, Métivier L, Rebischung P (2012) The International Terrestrial Reference Frame: lessons from the past and preparation for the future. Abstract 2678 presented at EGU General Assembly 2012, Vienna, Austria, 23-27 Apr.

Altamimi Z, Collilieux X, Métivier L (2013) Preliminary analysis in preparation for the ITRF2013. Abstract G12A-08 presented at AGU 2013 Fall Meeting, San Francisco, Calif., 9-13 Dec.

Antonello M, Baibussinov B, Benetti P, Boffelli F, Calligarich E, Canci N, Centro S, Cesana A, Cieslik K, Cline DB, et al. (2012) Precision measurement of the neutrino velocity with the ICARUS detector in the CNGS beam. Journal of High Energy Physics 2012(11):1–21, DOI 10.1007/JHEP11(2012)049

Argus DF (2012) Uncertainty in the velocity between the mass center and surface of Earth. Journal of Geophysical Research 117(B10):B10,405, DOI 10.1029/2012JB009196

Bähr H, Altamimi Z, Heck B (2007) Variance component estimation for combination of terrestrial reference frames. Master's thesis, Universität Karlsruhe

Baire Q, Bruyninx C, Legrand J, Pottiaux E, Aerts W, Defraigne P, Bergeot N, Chevalier JM (2013) Influence of different GPS receiver antenna calibration models on geodetic positioning. GPS Solutions DOI 10.1007/s10291-013-0349-1

Beckley BD, Lemoine SG, Luthcke SB, Ray RD, Zelensky NP (2007) A reassessment of global and regional mean sea level trends from TOPEX and Jason-1 altimetry based on revised reference frame and orbits. Geophysical Research Letters 34(14):L14,608, DOI 10.1029/2007GL030002

Belsley DA (1982) Assessing the presence of harmful collinearity and other forms of weak data through a test for signal-to-noise. Journal of Econometrics 20(2):211–253, DOI 10.1016/0304-4076(82)90020-3

Belsley DA (1991) A guide to using the collinearity diagnostics. Computer Science in Economics and Management 4(1):33–50, DOI 10.1007/BF00426854

Belsley DA, Kuh E, Welsch RE (1980) Regression diagnostics: Identifying influential data and sources of collinearity. Wiley, New York

Beutler G, Brockmann E, Gurtner W, Hugentobler U, Mervart L, Rothacher M, Verdun A (1994) Extended orbit modeling techniques at the CODE processing center of the International GPS Service for geodynamics (IGS): theory and initial results. Manuscripta Geodaetica 19(6):367–386

Blewitt G (1998) GPS data processing methodology: from theory to applications. In: GPS for geodesy, Springer, pp 231–270

Blewitt G (2003) Self-consistency in reference frames, geocenter definition, and surface loading of the solid Earth. Journal of Geophysical Research 108(B2):2103, DOI 10.1029/2002JB002082

Blewitt G, Lavallée D (2002) Effect of annual signals on geodetic velocity. Journal of Geophysical Research 107(B7):ETG 9–1 – ETG 9–11, DOI 10.1029/2001JB000570

Blewitt G, Lavallée D, Clarke P, Nurutdinov K (2001) A new global mode of Earth deformation: seasonal cycle detected. Science 294(5550):2342–2345, DOI 10.1126/science.1065328

Blewitt G, Altamimi Z, Davis J, Gross R, Kuo CY, Lemoine FG, Moore AW, Neilan RE, Plag HP, Rothacher M, Shum CK, Sideris MG, Schöne T, Tregoning P, Zerbini S (2010) Geodetic observations and global reference frame contributions to understanding sea-level rise and variability. In: Understanding sea-level rise and variability, Wiley-Blackwell, pp 256–284, DOI 10.1002/9781444323276.ch9

Blossfeld M, Seitz M, Angermann D (2013) Non-linear station motions in epoch and multi-year reference frames. Journal of Geodesy DOI 10.1007/s00190-013-0668-6

Boehm J, Niell A, Tregoning P, Schuh H (2006a) Global Mapping Function (GMF): a new empirical mapping function based on numerical weather model data. Geophysical Research Letters 33(7):L07,304, DOI 10.1029/2005JB003629

Boehm J, Werl B, Schuh H (2006b) Troposphere mapping functions for GPS and Very Long Baseline Interferometry from European Centre for Medium-range Weather Forecasts operational analysis data. Journal of Geophysical Research 111(B2):B02,406, DOI 10.1029/2005JB003629

Boucher C, Altamimi Z, Feissel M, Sillard P (1996) Results and analysis of the ITRF94. IERS Technical Note 20, Central Bureau of IERS, Observatoire de Paris

Cardellach E, Elósegui P, Davis JL (2007) Global distortion of GPS networks associated with satellite antenna model errors. Journal of Geophysical Research 112(B7):B07,405, DOI 10.1029/2006JB004675

Chen G, Herring TA (1997) Effects of atmospheric azimuthal asymmetry on the analysis of space geodetic data. Journal of Geophysical Research 102(B9):20,489–20,502, DOI 10.1029/97JB01739

Collilieux X (2008) Analyse des séries temporelles de positions des stations de géodésie spatiale : application au Repère International de Référence Terrestre (ITRF). PhD thesis, Observatoire de Paris

Collilieux X, Schmid R (2012) Evaluation of the ITRF2008 GPS vertical velocities using satellite antenna z-offsets. GPS Solutions 17(2):237–246, DOI 10.1007/s10291-012-0274-8

Collilieux X, Wöppelmann G (2011) Global sea-level rise and its relation to the terrestrial reference frame. Journal of Geodesy 85(1):9–22, DOI 10.1007/s00190-010-0412-4

Collilieux X, Altamimi Z, Ray J, van Dam T, Wu X (2009) Effect of the satellite laser ranging network distribution on geocenter motion estimation. Journal of Geophysical Research 114(B4):B04,402, DOI 10.1029/2008JB005727

Collilieux X, Altamimi Z, Coulot D, van Dam T, Ray J (2010) Impact of loading effects on determination of the International Terrestrial Reference Frame. Advances in Space Research 45(1):144–154, DOI 10.1016/j.asr.2009.08.024

Collilieux X, Métivier L, Altamimi Z, van Dam T, Ray J (2011) Quality assessment of GPS reprocessed terrestrial reference frame. GPS Solutions 15(3):219–231, DOI 10.1007/s10291-010-0184-6

Collilieux X, van Dam T, Ray J, Coulot D, Métivier L, Altamimi Z (2012) Strategies to mitigate aliasing of loading signals while estimating GPS frame parameters. Journal of Geodesy 86(1):1–14, DOI 10.1007/s00190-011-0487-6

Collilieux X, Altamimi Z, Argus DF, Boucher C, Dermanis A, Haines BJ, Herring TA, Kreemer CW, Lemoine FG, Ma C, MacMillan DS, Mäkinen J, Métivier L, Ries J, Teferle FN, Wu X (2014) External evaluation of the Terrestrial Reference Frame: report of the task force of the IAG sub-commission 1.2. In: Rizos C, Willis P (eds) Proceedings of the XXV IUGG General Assembly, Springer Berlin Heidelberg, International Association of Geodesy Symposia, vol 139, pp 197–202, DOI 10.1007/978-3-642-37222-3_25

van Dam T, Wahr J, Milly PCD, Shmakin AB, Blewitt G, Lavallée D, Larson KM (2001) Crustal displacements due to continental water loading. Geophysical Research Letters 28(4):651–654, DOI 10.1029/2000GL012120

van Dam T, Wahr J, Lavallée D (2007) A comparison of annual vertical crustal displacements from GPS and Gravity Recovery and Climate Experiment (GRACE) over Europe. Journal of Geophysical Research 112(B3):B03,404, DOI 10.1029/2006JB004335

van Dam T, Collilieux X, Wuite J, Altamimi Z, Ray J (2012) Non-tidal ocean loading: amplitudes and potential effects in GPS height time series. Journal of Geodesy 86(11):1043–1057, DOI 10.1007/s00190-012-0564-5

van Dam TM, Blewitt G, Heflin MB (1994) Atmospheric pressure loading effects on Global Positioning System coordinate determinations. Journal of Geophysical Research 99(B12):939–950, DOI 10.1029/2012JB009196

Davis JL, Elósegui P, Mitrovica JX, Tamisiea ME (2004) Climate-driven deformation of the solid earth from GRACE and GPS. Geophysical Research Letters 31(24):L24,605, DOI 10.1029/2004GL021435

Dermanis A (1977) Geodetic linear estimation techniques and the norm choice problem. Manuscripta Geodaetica 2:15–97

Dong D, Fang P, Bock Y, Cheng MK, Miyazaki S (2002) Anatomy of apparent seasonal variations from GPS-derived site position time series. Journal of Geophysical Research 107(B4), DOI 10.1029/2001JB000573

Dong D, Yunck T, Heflin M (2003) Origin of the International Terrestrial Reference Frame. Journal of Geophysical Research 108(B4):2200, DOI 10.1029/2002JB002035

Draper NR, Smith H (1998) Applied regression analysis, 3rd edn. Wiley, New York

Elósegui P, Davis JL, Jaldehag RTK, Johansson JM, Niell AE, Shapiro II (1995) Geodesy using the Global Positioning System: the effects of signal scattering on estimates of site position. Journal of Geophysical Research 100(B6):9921–9934, DOI 10.1029/95JB00868

Farrar DE, Glauber RR (1967) Multicollinearity in regression analysis: the problem revisited. The Review of Economics and Statistics 49(1):92–107

Farrell WE (1972) Deformation of the earth by surface loads. Reviews of Geophysics 10(3):761–797, DOI 10.1029/RG010i003p00761

Garcia-Fernandez M, Butala M, Komjathy A, Desai SD (2012) Intercomparison of approaches for modeling second order ionospheric corrections using GNSS measurements. Abstract G11B-0920 presented at AGU 2012 Fall Meeting, San Francisco, Calif., 3-7 Dec.

Ge M, Gendt G, Rothacher M, Shi C, Liu J (2008) Resolution of GPS carrier-phase ambiguities in Precise Point Positioning (PPP) with daily observations. Journal of Geodesy 82(7):389–399, DOI 10.1007/s00190-007-0187-4

Gobinddass ML, Willis P, de Viron O, Sibthorpe A, Zelensky NP, Ries JC, Ferland R, Bar-Sever Y, Diament M (2009a) Systematic biases in DORIS-derived geocenter time series related to solar radiation pressure mis-modeling. Journal of Geodesy 83(9):849–858, DOI 10.1007/s00190-009-0303-8

Gobinddass ML, Willis P, de Viron O, Sibthorpe A, Zelensky NP, Ries JC, Ferland R, Bar-Sever Y, Diament M, Lemoine FG (2009b) Improving DORIS geocenter time series using an empirical rescaling of solar radiation pressure models. Advances in Space Research 44(11):1279–1287, DOI 10.1016/j.asr.2009.08.00

Griffiths J, Ray JR (2013) Sub-daily alias and draconitic errors in the IGS orbits. GPS Solutions 17(3):413–422, DOI 10.1007/s10291-012-0289-1

Griffiths J, Gendt G, Nischan T, Ray J (2009) Assessment of the orbits from the first IGS reprocessing campaign. Abstract G13A-04 presented at AGU 2009 Fall Meeting, San Francisco, Calif., 14-18 Dec.

Gross R, Beutler G, Plag HP (2009) Integrated scientific and societal user requirements and functional specifications for the GGOS. In: Global Geodetic Observing System, Springer Berlin Heidelberg, pp 209–224, DOI 10.1007/978-3-642-02687-4_7

Hackel S, Steigenberger P, Hugentobler U, Uhlemann M, Montenbruck O (2014) Galileo orbit determination using combined GNSS and SLR observations. GPS Solutions DOI 10.1007/s10291-013-0361-5

Haines B, Bar-Sever Y, Bertiger W, Desai S, Willis P (2004) One-centimeter orbit determination for Jason-1: new GPS-based strategies. vol 27, pp 299–318, DOI 10.1080/01490410490465300

Haines B, Bar-Sever Y, Bertiger W, Desai S, Harvey N, Weiss J (2011) A GPS-based Terrestrial Reference Frame from a combination of terrestrial and orbiter data. Abstract G53A-0880 presented at AGU Fall Meeting 2011, San Francisco, 5-9 Dec.

Haines B, Bertiger W, Desai S, Harvey N, Sibois A, Weiss J (2013) Recent advances in realizing the Terrestrial Reference System from GPS. Abstract G13B-0946 presented at AGU Fall Meeting 2013, San Francisco, 9-13 Dec.

Haitovsky Y (1969) Multicollinearity in regression analysis: comment. The Review of Economics and Statistics 51(4):486–489

Heflin M, Argus D, Jefferson D, Webb F, Zumberge J (2002) Comparison of a GPS-defined global reference frame with ITRF2000. GPS Solutions 6(1-2):72–75, DOI 10.1007/s10291-002-0015-5

Hernández-Pajares M, Juan JM, Sanz J, Orús R (2007) Second-order ionospheric term in GPS: implementation and impact on geodetic estimates. Journal of Geophysical Research 112(B8):B08,417, DOI 10.1029/2006JB004707

Herring T (2011) Analysis impacts on gps reference frame realizations. Abstract 1704 presented at EGU General Assembly 2011, Vienna, Austria, 3-8 Apr.

Hugentobler U, van der Marel H, Springer T (2006) Identification and mitigation of GNSS errors. In: Springer T, Gendt G, Dow JM (eds) Proceedings of IGS Workshop 2006

Hugentobler U, Montenbruck O, Rodriguez-Solano C, Steigenberger P (2012) Modeling of the GIOVE-B clock as a tool for studying radiation pressure models. Abstract 13930 presented at EGU General Assembly 2012, Vienna, Austria, 22-27 Apr.

Jansen MJF, Gunter BC, Kusche J (2009) The impact of GRACE, GPS and OBP data on estimates of global mass redistribution. Geophysical Journal International 177(1):1–13, DOI 10.1111/j.1365-246X.2008.04031.x

Kang Z, Tapley B, Bettadpur S, Ries J, Nagel P, Pastor R (2006) Precise orbit determination for the GRACE mission using only GPS data. Journal of Geodesy 80(6):322–331, DOI 10.1007/s00190-006-0073-5

Kedar S, Hajj GA, Wilson BD, Heflin MB (2003) The effect of the second order GPS ionospheric correction on receiver positions. Geophysical Research Letters 30(16):1829, DOI 10.1029/2003GL017639

King MA, Watson CS (2010) Long GPS coordinate time series: multipath and geometry effects. Journal of Geophysical Research 115(B4):B04,403, DOI 10.1029/2009JB006543

King MA, Watson CS, Penna NT, Clarke PJ (2008) Subdaily signals in GPS observations and their effect at semiannual and annual periods. Geophysical Research Letters 35(3):L03,302, DOI 10.1029/2007GL032252

Kovalevsky J, Mueller II (1981) Comments on conventional terrestrial and quasi-inertial reference systems. In: Gaposchkin EM, Kolaczek B (eds) Reference coordinate systems for Earth dynamics, Astrophysics and space science library, vol 86, Springer, pp 375–384, DOI 10.1007/978-94-009-8456-1_48

Kovalevsky J, Mueller II (1989) Introduction. In: Kovalevsky J, Mueller II, Kolaczek B (eds) Reference frames in astronomy and geophysics, Astrophysics and space science library, vol 154, Springer, pp 1–12

Lavallée DA, van Dam T, Blewitt G, Clarke P (2006) Geocenter motions from GPS: a unified observation model. Journal of Geophysical Research 111(B5):B05,405, DOI 10.1029/2005JB003784

Lercier D, Collilieux X, Métivier L, Altamimi Z, Vigny C (2013) Assessment of parametric post-seismic models in reference frame determination. Abstract presented at IAG 2013 Scientific Assembly, Potsdam, Germany, 2-6 Sep.

MacMillan DS, Ma C (1997) Atmospheric gradients and the VLBI terrestrial and celestial reference frames. Geophysical Research Letters 24(4):453–456, DOI 10.1029/97GL00143

Marquardt DW (1970) Generalized inverses, ridge regression, biased linear estimation and nonlinear estimation. Technometrics 12(3):591–612

Meertens C, Blume F, Burgland H, Puskas C, Wahr J, van Dam T, Herring T (2012) Investigation of non-tectonic signals at GPS stations. Abstract presented at IGS Workshop 2012, Olsztyn, Poland, 23-27 Jul.

Meindl M (2011) Combined analysis of observations from different global navigation satellite systems. Geodätisch-geophysikalische Arbeiten in der Schweiz, Schweizerischen Geodätischen Kommission

Meindl M, Beutler G, Thaller D, Dach R, Jäggi A (2013) Geocenter coordinates estimated from GNSS data as viewed by perturbation theory. Advances in Space Research 51(7):1047–1064, DOI 10.1016/j.asr.2012.10.026

Mignard F (2005) FAMOUS: frequency analysis on unusual sampling. Tech. rep., Observatoire de la Côte d'Azur

Montenbruck O, Hugentobler U, Dach R, Steigenberger P, Hauschild A (2012a) Apparent clock variations of the Block IIF-1 (SVN62) GPS satellite. GPS Solutions 16(3):303–313, DOI 10.1007/s10291-011-0232-x

Montenbruck O, Steigenberger P, Schönemann E, Hauschild A, Hugentobler U, Dach R, Becker M (2012b) Flight characterization of new generation GNSS satellite clocks. Navigation 59(4):291–302, DOI 10.1002/navi.22

Montgomery DC, Peck EA, Vining GG (2012) Introduction to linear regression analysis, 5th edn. Wiley, New York

Nahmani S, Bock O, Bouin MN, Santamaria-Gomez A, Boy JP, Collilieux X, Métivier L, Panet I, Genthon P, de Linage C, Wöppelmann G (2012) Hydrological deformation induced by the West African monsoon: comparison of GPS, GRACE and loading models. Journal of Geophysical Research 117(B5):B05,409, DOI 10.1029/2011JB009102

Penna NT, Stewart MP (2003) Aliased tidal signatures in continuous GPS height time series. Geophysical Research Letters 30(23):2184, DOI 10.1029/2003GL018828

Petit G, Luzum B (2010) IERS Conventions (2010). IERS Technical Note 36, Verlag des Bundesamts für Kartographie und Geodäsie, Frankfurt-am-Main

Petrie EJ, King MA, Moore P, Lavallée DA (2010) HigherâĂŘorder ionospheric effects on the GPS reference frame and velocities. Journal of Geophysical Research 115(B3):B03,417, DOI 10.1029/2009JB006677

Ray J (1999) IERS analysis campaign to investigate motions of the geocenter. IERS Technical Note 25, Central Bureau of IERS, Observatoire de Paris

Ray J (2006) Systematic errors in GPS position estimates. Abstract presented at IGS Workshop 2006, Darmstadt, Germany, 8-12 May

Ray J, Altamimi Z, Collilieux X, van Dam T (2008) Anomalous harmonics in the spectra of GPS position estimates. GPS Solutions 12(1):55–64, DOI 10.1007/s10291-007-0067-7

Ray J, Collilieux X, Rebischung P, van Dam T, Altamimi Z (2011) Consistency of crustal loading signals derived from models and GPS: inferences for GPS positioning errors. Abstract G51B-06 presented at AGU Fall Meeting 2011, San Francisco, Calif., 5-9 Dec.

Ray J, Griffiths J, Collilieux X, Rebischung P (2013a) Subseasonal GNSS positioning errors. Geophysical Research Letters 40(22):5854–5860, DOI 10.1002/2013GL058160

Ray JR (1996) Measurements of length of day using the Global Positioning System. Journal of Geophysical Research 101(B9):20,141–20,149, DOI 10.1029/96JB01889

Ray JR (2009) A quasi-optimal, consistent approach for combination of UT1 and LOD. In: Drewes H (ed) Geodetic reference frames, Springer Berlin Heidelberg, International Association of Geodesy Symposia, vol 134, pp 239–243, DOI 10.1007/978-3-642-00860-3_37

Ray JR, Rebischung P, Schmid R (2013b) Dependence of IGS products on the ITRF datum. In: Altamimi Z, Collilieux X (eds) Reference Frames for Applications in Geosciences, Springer Berlin Heidelberg, International Association of Geodesy Symposia, vol 138, pp 63–67, DOI 10.1007/978-3-642-32998-2_11

Rebischung P, Garayt B (2013) Recent results from the IGS terrestrial frame combinations. In: Altamimi Z, Collilieux X (eds) Reference Frames for Applications in Geosciences, Springer Berlin Heidelberg, International Association of Geodesy Symposia, vol 138, pp 69–74, DOI 10.1007/978-3-642-32998-2_12

Rebischung P, Collilieux X, Altamimi Z (2012a) Geocenter motion estimates from the IGS Analysis Center solutions. Abstract 7446 presented at EGU General Assembly 2012, Vienna, Austria, 23-27 Apr.

Rebischung P, Collilieux X, van Dam T, Ray J, Altamimi Z (2012b) Analysis effects in IGS station motion time series. Abstract presented at IGS Workshop 2012, Olsztyn, Poland, 23-27 Jul.

Rebischung P, Griffiths J, Ray J, Schmid R, Collilieux X, Garayt B (2012c) IGS08: the IGS realization of ITRF2008. GPS Solutions 16(4):483–494, DOI 10.1007/s10291-011-0248-2

Ries JC (2011) Seasonal geocenter motion from space geodesy and models. Abstract presented at GGOS Unified Analysis Workshop, Zurich, Switzerland., 16-17 Sep.

Ries JC (2013) Annual geocenter motion from space geodesy and models. Abstract G12A-06 presented at AGU 2013 Fall Meeting, San Francisco, Calif., 9-13 Dec.

Rietbroek R, Fritsche M, Brunnabend SE, Daras I, Kusche J, Schröter J, Flechtner F, Dietrich R (2011) Global surface mass from a new combination of GRACE, modelled OBP and reprocessed GPS data. Journal of Geodynamics 59-60:64–71, DOI 10.1016/j.jog.2011.02.003

Rodriguez-Solano CJ, Hugentobler U, Steigenberger P, Lutz S (2011) Impact of Earth radiation pressure on GPS position estimates. Journal of Geodesy 86(5):309–317, DOI 10.1007/s00190-011-0517-4

Rodriguez-Solano CJ, Hugentobler U, Steigenberger P (2012) Adjustable box-wing model for solar radiation pressure impacting GPS satellites. Advances in Space Research 49(7):1113–1128, DOI 10.1016/j.asr.2012.01.016

Rodriguez-Solano CJ, Hugentobler U, Steigenberger P, Blossfeld M, Fritsche M (2014) Reducing the draconitic errors in GNSS geodetic products. Journal of Geodesy DOI 10.1007/s00190-014-0704-1

Romero I, Rebischung P, Ray J, Schmid R, Fisher S, Griffiths J (2013) Position corrections due to uncalibrated GNSS antenna radomes at IGS co-located geodetic observing stations. Abstract G13B-0946 presented at AGU Fall Meeting 2013, San Francisco, 9-13 Dec.

Rothacher M (2001) Comparison of absolute and relative antenna phase center variations. GPS Solutions 4(4):55–60, DOI 10.1007/PL00012867

Schmid R, Steigenberger P, Gendt G, Ge M, Rothacher M (2007) Generation of a consistent absolute phase-center correction model for GPS receiver and satellite antennas. Journal of Geodesy 81(12):781–798, DOI 10.1007/s00190-007-0148-y

Seitz M, Angermann D, Blossfeld M, Drewes H, Gerstl M (2012) The 2008 DGFI realization of the ITRS: DTRF2008. Journal of Geodesy 86(12):1097–1123, DOI 10.1007/s00190-012-0567-2

Sillard P (1999) Modélisation des systèmes de référence terrestres. PhD thesis, Observatoire de Paris

Sillard P, Boucher C (2001) A review of algebraic constraints in terrestrial reference frame datum definition. Journal of Geodesy 75(2-3):63–73, DOI 10.1007/s001900100166

van der Sluis A (1969) Condition numbers and equilibration of matrices. Numerische Mathematik 14(1):14–23, DOI 10.1007/BF02165096

Smith G, Campbell F (1980) A critique of some ridge regression methods. Journal of the American Statistical Association 75(369):74–81

Springer TA (2000) Modeling and validating orbits and clocks using the Global Positioning System. Geodätisch-geophysikalische Arbeiten in der Schweiz, Schweizerischen Geodätischen Kommission

Springer TA, Beutler G, Rothacher M (1999) A new solar radiation pressure model for the GPS satellites. GPS Solutions 2(3):50–62, DOI 10.1007/PL00012757

Steigenberger P, Boehm J, Tesmer V (2009) Comparison of GMF/GPT with VMF1/ECMWF and implications for atmospheric loading. Journal of Geodesy 83(10):943–951, DOI 10.1007/s00190-009-0311-8

Svehla D (2010) Complete relativistic modelling of the GIOVE-B clock parameters and its impact on POD, track-track ambiguity resolution and precise timing. Abstract presented at IGS Workshop 2010, Newcastle, United Kingdom, June 28 - July 2

Svehla D, Rothacher M, Hugentobler U, Steigenberger P, Ziebart M (2013) 10 years of precise geometrical positioning in space - Geometrical model of solar radiation pressure based on high-performing clocks onboard Galileo. Abstract presented at IAG Scientific Assembly 2013, Potsdam, Germany, 1-6 Sep.

Tesmer F, Steigenberger P, van Dam T, Mayer-Gürr T (2011) Vertical deformations from homogeneously processed GRACE and global GPS long-term series. Journal of Geodesy 85(5):291–310, DOI 10.1007/s00190-010-0437-8

Tregoning P, Herring TA (2006) Impact of a priori zenith hydrostatic delay errors on GPS estimates of station heights and zenith total delays. Geophysical Research Letters 33(23):L23,303, DOI 10.1029/2006GL027706

Tregoning P, Watson C, Ramillien G, McQueen H, Zhang J (2009) Detecting hydrologic deformation using GRACE and GPS. Geophysical Research Letters 36(15):L15,401, DOI 10.1029/2009GL038718

Trupin AS, Meier MF, Wahr JM (1992) Effect of melting glaciers on the Earth's rotation and gravitational field: 1965-1984. Geophysical Journal International 108(1):1–15, DOI 10.1111/j.1365-246X.1992.tb00835.x

Urschl C, Beutler G, Gurtner W, Hugentobler U, Schaer S (2007) Contribution of SLR tracking data to GNSS orbit determination. Advances in Space Research 39(10):1515–1523, DOI 10.1016/j.asr.2007.01.038

Valette JJ, Lemoine FG, Ferrage P, Yaya P, Altamimi Z, Willis P, Soudarin L (2010) IDS contribution to ITRF2008. Advances in Space Research 46(12):1614–1632, DOI 10.1016/j.asr.2010.05.029

Vigue Y, Lichten SM, Blewitt G, Heflin MB, Malla RP (1992) Precise determination of Earth's center of mass using measurements from the Global Positioning System. Geophysical Research Letters 19(14):1487–1490, DOI 10.1029/92GL01575

Wallace PT, Capitaine N (2006) Precession-nutation procedures consistent with IAU 2006 resolutions. Astronomy and Astrophysics 459(3):981–985, DOI 10.1051/0004-6361:20065897

Watson C, Tregoning P, Coleman R (2006) Impact of solid Earth tide models on GPS coordinate and tropospheric time series. Geophysical Research Letters 33(8):L08,306, DOI 10.1029/2005GL025538

Williams SDP (2003) Offsets in Global Positioning System time series. Journal of Geophysical Research 108(B6):2310, DOI 10.1029/2002JB002156

Wöppelmann G, Miguez BM, Bouin MN, Altamimi Z (2007) Geocentric sea-level trend estimates from GPS analyses at relevant tide gauges world-wide. Global and Planetary Change 57(3-4):396–406, DOI 10.1016/j.gloplacha.2007.02.002

Wu X, Heflin MB, Ivins ER, Fukumori I (2006) Seasonal and interannual global surface mass variations from multisatellite geodetic data. Journal of Geophysical Research 111(B9):B09,401, DOI 10.1029/2011GL047450

Wu X, Collilieux X, Altamimi Z, Vermeersen BLA, Gross RS, Fukumori I (2011) Accuracy of the International Terrestrial Reference Frame origin and Earth expansion. Geophysical Research Letters 38(13):L13,304, DOI 10.1029/2011GL047450

Wu X, Abbondanza C, Altamimi Z, Chin TM, Collilieux X, Gross R, Heflin M, Hurst K, Jiang Y, Parker J (2012a) KALREF - a Kalman filter approach to the International Terrestrial Reference Frame realization. Abstract G53B-1143 presented at AGU 2012 Fall Meeting, San Francisco, Calif., 3-7 Dec.

Wu X, Ray J, van Dam T (2012b) Geocenter motion and its geodetic and geophysical implications. Journal of Geodynamics 58:44–61, DOI 10.1016/j.jog.2012.01.00

Wu X, Abbondanza C, Altamimi Z, Chin TM, Collilieux X, Gross RS, Heflin MB, Jiang Y, Parker JW (2013) Direct determination of geocenter motion by combining SLR, VLBI, GNSS, and DORIS time series. Abstract G21C-07 presented at AGU 2013 Fall Meeting, San Francisco, Calif., 9-13 Dec.

Wübbena G, Schmitz M, Menge M, Seeber G, Völksen C (1997) A new approach for field calibration of absolute antenna phase center variations. In: Proceedings of ION GPS 1996, vol 9, pp 1205–1214

Yan H, Chen W, Zhu Y, Zhang W, Zhong M (2009) Contributions of thermal expansion of monuments and nearby bedrock to observed GPS height changes. Geophysical Research Letters 36(13):L13,301, DOI 10.1029/2009GL038152

Zhu SY, Massmann FH, Yu Y, Reigber C (2003) Satellite antenna phase center offsets and scale errors in GPS solutions. Journal of Geodesy 76(11-12):668–672, DOI 10.1007/s00190-002-0294-1

Ziebart M, Dare P (2001) Analytical solar radiation pressure modelling for GLONASS using a pixel array. Journal of Geodesy 75(11):587–599, DOI 10.1007/s001900000136

Ziebart M, Adhya S, Sibthorpe A, Cross P (2003) GPS Block IIR non-conservative force modeling: computation and implications. In: Proceedings of ION GP/GNSS 2003, Portland, Oregon, 9-12 Sep., pp 2671–2678

Ziebart M, Grey S, Allgeier S (2012) Current status of non-conservative force modelling: interface to repro2. Abstract presented at IGS Workshop 2012, Olsztyn, Poland, 23-27 Jul.

Publications and communications

Articles

Chen Q, van Dam T, Sneeuw N, Collilieux X, Weigelt M, Rebischung P (2013) Singular spectrum analysis for modeling seasonal signals from GPS time series. Journal of Geodynamics 72:25–35, DOI 10.1016/j.jog.2013.05.005

Coulot D, Rebischung P, Pollet A, Grondin L, Collot G (2014) Global optimization of GNSS station reference networks. GPS Solutions, submitted

Ray J, Griffiths J, Collilieux X, Rebischung P (2013) Subseasonal GNSS positioning errors. Geophysical Research Letters 40(22):5854–5860, DOI 10.1002/2013GL058160

Rebischung P, Griffiths J, Ray J, Schmid R, Collilieux X, Garayt B (2012) IGS08: the IGS realization of ITRF2008. GPS Solutions 16(4):483–494, DOI 10.1007/s10291-011-0248-2

Rebischung P, Altamimi Z, Springer T (2014) A collinearity diagnosis of the GNSS geocenter determination. Journal of Geodesy 88(1):65–85, DOI 10.1007/s00190-013-0669-5

Conference proceedings

Li Z, van Dam T, Collilieux X, Altamimi Z, Rebischung P, Nahmani S (2014) Quality evaluation of continental water storage models. In: IAG Scientific Assembly 2013 Proceedings, International Association of Geodesy Symposia, submitted

Ray JR, Rebischung P, Schmid R (2013) Dependence of IGS products on the ITRF datum. In: Altamimi Z, Collilieux X (eds) Reference Frames for Applications in Geosciences, Springer Berlin Heidelberg, International Association of Geodesy Symposia, vol 138, pp 63–67, DOI 10.1007/978-3-642-32998-2_11

Rebischung P, Garayt B (2013) Recent results from the IGS terrestrial frame combinations. In: Altamimi Z, Collilieux X (eds) Reference Frames for Applications in Geosciences, Springer Berlin Heidelberg, International Association of Geodesy Symposia, vol 138, pp 69–74, DOI 10.1007/978-3-642-32998-2_12

Technical reports

Rebischung P, Garayt B, Collilieux X, Altamimi Z (2012) IGS Reference Frame Working Group Coordinator Report 2011. In: Meindl M, Dach R, Jean Y (eds) IGS Technical Report 2011, pp 175–182

Rebischung P, Garayt B, Collilieux X, Altamimi Z (2013) IGS Reference Frame Working Group Coordinator Report 2012. In: Dach R, Jean Y (eds) IGS Technical Report 2012, pp 171–178

Rebischung P, Garayt B, Collilieux X, Altamimi Z (2014) IGS Reference Frame Working Group Coordinator Report 2013. In: Dach R, Jean Y (eds) IGS Technical Report 2013

Oral communications

Altamimi Z, Collilieux X, Métivier L, Rebischung P (2012) The International Terrestrial Reference Frame: lessons from the past and preparation for the future. Abstract 2678 presented at EGU General Assembly 2012, Vienna, Austria, 23-27 Apr.

Altamimi Z, Collilieux X, Métivier L, Rebischung P (2012) Strengths and weaknesses of the IGS contribution to the ITRF. Abstract presented at IGS Workshop 2012, Olsztyn, Poland, 23-27 Jul.

Altamimi Z, Collilieux X, Métivier L, Rebischung P, Lercier D (2013) The International Terrestrial Reference Frame: current status and future challenges. Abstract presented at IAG Scientific Assembly 2013, Potsdam, Germany, 1-6 Sep.

Altamimi Z, Collilieux X, Métivier L, Rebischung P, Lercier D (2014) ITRF2013: preliminary analysis and early results. Abstract 2694 presented at EGU General Assembly 2014, Vienna, Austria, 27 Apr. - 2 May

Chen Q, van Dam T, Sneeuw N, Collilieux X, Rebischung P (2012) Separation of modulated seasonal signals from GPS time series with singular spectrum analysis. Abstract presented at International Symposium and Summer School on Space Geodesy and Earth System, Shanghai, China, 21-25 Aug.

Collilieux X, Altamimi Z, Rebischung P, Métivier L (2011) ITRF: a reference frame for sea level studies. Abstract presented at Workshop on Geodetic Vertical Monitoring of Tide Gauge Benchmarks, Paris, France, 8-9 Oct.

Collilieux X, Rebischung P, van Dam T, Ray J, Altamimi Z (2011) Consistency of crustal loading signals derived from models and GPS: a re-examination. Abstract G31C-01 presented at AGU Fall Meeting 2011, San Francisco, Calif., 5-9 Dec.

Coulot D, Pollet A, Rebischung P, Collot G, Grondin L (2013) Global optimization of GNSS station reference networks. Abstract presented at IAG Scientific Assembly 2013, Potsdam, Germany, 1-6 Sep.

Coulot D, Deleflie F, Rebischung P, Decosta R, Pollet A, Grondin L, Collot G (2014) Application d'algorithmes génétiques au calcul d'orbites de satellites artificiels et à la recherche de sous-réseaux de stations GNSS. Présentation aux Journées de la Recherche de l'IGN, Saint-Mandé, France, 20-21 Mar.

van Dam T, Collilieux X, Rebischung P, Ray J, Altamimi Z (2012) Comparison of IGS station position time series with loading model: what can we learn? Abstract presented at AOGS Meeting 2012, Singapore, 13-17 Aug.

van Dam T, Collilieux X, Rebischung P, Ray J, Altamimi Z (2013) Evaluating load model errors by comparison to a global GPS time series solution. Abstract G12A-05 presented at AGU Fall Meeting 2013, San Francisco, 9-13 Dec.

Griffiths J, Rebischung P, Garayt B, Ray J (2012) IGS preparations for the next reprocessing and ITRF. Abstract 3181 presented at EGU General Assembly 2012, Vienna, Austria, 23-27 Apr.

Ray J, Collilieux X, Rebischung P, van Dam T, Altamimi Z (2011) Consistency of crustal loading signals derived from models and GPS: inferences for GPS positioning errors. Abstract G51B-06 presented at AGU Fall Meeting 2011, San Francisco, Calif., 5-9 Dec.

Ray J, Griffiths J, Rebischung P, Kouba J, Chen W (2012) Rotational errors in IGS orbit and ERP products. Abstract presented at IGS Workshop 2012, Olsztyn, Poland, 23-27 Jul.

Ray J, Griffiths J, Collilieux X, Rebischung P (2014) Subseasonal GNSS errors in IGS products. Abstract 8504 presented at EGU General Assembly 2014, Vienna, Austria, 27 Apr. - 2 May

Rebischung P, Garayt B, Schmid R, Ray J, Collilieux X (2011) IGS08: elaboration, consequences and maintenance of the IGS realization of ITRF2008. Abstract 6850 presented at EGU General Assembly 2011, Vienna, Austria, 3-8 Apr.

Rebischung P, Collilieux X, Altamimi Z (2012) Geocenter motion estimates from the IGS Analysis Center solutions. Abstract 7446 presented at EGU General Assembly 2012, Vienna, Austria, 23-27 Apr.

Rebischung P, Collilieux X, van Dam T, Ray J, Altamimi Z (2012) Analysis effects in IGS station motion time series. Abstract presented at IGS Workshop 2012, Olsztyn, Poland, 23-27 Jul.

Rebischung P, Altamimi Z, Springer T (2013) (In)sensibilité des GNSS aux mouvements du géocentre. Présentation aux Journées de la Recherche de l'IGN, Marne-la-Vallée, France, 24-25 Apr.

Rebischung P, Altamimi Z, Springer T (2013) A collinearity diagnosis of the GNSS geocenter determination. Abstract presented at IAG Scientific Assembly 2013, Potsdam, Germany, 1-6 Sep.

Rebischung P, Altamimi Z, Springer T (2013) Insensitivity of GNSS to geocenter motion through the network shift approach. Abstract G12A-03 presented at AGU Fall Meeting 2013, San Francisco, 9-13 Dec.

Poster presentations

Chen Q, van Dam T, Sneeuw N, Collilieux X, Rebischung P (2012) Extracting seasonal signals from continuous GPS time series with modern statistical methods. Abstract 4801 presented at EGU General Assembly 2012, Vienna, Austria, 23-27 Apr.

van Dam T, Collilieux X, Rebischung P, Ray J, Altamimi Z (2011) Quantifying load model errors by comparison to a global GPS time series solution. Abstract G53B-0905 presented at AGU Fall Meeting 2011, San Francisco, Calif., 5-9 Dec.

Legrand J, Bruyninx C, Craymer M, Dawson J, Griffiths J, Kenyeres A, Rebischung P, Sanchez L, Santamaría-Gómez A, Saria E, Altamimi Z (2013) A collaborative approach toward the densification of the ITRF velocity field. Abstract G13B-0947 presented at AGU Fall Meeting 2013, San Francisco, 9-13 Dec.

Li Z, van Dam T, Collilieux X, Altamimi Z, Ray J, Rebischung P, Nahmani S (2013) Quality evaluation of continental water storage models. Abstract presented at IAG Scientific Assembly 2013, Potsdam, Germany, 1-6 Sep.

Rebischung P (2011) Quelles pistes pour améliorer la contribution des GNSS à l'ITRF ? Présentation aux Journées de la Recherche de l'IGN, Saint-Mandé, France, 10-11 Mar.

Rebischung P (2012) Le mouvement du géocentre vu par les centres d'analyse de l'IGS. Présentation aux Journées de la Recherche de l'IGN, Saint-Mandé, France, 8-9 Mar.

Rebischung P, Springer T, Altamimi Z (2012) An attempt to decorrelate geocenter motion from empirical accelerations. Abstract presented at IGS Workshop 2012, Olsztyn, Poland, 23-27 Jul.

Rebischung P, Altamimi Z, Springer T (2013) (In)sensitivity of GNSS techniques to geocenter motion. Abstract 6896 presented at EGU General Assembly 2013, Vienna, Austria, 7-12 Apr.

Romero I, Rebischung P, Ray J, Schmid R, Fisher S, Griffiths J (2012) The IGS campaign to measure position corrections for un-calibrated IGS radome stations. Abstract presented at IGS Workshop 2012, Olsztyn, Poland, 23-27 Jul.

Romero I, Rebischung P, Ray J, Schmid R, Fisher S, Griffiths J (2013) Position corrections due to uncalibrated GNSS antenna radomes at IGS co-located geodetic observing stations. Abstract G13B-0946 presented at AGU Fall Meeting 2013, San Francisco, 9-13 Dec.

Zoulida M, Pollet A, Coulot D, Biancale R, Rebischung P (2014) Combinaison multi-technique d'observations de géodésie spatiale. Présentation aux Journées de la Recherche de l'IGN, Saint-Mandé, France, 20-21 Mar.

Zoulida M, Pollet A, Coulot D, Biancale R, Rebischung P, Collilieux X (2014) Multi-technique combination of space geodesy observations. Abstract 10330 presented at EGU General Assembly 2014, Vienna, Austria, 27 Apr. - 2 May

Appendix A

Some linear algebra

A.1 Images, ranks and kernels of real matrices

Let $\boldsymbol{A} \in \mathcal{M}_{m,n}(\mathbb{R})$ be an $m \times n$ matrix of real numbers.

- The *image* of $\boldsymbol{A}$ is the set of all possible linear combinations of its row vectors, i.e. $\{\boldsymbol{A}\boldsymbol{x}, \boldsymbol{x} \in \mathbb{R}^n\}$. It is a linear subspace of $\mathbb{R}^m$ and will be denoted $\mathrm{Im}(\boldsymbol{A})$.
- The *rank* of $\boldsymbol{A}$ is the dimension of its row space: $\mathrm{rank}(\boldsymbol{A}) = \dim(\mathrm{Im}(\boldsymbol{A}))$.
- The *kernel* of $\boldsymbol{A}$ is the set of all possible vectors $\boldsymbol{x} \in \mathbb{R}^n$ such that $\boldsymbol{A}\boldsymbol{x} = \boldsymbol{0}$. It is a linear subspace of $\mathbb{R}^n$ and will be denoted $\mathrm{Ker}(\boldsymbol{A})$.

Let us recall some basic properties of the images, ranks and kernels of real matrices.

Proposition A.1. *$\forall \boldsymbol{A} \in \mathcal{M}_{m,n}(\mathbb{R})$, $rank(\boldsymbol{A}) \leq \min(m, n)$. $\boldsymbol{A}$ is said to be of full rank if $rank(\boldsymbol{A}) = \min(m, n)$. Otherwise, $\boldsymbol{A}$ is said to be rank deficient.*

Proposition A.2. *$\forall \boldsymbol{A} \in \mathcal{M}_{n,n}(\mathbb{R})$, $\boldsymbol{A}$ is invertible if and only if $rank(\boldsymbol{A}) = n$, i.e. $\boldsymbol{A}$ is of full rank.*

Proposition A.3. *$\forall \boldsymbol{A} \in \mathcal{M}_{m,n}(\mathbb{R})$, $rank(\boldsymbol{A}) = rank(\boldsymbol{A}^T) = rank(\boldsymbol{A}\boldsymbol{A}^T) = rank(\boldsymbol{A}^T\boldsymbol{A})$.*

Proposition A.4. *$\forall \boldsymbol{A} \in \mathcal{M}_{m,n}(\mathbb{R})$, $Ker(\boldsymbol{A})$ is the orthogonal complement of $Im(\boldsymbol{A}^T)$ in $\mathbb{R}^n$ equipped with the standard dot product, i.e. $Ker(\boldsymbol{A}) = Im(\boldsymbol{A}^T)^\perp$. Consequently, $rank(\boldsymbol{A}) + dim(Ker(\boldsymbol{A})) = n$.*

Proposition A.5. *$\forall (\boldsymbol{A}, \boldsymbol{B}) \in \mathcal{M}_{m,n}(\mathbb{R}) \times \mathcal{M}_{n,p}(\mathbb{R})$, $rank(\boldsymbol{A}\boldsymbol{B}) \leq \min(rank(\boldsymbol{A}), rank(\boldsymbol{B}))$.*

Proposition A.6. *$\forall (\boldsymbol{A}, \boldsymbol{B}) \in \mathcal{M}_{m,n}(\mathbb{R}) \times \mathcal{M}_{n,p}(\mathbb{R})$, if $rank(\boldsymbol{B}) = n$, then $rank(\boldsymbol{A}\boldsymbol{B}) = rank(\boldsymbol{A})$.*

Let us now introduce some more properties used in the following.

Proposition A.7. *Let $\boldsymbol{A}$ be any $m \times n$ real matrix and $\boldsymbol{P}$ be any $n \times n$ symmetric positive-semidefinite matrix such that rank($\boldsymbol{PA}$) = rank($\boldsymbol{A}$). Then rank($\boldsymbol{A}^T\boldsymbol{PA}$) = rank($\boldsymbol{A}$).*

Proof. As a symmetric positive-semidefinite matrix, $\boldsymbol{P}$ has a unique symmetric positive-semidefinite square root $\sqrt{\boldsymbol{P}}$. Using proposition A.5 twice leads to the following inequalities:

$$\text{rank}(\boldsymbol{PA}) = \text{rank}(\sqrt{\boldsymbol{P}}\sqrt{\boldsymbol{P}}\boldsymbol{A}) \leq \text{rank}(\sqrt{\boldsymbol{P}}\boldsymbol{A}) \leq \text{rank}(\boldsymbol{A})$$

The hypothesis that $\text{rank}(\boldsymbol{PA}) = \text{rank}(\boldsymbol{A})$ therefore implies that $\text{rank}(\sqrt{\boldsymbol{P}}\boldsymbol{A}) = \text{rank}(\boldsymbol{A})$, so that, according to proposition A.4,

$$\text{rank}(\boldsymbol{A}^T\boldsymbol{PA}) = \text{rank}((\sqrt{\boldsymbol{P}}\boldsymbol{A})^T(\sqrt{\boldsymbol{P}}\boldsymbol{A})) = \text{rank}(\sqrt{\boldsymbol{P}}\boldsymbol{A}) = \text{rank}(\boldsymbol{A})$$

□

Corollary A.8. *Let $\boldsymbol{A}$ be any $m \times n$ real matrix and $\boldsymbol{P}$ be any $n \times n$ symmetric positive definite matrix. Then rank($\boldsymbol{A}^T\boldsymbol{PA}$) = rank($\boldsymbol{A}$).*

Proof. As a symmetric positive definite matrix, $\boldsymbol{P}$ is invertible, hence of rank n. Proposition A.6 therefore implies that $\text{rank}(\boldsymbol{PA}) = \text{rank}(\boldsymbol{A})$. Proposition A.7 completes the proof. □

Corollary A.9. *Let $\boldsymbol{A}$ be any $m \times n$ real matrix and $\boldsymbol{P}$ be any $n \times n$ symmetric positive semidefinite matrix such that rank($\boldsymbol{PA}$) = rank($\boldsymbol{A}$). Then Im($\boldsymbol{A}^T\boldsymbol{PA}$) = Im($\boldsymbol{A}^T$).*

Proof. $\text{Im}(\boldsymbol{A}^T\boldsymbol{PA})$ is trivially included in $\text{Im}(\boldsymbol{A}^T)$. But according to proposition A.6, both these subspaces have the same dimension. They are therefore equal. □

Proposition A.10. *Let $\boldsymbol{A}$ and $\boldsymbol{B}$ be two $n \times p$ matrices of rank p with $p \leq n$. Then $\boldsymbol{A}^T\boldsymbol{B}$ is invertible if and only if:*

- *rank($\boldsymbol{A}$) = rank($\boldsymbol{B}$) = p;*
- *Im($\boldsymbol{B}$) and Ker($\boldsymbol{A}^T$) are direct complementary subspaces of $\mathbb{R}^n$.*

Proof. Let first suppose that the $p \times p$ matrix $\boldsymbol{A}^T\boldsymbol{B}$ is invertible, i.e. of rank p. Proposition A.5 implies that $\text{rank}(\boldsymbol{A}) = \text{rank}(\boldsymbol{B}) = p$, i.e. that $\dim(\text{Im}(\boldsymbol{B})) = p$ and $\dim(\text{Ker}(\boldsymbol{A}^T)) = n - p$. Now, let $\boldsymbol{x} \in \text{Im}(\boldsymbol{B}) \cap \text{Ker}(\boldsymbol{A}^T)$. There exists $\boldsymbol{y} \in \mathbb{R}^n$ such that $\boldsymbol{x} = \boldsymbol{By}$. But as $\boldsymbol{x} \in \text{Ker}(\boldsymbol{A}^T)$, $\boldsymbol{A}^T\boldsymbol{x} = \boldsymbol{A}^T\boldsymbol{By} = \boldsymbol{0}$. And since $\boldsymbol{A}^T\boldsymbol{B}$ is invertible, $\boldsymbol{y}$ and $\boldsymbol{x}$ are necessarily $\boldsymbol{0}$. The dimensions of $\text{Im}(\boldsymbol{B})$ and $\text{Ker}(\boldsymbol{A}^T)$ sum up to n and their intersection is restricted to $\{\boldsymbol{0}\}$. They are therefore direct complementary subspaces of $\mathbb{R}^n$.

Let us now suppose that $\text{rank}(\boldsymbol{A}) = \text{rank}(\boldsymbol{B}) = p$ and that $\text{Im}(\boldsymbol{B})$ and $\text{Ker}(\boldsymbol{A}^T)$ are direct complementary subspaces of $\mathbb{R}^n$. The intersection of these two subspaces is restricted to $\{\boldsymbol{0}\}$. Consequently, $\forall \boldsymbol{x} \in \text{Im}(\boldsymbol{B})$, $\boldsymbol{A}^T\boldsymbol{x} = \boldsymbol{0}$ if and only if $\boldsymbol{x} = \boldsymbol{0}$. Now, let $\boldsymbol{y} \in \mathbb{R}^p$. $\boldsymbol{By}$ lies in $\text{Im}(\boldsymbol{B})$ so that $\boldsymbol{A}^T\boldsymbol{By} = \boldsymbol{0}$ if and only if $\boldsymbol{By} = \boldsymbol{0}$. And, as $\boldsymbol{B}$ is of full rank, $\boldsymbol{A}^T\boldsymbol{By} = \boldsymbol{0}$ if and only if $\boldsymbol{y} = \boldsymbol{0}$. This last statement means that $\text{Ker}(\boldsymbol{A}^T\boldsymbol{B}) = \{\boldsymbol{0}\}$, i.e. that $\boldsymbol{A}^T\boldsymbol{B}$ is of full rank and hence invertible. □

Proposition A.11. *Let $\boldsymbol{N}$ be any $p \times p$ symmetric positive semidefinite matrix, let $\boldsymbol{C}$ be any $p \times c$ matrix of rank r such that rank($[\boldsymbol{N}\ \boldsymbol{C}]$) = p and let $\boldsymbol{B}$ denote any $p \times p - r$ matrix whose columns form a basis of Ker($\boldsymbol{C}^T$). Then Im($\boldsymbol{C}$) and Im($\boldsymbol{NB}$) are direct complementary subspaces of $\mathbb{R}^p$.*

Proof. According to proposition A.6, the fact that rank($[\boldsymbol{N}\ \boldsymbol{C}]$) $= p$ implies that rank($\boldsymbol{B}^T[\boldsymbol{N}\ \boldsymbol{C}]$) $=$ rank($\boldsymbol{B}^T$). As the column vectors of $\boldsymbol{B}$ lie in Ker($\boldsymbol{C}^T$), $\boldsymbol{C}^T\boldsymbol{B} = \boldsymbol{0}$, so that $\boldsymbol{B}^T[\boldsymbol{N}\ \boldsymbol{C}] = [\boldsymbol{B}^T\boldsymbol{N}\ \boldsymbol{0}]$ and that Im($\boldsymbol{B}^T[\boldsymbol{N}\ \boldsymbol{C}]$) $=$ Im($\boldsymbol{B}^T\boldsymbol{N}$). Consequently, rank($\boldsymbol{B}^T\boldsymbol{N}$) $=$ rank($\boldsymbol{B}^T[\boldsymbol{N}\ \boldsymbol{C}]$) $=$ rank($\boldsymbol{B}^T$) and, according to proposition A.7, rank($\boldsymbol{B}^T\boldsymbol{N}\boldsymbol{B}$) $=$ rank($\boldsymbol{B}$). As its columns form a basis of the $p-r$-dimensional subspace Ker($\boldsymbol{C}^T$), $\boldsymbol{B}$ is of rank $p-r$. The $p-r \times p-r$ matrix $\boldsymbol{B}^T\boldsymbol{N}\boldsymbol{B}$ is therefore invertible. Proposition A.10 completes the proof. □

Corollary A.12. *Let* $\boldsymbol{N}$ *be any* $p \times p$ *symmetric positive semidefinite matrix, let* $c = p -$ *rank*($\boldsymbol{N}$)*, let* $\boldsymbol{C}$ *be a* $p \times c$ *full-rank matrix such that rank*($[\boldsymbol{N}\ \boldsymbol{C}]$) $= p$ *and let* $\boldsymbol{B}$ *denote any* $p \times p - c$ *matrix whose columns form a basis of Ker*($\boldsymbol{C}^T$)*. Then Im*($\boldsymbol{C}$) *and Im*($\boldsymbol{N}\boldsymbol{B}$) $=$ *Im*($\boldsymbol{N}$) *are direct complementary subspaces of* $\mathbb{R}^p$*.*

Proof. Corollary A.12 is a particular case of proposition A.11. The only additional thing to be proven is that Im($\boldsymbol{N}\boldsymbol{B}$) $=$ Im($\boldsymbol{N}$). The inclusion Im($\boldsymbol{N}\boldsymbol{B}$) $\subset$ Im($\boldsymbol{N}$) is trivial. There just remains to prove that both subspaces have the same dimension. According to proposition A.11, dim(Im($\boldsymbol{N}\boldsymbol{B}$)) $=$ dim(Ker($\boldsymbol{C}^T$)). But under the hypotheses of corollary A.12, dim(Ker($\boldsymbol{C}^T$)) $= p - c =$ rank($\boldsymbol{N}$), so that dim(Im($\boldsymbol{N}\boldsymbol{B}$)) $=$ dim(Im($\boldsymbol{N}$)). □

A.2 Projections

Let E and F be two direct complementary subspaces of $\mathbb{R}^n$. For all $\boldsymbol{x} \in \mathbb{R}^n$, there exist a unique pair $(\boldsymbol{y}, \boldsymbol{z}) \in E \times F$ such that $\boldsymbol{x} = \boldsymbol{y} + \boldsymbol{z}$. The linear application that associates, to each $\boldsymbol{x}$, the corresponding $\boldsymbol{y}$ is called projection onto E parallelly to F. The complementary application that associates, to each $\boldsymbol{x}$, the corresponding $\boldsymbol{z}$ is the projection onto F parallelly to E. Both complementary projections obviously sum up to the identity application. If $\mathbb{R}^n$ is equipped with some dot product, the orthogonal projection onto E is defined as the projection onto E parallelly to its orthogonal complement.

Let us give some properties of projections.

Proposition A.13. *A linear application* p *is the projection onto* E *parallelly to* F *if and only if* p *is idempotent, Im*(p) $= E$ *and Ker*(p) $= F$*.*

Proof. From the definition above, it is obvious that, if p is the projection onto E parallelly to F, then p is idempotent, Im(p) $= E$ and Ker(p) $= F$. Let us now suppose that p is idempotent, Im(p) $= E$ and Ker(p) $= F$. Im(p) $= E$ means that, $\forall \boldsymbol{x} \in E$, there exists $\boldsymbol{y}$ in $\mathbb{R}^n$ such that $\boldsymbol{x} = p(\boldsymbol{y})$. The fact that p is idempotent then implies that $p(\boldsymbol{x}) = p(p(\boldsymbol{y})) = p(\boldsymbol{y}) = \boldsymbol{x}$, so that, $\forall \boldsymbol{x} \in E$, $p(\boldsymbol{x}) = \boldsymbol{x}$.

Consider now any $\boldsymbol{x} \in \mathbb{R}^n$ and its unique decomposition into $\boldsymbol{x} = \boldsymbol{y} + \boldsymbol{z}$ with $(\boldsymbol{y}, \boldsymbol{z}) \in E \times F$. The linearity of p implies that $p(\boldsymbol{x}) = p(\boldsymbol{y}) + p(\boldsymbol{z})$. As $\boldsymbol{z} \in F =$ Ker(p), $p(\boldsymbol{z}) = \boldsymbol{0}$, and as $\boldsymbol{y} \in E$, $p(\boldsymbol{y}) = \boldsymbol{y}$, so that $p(\boldsymbol{x}) = \boldsymbol{y}$. This proves that p is the projection onto E parallelly to F. □

Proposition A.14. *Let* $\boldsymbol{A}$ *be any matrix whose columns form a basis of* E *and* $\boldsymbol{B}$ *a full rank matrix such that Ker*($\boldsymbol{B}^T$) $= F$*. Then, the matrix form of the projection onto* E *parallelly to* F *is* $\boldsymbol{A}(\boldsymbol{B}^T\boldsymbol{A})^{-1}\boldsymbol{B}^T$*.*

Proof. A and B are two full-rank matrices such that $\mathrm{Im}(A)$ and $\mathrm{Ker}(B^T)$ are two complementary subspaces of $\mathbb{R}^n$, so that proposition A.10 first ensures the invertibility of $B^T A$.

Let us now consider the linear application $p : x \hookrightarrow A(B^T A)^{-1} B^T x$. It is obvious that p is idempotent, that $\mathrm{Im}(p) \subset \mathrm{Im}(A)$ and that $\mathrm{Ker}(p) \subset \mathrm{Ker}(B^T)$. Consequently, $\dim(\mathrm{Im}(p)) \leq \dim(\mathrm{Im}(A))$ and $\dim(\mathrm{Ker}(p)) \leq \dim(\mathrm{Ker}(B^T)) = n - \dim(\mathrm{Im}(A))$. But according to proposition A.4, $\dim(\mathrm{Im}(p)) + \dim(\mathrm{Ker}(p)) = n$, so that the above inclusions are necessarily equalities. p is idempotent, $\mathrm{Im}(p) = \mathrm{Im}(A) = E$ and $\mathrm{Ker}(p) = \mathrm{Ker}(B^T) = F$. p is therefore the projection onto E parallelly to F. ☐

Proposition A.15. *Let A be any matrix whose columns form a basis of E. In $\mathbb{R}^n$ equipped with the standard dot product, the matrix form of the orthogonal projection onto E is $A(A^T A)^{-1} A^T$.*

Proof. According to proposition A.4, $\mathrm{Ker}(A^T)$ is the orthogonal complement of $\mathrm{Im}(A) = E$ in $\mathbb{R}^n$ equipped with the standard dot product. A is thus a full rank matrix such that $\mathrm{Ker}(A^T)$ is the orthogonal complement of E. Proposition A.13 completes the proof. ☐

Proposition A.16. *Let A be any matrix whose columns form a basis of E. In $\mathbb{R}^n$ equipped with the dot product $< x, y >= x^T P y$, P being an $n \times n$ symmetric positive definite matrix, the matrix form of the orthogonal projection onto E is $A(A^T P A)^{-1} A^T P$.*

Proof. $\mathrm{Ker}(A^T P)$ is trivially included in the orthogonal complement of $\mathrm{Im}(A) = E$. According to proposition A.6, $\mathrm{rank}(A^T P) = \mathrm{rank}(A)$, so that $\dim(\mathrm{Ker}(A^T P)) = \dim(\mathrm{Ker}(A^T)) = n - \dim(\mathrm{Im}(A))$. $\mathrm{Ker}(A^T P)$ is therefore the orthogonal complement of E, and $A^T P$ is of full rank. Proposition A.13 completes the proof. ☐

A.3 Other useful propositions

Proposition A.17 (Block matrix inversion formula - I). *Let $M = \begin{bmatrix} A & B \\ C & D \end{bmatrix}$ be a square invertible matrix such that its upper left block A is also invertible. Then, $D - CA^{-1}B$ is invertible and the inverse of M can be expressed as:*

$$M^{-1} = \begin{bmatrix} A^{-1} + A^{-1}B(D - CA^{-1}B)^{-1}CA^{-1} & -A^{-1}B(D - CA^{-1}B)^{-1} \\ -(D - CA^{-1}B)^{-1}CA^{-1} & (D - CA^{-1}B)^{-1} \end{bmatrix}$$

Proof. Since A is invertible, M can be decomposed into the following product:

$$M = \begin{bmatrix} A & 0 \\ C & I \end{bmatrix} \begin{bmatrix} I & A^{-1}B \\ 0 & D - CA^{-1}B \end{bmatrix}$$

Since the determinant of the product of two square matrices is the product of their determinants,

$$\det(M) = \det\left(\begin{bmatrix} A & 0 \\ C & I \end{bmatrix}\right) \det\left(\begin{bmatrix} I & A^{-1}B \\ 0 & D - CA^{-1}B \end{bmatrix}\right)$$

And since the determinant of a triangular block matrix is the product of the determinants of its diagonal blocks,

$$\det(M) = \det(A)\det(D - CA^{-1}B)$$

As M and A are invertible, their determinants are both different from zero, so that the determinant of $D - CA^{-1}B$ is necessarily also different from zero and that $D - CA^{-1}B$ is invertible.

To complete the proof, form the product of M with the expression of M^{-1} given above. It simplifies to I. □

Proposition A.18 (Block matrix inversion formula - II). *Let* $M = \begin{bmatrix} A & B \\ C & D \end{bmatrix}$ *be a square invertible matrix such that its lower right block* D *is also invertible. Then,* $A - BD^{-1}C$ *is invertible and the inverse of* M *can be expressed as:*

$$M^{-1} = \begin{bmatrix} (A - BD^{-1}C)^{-1} & -(A - BD^{-1}C)^{-1}BD^{-1} \\ -D^{-1}C(A - BD^{-1}C)^{-1} & D^{-1} + D^{-1}C(A - BD^{-1}C)^{-1}BD^{-1} \end{bmatrix}$$

Proof. Proposition A.18 can be proven in the same way as proposition A.17, using the following decomposition of M:

$$M = \begin{bmatrix} A - BD^{-1}C & BD^{-1} \\ 0 & I \end{bmatrix} \begin{bmatrix} I & 0 \\ C & D \end{bmatrix}$$

□

Proposition A.19. *Let* M *be a* $n \times n$ *invertible matrix,* A *a* $n \times m$ *full-rank matrix* $(0 < m < n)$ *and* B *a* $n \times n - m$ *matrix whose columns form a basis of* $Ker(A^T)$. *Then:*

$$M - MA(A^TMA)^{-1}A^TM = B(B^TM^{-1}B)^{-1}B^T$$

Proof. The columns of $R = [A\ B]$ form a basis of $\mathbb{R}^n$. R is therefore invertible and its inverse can be expressed as:

$$R^{-1} = \begin{bmatrix} (A^TA)^{-1}A^T \\ (B^TB)^{-1}B^T \end{bmatrix}$$

To prove this expression of R^{-1}, right-multiply it with R. As $A^TB = 0$ and $B^TA = 0$, this product simplifies to I. Forming the other product, RR^{-1}, leads to:

$$A(A^TA)^{-1}A^T + B(B^TB)^{-1}B^T = I$$

The product:

$$R^TMR = \begin{bmatrix} A^TMA & A^TMB \\ B^TMA & B^TMB \end{bmatrix}$$

is itself invertible. Using the matrix block inversion formula (A.17), the right-bottom block X of $(R^TMR)^{-1}$ can be expressed as:

$$X = \left(B^TMB - B^TMA(A^TMA)^{-1}A^TMB\right)^{-1}$$

On the other hand:

$$(R^TMR)^{-1} = R^{-1}M^{-1}(R^{-1})^T$$

so that another expression of the right-bottom block of $(R^TMR)^{-1}$ is:

$$X = (B^TB)^{-1}B^TM^{-1}B(B^TB)^{-1}$$

Both expressions of $\boldsymbol{X}$ given above lead to two expressions of $\boldsymbol{Y} = \boldsymbol{B}(\boldsymbol{B}^T\boldsymbol{B})^{-1}\boldsymbol{X}^{-1}(\boldsymbol{B}^T\boldsymbol{B})^{-1}\boldsymbol{B}^T$:

$$\boldsymbol{Y} = \boldsymbol{B}(\boldsymbol{B}^T\boldsymbol{B})^{-1}\boldsymbol{B}^T\left(\boldsymbol{M} - \boldsymbol{M}\boldsymbol{A}(\boldsymbol{A}^T\boldsymbol{M}\boldsymbol{A})^{-1}\boldsymbol{A}^T\boldsymbol{M}\right)\boldsymbol{B}(\boldsymbol{B}^T\boldsymbol{B})^{-1}\boldsymbol{B}^T$$

$$\boldsymbol{Y} = \boldsymbol{B}(\boldsymbol{B}^T\boldsymbol{M}^{-1}\boldsymbol{B})^{-1}\boldsymbol{B}^T$$

Replacing $\boldsymbol{B}(\boldsymbol{B}^T\boldsymbol{B})^{-1}\boldsymbol{B}^T$ by $\boldsymbol{I} - \boldsymbol{A}(\boldsymbol{A}^T\boldsymbol{A})^{-1}\boldsymbol{A}^T$ in the first expression of $\boldsymbol{Y}$ leads, after simplification, to:

$$\boldsymbol{Y} = \boldsymbol{M} - \boldsymbol{M}\boldsymbol{A}(\boldsymbol{A}^T\boldsymbol{M}\boldsymbol{A})^{-1}\boldsymbol{A}^T\boldsymbol{M}$$

The comparison of the two last equations completes the proof. □

Appendix B

The basics of geodetic least-squares regression

B.1 Generalized least-squares regression

Consider a vector $\boldsymbol{l} = [l_1, l_2, ..., l_n]^T$ of n observations. From physical and mathematical considerations, it is expected that these observations can be explained by a set of p parameters $\boldsymbol{x} = [x_1, x_2, ..., x_p]^T$ through the predictive model:

$$\boldsymbol{f} : \left\{ \begin{array}{ccc} \mathbb{R}^p & \rightarrow & \mathbb{R}^n \\ \boldsymbol{x} & \hookrightarrow & \boldsymbol{f}(\boldsymbol{x}) \end{array} \right. \tag{B.1}$$

Parameter regression consists in inferring a set of optimal (best fitting) parameters from the observations $\boldsymbol{l}$. There exists various regression methods associated with different optimality criteria. We consider here the generalized least-squares regression method which is widely used in the geodetic community.

In generalized least-squares regression, it is assumed that the observations have a known covariance matrix $\boldsymbol{Q_l}$. $\boldsymbol{P_l} = \boldsymbol{Q_l}^{-1}$ is called the weight matrix of the observations. Specifying a weight matrix for the observations corresponds to the choice of a particular metric[1] in the observation space $\mathbb{R}^n$, i.e. of an inner product $< \boldsymbol{l}, \boldsymbol{l}' >= \boldsymbol{l}^T \boldsymbol{P_l} \boldsymbol{l}'$ and of the associated norm $||\boldsymbol{l}|| = \sqrt{\boldsymbol{l}^T \boldsymbol{P_l} \boldsymbol{l}}$. Let us call E the Hilbert observation space $\mathbb{R}^n$ equipped with this metric.

The generalized least-squares criterion to find best fitting parameters $\hat{\boldsymbol{x}}$ is the

---

[1] The choice of this particular metric may seem arbitrary. But $\boldsymbol{P_l}$ is in fact an optimal weight matrix in the sense that it leads to a minimum parameter variance (Dermanis, 1977).

minimization of the (squared) distance between $\boldsymbol{l}$ and $\boldsymbol{f}(\boldsymbol{x})$ in E:

$$\begin{aligned} \hat{\boldsymbol{x}} &= \underset{\boldsymbol{x}\in\mathbb{R}^p}{\operatorname{argmin}}(\|\boldsymbol{l}-\boldsymbol{f}(\boldsymbol{x})\|^2) \\ &= \underset{\boldsymbol{x}\in\mathbb{R}^p}{\operatorname{argmin}}\left((\boldsymbol{l}-\boldsymbol{f}(\boldsymbol{x}))^T \boldsymbol{P_l}(\boldsymbol{l}-\boldsymbol{f}(\boldsymbol{x}))\right) \end{aligned} \tag{B.2}$$

To explicitly compute $\hat{\boldsymbol{x}}$ in practice, one first has to linearize the predictive function $\boldsymbol{f}$ around an a priori set of parameters $\boldsymbol{x}_0$ and then solve for $\boldsymbol{\delta x} = \boldsymbol{x} - \boldsymbol{x}_0$. But for sake of notation simplicity, we assume here that the problem was linearized beforehand, i.e. that $\boldsymbol{f}(\boldsymbol{x}) = \boldsymbol{Ax}$, where $\boldsymbol{A} = \partial\boldsymbol{f}/\partial\boldsymbol{x}$ is an $n \times p$ matrix called design matrix. Under this assumption:

$$\begin{aligned} \|\boldsymbol{l}-\boldsymbol{f}(\boldsymbol{x})\|^2 &= (\boldsymbol{l}-\boldsymbol{Ax})^T\boldsymbol{P_l}(\boldsymbol{l}-\boldsymbol{Ax}) \\ &= \boldsymbol{l}^T\boldsymbol{P_l}\boldsymbol{l} - 2\boldsymbol{l}^T\boldsymbol{P_l}\boldsymbol{Ax} + \boldsymbol{x}^T\boldsymbol{A}^T\boldsymbol{P_l}\boldsymbol{Ax} \end{aligned} \tag{B.3}$$

A necessary condition to minimize $\|\boldsymbol{l}-\boldsymbol{f}(\boldsymbol{x})\|^2$, is to nullify the partial derivatives:

$$\frac{\partial\|\boldsymbol{l}-\boldsymbol{f}(\boldsymbol{x})\|^2}{\partial\boldsymbol{x}} = -2\boldsymbol{l}^T\boldsymbol{P_l}\boldsymbol{A} + 2\boldsymbol{x}^T\boldsymbol{A}^T\boldsymbol{P_l}\boldsymbol{A} \tag{B.4}$$

This condition leads to the well-known normal equation:

$$\begin{aligned} (\boldsymbol{A}^T\boldsymbol{P_l}\boldsymbol{A})\boldsymbol{x} &= \boldsymbol{A}^T\boldsymbol{P_l}\boldsymbol{l} \\ \Leftrightarrow \qquad \boldsymbol{Nx} &= \boldsymbol{b} \end{aligned} \tag{B.5}$$

where $\boldsymbol{N} = \boldsymbol{A}^T\boldsymbol{P_l}\boldsymbol{A}$ is called normal matrix and $\boldsymbol{b} = \boldsymbol{A}^T\boldsymbol{P_l}\boldsymbol{l}$.

In case where the design matrix $\boldsymbol{A}$ is of full rank, the normal matrix $\boldsymbol{N}$ is invertible (corollary A.8) so that the normal equation has a unique solution:

$$\hat{\boldsymbol{x}} = \boldsymbol{N}^{-1}\boldsymbol{b} = (\boldsymbol{A}^T\boldsymbol{P_l}\boldsymbol{A})^{-1}\boldsymbol{A}^T\boldsymbol{P_l}\boldsymbol{l} \tag{B.6}$$

In virtue of the error propagation law, the estimated parameters $\hat{\boldsymbol{x}}$ have $\boldsymbol{Q} = \boldsymbol{N}^{-1}$ as covariance matrix. The observations predicted by the estimated parameters are $\boldsymbol{A}\hat{\boldsymbol{x}} = \boldsymbol{A}(\boldsymbol{A}^T\boldsymbol{P_l}\boldsymbol{A})^{-1}\boldsymbol{A}^T\boldsymbol{P_l}\boldsymbol{l}$, while $\hat{\boldsymbol{v}} = \boldsymbol{l} - \boldsymbol{A}\hat{\boldsymbol{x}}$ are the residuals of the fit.

Noting that $\boldsymbol{A}(\boldsymbol{A}^T\boldsymbol{P_l}\boldsymbol{A})^{-1}\boldsymbol{A}^T\boldsymbol{P_l}$ is the matrix of the orthogonal projector onto $\mathrm{Im}(\boldsymbol{A})$ in E allows a simple geometric interpretation of the generalized least-squares regression illustrated in Fig. B.1. $\mathrm{Im}(\boldsymbol{A}) = \{\boldsymbol{Ax}, \boldsymbol{x} \in \mathbb{R}^p\}$ is the subspace of E which spans all possible model predictions. Fitting parameters $\boldsymbol{x}$ to the observations $\boldsymbol{l}$ consists in splitting them into the sum of a predicted part $\boldsymbol{Ax} \in \mathrm{Im}(\boldsymbol{A})$ and of residuals $\boldsymbol{l} - \boldsymbol{Ax}$. Generalized least-squares do this by orthogonally projecting $\boldsymbol{l}$ onto $\mathrm{Im}(\boldsymbol{A})$, which obviously ensures that $\|\hat{\boldsymbol{v}}\| = \|\boldsymbol{l} - \boldsymbol{A}\hat{\boldsymbol{x}}\|$ is minimal.

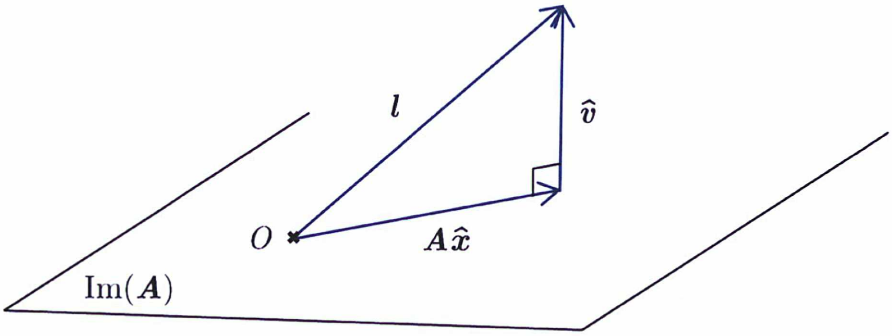

Figure B.1 Generalized least-squares regression as an orthogonal projection onto Im(A)

B.2 Constraints

In many geodetic problems, the design matrix $\boldsymbol{A}$ is not of full rank, so that the normal matrix $\boldsymbol{N}$ is not invertible and that the normal equation B.5 has an infinite number of solutions. The singularities inherent to the data analysis of the four geodetic techniques contributing to the ITRF are for instance discussed in Sect. 1.2.1. So as to supplement the rank deficiencies of $\boldsymbol{A}$ and $\boldsymbol{N}$ and thus obtain a unique set of best fitting parameters, a common practice in geodesy is the application of constraints. Constraints can generically be defined as linear relationships that should be satisfied by the estimated parameters[2]:

$$\boldsymbol{C}^T \boldsymbol{x} = \boldsymbol{0} \tag{B.7}$$

where $\boldsymbol{C}^T$ is a $c \times p$ full-rank matrix whose lines define c linear relationships among the parameters, i.e. c constraints.

Constraints can concretely be applied in two different ways in a generalized least-squares regression. These two ways are distinguished in the two next subsections. Special cases of constraints are discussed in the following subsections.

B.2.1 Constraints as pseudo-observations

The first way of applying constraints in a generalized least-squares problem is to introduce them as pseudo-observations associated with a $c \times c$ weight matrix $\boldsymbol{P}_c$.

---

[2] The particular choice of $\boldsymbol{0}$ as second member of Eq. B.7 in fact corresponds to the application of constraints with respect to the a priori parameters $\boldsymbol{x}_0$. Provided that $\boldsymbol{C}^T$ is of full rank, it is always possible to get back to this case by choosing appropriate a priori parameters.

The observation vector and the observation weight matrix are thus extended to:

$$\boldsymbol{l}_c = \begin{bmatrix} \boldsymbol{l} \\ 0 \end{bmatrix} \text{ and } \boldsymbol{P}_{l,c} = \begin{bmatrix} \boldsymbol{P}_l & 0 \\ 0 & \boldsymbol{P}_c \end{bmatrix} \tag{B.8}$$

while the model function and the design matrix are extended to:

$$\boldsymbol{f}_c : \left\{ \begin{array}{ccc} \mathbb{R}^p & \rightarrow & \mathbb{R}^{n+c} \\ \boldsymbol{x} & \hookrightarrow & \begin{bmatrix} \boldsymbol{A}\boldsymbol{x} \\ \boldsymbol{C}^T\boldsymbol{x} \end{bmatrix} \end{array} \right. \text{ and } \boldsymbol{A}_c = \begin{bmatrix} \boldsymbol{A} \\ \boldsymbol{C}^T \end{bmatrix} \tag{B.9}$$

This defines an extended least-squares regression problem which leads to the constrained normal equation:

$$\begin{array}{rrcl} & \left(\boldsymbol{A}^T\boldsymbol{P}_l\boldsymbol{A} + \boldsymbol{C}\boldsymbol{P}_c\boldsymbol{C}^T\right)\boldsymbol{x} & = & \boldsymbol{A}^T\boldsymbol{P}_l\boldsymbol{l} \\ \Leftrightarrow & (\boldsymbol{N} + \boldsymbol{N}_c)\boldsymbol{x} & = & \boldsymbol{b} \end{array} \tag{B.10}$$

where $\boldsymbol{N}_c = \boldsymbol{C}\boldsymbol{P}_c\boldsymbol{C}^T$ is the normal matrix of constraints.

Provided that $\operatorname{rank}(\boldsymbol{A}_c) = p$, i.e. that the introduced constraints properly supplement the rank deficiencies of $\boldsymbol{A}$, the constrained normal matrix $\boldsymbol{N} + \boldsymbol{N}_c$ is invertible (corollary A.8), so that the constrained normal equation B.10 has a unique solution:

$$\hat{\boldsymbol{x}}_c = (\boldsymbol{N} + \boldsymbol{N}_c)^{-1}\boldsymbol{b} \tag{B.11}$$

which has $\boldsymbol{Q}_c = (\boldsymbol{N} + \boldsymbol{N}_c)^{-1}$ as covariance matrix. As a curiosity, let us give the following expression of $\boldsymbol{Q}_c$, valid in case where $\boldsymbol{C}$ is of full rank:

$$\begin{array}{rcl} \boldsymbol{Q}_c & = & \boldsymbol{B}\left(\boldsymbol{B}^T\boldsymbol{N}\boldsymbol{B}\right)^{-1}\boldsymbol{B}^T \\ & + & \boldsymbol{D}(\boldsymbol{C}^T\boldsymbol{D})^{-1}\left(\boldsymbol{P}_c + (\boldsymbol{C}^T\boldsymbol{D})^{-1}\boldsymbol{D}^T\boldsymbol{N}\boldsymbol{D}(\boldsymbol{D}^T\boldsymbol{C})^{-1}\right)^{-1}(\boldsymbol{D}^T\boldsymbol{C})^{-1}\boldsymbol{D}^T \end{array} \tag{B.12}$$

where $\boldsymbol{B}$ denotes any matrix whose columns form a basis of $\operatorname{Ker}(\boldsymbol{C}^T)$ and $\boldsymbol{D}$ denotes any matrix whose columns form a basis of $\operatorname{Ker}(\boldsymbol{B}^T\boldsymbol{N})$.

B.2.2 Constraints as condition equations

The second way of introducing constraints in a generalized least-squares regression consists in reducing the parameter search space to the only sets of parameters which strictly satisfy the constraint equation B.7, i.e. to $\operatorname{Ker}(\boldsymbol{C}^T) = \left\{\boldsymbol{x} \in \mathbb{R}^p / \boldsymbol{C}^T\boldsymbol{x} = \boldsymbol{0}\right\}$. The constrained problem can in this case be written:

$$\hat{\boldsymbol{x}}_c = \underset{\boldsymbol{x} \in \mathsf{Ker}(\boldsymbol{C}^T)}{\operatorname{argmin}} \left(\|\boldsymbol{l} - \boldsymbol{f}(\boldsymbol{x})\|^2\right) \tag{B.13}$$

It can be solved with the method of Lagrange multipliers (hereafter denoted by $\boldsymbol{\lambda}$) through the auxiliary problem:

$$(\hat{\boldsymbol{x}}_c, \hat{\boldsymbol{\lambda}}) = \underset{\boldsymbol{x}\in\mathbb{R}^p, \boldsymbol{\lambda}\in\mathbb{R}^c}{\operatorname{argmin}} \left(\|\boldsymbol{l} - \boldsymbol{f}(\boldsymbol{x}) + \boldsymbol{\lambda}^T \boldsymbol{C}^T \boldsymbol{x}\|^2\right) \tag{B.14}$$

Derivating the cost function in Eq. B.14 with respect to $\boldsymbol{x}$ and $\boldsymbol{\lambda}$ leads to the following normal equation extended with condition equations:

$$\begin{aligned} &\begin{bmatrix} \boldsymbol{A}^T \boldsymbol{P}_l \boldsymbol{A} & \boldsymbol{C} \\ \boldsymbol{C}^T & 0 \end{bmatrix} \begin{bmatrix} \boldsymbol{x} \\ \boldsymbol{\lambda} \end{bmatrix} = \begin{bmatrix} \boldsymbol{A}^T \boldsymbol{P}_l \boldsymbol{l} \\ 0 \end{bmatrix} \\ \Leftrightarrow \quad &\begin{bmatrix} \boldsymbol{N} & \boldsymbol{C} \\ \boldsymbol{C}^T & 0 \end{bmatrix} \begin{bmatrix} \boldsymbol{x} \\ \boldsymbol{\lambda} \end{bmatrix} = \begin{bmatrix} \boldsymbol{b} \\ 0 \end{bmatrix} \end{aligned} \tag{B.15}$$

Provided that $\boldsymbol{C}$ is of full rank and that $\operatorname{rank}([\boldsymbol{A}^T \boldsymbol{C}]) = p$, i.e. that the introduced constraints are not redundant and properly supplement the rank deficiencies of $\boldsymbol{A}$, the extended normal matrix is invertible (see proof below) so that the extended normal equation B.15 has a unique solution:

$$\begin{bmatrix} \hat{\boldsymbol{x}}_c \\ \hat{\boldsymbol{\lambda}} \end{bmatrix} = \begin{bmatrix} \boldsymbol{N} & \boldsymbol{C} \\ \boldsymbol{C}^T & 0 \end{bmatrix}^{-1} \begin{bmatrix} \boldsymbol{b} \\ 0 \end{bmatrix} \tag{B.16}$$

Let $\boldsymbol{B}$ denote any matrix whose columns form a basis of $\operatorname{Ker}(\boldsymbol{C}^T)$. It is shown below that the solution of the extended normal equation B.15 can be expressed as:

$$\hat{\boldsymbol{x}}_c = \boldsymbol{B}\left(\boldsymbol{B}^T \boldsymbol{N} \boldsymbol{B}\right)^{-1} \boldsymbol{B}^T \boldsymbol{b} = \boldsymbol{B}\left(\boldsymbol{B}^T \boldsymbol{N} \boldsymbol{B}\right)^{-1} \boldsymbol{B}^T \boldsymbol{A}^T \boldsymbol{P}_l \boldsymbol{l} \tag{B.17}$$

Propagating the covariance matrix $\boldsymbol{Q}_l = \boldsymbol{P}_l^{-1}$ of the observations to the estimated parameters $\hat{\boldsymbol{x}}_c$ using Eq. B.17 leads to the following expression of their covariance matrix:

$$\boldsymbol{Q}_c = \boldsymbol{B}\left(\boldsymbol{B}^T \boldsymbol{N} \boldsymbol{B}\right)^{-1} \boldsymbol{B}^T \tag{B.18}$$

It can finally be shown that the $p \times p$ upper-left block of the inverse of the extended normal matrix can be identified with $\boldsymbol{Q}_c$, which gives practical access to the covariance matrix of the estimated parameters.

Proof of the above assertions. The condition that $\operatorname{rank}([\boldsymbol{A}^T \boldsymbol{C}]) = p$ is equivalent to $\operatorname{Im}(\boldsymbol{A}^T) + \operatorname{Im}(\boldsymbol{C}) = \mathbb{R}^p$. According to corollary A.9, $\operatorname{Im}(\boldsymbol{N}) = \operatorname{Im}(\boldsymbol{A}^T)$. Therefore, $\operatorname{Im}(\boldsymbol{N}) + \operatorname{Im}(\boldsymbol{C}) = \mathbb{R}^p$ and $\operatorname{rank}([\boldsymbol{N}\ \boldsymbol{C}]) = p$. Let $\boldsymbol{B}$ denote any $p \times p - c$ matrix whose columns form a basis of $\operatorname{Ker}(\boldsymbol{C}^T)$. According to proposition A.11, $\operatorname{Im}(\boldsymbol{C})$ and $\operatorname{Im}(\boldsymbol{N}\boldsymbol{B})$ are direct complementary subspaces of $\mathbb{R}^p$. Their respective orthogonal complements, $\operatorname{Im}(\boldsymbol{C})^\perp = \operatorname{Ker}(\boldsymbol{C}^T) = \operatorname{Im}(\boldsymbol{B})$ and $\operatorname{Im}(\boldsymbol{N}\boldsymbol{B})^\perp = \operatorname{Ker}(\boldsymbol{B}^T\boldsymbol{N})$ are therefore direct complementary subspaces of $\mathbb{R}^p$ as well. One can consequently define the orthogonal projection onto $\operatorname{Im}(\boldsymbol{B})$ parallelly to $\operatorname{Ker}(\boldsymbol{B}^T\boldsymbol{N})$. According to proposition A.13, the matrix form of this projection is: $\boldsymbol{B}(\boldsymbol{B}^T\boldsymbol{N}\boldsymbol{B})^{-1}\boldsymbol{B}^T\boldsymbol{N}$. If $\boldsymbol{D}$ denotes any matrix whose columns form a basis of $\operatorname{Ker}(\boldsymbol{B}^T\boldsymbol{N})$, the complementary projection onto $\operatorname{Ker}(\boldsymbol{B}^T\boldsymbol{N})$ parallelly to $\operatorname{Im}(\boldsymbol{B}) = \operatorname{Ker}(\boldsymbol{C}^T)$ can be expressed as $\boldsymbol{D}(\boldsymbol{C}^T\boldsymbol{D})^{-1}\boldsymbol{C}^T$. Both projections sum up to the identity application, so that:

$$\boldsymbol{B}(\boldsymbol{B}^T\boldsymbol{N}\boldsymbol{B})^{-1}\boldsymbol{B}^T\boldsymbol{N} + \boldsymbol{D}(\boldsymbol{C}^T\boldsymbol{D})^{-1}\boldsymbol{C}^T = \boldsymbol{I}$$

One can additionally define the orthogonal projection onto $\mathrm{Im}(\boldsymbol{C})$ and the complementary orthogonal projection onto $\mathrm{Im}(\boldsymbol{C})^{\perp} = \mathrm{Ker}(\boldsymbol{C}^T) = \mathrm{Im}(\boldsymbol{B})$. According to proposition A.14, they can respectively be expressed as $\boldsymbol{C}(\boldsymbol{C}^T\boldsymbol{C})^{-1}\boldsymbol{C}^T$ and $\boldsymbol{B}(\boldsymbol{B}^T\boldsymbol{B})^{-1}\boldsymbol{B}^T$, so that:

$$\boldsymbol{B}(\boldsymbol{B}^T\boldsymbol{B})^{-1}\boldsymbol{B}^T + \boldsymbol{C}(\boldsymbol{C}^T\boldsymbol{C})^{-1}\boldsymbol{C}^T = \boldsymbol{I}$$

Let us now consider the following matrix:

$$\boldsymbol{R} = \begin{bmatrix} \boldsymbol{B}\left(\boldsymbol{B}^T\boldsymbol{N}\boldsymbol{B}\right)^{-1}\boldsymbol{B}^T & \boldsymbol{D}(\boldsymbol{C}^T\boldsymbol{D})^{-1} \\ (\boldsymbol{D}^T\boldsymbol{C})^{-1}\boldsymbol{D}^T & -(\boldsymbol{C}^T\boldsymbol{C})^{-1}\boldsymbol{C}^T\boldsymbol{N}\boldsymbol{D}(\boldsymbol{C}^T\boldsymbol{D})^{-1} \end{bmatrix}$$

Left-multiplying R with the extended normal matrix yields:

$$\begin{bmatrix} \boldsymbol{N} & \boldsymbol{C} \\ \boldsymbol{C}^T & \boldsymbol{0} \end{bmatrix} \boldsymbol{R} = \begin{bmatrix} \boldsymbol{N}\boldsymbol{B}\left(\boldsymbol{B}^T\boldsymbol{N}\boldsymbol{B}\right)^{-1}\boldsymbol{B}^T + \boldsymbol{C}(\boldsymbol{D}^T\boldsymbol{C})^{-1}\boldsymbol{D}^T & \left(\boldsymbol{I} - \boldsymbol{C}(\boldsymbol{C}^T\boldsymbol{C})^{-1}\boldsymbol{C}^T\right)\boldsymbol{N}\boldsymbol{D}(\boldsymbol{C}^T\boldsymbol{D})^{-1} \\ \boldsymbol{C}^T\boldsymbol{B}\left(\boldsymbol{B}^T\boldsymbol{N}\boldsymbol{B}\right)^{-1}\boldsymbol{B}^T & \boldsymbol{I} \end{bmatrix}$$

The upper-left block of this product was shown to be equal to $\boldsymbol{I}$. Since the columns of $\boldsymbol{B}$ lie in $\mathrm{Ker}(\boldsymbol{C}^T)$, $\boldsymbol{C}^T\boldsymbol{B} = \boldsymbol{0}$, so that the lower-left block is $\boldsymbol{0}$. Finally, the upper-right block can be rearranged into $\boldsymbol{B}(\boldsymbol{B}^T\boldsymbol{B})^{-1}\boldsymbol{B}^T\boldsymbol{N}\boldsymbol{D}(\boldsymbol{C}^T\boldsymbol{D})^{-1}$. Since the columns of $\boldsymbol{D}$ lie in $\mathrm{Ker}(\boldsymbol{B}^T\boldsymbol{N})$, $\boldsymbol{B}^T\boldsymbol{N}\boldsymbol{D} = \boldsymbol{0}$, so that this upper-right block is $\boldsymbol{0}$.

We have thus shown that the product of the extended normal matrix with $\boldsymbol{R}$ is $\boldsymbol{I}$. The extended normal matrix is thus invertible. Multiplying the expression of its inverse $\boldsymbol{R}$ given above with the right-hand side of the extended normal equation leads to the expression of $\hat{\boldsymbol{x}}_c$ given in Eq. B.17. From the expression of $\boldsymbol{R}$ given above, it is finally clear its upper-left block can be identified with the covariance matrix $\boldsymbol{Q}_c$ of the estimated parameters. □

B.2.3 Minimal constraints

The $c \times p$ constraint matrix $\boldsymbol{C}^T$ is said to define minimal constraints when $\mathrm{rank}([\boldsymbol{A}^T\ \boldsymbol{C}]) = p$ and $c = p - \mathrm{rank}(\boldsymbol{A}) = \dim(\mathrm{Ker}(\boldsymbol{A}))$. In other words, minimal constraints properly supplement the rank deficiencies of $\boldsymbol{A}$ with as few constraints as possible, i.e. a number of constraints c equal to the number of singularities of $\boldsymbol{A}$. Like any constraints, minimal constraints can be introduced as pseudo-observations or as condition equations.

Let $\boldsymbol{B}$ still denote a matrix whose columns form a basis of $\mathrm{Ker}(\boldsymbol{C}^T)$. In case where minimal constraints are introduced as condition equations, the expressions of the estimated parameters $\hat{\boldsymbol{x}}_c$ and of their covariance matrix $\boldsymbol{Q}_c$ given in Eq. B.17 and B.18 still hold.

According to corollary A.12, $\mathrm{Ker}(\boldsymbol{B}^T\boldsymbol{N}) = \mathrm{Ker}(\boldsymbol{N})$ in case of minimal constraints. Consequently, if $\boldsymbol{D}$ denotes a matrix whose columns form a basis of $\mathrm{Ker}(\boldsymbol{B}^T\boldsymbol{N})$, the columns of $\boldsymbol{D}$ lie in $\mathrm{Ker}(\boldsymbol{N})$ so that $\boldsymbol{N}\boldsymbol{D} = \boldsymbol{0}$. In case where minimal constraints are introduced as pseudo-observations, the expression of $\boldsymbol{Q}_c$ given in Eq. B.12 can thus be simplified into:

$$\boldsymbol{Q}_c = \boldsymbol{B}\left(\boldsymbol{B}^T\boldsymbol{N}\boldsymbol{B}\right)^{-1}\boldsymbol{B}^T + \boldsymbol{D}(\boldsymbol{C}^T\boldsymbol{D})^{-1}\boldsymbol{P}_c^{-1}(\boldsymbol{D}^T\boldsymbol{C})^{-1}\boldsymbol{D}^T \tag{B.19}$$

Right-multiplying this expression of $\boldsymbol{Q}_c$ with the right-hand side $\boldsymbol{b}$ of the constrained normal equation B.10 and noting that, since the columns of $\boldsymbol{D}$ lie in $\mathrm{Ker}(\boldsymbol{N}) = \mathrm{Ker}(\boldsymbol{A})$, $\boldsymbol{D}^T\boldsymbol{b} = \boldsymbol{D}^T\boldsymbol{A}^T\boldsymbol{P}_l\boldsymbol{l} = \boldsymbol{0}$, one gets the following expression of the estimated parameters in case where minimal constraints are introduced as pseudo-observations:

$$\hat{\boldsymbol{x}}_c = \boldsymbol{B}\left(\boldsymbol{B}^T\boldsymbol{N}\boldsymbol{B}\right)^{-1}\boldsymbol{B}^T\boldsymbol{b} \tag{B.20}$$

In case of minimal constraints, the pseudo-observation and the condition equation methods thus lead to the same set of estimated parameters, but with different covariance matrices. One can moreover note that, when the weights of the pseudo-observations tend to infinity, the covariance matrix obtained with the pseudo-observation method (Eq. B.19) tends to the covariance matrix obtained with the condition equation method (Eq. B.18). That is why it can be said that condition equations are equivalent to pseudo-observations with infinite weights.

It is also worth noting that the parameters estimated with minimal constraints satisfy the non-constrained normal equation, i.e. that $\boldsymbol{N}\hat{\boldsymbol{x}}_c = \boldsymbol{b}$. That is why minimal constraints can be said to be *non-distorting* constraints.

Proof. According to corollary A.12, $\mathrm{Im}(\boldsymbol{N})$ and $\mathrm{Im}(\boldsymbol{C})$ are direct complementary subspaces of $\mathbb{R}^p$. One can consequently define the projection onto $\mathrm{Im}(\boldsymbol{N})$ parallelly to $\mathrm{Im}(\boldsymbol{C}) = \mathrm{Ker}(\boldsymbol{B}^T)$. Since $\mathrm{Im}(\boldsymbol{N}) = \mathrm{Im}(\boldsymbol{N}\boldsymbol{B})$, the $p - c$ columns of $\boldsymbol{N}\boldsymbol{B}$ form a basis of $\mathrm{Im}(\boldsymbol{N})$, so that the matrix form of this projection is $\boldsymbol{N}\boldsymbol{B}(\boldsymbol{B}^T\boldsymbol{N}\boldsymbol{B})^{-1}\boldsymbol{B}^T$. $\boldsymbol{b} = \boldsymbol{A}^T\boldsymbol{P}_l\boldsymbol{l} \in \mathrm{Im}(\boldsymbol{A}^T) = \mathrm{Im}(\boldsymbol{N})$. $\boldsymbol{b}$ is therefore equal to its own projection onto $\mathrm{Im}(\boldsymbol{N})$ parallelly to $\mathrm{Im}(\boldsymbol{C})$: $\boldsymbol{b} = \boldsymbol{N}\boldsymbol{B}(\boldsymbol{B}^T\boldsymbol{N}\boldsymbol{B})^{-1}\boldsymbol{B}^T\boldsymbol{b} = \boldsymbol{N}\hat{\boldsymbol{x}}_c$. ☐

Let us finally give a geometric interpretation of minimal constraints illustrated in Fig. B.2. The non-constrained normal equation $\boldsymbol{N}\boldsymbol{x} = \boldsymbol{b}$ is in fact the equation of a c-dimensional affine subspace of $\mathbb{R}^p$ parallel to $\mathrm{Ker}(\boldsymbol{N})$. The constraint equation $\boldsymbol{C}^T\boldsymbol{x} = \boldsymbol{0}$ additionally imposes that the estimated parameters lie in the $p - c$-dimensional subspace $\mathrm{Ker}(\boldsymbol{C}^T)$. The solution $\hat{\boldsymbol{x}}_c$ of the constrained normal equation is the unique intersection between the affine subspace $\boldsymbol{N}\boldsymbol{x} = \boldsymbol{b}$ and $\mathrm{Ker}(\boldsymbol{C}^T)$.

B.2.4 Removing unreported minimal constraints

In their SINEX files, some Analysis Centers provide minimally constrained solutions without providing information about which exact constraints they applied. It is thus impossible to recover the AC non-constrained normal equation in the standard way

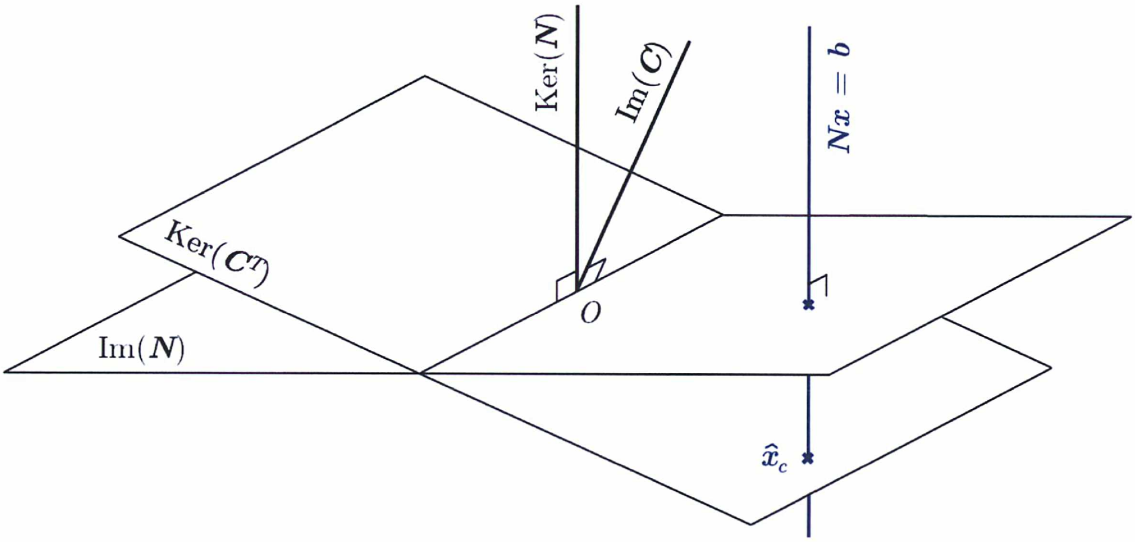

Figure B.2 Geometrical interpretation of minimal constraints

(i.e. using Eq. 1.9). As described below, there however exists a trick to remove such unreported minimal constraints.

Suppose that an AC solved the minimally constrained normal equation:

$$(\boldsymbol{N} + \boldsymbol{C}\boldsymbol{P}_c\boldsymbol{C}^T)(\boldsymbol{x} - \boldsymbol{x}_0) = \boldsymbol{b} \tag{B.21}$$

and provided in its SINEX file the a priori parameters $\boldsymbol{x}_0$, the estimated parameters $\boldsymbol{x}$ and their covariance matrix $\boldsymbol{Q} = (\boldsymbol{N} + \boldsymbol{C}\boldsymbol{P}_c\boldsymbol{C}^T)^{-1}$. By inverting $\boldsymbol{Q}$, it is possible to recover the constrained normal matrix $\boldsymbol{N}_{tot} = \boldsymbol{N} + \boldsymbol{C}\boldsymbol{P}_c\boldsymbol{C}^T$. But without knowing the normal matrix of constraints $\boldsymbol{C}\boldsymbol{P}_c\boldsymbol{C}^T$, it is a priori not possible to recover the non-constrained normal matrix $\boldsymbol{N}$.

Suppose now that the theoretical singularities of $\boldsymbol{N}$ are known so that a matrix $\boldsymbol{D}$ can be built whose columns form a basis of Ker($\boldsymbol{N}$). The non-constrained normal matrix $\boldsymbol{N}$ can in this case actually be recovered, without knowing the normal matrix of constraints, by:

$$\boldsymbol{N} = \boldsymbol{N}_{tot} - \boldsymbol{N}_{tot}\boldsymbol{D}(\boldsymbol{D}^T\boldsymbol{N}_{tot}\boldsymbol{D})^{-1}\boldsymbol{D}^T\boldsymbol{N}_{tot} \tag{B.22}$$

Proof. Since $\boldsymbol{D}$ is of full rank and $\boldsymbol{N}_{tot}$ is symmetric positive definite, corollary A.8 first ensures the invertibility of $\boldsymbol{D}^T\boldsymbol{N}_{tot}\boldsymbol{D}$. Let us now expand $\boldsymbol{N}_{tot}$ into $\boldsymbol{N} + \boldsymbol{C}\boldsymbol{P}_c\boldsymbol{C}^T$ in the right-hand side of Eq. B.22. Since the columns of $\boldsymbol{D}$ lie in Ker($\boldsymbol{N}$), $\boldsymbol{D}\boldsymbol{N} = \boldsymbol{0}$, so that:

$$\boldsymbol{N}_{tot} - \boldsymbol{N}_{tot}\boldsymbol{D}(\boldsymbol{D}^T\boldsymbol{N}_{tot}\boldsymbol{D})^{-1}\boldsymbol{D}^T\boldsymbol{N}_{tot} = \boldsymbol{N} + \boldsymbol{C}\boldsymbol{P}_c\boldsymbol{C}^T - \boldsymbol{C}\boldsymbol{P}_c\boldsymbol{C}^T\boldsymbol{D}(\boldsymbol{D}^T\boldsymbol{C}\boldsymbol{P}_c\boldsymbol{C}^T\boldsymbol{D})^{-1}\boldsymbol{D}^T\boldsymbol{C}\boldsymbol{P}_c\boldsymbol{C}^T \tag{B.23}$$

According to corollary A.12, Im($\boldsymbol{C}$) and Im($\boldsymbol{N}$) = Ker($\boldsymbol{D}^T$) are direct complementary subspaces of $\mathbb{R}^p$. Proposition A.10 therefore ensures the invertibility of $\boldsymbol{D}^T\boldsymbol{C}$ and $\boldsymbol{C}^T\boldsymbol{D}$. The third term in Eq. B.23 thus simplifies to $-\boldsymbol{C}\boldsymbol{P}_c\boldsymbol{C}^T$ and cancels with the second term. This proves Eq. B.22. ☐

B.2.5 No-net-rotation, no-net-translation and no-net-scale constraints

As mentioned in Sect. 1.2.1, none of the four geodetic techniques contributing to the ITRF provides enough information to unambiguously estimate the tracking station coordinates. In an SLR, GNSS or DORIS analysis, the normal matrix thus has three "orientation singularities", while a VLBI normal matrix has three additional "origin singularities". A common practice to overcome these singularities is to apply so-called *no-net-rotation* and *no-net-translation* constraints. Such constraints respectively guarantee that the orientation and the origin of the estimated terrestrial frame are the same as that of the a priori terrestrial frame (for instance the ITRF, if ITRF coordinates are used as a priori station coordinates).

No-net-rotation constraints Let us consider a parameter vector $\boldsymbol{x} = [X^1, Y^1, Z^1, \ldots, X^k, Y^k, Z^k]$ made of $3k$ station coordinates and a corresponding vector of a priori parameters $\boldsymbol{x}_0 = [X_0^1, Y_0^1, Z_0^1, \ldots, X_0^k, Y_0^k, Z_0^k]$. The goal of no-net-rotation constraints is to ensure that, if differential rotations are estimated between $\boldsymbol{x}$ and $\boldsymbol{x0}$, they should be zero. The estimation of differential rotations between $\boldsymbol{x}$ and $\boldsymbol{x0}$ corresponds to the following observation equations:

$$\begin{bmatrix} X^1 \\ Y^1 \\ Z^1 \\ \vdots \\ X^k \\ Y^k \\ Z^k \end{bmatrix} = \begin{bmatrix} X_0^1 \\ Y_0^1 \\ Z_0^1 \\ \vdots \\ X_0^k \\ Y_0^k \\ Z_0^k \end{bmatrix} + \begin{bmatrix} 0 & Z_0^1 & -Y_0^1 \\ -Z_0^1 & 0 & X_0^1 \\ Y_0^1 & -X_0^1 & 0 \\ \vdots & \vdots & \vdots \\ 0 & Z_0^k & -Y_0^k \\ -Z_0^k & 0 & X_0^k \\ Y_0^k & -X_0^k & 0 \end{bmatrix} \begin{bmatrix} r_X \\ r_Y \\ r_Z \end{bmatrix} \tag{B.24}$$

or, in matrix notations, $\boldsymbol{x} = \boldsymbol{x}_0 + \boldsymbol{A}_r\boldsymbol{r}$. It leads to the following differential rotation estimates:

$$\hat{\boldsymbol{r}} = (\boldsymbol{A}_r^T\boldsymbol{A}_r)^{-1}\boldsymbol{A}_r^T(\boldsymbol{x} - \boldsymbol{x}_0) \tag{B.25}$$

Nullifying the differential rotations between $\boldsymbol{x}$ and $\boldsymbol{x}_0$ can thus be done by imposing the following constraint equation:

$$(\boldsymbol{A}_r^T\boldsymbol{A}_r)^{-1}\boldsymbol{A}_r^T(\boldsymbol{x} - \boldsymbol{x}_0) = \boldsymbol{0} \tag{B.26}$$

i.e. by taking $\boldsymbol{C}^T = (\boldsymbol{A}_r^T\boldsymbol{A}_r)^{-1}\boldsymbol{A}_r^T$ as constraint matrix.

No-net-translation constraints Similarly, nullifying the differential translations between $\boldsymbol{x}$ and $\boldsymbol{x}_0$ can be done by taking $\boldsymbol{C}^T = (\boldsymbol{A}_t^T\boldsymbol{A}_t)^{-1}\boldsymbol{A}_t^T$ as constraint matrix, where the matrix $\boldsymbol{A}_t$ of station coordinate / translation partial derivatives has the following form:

$$A_t = \begin{bmatrix} 1 & 0 & 0 \\ 0 & 1 & 0 \\ 0 & 0 & 1 \\ \vdots & \vdots & \vdots \\ 1 & 0 & 0 \\ 0 & 1 & 0 \\ 0 & 0 & 1 \end{bmatrix} \tag{B.27}$$

No-net-scale constraints There may finally be some special cases in which the scale of the estimated frame should be the same as that of the a priori frame. This is done by taking $\boldsymbol{C}^T = (\boldsymbol{A}_s^T \boldsymbol{A}_s)^{-1} \boldsymbol{A}_s^T$ as constraint matrix where $\boldsymbol{A}_s$ has the following form:

$$\boldsymbol{A}_s = [X_0^1, Y_0^1, Z_0^1, \ldots, X_0^k, Y_0^k, Z_0^k]^T \tag{B.28}$$

It is possible to simultaneously impose several of the previous constraints, by grouping the corresponding matrices $\boldsymbol{A}_r$, $\boldsymbol{A}_t$ and $\boldsymbol{A}_s$ into a single matrix $\boldsymbol{A}$ and taking $\boldsymbol{C}^T = (\boldsymbol{A}^T \boldsymbol{A})^{-1} \boldsymbol{A}^T$ as constraint matrix. By nullifying specific lines of the matrix $\boldsymbol{A}$, it is also possible to apply the desired constraints via a specific subset of stations only. Note, finally, that in case of a long-term linear frame made of station positions and velocities, no-net-rotation-rate, no-net-translation-rate and no-net-scale-rate constraints can additionally be defined. They respectively take exactly the same form as no-net-rotation, no-net-translation and no-net-scale constraints except that they apply to station velocities.

B.3 Reduction and fixation of parameters

In huge least-squares problems with thousands of parameters, such as GNSS data analysis, not all parameters may be of interest. A well-known method to reduce the size of such problems is called *reduction* of the nuisance parameters and basically consists in a block-inversion of the normal matrix. Reducing nuisance parameters does not affect the estimated values of the parameters of interest, neither their covariance matrix, as the reduced parameters are still implicitly present in the reduced normal equation.

Another way to get rid of certain parameters is to simply fix them to their a priori values, i.e. to remove the corresponding lines and columns from the normal matrix. Unlike parameter reduction, the fixation of some parameters generally changes the values of the other parameters as well as their covariance matrix, as the subsequent model does not allow implicit variations of the fixed parameters.

This section reviews the mathematical formulations of parameter reduction and fixation and gives geometric interpretations of both operations. An inequality is finally given between the parameter covariance matrix obtained after reduction of some parameters and the parameter covariance matrix obtained after fixation of the same parameters.

For the sake of simplicity, it is assumed in this section that the design matrix $\boldsymbol{A}$ is of full rank, so that the normal matrix $\boldsymbol{N}$ is symmetric positive definite and no constraints are required. However, the results presented in this section can easily be extended to the case where $\boldsymbol{A}$ and $\boldsymbol{N}$ have rank deficiencies supplemented by (not necessarily minimal) constraints.

B.3.1 Parameter reduction

Reduced normal equation Suppose that the model parameters are ordered in such a way that $\boldsymbol{x} = [\boldsymbol{x}_1^T, \boldsymbol{x}_2^T]^T$, where $\boldsymbol{x}_1$ contains the parameters of interest, while $\boldsymbol{x}_2$ contains the nuisance parameters we would like to reduce. The normal equation $\boldsymbol{N}\boldsymbol{x} = \boldsymbol{b}$ can be block-decomposed into:

$$\begin{bmatrix} \boldsymbol{N}_{11} & \boldsymbol{N}_{12} \\ \boldsymbol{N}_{21} & \boldsymbol{N}_{22} \end{bmatrix} \begin{bmatrix} \boldsymbol{x}_1 \\ \boldsymbol{x}_2 \end{bmatrix} = \begin{bmatrix} \boldsymbol{b}_1 \\ \boldsymbol{b}_2 \end{bmatrix} \tag{B.29}$$

Under the hypothesis that $\boldsymbol{N}$ is symmetric definite positive, hence invertible, its lower right block $\boldsymbol{N}_{22}$ is itself invertible so that the second set of equations in B.24 can be used to obtain an expression of the nuisance parameters $\boldsymbol{x}_2$ in function of $\boldsymbol{x}_1$:

$$\boldsymbol{x}_2 = \boldsymbol{N}_{22}^{-1}(\boldsymbol{b}_2 - \boldsymbol{N}_{21}\boldsymbol{x}_1) \tag{B.30}$$

Substituting B.30 into the first set of equations in B.29 yields:

$$\begin{array}{rrcl} & (\boldsymbol{N}_{11} - \boldsymbol{N}_{12}\boldsymbol{N}_{22}^{-1}\boldsymbol{N}_{21})\,\boldsymbol{x}_1 & = & \boldsymbol{b}_1 - \boldsymbol{N}_{12}\boldsymbol{N}_{22}^{-1}\boldsymbol{b}_2 \\ \Leftrightarrow & \boldsymbol{N}_r\,\boldsymbol{x}_1 & = & \boldsymbol{b}_r \end{array} \tag{B.31}$$

Eq. B.31 is called reduced normal equation and allows to compute the values of the parameters of interest by solving a smaller system than the full normal equation. To obtain the reduced normal equation, one however needs to invert the right-bottom block $\boldsymbol{N}_{22}$ of the full normal matrix, which may be almost as huge as the full normal matrix itself. However, in the case of GNSS data analysis, the reduced parameters are usually epoch-wise station and satellite clock offsets, so that $\boldsymbol{N}_{22}$ has a block-diagonal structure and is efficiently invertible.

Still assuming that $\boldsymbol{N}$ is invertible, the reduced normal matrix $\boldsymbol{N}_r$ is itself invertible (see proof of proposition A.18). The parameter covariance matrix obtained from the reduced normal equation is thus $\boldsymbol{Q}_r = \boldsymbol{N}_r^{-1} = (\boldsymbol{N}_{11} - \boldsymbol{N}_{12}\boldsymbol{N}_{22}^{-1}\boldsymbol{N}_{21})^{-1}$. According to the block matrix inversion formula A.18, $\boldsymbol{Q}_r$ is nothing but the upper-left block $\boldsymbol{Q}_{11}$ of the full covariance matrix $\boldsymbol{Q}$. This proves that the covariance matrix obtained for $\boldsymbol{x}_1$ is unaffected by the reduction of $\boldsymbol{x}_2$.

Parameter reduction as an oblique projection Let us also split the design matrix $\boldsymbol{A}$ into two column blocks $[\boldsymbol{A}_1\boldsymbol{A}_2]$. $\mathrm{Im}(\boldsymbol{A}_1)$ is the subspace of $\mathrm{Im}(\boldsymbol{A})$ generated by the parameters of interest. If $\boldsymbol{A}$ is assumed of full rank, the subspace $\mathrm{Im}(\boldsymbol{A}_2)$ generated by the nuisance parameters is a direct supplementary subspace of $\mathrm{Im}(\boldsymbol{A}_1)$ in $\mathrm{Im}(\boldsymbol{A})$. The observations $\boldsymbol{A}\boldsymbol{x}$ predicted by the whole set of parameters $\boldsymbol{x}$ can thus be decomposed into a unique sum of two terms:

- $\boldsymbol{A}_1\boldsymbol{x}_1$: part of the observations predicted by the parameters of interest;
- $\boldsymbol{A}_2\boldsymbol{x}_2$: part of the observations predicted by the nuisance parameters.

Reducing $\boldsymbol{x}_2$ consists in finding $\boldsymbol{A}_1\boldsymbol{x}_1$ and consequently $\boldsymbol{x}_1$ directly from the observations $\boldsymbol{l}$. We will now show that it is achieved through an oblique projection of $\boldsymbol{l}$ onto $\mathrm{Im}(\boldsymbol{A}_1)$.

Noting that

$$\begin{bmatrix} \boldsymbol{N}_{11} & \boldsymbol{N}_{12} \\ \boldsymbol{N}_{21} & \boldsymbol{N}_{22} \end{bmatrix} = \begin{bmatrix} \boldsymbol{A}_1^T\boldsymbol{P}_l\boldsymbol{A}_1 & \boldsymbol{A}_1^T\boldsymbol{P}_l\boldsymbol{A}_2 \\ \boldsymbol{A}_2^T\boldsymbol{P}_l\boldsymbol{A}_1 & \boldsymbol{A}_2^T\boldsymbol{P}_l\boldsymbol{A}_2 \end{bmatrix} \quad \text{and} \quad \begin{bmatrix} \boldsymbol{b}_1 \\ \boldsymbol{b}_2 \end{bmatrix} = \begin{bmatrix} \boldsymbol{A}_1^T\boldsymbol{P}_l\boldsymbol{l} \\ \boldsymbol{A}_2^T\boldsymbol{P}_l\boldsymbol{l} \end{bmatrix} \tag{B.32}$$

the solution of the reduced normal equation can be re-written as

$$\boldsymbol{x}_1 = (\boldsymbol{B}^T\boldsymbol{P}_l\boldsymbol{A}_1)^{-1}\boldsymbol{B}^T\boldsymbol{P}_l\boldsymbol{l} \;\text{ with }\; \boldsymbol{B}^T = \boldsymbol{A}_1^T\left(\boldsymbol{I} - \boldsymbol{P}_l\boldsymbol{A}_2(\boldsymbol{A}_2^T\boldsymbol{P}_l\boldsymbol{A}_2)^{-1}\boldsymbol{A}_2^T\right) \tag{B.33}$$

The observations predicted by the parameters of interest $\boldsymbol{x}_1$ are consequently:

$$\boldsymbol{A}_1\boldsymbol{x}_1 = \boldsymbol{A}_1(\boldsymbol{B}^T\boldsymbol{P}_l\boldsymbol{A}_1)^{-1}\boldsymbol{B}^T\boldsymbol{P}_l\boldsymbol{l} \tag{B.34}$$

$\boldsymbol{A}_1(\boldsymbol{B}^T\boldsymbol{P}_l\boldsymbol{A}_1)^{-1}\boldsymbol{B}^T\boldsymbol{P}_l$ can be recognized as the matrix form of an oblique projection onto $\mathrm{Im}(\boldsymbol{A}_1)$. It is in fact equivalent to an orthogonal projection onto $\mathrm{Im}(\boldsymbol{A})$ followed by a projection onto $\mathrm{Im}(\boldsymbol{A}_1)$ parallelly to $\mathrm{Im}(\boldsymbol{A}_2)$ (see Fig. B.3). Very informally, one could say that the reduced system keeps in memory the existence of the reduced parameters, so that it "knows" which part of the observations should be attributed to the parameters of interest and which part to the nuisance parameters, i.e. what is the "right" direction for projecting the observations onto $\mathrm{Im}(\boldsymbol{A}_1)$.

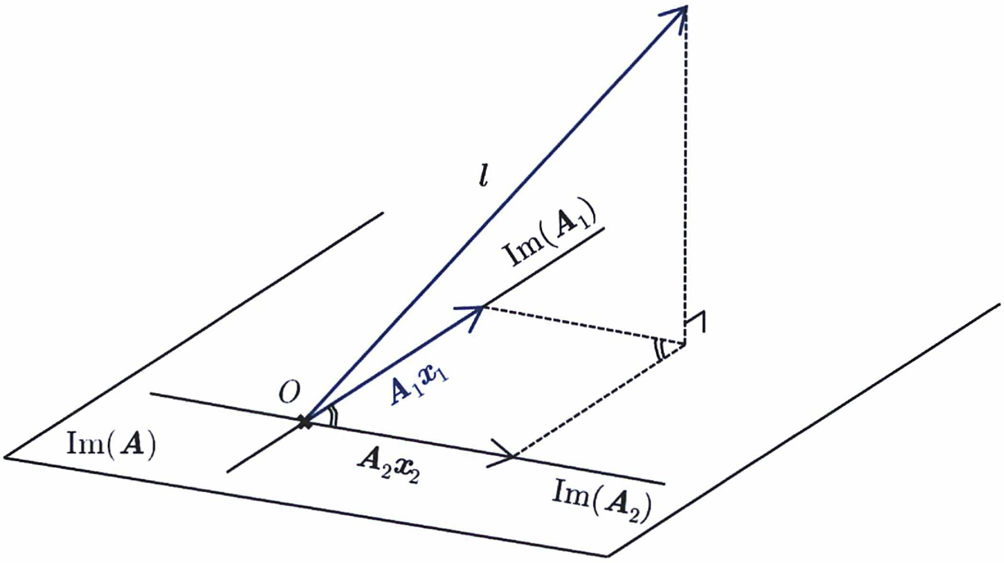

Figure B.3 Parameter reduction as an oblique projection onto $\mathrm{Im}(\boldsymbol{A}_1)$

B.3.2 Parameter fixation

Let us now examine the case where the subset of parameters $\boldsymbol{x}_2$ are simply removed from the model, or, in other words, fixed to their a priori values. This leads to a smaller least-squares system with $\boldsymbol{A}_f = \boldsymbol{A}_1$ as design matrix, $\boldsymbol{N}_f = \boldsymbol{A}_1^T \boldsymbol{P}_l \boldsymbol{A}_1 = \boldsymbol{N}_{11}$ as normal matrix, and $\boldsymbol{b}_f = \boldsymbol{A}_1^T \boldsymbol{P}_l \boldsymbol{l} = \boldsymbol{b}_1$ as second member of the normal equation. Under the hypothesis that $\boldsymbol{N}$ is symmetric definite positive, hence invertible, its upper left block $\boldsymbol{N}_{11}$ is itself invertible. The solution of the new system is therefore $\boldsymbol{x}_f = \boldsymbol{N}_{11}^{-1}\boldsymbol{b}_1 = (\boldsymbol{A}_1^T \boldsymbol{P}_l \boldsymbol{A}_1)^{-1}\boldsymbol{A}_1^T \boldsymbol{P}_l \boldsymbol{l}$ and the predicted observations are $\boldsymbol{A}_f\boldsymbol{x}_f = \boldsymbol{A}_1(\boldsymbol{A}_1^T \boldsymbol{P}_l \boldsymbol{A}_1)^{-1}\boldsymbol{A}_1^T \boldsymbol{P}_l \boldsymbol{l}$, i.e. the orthogonal projection of $\boldsymbol{l}$ onto $\mathrm{Im}(\boldsymbol{A}_1)$.

While, if reduced, the parameters $\boldsymbol{x}_2$ implicitly remain in the reduced system, this is not the case when they are fixed. The new system does not "remember" the existence of the fixed parameters, so that it projects the observations directly orthogonally onto $\mathrm{Im}(\boldsymbol{A}_1)$. As a consequence, its solution $\boldsymbol{x}_f$ is generally different from $\boldsymbol{x}_1$. The covariance matrix of $\boldsymbol{x}_f$, $\boldsymbol{Q}_f = \boldsymbol{N}_f^{-1} = \boldsymbol{N}_{11}^{-1}$ is also generally different from $\boldsymbol{Q}_r = \boldsymbol{Q}_{11}$.

B.3.3 Inequality between $\boldsymbol{Q}_f$ and $\boldsymbol{Q}_r$

Still assuming that $\boldsymbol{N}$ and hence $\boldsymbol{Q} = \boldsymbol{N}^{-1}$ are positive definite, the parameter covariance matrix $\boldsymbol{Q}_f$ obtained in the fixation case can be expressed, using the block matrix inversion formula A.18, in function of the blocks of the full covariance matrix $\boldsymbol{Q}$:

$$\boldsymbol{Q}_f = \boldsymbol{N}_{11}^{-1} = \boldsymbol{Q}_{11} - \boldsymbol{Q}_{12}\boldsymbol{Q}_{22}^{-1}\boldsymbol{Q}_{21} \tag{B.35}$$

$\boldsymbol{Q}_r - \boldsymbol{Q}_f = \boldsymbol{Q}_{11} - \boldsymbol{Q}_f = \boldsymbol{Q}_{12}\boldsymbol{Q}_{22}^{-1}\boldsymbol{Q}_{21}$ is clearly positive definite, so that we have

$$\boldsymbol{Q}_f < \boldsymbol{Q}_r \tag{B.36}$$

in the sense that for two square matrices $\boldsymbol{A}$ and $\boldsymbol{B}$, $\boldsymbol{A} < \boldsymbol{B}$ if $\boldsymbol{B} - \boldsymbol{A}$ is positive definite.

To give a more concrete interpretation of this inequality, let $q = \boldsymbol{\lambda}^T\boldsymbol{x}_1$ be any non-zero linear combination of the parameters $\boldsymbol{x}_1$. The variance of q obtained in the reduction case is $\sigma_r^2 = \boldsymbol{\lambda}^T\boldsymbol{Q}_r\boldsymbol{\lambda}$, while its variance in the fixation case is $\sigma_f^2 = \boldsymbol{\lambda}^T\boldsymbol{Q}_f\boldsymbol{\lambda}$. We have

$$\sigma_r^2 - \sigma_f^2 = \boldsymbol{\lambda}^T(\boldsymbol{Q}_r - \boldsymbol{Q}_f)\boldsymbol{\lambda} = \boldsymbol{\lambda}^T\boldsymbol{Q}_{12}\boldsymbol{Q}_{22}^{-1}\boldsymbol{Q}_{21}\boldsymbol{\lambda} > 0 \tag{B.37}$$

so that any non-zero linear combination of the parameters $\boldsymbol{x}_1$ has a larger variance in the reduction case than in the fixation case. This inequality applies in particular to the variances of each individual parameter in $\boldsymbol{x}_1$.

Informally, one could say that in the reduction case, the reduced system "remembers" the uncertainties of the pre-eliminated parameters $\boldsymbol{x}_2$ and their correlations with $\boldsymbol{x}_1$, which contribute together to the total uncertainty of $\boldsymbol{x}_1$. On the other hand, this additional source of uncertainty is "forgotten" in the fixation case, as can be readily seen in Eq. B.35.

Appendix C

Geocenter motion estimates from the IGS Analysis Centres

Several figures mentioned in Sect. 2.4.1 are grouped in this appendix for practical reasons. The translation time series shown therein result from Rebischung et al. (2012)'s study. Their computation is detailed in Sect. 2.4.1.

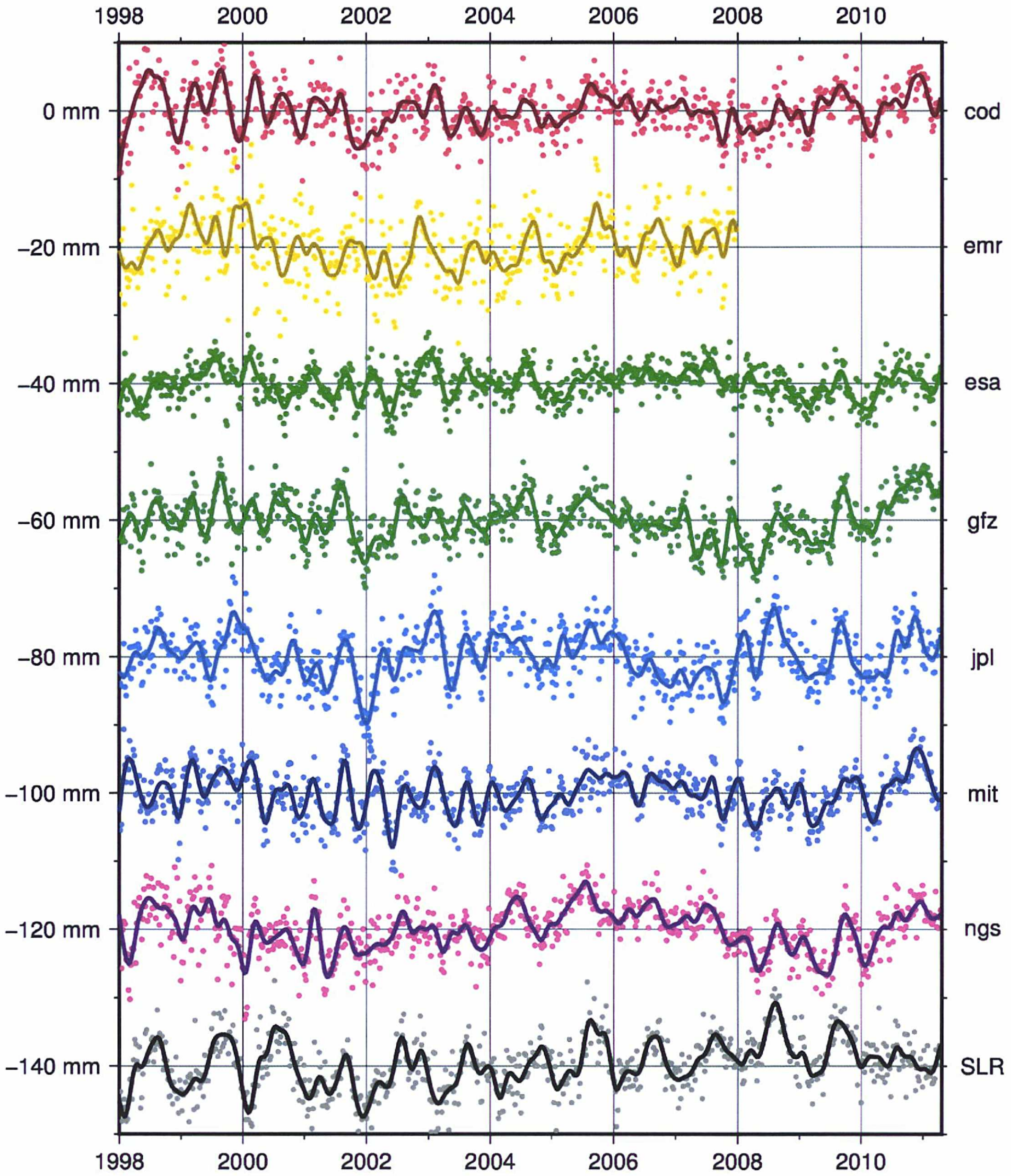

Figure C.1 X translation time series derived from the reprocessed solutions of seven IGS ACs as well as from reprocessed SLR solutions, shifted by multiples of 20 mm. The dots represent weekly translation estimates. The solid lines were obtained by Vondrak-filtering each of the series with a cut-off frequency of 3 cpy.

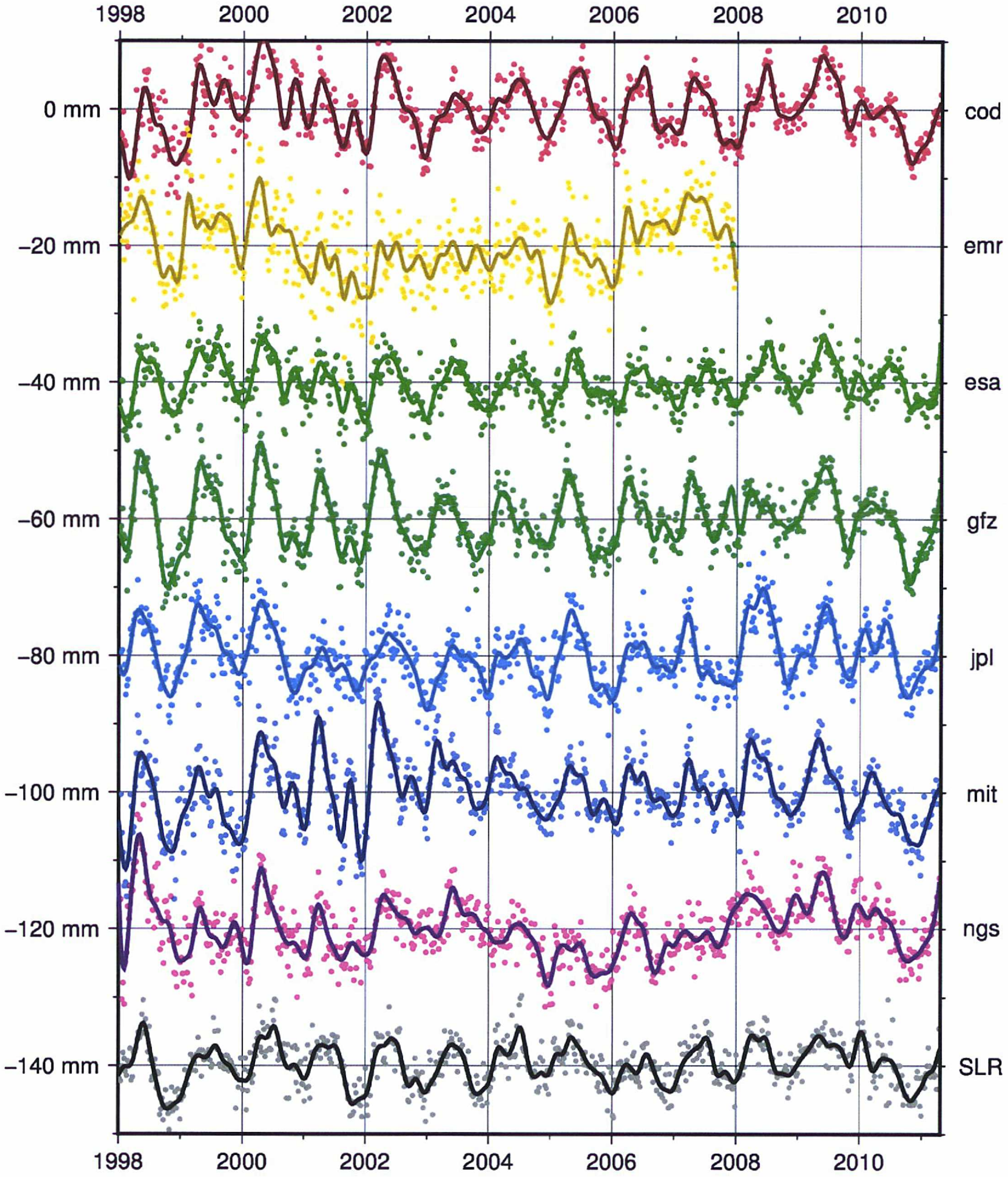

Figure C.2 Y translation time series derived from the reprocessed solutions of seven IGS ACs as well as from reprocessed SLR solutions, shifted by multiples of 20 mm. The dots represent weekly translation estimates. The solid lines were obtained by Vondrak-filtering each of the series with a cut-off frequency of 3 cpy.

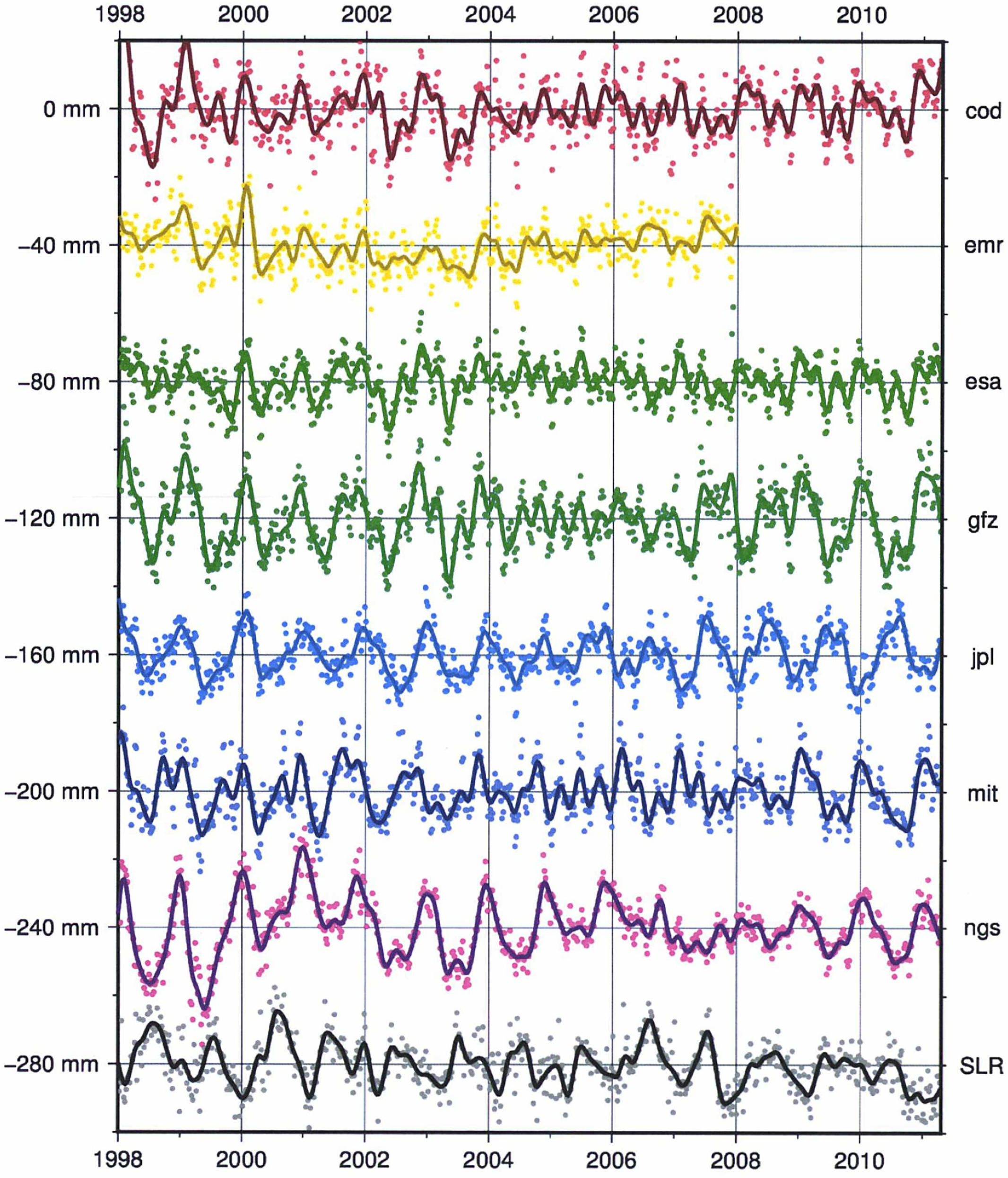

Figure C.3 Z translation time series derived from the reprocessed solutions of seven IGS ACs as well as from reprocessed SLR solutions, shifted by multiples of 40 mm. The dots represent weekly translation estimates. The solid lines were obtained by Vondrak-filtering each of the series with a cut-off frequency of 3 cpy.

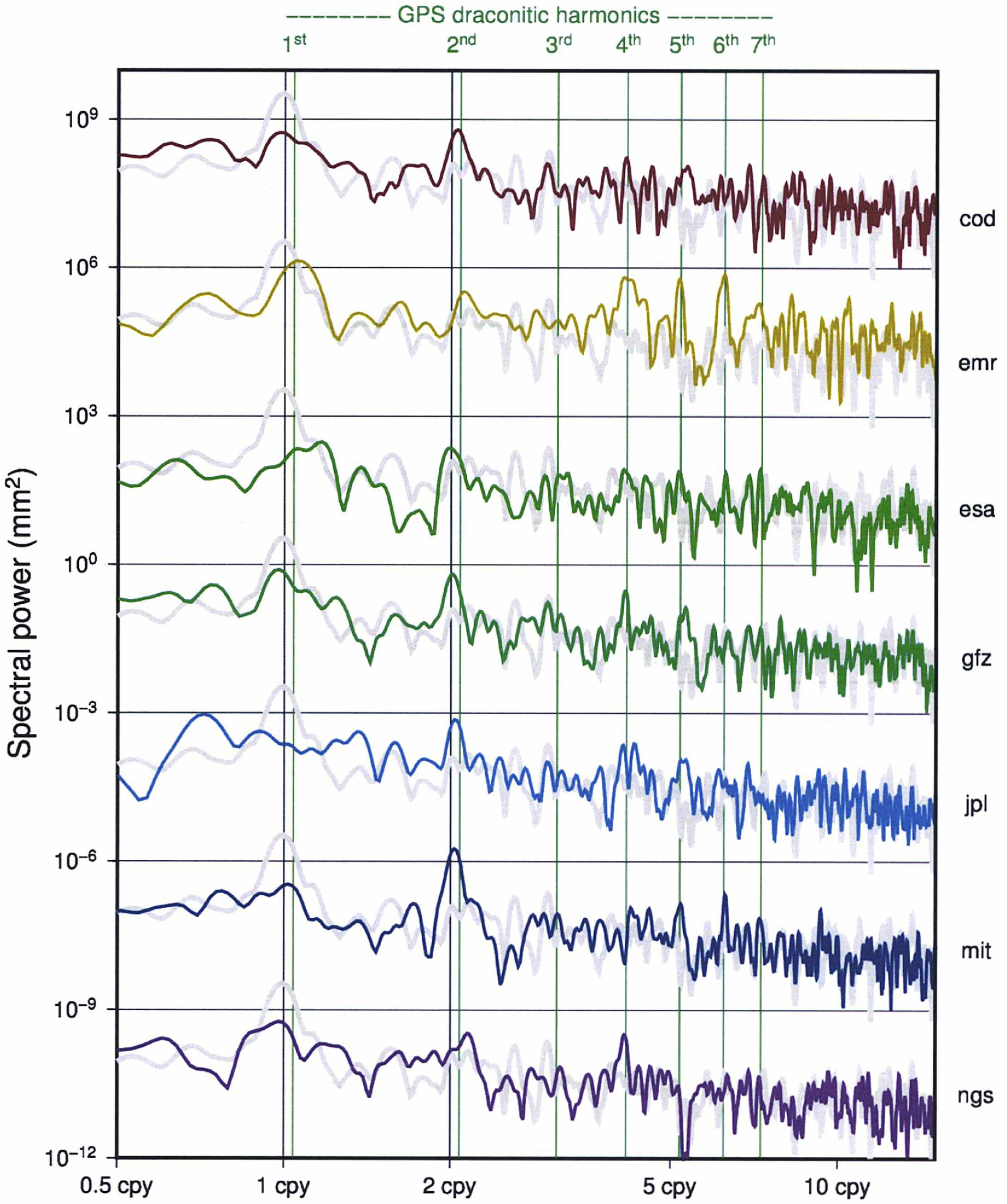

Figure C.4 Lomb-Scargle periodograms of the X translation time series shown in Fig. C.1, shifted by powers of 10^3 mm^2. The background grey lines correspond to the SLR X translation time series. For better legibility, the periodograms were computed over a 4 times oversampled frequency set and boxcar smoothed over 5 adjacent frequencies.

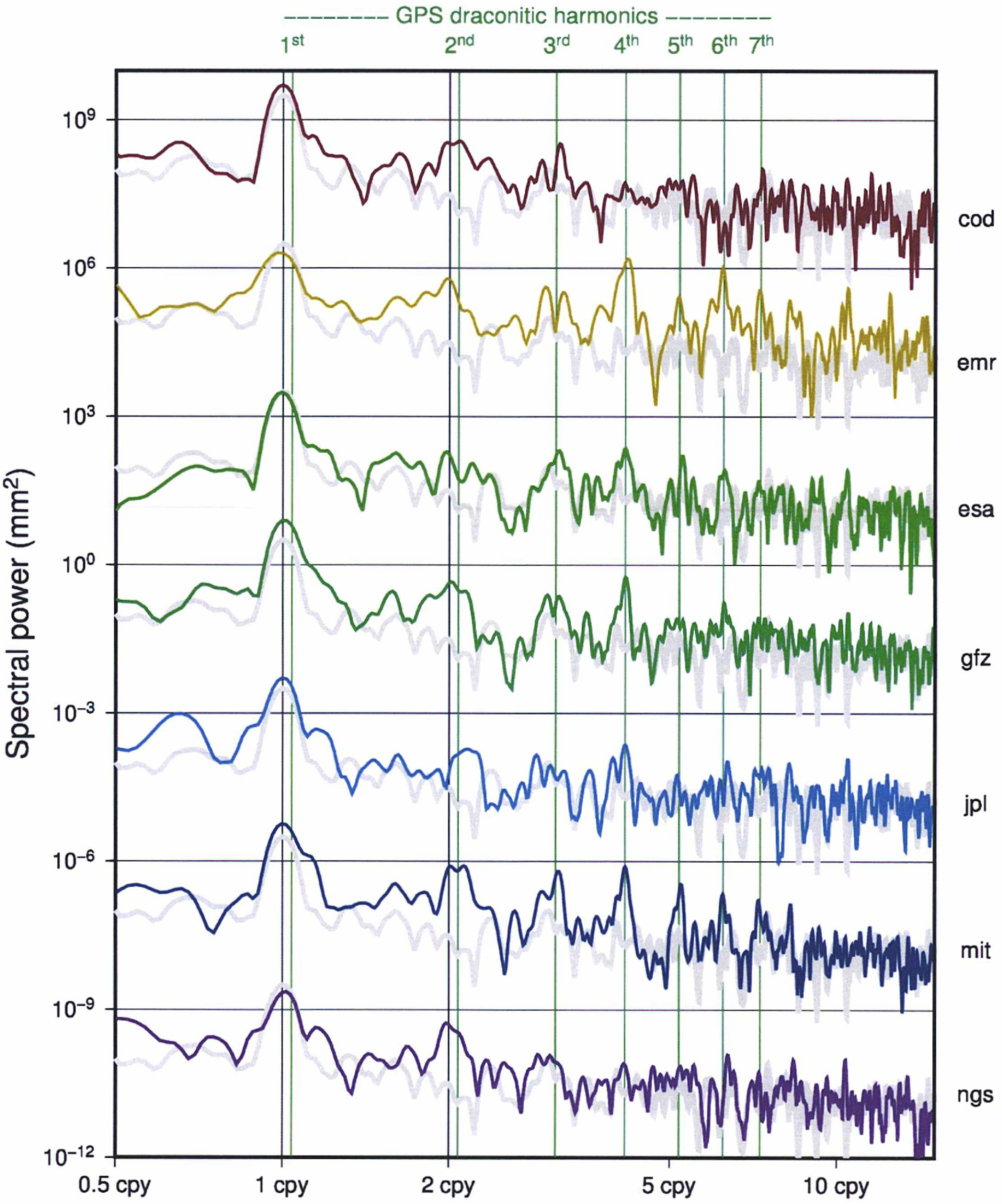

Figure C.5 Lomb-Scargle periodograms of the Y translation time series shown in Fig. C.2, shifted by powers of 10^3 mm^2. The background grey lines correspond to the SLR Y translation time series. For better legibility, the periodograms were computed over a 4 times oversampled frequency set and boxcar smoothed over 5 adjacent frequencies.

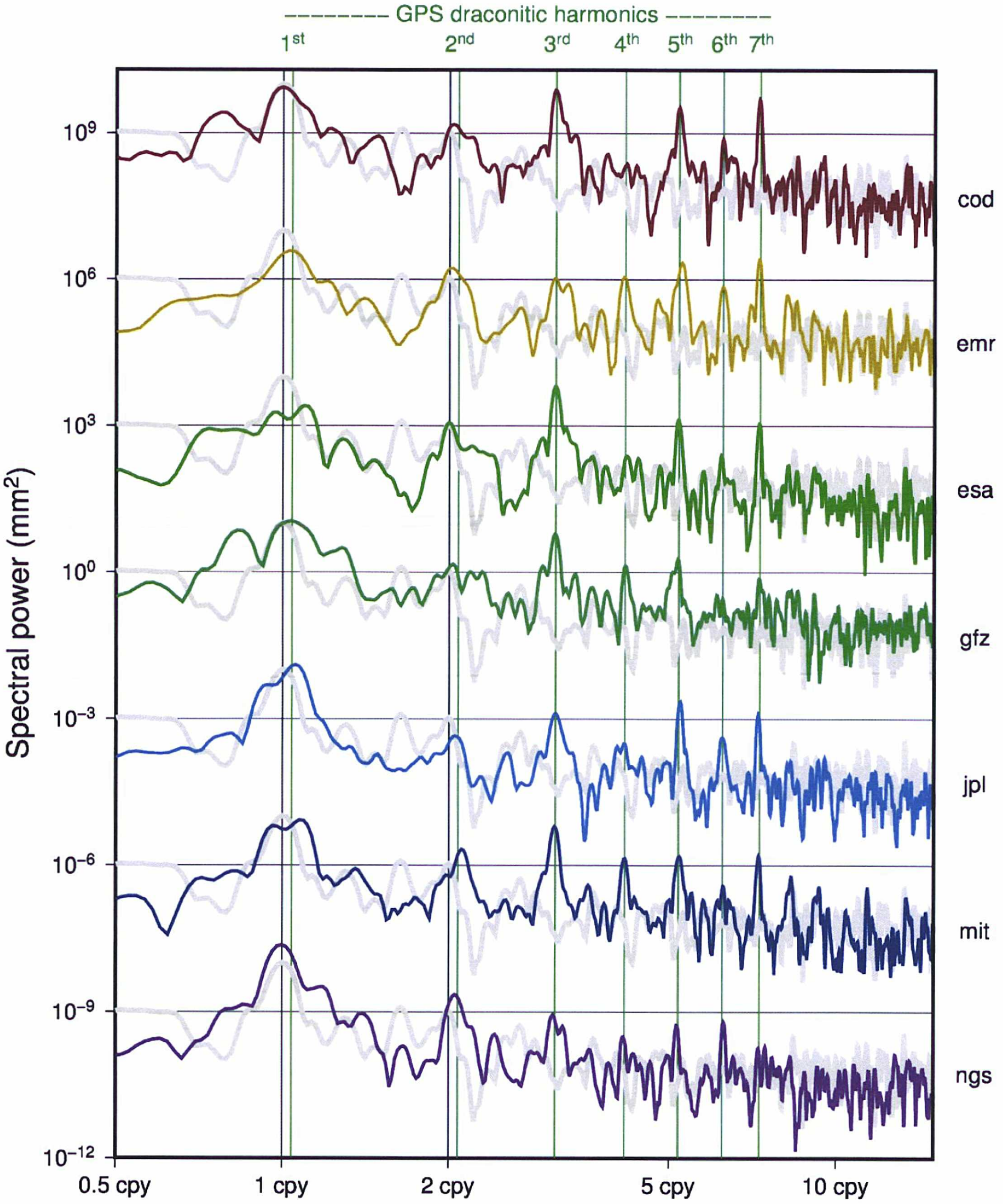

Figure C.6 Lomb-Scargle periodograms of the Z translation time series shown in Fig. C.3, shifted by powers of 10^3 mm^2. The background grey lines correspond to the SLR Z translation time series. For better legibility, the periodograms were computed over a 4 times oversampled frequency set and boxcar smoothed over 5 adjacent frequencies.

Appendix D

Collinearity of the Z geocenter coordinate with the osculating elements of elliptical orbits

The purpose of this appendix is to show how the epoch mean signature of the Z geocenter coordinate can be reproduced by variations of the satellite osculating elements in case of ellipitical orbits. The case of circular orbits was treated in Sect. 4.4.3: in that case, the epoch mean signature of the Z geocenter coordinate can simply be reproduced by slight "ellipticizations" of the satellite orbits.

D.1 Signature of the Z geocenter coordinate in case of elliptical orbits

Fig. D.1 shows the signature of a variation $\delta t = 1$ cm of the Z geocenter coordinate on simulated observations made by a tracking network of 400 stations on a satellite with an elliptical orbit. The orbit of the considered satellite is similar to a LAGEOS orbit, except for the eccentricity ($a = 12200$ km, $e = 0.2$, $i = 110°$). The magenta line in Fig. D.1 does not represent an epoch mean signature, but $-\delta t \sin \phi$, where ϕ denotes the latitude of the satellite. It can in fact be shown that, for an infinitely dense tracking network on a spherical Earth, the epoch mean signature of the Z geocenter coordinate would exactly match the epoch mean signature of a shift of the orbit radius by $\delta r = -\delta t \sin \phi$.

This equality does not strictly hold in real observation conditions. But the epoch mean signature of the Z geocenter coordinate nevertheless remains close to the epoch mean signature of a shift of the orbit radius by $\delta r = -\delta t \sin\phi$. We will therefore limit ourselves to showing how specific variations of the satellite osculating elements can lead to a variation of the orbit radius by $\delta r = -\delta t \sin\phi$.

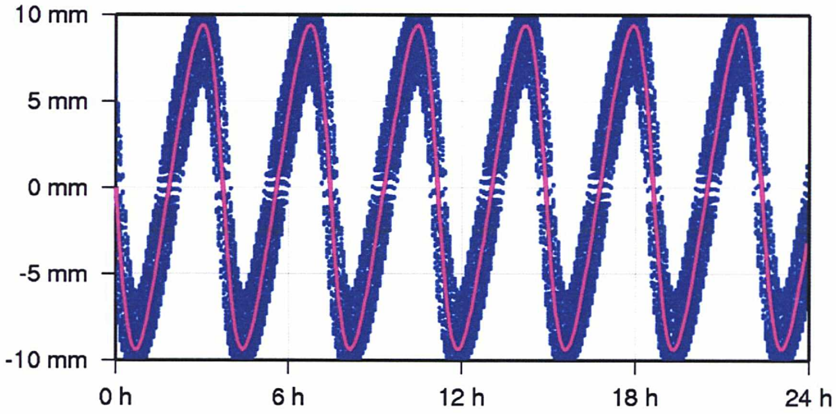

Figure D.1 Signature of a 1 cm variation of the Z geocenter coordinates on simulated observations made on a satellite with an elliptical orbit. Each blue dot represents an element of S_y. The magenta line represents $-\delta t \sin\phi$, where ϕ denotes the latitude of the satellite.

D.2 Reproduction by variations of the satellite osculating elements

Consider the orbital perturbation induced by:

- a constant variation of the satellite eccentricity by:

$$\delta e = -\frac{\sin i \sin\omega}{a}\delta t \tag{D.1}$$

- a constant variation of the satellite mean anomaly by:

$$\delta M = \frac{\sqrt{1-e^2}}{ae}\sin i \cos\omega \delta t \tag{D.2}$$

From Kepler's equation $M = E - e\sin E$, one finds that δe and δM induce a variation of the satellite eccentric anomaly by:

$$\delta E = \frac{\delta M + \sin E \delta e}{1 - e\cos E} \tag{D.3}$$

Using the relationships between E and the satellite true anomaly ν, one can then express the induced variation of the satellite true anomaly as:

$$\delta\nu = \frac{1 + e\cos\nu}{\sqrt{1-e^2}}\delta E + \frac{\sin\nu}{1-e^2}\delta e = \frac{(1+e\cos\nu)^2}{(1-e^2)^{3/2}}\delta M + \frac{\sin\nu(2+e\cos\nu)}{1-e^2}\delta e \tag{D.4}$$

Finally, from the expression of the orbit radius,

$$r = \frac{a(1-e^2)}{1+e\cos\nu} \tag{D.5}$$

one can obtain the induced variation of the orbit radius:

$$\begin{aligned} \delta r &= \frac{ae(1-e^2)\sin\nu}{(1+e\cos\nu)^2}\delta\nu - \frac{a}{1+e\cos\nu}\left(2e + \frac{(1-e^2)\cos\nu}{1+e\cos\nu}\right)\delta e \\ &= \frac{ae\sin\nu}{\sqrt{1-e^2}}\delta M - a\cos\nu\,\delta e \end{aligned} \tag{D.6}$$

Let us now insert the proposed expressions of δe and δM (Eq. D.1 and D.2) into Eq. D.6. This leads to:

$$\begin{aligned} \delta r &= -\delta t \sin i(\sin\omega\cos\nu + \cos\omega\sin\nu) = -\delta t\sin i\sin u \\ &= -\delta t\sin\phi \end{aligned} \tag{D.7}$$

We have thus shown how specific variations of the satellite osculating elements can induce a variation of the orbit radius by $\delta r = -\delta t\sin\phi$, and therefore approximately reproduce the epoch mean signature of the Z geocenter coordinate.